DESIGN AND SYNTHESIS OF PEROVSKITES AND CORUNDUM DERIVATIVES WITH UNUSUAL MAGNETIC, ELECTRONIC, AND STRUCTURAL COUPLING

By Corey Elizabeth Frank

A dissertation submitted to the
School of Graduate Studies
Rutgers, The State University of New Jersey
in partial fulfillment of the requirements
for the degree of
Doctor of Philosophy
Graduate Program in Chemistry

Written under the direction of
Professor Martha Greenblatt
and approved by

_____

_____

_____

_____

New Brunswick, NJ
January 2021

ABSTRACT OF THE DISSERTATION

Design and Synthesis of Perovskites and Corundum Derivatives with Unusual Magnetic, Electronic, and Structural Coupling

By Corey Elizabeth Frank

Dissertation Director:

Martha Greenblatt

ABO_3 perovskites and derivative structures are versatile materials, critical to the function of modern life, and the discovery of new perovskites is essential to developing the fields of photovoltaics, microelectronics, and telecommunication among others. The Goldschmidt tolerance factor ($t = \frac{(r_A + r_X)}{\sqrt{2}(r_B + r_X)}$) has been used for years to qualitatively predict stable perovskites; this formula predicts that with small A-cations (effective ionic radius < 0.9 Å) and B transition metal B-cations the perovskite structure will not form. With careful synthesis techniques, and the application of high pressure, this limitation can be overcome, unlocking distorted materials with interesting electronic-magnetic-structural coupling behaviors. These materials include highly distorted transition metal only double perovskites, such as Mn_2CoReO_6; quadruple perovskites with a square-planar coordinated A' cation, such as $La_3Mn_4RhO_{12}$; and even double corundum derivatives which feature face-sharing dimers of octahedrally coordinated A and B cations, such as $Fe_{3-x}InSn_xO_6$ (x = 0, 0.25, 0.5) and $In_2Mn_{1.1}Sn_{0.9}O_6$.

Mn_2CoReO_6, the fourth known magnetic transition-metal-only double perovskite oxide (space group $P2_1/n$) was synthesized at high pressure and

temperature (8 GPa, 1350 °C). Double perovskites in which A and B are close in size have been known to exhibit distinct magneto-structural coupling behaviours which are associated with large structural distortions. Single crystal X-ray diffraction and powder synchrotron diffraction confirm that structural distortions are induced by the small A-site Mn^{2+} cations, which are 8-fold coordinated in this structure, in contrast to the 12-fold coordination typical of undistorted perovskites. Mn_2CoReO_6 exhibits complex magnetic properties with exceptionally robust antiferromagnetic order ($T_N \approx$ 94 K) involving all cation sublattices.

When ¾ of the A cations in a perovskite are substituted by a square planar cation or Jahn-Teller distorted transition metal, a quadruple perovskite, such as $LaMn_3Rh_4O_{12}$, may form. These phases typically require high pressure and temperature for their synthesis. $LaMn_3Rh_4O_{12}$ was synthesized at 8 GPa, 1150° C with an exceptionally long reaction time required for a high pressure synthesis (3 days). It is an antiferromagnetic ($T_N \approx 41$ K) 3-dimensional Mott variable-range hopping semiconductor, and the first quadruple perovskite with Mn on the A' site and 4d Rh on the B site.

When the *t* is very small (≤ 0.85) corundum and double corundum derivative structures are predicted to form. In this structure, the A and B form dimers of octahedrally coordinated cations which face share along the c axis. When cations of difference sizes and charges are inserted into these sites, they push each other away from the octahedral centroid at different strengths, due to Coulombic repulsion, which can lead to large polarization constants in polar structures. Additionally, cations with unpaired d electrons (magnetic cations) can be inserted into these sites without

disrupting the mechanism of polarization, making these materials excellent candidates for potential multiferroics.

In Chapter Five, three new double corundum derived compounds, $Fe_{3-x}InSn_xO_6$, with magnetic transitions well above room temperature ($T_N \approx 615$ K, 550K, and 445 K for x = 0, 0.25, 0.5, respectively) are presented. Current data indicate that x = 0, and 0.25 crystalize as centrosymmetric, $R\bar{3}c$, but increasing the concentration of closed-shell d^{10} Sn^{4+} to 12.5% causes x = 0.5 to crystallize as noncentrosymmetric, $R3c$, as confirmed by temperature dependent second harmonic generation measurements. Microprobe measurements indicate that for x = 0.25, 0.5, the inclusion of Sn^{4+} is not compensated for by vacancies, implying the presence of Fe^{2+}, as corroborated by X-ray absorption near edge spectroscopy and single crystal structure refinements. Neutron powder diffraction experiments on x = 0.5 indicate that, like $InFeO_3$, these compounds are canted A-type antiferromagnets with ferromagnetic layers that stack antiferromagnetically and with a single magnetic transition. Weak ferromagnetic interactions persist to very high temperatures. While investigations are ongoing and some properties need to be confirmed, these new compounds provide new information on tuning the magnetic and structural properties of corundum derived compounds in the search for new multiferroic materials.

Finally, $In_2Mn_{1.1}Sn_{0.9}O_6$ is presented in Chapter 6. This double corundum derivative compound crystallizes in the $R\bar{3}c$ space group, and the cations are distributed statistically between the available sites. There is no observed magnetic transition down to 5 K, the so-far limit of measurement. However, the negative Weiss constant (θ = -87 K) indicates that short-range antiferromagnetic interactions dominate. Additionally, there appears to be a large Curie tail at low temperatures,

which suggests the possibility of magnetic frustration, likely linked to disorder, which is known to lead to subtle and interesting magnetic phenomena. Future work on this system will include magnetization measurements to even lower temperatures and at a range of different fields, which should reveal spin freezing, or other subtle magnetic phenomena.

TABLE OF CONTENTS

LIST OF FIGURES

LIST OF TABLES

LIST OF ABBREVIATIONS

AFM	Antiferromagnetic
CW	Curie-Weiss
DP	Double Perovskite
f	Frustration Factor
FiM	Ferrimagnetic
FM	Ferromagnetic
GPa	Gigapascal
HAADF-STEM	High Angle Annular Dark Field-Scanning Transmission Electron Microscopy
HPHT	High Pressure, High Temperature
LMRO	$LaMn_3Rh_4O_{12}$
NPD	Neutron Powder Diffraction
PPMS	Physical PropertyMeasurement System
PXD	Powder X-ray Diffraction
QP	Quadruple Perovskite
RT	Room Temperature
SCXRD	Single Crystal X-ray Diffraction
SEM-EDX	Scanning Electron Microscopy-Energy Dispersive X-ray Spectroscopy
SPXD	Synchrotron Powder X-ray Diffraction
SQUID	Superconducting Quantum Interference Device
t	Tolerance Factor
T_C	Curie Point
TM	Transition Metal
T_N	Néel Point
XANES	X-ray Absorption Near Edge Spectroscopy

Parts of this thesis have been previously published as follows:

Chapter 3 has been published as:

> **Corey E. Frank**; Emma E. McCabe; Fabio Orlandi; Pascal Manuel; Xiaoyan Tan; Zheng Deng; Mark Croft; Vanessa Cascos; Thomas Emge; Hai L. Feng; Saul Lapidus; Changqing Jin; MeiXia Wu; Man Rong Li; Steven Ehrlich; Syed Khalid; Nicholas Quackenbush; Shuang Yu; David Walker; and Martha Greenblatt. **Mn_2CoReO_6: A Robust Multisublattice Antiferromagnetic Perovskite with Small A-site Cations.** *Chem. Commun*., 2019, 55, 3331

Chapter 4 has been published as:

> Meixia Wu and **Corey E. Frank**; Yifeng Han; Mark Croft, David Walker; Martha Greenblatt; and Man-Rong Li. **$LaMn_3Rh_4O_{12}$: an Antiferrmagnetic Quadruple Perovskite Synthesized at High Pressure**. *Inorg. Chem*. 2019, 58, 15, 10280-10286

ACKNOWLEDGEMENTS

I first want to thank my advisor, Professor Martha Greenblatt, for accepting me into her group after so long without a student. It could not have been an easy adjustment for you, and I so appreciate you taking the chance on me. For me, this journey has been difficult, enlightening, humbling, and exciting, and none of it would have been possible without your patience, guidance, and trust. Thank you for showing me how to be a scientist, and for teaching me how to be a better, stronger person.

I also must thank the Greenblatt group members, Drs. Spencer Porter, Sun-Woo Kim, Zheng Deng, Man-Rong Li, Hai Feng, and Alessia Provino- a group of post docs who welcomed me into their midst, mentored me through my early years in Solid State Chemistry, and were so, so patient with me when I needed it most. Thank you especially to Prof. Xiaoyan Tan; without you I would not have made it through my second year in this program. I am forever grateful to you, and I continue to be inspired by you as a scientist and friend.

I would also like to thank Dr. Mark Croft, the physicist without whom I would not have the tools to be here. You are an amazing mentor and hope that one day that I will be able to weave teaching science and doing science together as seamlessly for my own students as you have for me. It has truly been an honor to work with you.

I would like to thank Dr. Thomas Emge, for teaching me crystallography over and over again. Your humor, kindness, and infinite patience are as much of a credit to Rutgers as your scientific skill.

Thank you to Prof. David Walker for treating me like one of your own students for the past four years and introducing me to experimental petrology. I can’t begin to express how much your mentorship has meant to me. Visiting your lab is sincerely the best part of the week for me. I hope that you realize how you lift everyone around you to a higher level by your curiosity, tenacity, and leadership. We are all better for knowing you.

I would like to thank the many, many collaborators who work with the Greenblatt group especially at Sun Yat-Sen University, Penn State University, the University of Antwerp, and the Chinese Academy of Sciences for the excellent and

essential data. I also want to thank Prof. Emma McCabe especially for so much help with NPD analysis, and through that the understanding of magnetic phenomena in our materials.

Thank you to my committee, Prof. Jing Li and Prof. Deirdre O'Carroll, for the many talks, check ins, and questions over the years. So much of my growth and understanding is due to meeting with you. Thank you to Prof. Weiwei Xie for enthusiastically jumping in at the last minute to make this dissertation possible.

Thank you to all of the students, especially in the Dismukes and Goldman groups, who adopted me to one degree or another when my home group got small. Thank you to my cohort. I am forever grateful to that thermodynamics course for bringing us all together.

Finally, thank you so much to my family. You stood by me from the beginning, through my lowest points, to this moment. When I couldn't stand on my own, you held me up until I learned to breathe again. I could work every second from now until forever and I would still never come close to putting the scales into balance. I love you. I love you. I love you.

DEDICATION

To my grandfather, James S. Proctor, PhD, who showed me the way to go

and to my family, who helped me walk every step

Chapter 1: Introduction

1.1 A Brief Introduction to Multiferroicity

1.1.1 Magnetism and Magnetic Order

Since the shepherd Magnes lost his shoe nails to a lodestone on the slopes of Mount Ida in Ancient Greece, mankind has been utilizing and studying magnets.[1] Nevertheless, it was not until the seminal textbook Magnetochemie written by German chemist Wilhelm Klemm in 1936 that the field of magnetochemistry- the study of the magnetic properties of chemical compounds was formalized into a rational scheme of study.[2-3]

Magnetism is generated by spin and orbital motion of electrons. When an electron orbits a *d, f,* or *p* orbital, angular momentum generates some magnetism (this is not the case for *s* orbitals, as the electrons' path has no angular momentum). Electron spins, either up or down, generate a much stronger spin angular momentum, and so for many compounds, especially those consisting of first row transition metals, the orbital contribution to the magnetic moment is ignored for simple or preliminary calculations. Thus:

$$\mu_{s.o.} = \sqrt{n(n+2)} = \sqrt{4S(S+1)} \qquad (1.1)$$

where $\mu_{s.o.}$ is the spin only magnetic moment, n is the number of unpaired electrons, and S is the total electron spin quantum number for all unpaired spins.

The validity of this approach is, of course, highly dependent on both the identity and especially the coordination of the magnetic cation. In an octahedrally coordinated complex, for example, the t_{2g} orbitals d_{xz}, d_{yx}, and d_{yz}, are triply degenerate. This means that an electron in one of these orbitals can be transformed into another of

these by simple rotation. Because the angular momentum of electron rotation is what causes an orbital contribution, a non-negligible orbital contribution should thus be anticipated, even in first-row transition metals.[4] "Quenching" of this contribution occurs when rotation cannot result in an identical transformation.

Broadly speaking, quenching occurs when the orbitals are differently shaped (e.g. octahedral e_g orbitals d_{z^2} and $d_{x^2-y^2}$) or when an electron would have to change spin in addition to rotating (an electron in a d_{xz} orbital cannot be rotated into a half filled d_{yx} orbital because there is already an electron present with that spin). Quenching of the orbital contribution to the magnetic moment can also occur when the orbitals are strongly coupled to the crystal lattice (which happens particularly often in condensed matter materials consisting of first row transition metals), resulting in orbitals which cannot reorient to an applied field and thus cannot contribute to the total magnetic moment, unlike spins.[5] When the orbital contribution is not quenched, the spin only magnetic moment can be modified to include the orbital angular momentum (L):

$$\mu_{S+L}=\sqrt{4S(S+1)+L(L+1)} \tag{1.2}$$

The effective magnetic moment (μ_{crys}) which accounts for crystal field effects is often much closer to the effective magnetic moment, μ_{eff}, determined via experimentation. This μ_{crys} can be calculated by the following equation:

$$\mu_{crys} = \mu_{s.o.}(1-\alpha\lambda/\Delta) \tag{1.3}$$

where α is a constant (either 2 or 4 depending on the ground state), Δ is the crystal field splitting factor (which is often only available for the free ion), and λ is the spin-orbit coupling constant (also often only available for the free ion).[4] It should be noted that the sign of λ changes from positive to negative as the *d* orbital fills. Therefore, for

d^1-d^4 cations μ_{eff} /μ_{crys} should be less than $\mu_{s.o}$, and for d^6-d^9 μ_{eff}/μ_{crys} should be greater than $\mu_{s.o}$.

While this work is more concerned with materials that have unpaired-electron spins, a moment must be taken to consider substances in which all spins are paired ($\mu_{s.o} = 0$). In these substances, the spin magnetic moments quench one another, leaving only orbital magnetic moments. According to Lenz's Law, an applied magnetic field will cause these substances to generate only an opposing field, which ejects magnetic flux and will push the material towards the area of lower magnetic flux density in an inhomogeneous magnetic field. Since the distance between an electron orbital and the atomic nucleus is not appreciably affected by temperature, this diamagnetic contribution is independent of temperature, and all substances have a temperature-independent diamagnetic contribution to the total magnetic susceptibility. In materials with unpaired electron spins, however, the magnetic moment due to the electron spin contribution will be attracted to a magnetic field, generating an increase in magnetic flux density that is, in most cases, much stronger than the diamagnetic contribution (see **Figure 1.1**). In a paramagnet, the magnetic susceptibility

$$\chi = \frac{M}{H} \tag{1.4}$$

(where M is the magnetization and H is the applied magnetic field) is greater than 0. It is also equal to the sum of both the paramagnetic and diamagnetic contributions to the susceptibility and temperature dependent; in a diamagnet $\chi < 0$.

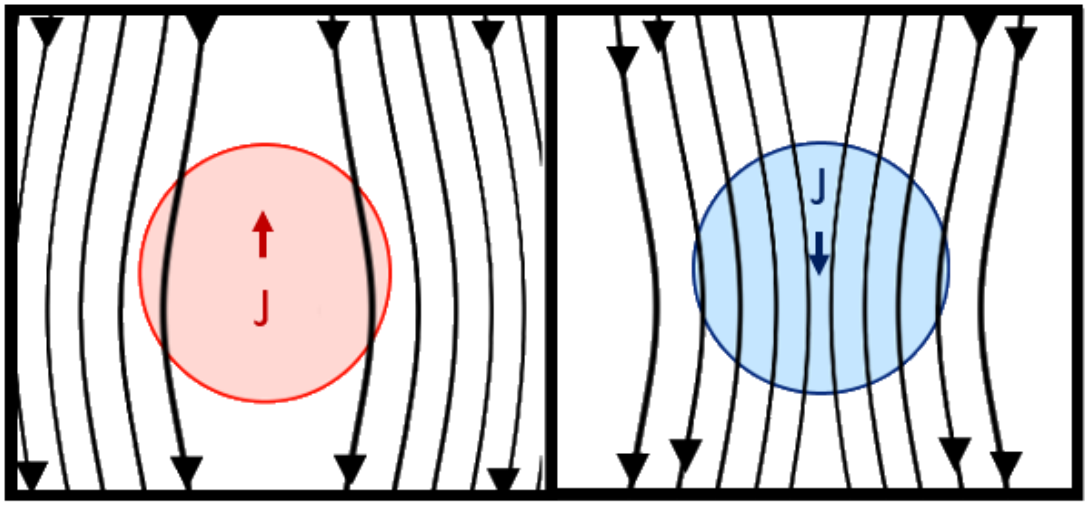

Figure 1.1 A diamagnetic substance (left) will repel an applied magnetic field, whereas a paramagnetic substance (right) will increase magnetic flux density. (J in both cases the total angular momentum vector and is equal to the sum of the spin and orbital angular moment vectors).

When magnetic coupling is low, such as at high temperature (T) and low field (H), the magnetic susceptibility of paramagnets is defined by the unmodified Curie law:

$$\chi = C/T \tag{1.5}$$

where C is the Curie constant:

$$C = \frac{\mu_0 N_A}{3k_B}\mu_{eff} \tag{1.6}$$

(μ_0 is the magnetic field constant, N_A is Avogadro's number, k_B is Boltzmann's Constant, and μ_{eff} is the effective magnetic moment of the substance). Plotting the inverse of the susceptibility vs temperature should thus lead to a straight line which passes through the origin, and from the slope, which is 1/C, μ_{eff} can be calculated. However, in cases with more pronounced magnetic exchange coupling it is necessary to modify the Curie law with a Weiss constant (θ) and apply the Curie-Weiss law:

$$\chi = \frac{C}{T-\theta} \tag{1.7}$$

The magnitude and sign of the Weiss constant is usually correlated with the nature of long range magnetic order in a substance.

These more pronounced magnetic exchanges lead to long-range magnetic order, where at some critical temperature (T_C or T_N), spins will typically align themselves in one of three ways: ferromagnetically, that is in one direction (↑↑↑↑); antiferromagnetically, which is antiparallel (↑↓↑↓); or ferrimagnetically, antiparallel with spins in one direction of a different magnitude than the other. This can be seen in **Figure 1.2** which also shows the expected shape of ideal ferro/antiferro/paramagnets.

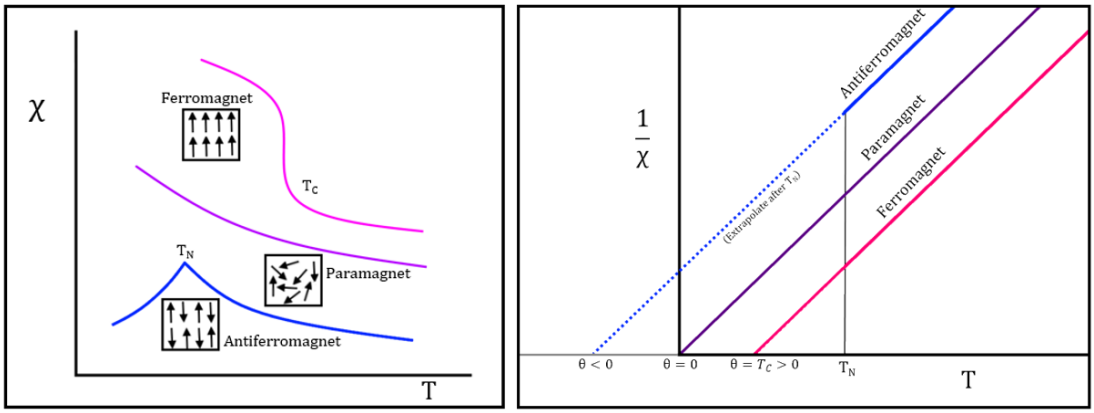

Figure 1.2 (Left) Magnetic susceptibility vs temperature for an idealized ferromagnet (pink) with all spins perfectly parallel, a paramagnet (purple) with random spins, and an idealized antiferromagnet (blue) with spins perfectly antiparallel. (Right) Inverse susceptibility vs temperature for an idealized ferromagnet (pink), a paramagnet (purple), and an idealized antiferromagnet (blue). (Figure adapted)[6]

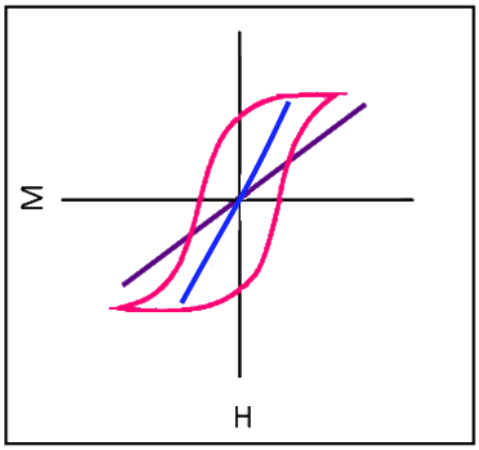

Figure 1.3 Typical magnetization vs field (M(H)) curves for a paramagnet (purple), ferromagnet (pink) and canted antiferromagnet (blue). Ferromagnets show hysteresis, coercivity, and saturation (which will be defined shortly). A paramagnetic M(H) curve is expected to be a straight line. Typically, antiferromagnetic M(H) curves are very similar to paramagnetic curves; they do not show coercivity or hysteresis and are unsaturated,[7] though canting, for example, can induce some FM-like character. (A more detailed version of ferromagnetic portion of this figure can be seen on page 14, in the discussion of ferroelectric materials).

1.1.2 Conductors, Semiconductors and Insulators: A Second Type of Long Range Order

Because an electrical current is fundamentally the flow of charge carriers through a material, the foundation for understanding conductors, semiconductors, and insulators lies in band theory. Recall the Rutherford-Bohr model of the atom, first presented in 1913, which describes electrons orbiting a nucleus in discrete, quantized energy levels.[8] Atomic absorption and emission will be discussed more thoroughly in Chapter 2 (see page 54), but basically in the quantized atomic model if an electron is excited into a higher energy state and then falls back to a lower energy state, a photon should be emitted, the wavelength of which depends on the energy difference between the two orbitals. The equation which predicts this wavelength is:

$$h\nu = E_2 - E_1 \tag{1.8}$$

where E_2 and E_1 are the higher and lower energy states, respectively, *h* is Planck's constant, and *v* is frequency of the emitted light. In isolated atoms, this results in very sharp emission spectra.

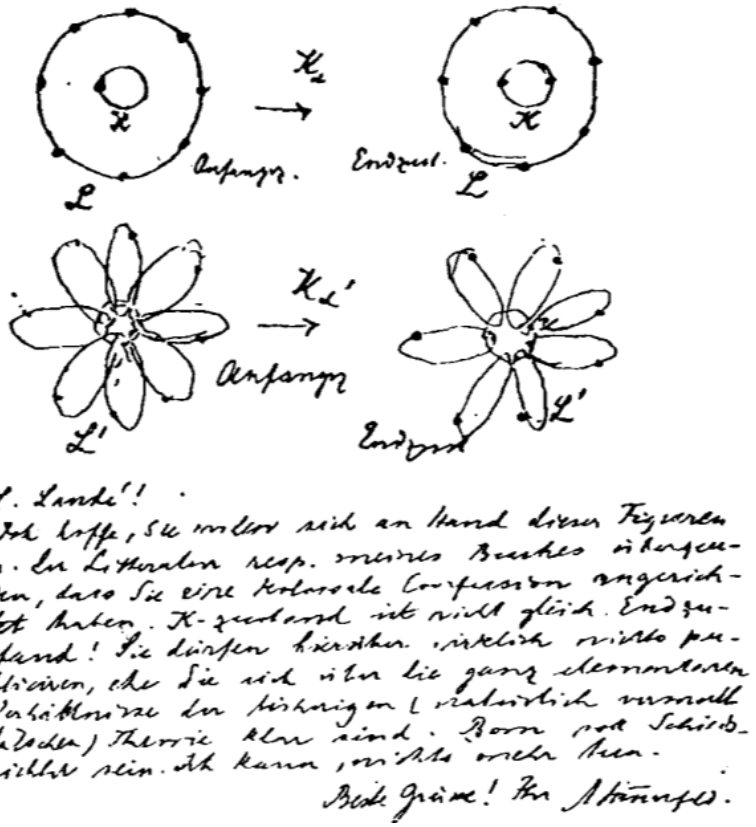

Figure 1.4[9] A card drawn by Arnold Sommerfield, the mathematician who systematized and expanded Bohr's original work explaining multiple spectra, used to explain his original conception of the *Ellipsenverein*, the "true atomic music of the spheres" to his student and collaborator Alfred Landé.

However, in a solid metal like aluminum or copper, these sharp emission lines broaden into bands, indicating that the atoms in these condensed matter materials cannot be treated as isolated objects.[8] Instead, due to chemical bonding with and proximity to their nearest neighbors, the electrons on each atom "see" the electric field on the near-neighbor atoms, which broadens the isolated atomic energy states of the valence electrons into bands of molecular orbitals that are associated with the crystal as a whole. For every atomic orbital added to the crystal system, a corresponding molecular orbital occurs. Thus a crystal system of solid aluminum

consisting of N atoms will also consist of N 3s and N 3p molecular orbitals, and as the number of molecular orbitals increases the average energy difference between adjacent orbitals decreases until there is "essentially a continuum" of energy levels.[8] In metals, the enormous number of molecular orbitals (one mole of orbitals for one mole of atoms) are simply referred to as "energy levels" or "energy states."[8] (Under standard conditions the inner shell orbitals of most metals remain discrete around their individual atoms because the atoms are too far from each other for these orbitals to interact with each other.)

Due to the delocalization of energy levels, electrons in bands can appear with equal probability anywhere on the crystal. This implies: 1. the possibility for electrons to "flow" through the material (metallic conduction) and 2. that physical structure, specifically atomic distances, is critically important for the formation of energy bands. As stated above, if atomic orbitals do not overlap, they cannot form delocalized molecular orbitals. However, decreasing interatomic distances could cause formerly discrete atomic orbitals to form overlapping energy states. For example, it has been calculated that even the discrete atomic orbitals of solid hydrogen could form a delocalized 1s band at high pressure ($>10^6$ atm) resulting in metallic hydrogen.[8]

If, as Sommerfield and Pauli did, one considers a metal to be a "potential well" with freely moving electrons, then at 0 K electrons fill the energy levels from lowest energy to highest in an orderly and easily predictable fashion.[8] The highest filled energy level under these conditions is the Fermi level, the energy of which is the fermi energy (E_F) which is illustrated in **Figure 1.5** by a solid black line. In a metal, the valence band (the highest occupied band) is partially full, which can be attributed to either to a single partially filled band (as in the case of Na's partially filled 3s band) or due to the overlap of multiple bands (as in the case of Mg, which has overlap

between the 3s and 3p bands).[8] This means that in a metal, it is very easy for electrons to move from one atom to another; electrons near or above E_F can easily move among the partially occupied energy states. As temperature increases conduction decreases because the thermal motion of atoms interferes with the free flow of itinerant electrons. As seen in **Figure 1.5**, a semimetal, such as α-Sn (gray tin)[10] exhibits a very slight overlap between the valence and conduction bands, resulting in worse conduction than metals and, generally, less malleability.

On the other extreme of the aforementioned diagram (and reality) are insulators, which feature very large band gaps (the forbidden energy level between the valence band and the lowest unoccupied energy band, known as the conduction band, **Figure 1.5**). Since the forbidden band gap is so large in these materials, very few electrons have the necessary thermal energy to move from the valence band to the conduction band, and thus conduction is negligibly small. For example, diamond with its a large band gap of ~6 eV is an excellent insulator.[8] The range of specific electrical conductivity (that is, the strength at which a charged current flows through a material) of insulators is $< 10^{-10}\ \Omega^{-1}\ cm^{-1}$ versus that of metallic conductors: $> 10^{1}\ \Omega^{-1}\ cm^{-1}$.[2]

Semiconductors, materials with a conductivity between metals and insulators, are of particular interest to this work. The band structures of conventional semiconductors are very similar to those of insulators, but with a much smaller band gap (0.5 – 3 eV) meaning that some electrons will have sufficient thermal energy to move into the empty band leaving positive "holes" behind.[8] These holes will appear to flow in equal magnitude and opposite direction to the electron current, and "move" towards a negative electrode under applied current. The number of mobile electrons, n, (and thus the strength of conduction) in a semiconductor is given by the following equation:

$$n = n_0 \exp\left(-\frac{E}{kT}\right) \quad (1.9)$$

where n_0 is the total number of electrons (a constant), E is the magnitude of the band gap, *k* is Boltzmann's constant, and T is the temperature of the system. The number of mobile electrons increases exponentially with temperature, and consequently a semiconductor will have greater conductivity at higher temperatures.

Semiconductors are intrinsic to the function of modern society, and are used in data storage, fuel cells, electrodes, and countless other devices. (See **Table 1.1** for a brief list of notable oxide semiconductors). Some semiconductors, such as germanium,[11] are intrinsically semiconducting (that is, they are semiconducting without any significant doping), and band structure theory satisfactorily explains the mechanism of their conduction.[8] However, band structure is not quite enough to explain the conduction mechanism of many oxide semiconductors such as MnO; a simple band structure would predict metallic conduction in this material, similar to the behavior seen in metallic VO.[8] Instead, one must take into account the degree of orbital overlap. While the t_{2g} orbitals of MnO may overlap somewhat, it is not to the degree necessary for a band to form. The difference in conduction between MnO and VO could therefore be ascribed to the increased atomic number from V to Mn.[8] As atomic number increases, electrons experience increased nuclear charge which holds them more tightly to the nucleus, keeping them localized in orbitals rather than shared in energy bands.

When band theory is not adequate to explain the conduction of a semiconductor, it is deemed as a "hopping semiconductor" because the localized conduction electrons "hop" to neighboring atoms after a certain activation energy is overcome.[8] Unlike in a conventional semiconductor, however, the hopping electron does not continue to

freely flow throughout the material: instead, it is trapped on the atom to which it hopped unless the activation energy is met or exceeded again.

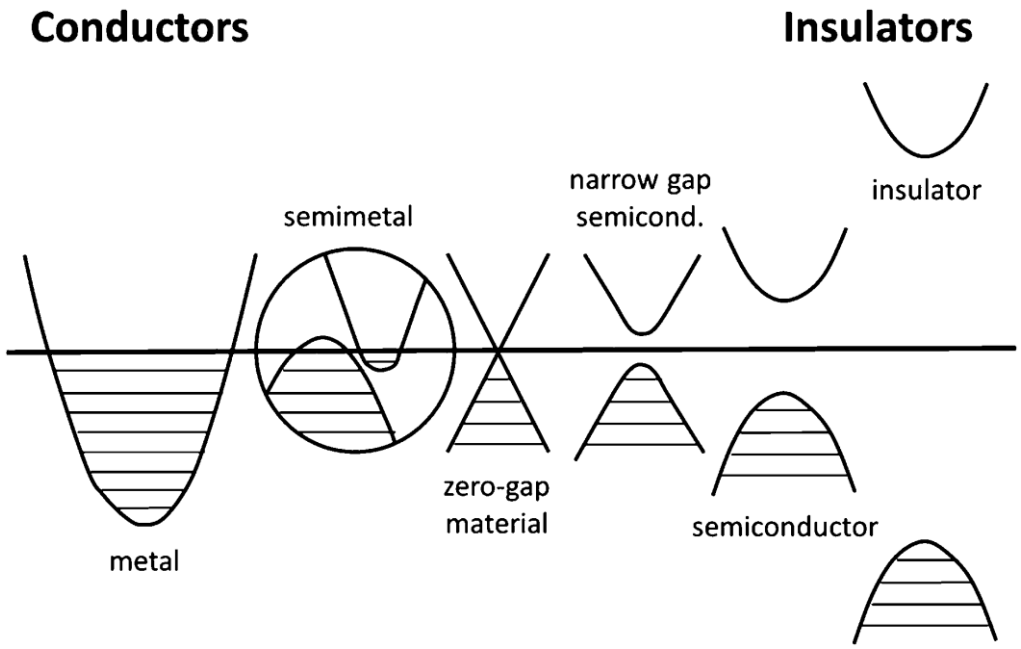

Figure 1.5[12] An idealized view of the overlap between the valence and conduction bands of metals and semimetals. Zero gap materials (middle) can be made from narrow band gap semiconductors by doping or by the application of pressure. Semiconductors have a forbidden energy gap between the valence and conduction bands which can be overcome by electrons with sufficient energy. In insulators, this band is so large as to be fundamentally insurmountable to electrons, and so conduction is negligible. In this figure the Fermi level is indicated by a black line.

Table 1.1 A brief, illustrative list of widely used oxide semiconductors and their applications

Material	**Formula**	**Type**	**Notable Details**
Cuprous Oxide[13], cuprite	Cu_2O	*p*-type	One of the oldest and most widely studied semiconducting materials.
Tin dioxide[14], cassiterite	SnO_2	*n*-type	Widely used in gas sensors, often doped with other cations.
Indium oxide[15], indium sesquioxide	In_2O_3	Wide-band gap*	Used in gas sensors and advanced transparent devices.
Cadmium oxide[16], monteponite	CdO	*n*-type	Thin films of CdO are used in photodiodes, electrodes, and liquid crystal displays.
Zinc Oxide[17], zincite	ZnO	Wide-band gap	Used in pigments, foods, batteries, ointments, and many other products.
Bismuth trioxide[18], bismite	Bi_2O_3	*n*-type or *p*-type, temperature dependent	One of the most important bismuth compounds, the conduction type (and structure) changes with temperature due to thermal expansion[19]. Critical for applications in solid-oxide fuel cells.

*Wide-band gap semiconductors are intrinsic semiconductors with larger band gaps that are typical, sharing some properties with insulators.[20]

1.1.3 Ferroelectric Materials

Of particular to interest to this work are ferroelectric materials. These substances are, firstly, dielectric, meaning that they are almost perfectly insulating. The dielectric permittivity of a material is measured as a function of capacitance. The material is placed between two conducting plates of opposite charge within a vacuum. In this environment, capacitance (C_0) is defined:

$$C_0 = \frac{e_0 A}{d} \tag{1.10}$$

In this equation, e_0 is the permittivity of the free space (a constant, 8.854 x 10^{-12} F/m), and *A* and *d* are the area of the plates and the thickness of the distance between them, respectively. When a potential difference (*V*) is applied to the plates, some charge (Q_0) is stored on them.

$$Q_0 = C_0 V \tag{1.11}$$

Placing a dielectric substance between the plates and applying the same potential difference, the amount of charge stored between the plates will increase. Comparing the capacitance before and after the dielectric material is placed on the plates thus allows one to measure the dielectric constant (ε'), or relative permittivity, of the dielectric material, which is dependent on the degree of polarization induced by the applied electrical field.

$$\varepsilon' = \frac{C_1}{C_0} \tag{1.12}$$

Polarization in ferroelectric materials is much larger than for simple dielectrics. Additionally, this polarization is spontaneous and will remain for a time after the electrical field is removed. Finally, ferroelectric polarization is switchable in orientation;[21] reversing the applied current will cause the polarization to change orientations, generating a hysteresis loop which is visually very similar to the

hysteresis seen in magnetization vs field measurements. (This visual similarity is why this phenomenon was dubbed **ferro**electricity when it was proposed by Schrodinger in 1912[22] and first documented in Rochelle salt[23] in 1920, despite it and most other ferroelectrics containing no iron whatsoever). Above some transition temperature (T_C), which is marked by a distinct anomaly in the dielectric plot, the ferroelectric material no longer exhibits ferroelectricity, and thus is said to be in a "paraelectric" state. As ferroelectricity is fundamentally a structural transition, usually a specific heat vs temperature plot will exhibit an anomaly at the ferroelectric T_c as well.

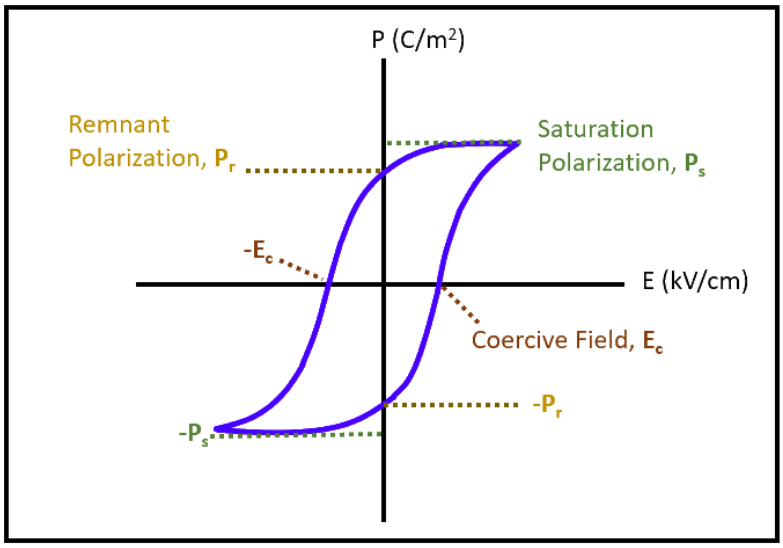

Figure 1.6 A hysteresis loop for an idealized ferroelectric material. Polarization (y axis) is expressed in C/m^2 and field strength (x axis) in kV/cm. The saturation polarization (P_s, green) is the maximum polarization, and is equal to $-P_s$. The remnant polarization(P_r, gold) is the polarization which remains after the electric field is removed, and the specific field strength at which polarization becomes zero when transitioning from positive to negative field is the coercive field strength (E_c, orange).

Most known ferroelectric materials are of the ABO_3 perovskite structure type,[24] the structural configuration(s) of which will be discussed in detail in the next section. Basically, the structure of ABO_3 perovskite consists of a corner sharing array of BO_6 octahedra arranged around a much larger 12-coordinated A site cation. Ferroelectricity in perovskites is usually attributed to hybridization between an empty

d orbital of the transition metal B cation and the oxygen 2*p* orbital, as exemplified in the most widely used ferroelectric material, $BaTiO_3$.[25] This hybridization weakens short-range repulsions within the unit cell and allows for "ferroelectric instability," and polarizable distortion, of the TiO_6 octhahedra.[24]

1.1.4 Multiferroicity: Multiple Types of Long Range Order

As the name implies, a multiferroic material is one which has two or more types of spontaneous, stable, switchable macroscopic order.[26] These orders can be ferroelastic, in which the microscopic property of unit cell deformation manifests macroscopically as strain, or the macroscopic order can be the previously discussed ferromagnetic and ferroelectric, in which the microscopic properties of unpaired electron spins and electrical dipole moments manifest as magnetization and polarization, respectively. In rarer cases, these properties can be cross coupled, e.g. magnetoelectrics where a magnetic field can induce polarization, and an electrical field can induce magnetization. The magnetoelectric effect caused a great deal of excitement after its first observation due to the vast potential technical applications, such as in four-state memory devices, and the discovery of stable materials with strong magnetoelectric coupling constants could lead to more energy and space efficient data storage technologies.[27-29]

It has been proposed that the biggest problem in the field of multiferroics "is that we do not know many of them."[30] Because the forces that cause long range magnetic and electrical order compete with one another, at one time the coexistence of ferroelectricity with magnetism was considered to be impossible.[29] The scarcity of multiferroic materials is due to several factors. First, for there to exist an electrical dipole, there must be a break in inversion symmetry. In other words, the unit cell must

be noncentrosymmetric. Secondly, the magnetic unit cell must allow for time reversal. Magnetic moments in closed orbits can be imagined as pseudovectors- that is, charges which are immune to spatial inversion, and subject only to the fourth dimension: time. Switching the direction of the spin, thus switching the moment, requires time reversal.[31] The space group of a multiferroic material must allow for both types of symmetry breaks, and out of 122 magnetic symmetry point groups defined by Shubnikov, only 13 allow for both magnetization and polarization, which statistically at least, greatly reduces the number of candidates for multiferroic materials.[27]

After symmetry, electrical properties must be considered- a ferroelectric must be an insulator because an applied current must cause polarization, not flow through the material as it would in a metallic conductor or semiconductor. Most magnetic ferroelectric materials are of the aforementioned ABO_3 perovskite structure type, for reasons which certainly relate to the strong capacity for synergistic motion of the B-cation and O-anions in the octahedra, but which (it has been suggested) perhaps also relate to the detailed theoretical understanding of perovskite ferroelectrics that preexists in the field.[31] Unfortunately, unpaired d electrons- essential for magnetism- interfere with the structural distortions required for ferroelectricity in perovskites. The reasons behind this are not definitively known at this stage, but some possible explanations include ionic sizes, as filled d-shell cations could be too big to appreciably distort in an octahedron, or the dominance of non-ferroelectric distortions, such as Jahn Teller or structure defects that increase as more d electrons are present in the material.[31]

1.2 Ideal Perovskites and Derivative Structures, An Explanation of Type

1.2.1 Goldschmidt's Tolerance Factor and the Ideal Perovskite

$CaTiO_3$, the first material to be called "perovskite" was named in honor of mineralogist Count Lev Alekseyevich von Perovski in 1839 by its discoverer, German scientist Gustav Rose.[32-33] Despite the apparent simplicity of the ABO_3 perovskite unit cell, especially when compared to other natural mineral structure types, it is remarkably flexible in terms of application due to its sensitivity to defects[34-35], composition[36-37], pressure[38-39], and grain size and boundary effects.[40-41] Perovskites also tend to retain the basic perovskite structure despite diverse compositions and substitutions.[24, 40, 42-46] Perovskites are essential components for many current and potential future applications; almost every solid state device, from photovoltaic cells, to memory devices, to sensors and microwave tuners, involve perovskites in some way.[32, 47-49]

The structural stability of a perovskite at ambient pressure can be roughly predicted by the Goldschmidt[50] tolerance factor equation:

$$t = \frac{r_A + r_O}{\sqrt{2}(r_B + r_O)} \tag{1.13}$$

where r_A and r_B are the radii of the A and B cations, respectively, and r_O is the radius of the anion, which in this case is oxygen. In an ideal ABO_3 perovskite, with a *t* of approximately 1, a large A-cation is 12-coordinated to oxygens and is located in the voids of a three-dimensional (3D) corner-sharing array of BO_6 octahedra (see **Figure 1.7**).

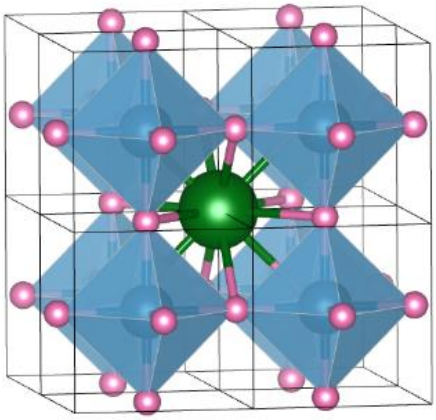

Figure 1.7 An ideal perovskite based on $SrTiO_3$,[51] with a tolerance factor, t, of ~1. The AO_{12} coordination polyhedron has been deleted for clarity, though A cation itself is shown in green.

If cations of different sizes and charges are inserted into the lattice, the BO_6 octahedra will tilt and distort to accommodate them. Generally, at ambient pressure, perovskites are stable when *t* is between 0.77 to 0.99,[52] and relatively smaller or larger A-site cations will lead to increasing structural distortions until *t* deviates too far from these values and the proposed material does not form at all, or sometimes forms as a different ABO_3 structure (**Figure 1.8**) such as bixbyite, ilmenite, or corundum which are occasionally stable at ambient pressures (as in the case of rare examples like Ni_3TeO_6[53]). However, most examples of small A-cation structures ($t < \sim 0.8$), even those of the corundum and double-corundum structure types, require high pressure for their synthesis.[45, 54-55]

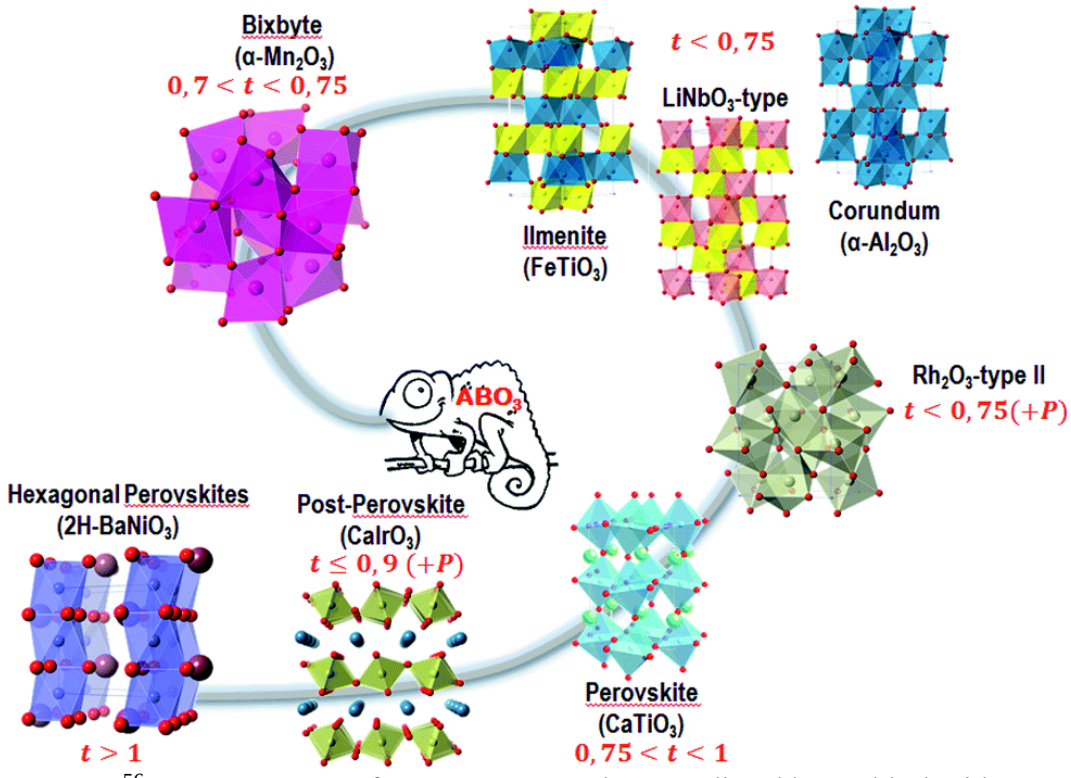

Figure 1.8[56] Structure types of ABO_3 compounds as predicted by Goldschmidt's tolerance factor. As *t* becomes smaller, compounds are less likely to form at ambient pressure

1.2.2 Double Perovskites with Large or Small A-Cations

A common way to tune the properties of a perovskite is through substitution of one or more of the cations for one of a different charge and/or size. This can happen at either the A or B site, but because any interesting magnetic (and transport) properties in these materials are usually due to double-exchange or super-exchange interactions between cations on the B site(s), substitution is most commonly attempted such that double perovskites (DPs) with the formula $A_2BB'O_6$ result.[57] As can be seen in **Figure 1.9**, three types of order are typically seen between the B and B'-site cation octahedra in a B-site ordered DP: rock salt, layered, or columnar. The type of B-cation order is generally determined by the degree of difference in size and charge between the B and B' cations, though other factors such as distortions and vacancies play important roles.[42] Since magnetic exchange is directly related to the physical

properties of solid state materials, controlling the degree of disorder can profoundly affect the manifestation of desirable properties.[58-60] For example, in some ordered lead-based $A_2BB'O_6$ perovskites such as Pb_2ScTaO_6 and Pb_2ScNbO_6, a small degree of disorder is necessary for relaxor-like ferroelectric behavior to emerge, but increasing disorder can degrade dielectric properties by "orders of magnitude."[61-62]

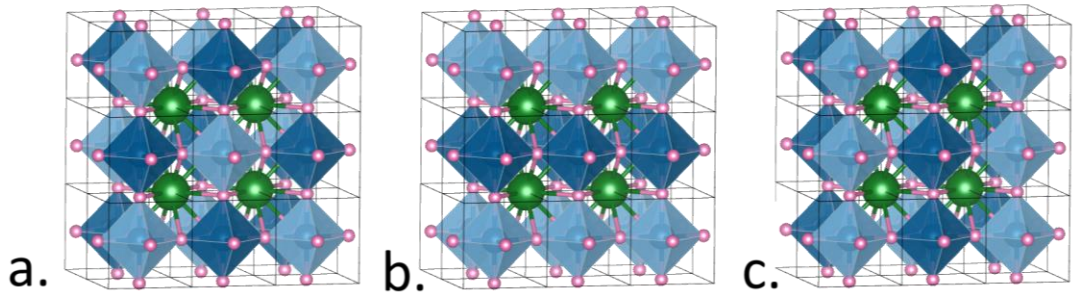

Figure 1.9 Three types of order in $A_2BB'O_6$ perovskites, **a**. rock salt which is the most common, **b**. layered, and **c**. columnar, which tends to only occur when A is also substituted to some degree.[57]

One of the most studied double perovskites, Sr_2FeMoO_6, was reported by Kobayashi et. al. in 1998 and has stimulated a great deal of research into mixed 3d and 4d (and eventually 5d) DPs.[63] This rock-salt ordered 3d/4d hybrid DP has a Tc of ~415 K, negative colossal magnetoresistance, and shows half metallic (that is, spin polarized) ferromagnetism in the ordered form. The ferromagnetic nature of these interactions is especially intriguing, as superexchange rules (Goodenough-Kanamori rules[64-65]) predict that the ground state could be antiferromagnetic, and moreover antiferromagnetic ground states were seen in the related compounds, Sr_2CoMoO_6,[66] and Sr_2MnMoO_6.[67] This implies the possibility that double-exchange is responsible for ferromagnetic coupling between the Fe sites in Sr_2FeMoO_6, and that the $4d^1$ Mo electron could be delocalized.[68]

Subsequently, Sarma et al. were able to synthesize a disordered form of Sr_2FeMoO_6 and demonstrated how B/B' order can be key to tuning properties in double perovskites. Increasing B/B' disorder immediately begins to reduce spin polarization. The most disordered version of Sr_2FeMoO_6 is still a high temperature ferromagnet, but it loses the half-metallicity and extrinsic "intergrain dependent" low-field magnetoresistance that is present in the ordered analogue.[69] In addition to illustrating very clearly the criticality of cation order to double perovskite exchange-interaction properties, in many ways, the explosion of interest in ordered DPs for spintronics applications can be traced back to Sr_2FeMoO_6, and investigations into related DPs with different schemes for tuning room temperature properties are still ongoing.[70-74]

In addition to tuning regimes that focus on B/B' substitutions (and on the synthetic conditions that can increase or decrease order), properties of $A_2BB'O_6$ perovskites can also be tuned by the introduction of a small cation into the A-site. This causes the $B/B'O_6$ octahedra to tilt strongly away from the ideal 180° exchange angle, and in many cases these large distortions can lead to interesting and unique magneto-structural coupling behaviors which are not easily predicted.[52, 75] For example, In_2NiMnO_6[76] ($t \approx 0.86$) and Sc_2NiMnO_6[77] ($t \approx 0.84$) have similar tolerance factors and both show antiferromagnetic ground states, but uniquely show field induced phase transitions and magnetic-field-induced changes in electrical resistivity, respectively.

Predicting the properties of small A-site cation containing DPs a priori is also difficult due to the small number of example compounds available for study. To date, there are still only four known transition-metal-only DPs. Mn_2FeReO_6 and Mn_2MnReO_6 were reported independently by Li et al.[78-79] and Arévalo-Lopez *et al.*[80-

[81] several years ago with similar results. Mn_2FeReO_6 is a half metallic ferrimagnet with giant magnetoresistance (220%) at 5K, whereas the antiferromagnetic coupling of the A and B magnetic sublattices of Mn_2MnReO_6 prevents magnetoresistance entirely. $Mn_2(Fe_{0.8}Mo_{0.2})MoO_6$[82] is a line phase of the polar ferrimagnetic double corundum Mn_2FeMoO_6 and it has been proposed that its formation at the same temperature and pressure as the parent compound suggests a "synergy" between thermodynamics and crystal structure, and highlights the pitfalls of attempting even structure prediction from *t* alone. The most recent transition metal only double perovskite, Mn_2CoReO_6,[83] was published by our group in 2019 and will be discussed in detail in a later chapter. It is a semiconducting antiferromagnet with a very robust transition at T_N = 94 K. Due to the small *t* of small A-cation perovskites ($t \leq \sim 0.8$), most will not form at ambient pressure, and instead require high pressure for their synthesis.[75]

1.2.3 Increasing Complexity: Quadruple Perovskites

An even more complex perovskite, the quadruple perovskite (QP, $AA'_3B_4O_{12}$), may result when 75% of the A-site is substituted with a Jahn-Teller distorted ion like Cu^{2+} or Mn^{3+}, or other cation which allows square-planar coordination (Mn^{2+}, Fe^{2+}, Co^{2+}, or Pd^{2+}).[84] The distinguishing feature of this structure is the inclusion of perpendicularly-aligned square planar coordinated A' units. These small A' ions cause significant tilting of the BO_6 octahedra (**Figure 1.10,** the B-O-B bond angle is generally 140°, rather than the ideal 180°).[85-86] This can cause more complicated types of exchange interactions, like double exchange, to appear in addition to the typical oxygen-mediated super exchange, and can lead to such exotic phenomena as colossal magnetoresistance and gigantic permittivity.[87] Due to the small size of the A' cations

and the large distortions of the BO_6 array, high pressure is usually needed for the synthesis of quadruple perovskite compounds.[86]

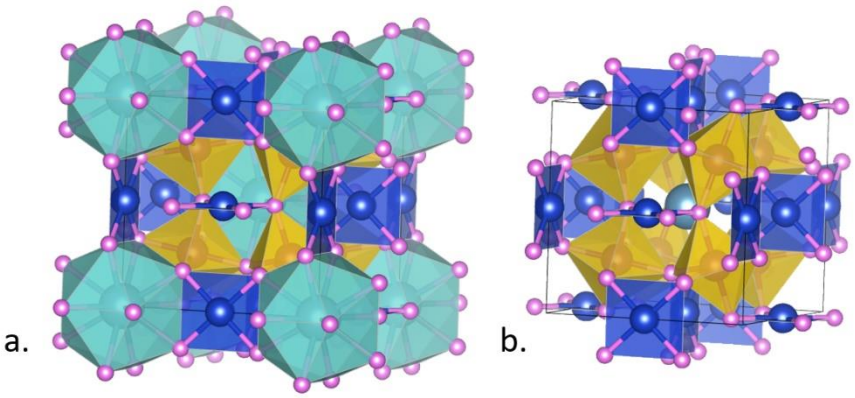

Figure 1.10 An idealized $AA'_3B_4O_{12}$ quadruple perovskite in space group $Im\bar{3}$ (204) based on $CaCu_3Mn_4O_{12}$[88] shown in its complete form in Figure 1.10.a. Figure 1.10.b shows the same unit cell with the corner sharing AO_{12} polyhedra deleted to more clearly show the blue square planar $A'O_4$ units and distorted BO_6 lattice surrounding the central A cation (the central cation itself is still shown in green).

QPs were first reported in 1967, but accurate structures were not reliably reported until the mid-1970's when QPs were recognized as their own sub family of perovskites.[89-90] Initial investigations were focused on structures in which A' = $Mn^{3+/4+}$ and B = Mn^{3+}, a particularly interesting example of which is the so-called $NaMn_7O_{12}$ (more accurately $NaMn_3(Mn^{3+}{}_2Mn^{4+}{}_2)O_{12}$), which crystalizes as $Im\bar{3}$. Neutron diffraction studies show that $NaMn_7O_{12}$ transitions from $Im\bar{3}$ to I2/*m* upon cooling, which is attributed to "ordering of the spin, charge, and orbital subsystems" as Jahn-Teller distortions of (compressive in the case of $Mn^{3+}O_6$, and apical stretching in $Mn^{4+}O_6$, respectively) cause ordering in the B position.[87, 91-92]

Currently, research into quadruple perovskites is intense: there are over 200 entries in the Inorganic Crystal Structure Database for QPs in the $Im\bar{3}$ space group alone.[93] Despite crystallizing in the same space group, and sometimes only consisting of slight compositional modulations, these QPs still show a remarkable variety of

properties. For example, $SrCu_3Fe_4O_{12}$ shows giant negative thermal expansion between 170 and 270 K due to charge disproportionation of Fe^{4+} to $Fe^{3+/5+}$ below 200 K[94], similar to its analogous A = Ca compound $CaCu_3Fe_4O_{12}$[95-96] (the associated lattice parameter changes are much less dramatic, however). Substituting the divalent A cation for trivalent La^{3+} causes $LaCu_3Fe_4O_{12}$ to crystalize as $LaCu^{2+}{}_3Fe^{3.75+}{}_4O_{12}$. There is a proposed charge transfer between copper and iron at low temperatures, causing an isomorphic phase transition to $LaCu^{3+}{}_3Fe^{3+}{}_4O_{12}$.[97] This implies the inclusion of octahedrally coordinated Cu^{3+}, which is generally considered unstable, but could be stabilized in this case by the complicated exchange mechanisms of A-site ordered QPs. Other interesting examples of QPs are too numerous to thoroughly discuss here (I recommend the comprehensive reviews of Vasil'ev,[87] Long[86], and Belik[98]) but include giant dielectric response in $CaCu_3Ti_4O_{12}$,[89, 99] large low-field magnetoresistance in $LaCu_3Mn_4O_{12}$, and coupling of magnetic and dielectric properties in $BiMn_3Mn_4O_{12}$.[100]

1.2.4 Very Small A-Cations: Corundum and Double Corundum Compounds

When the Goldschmidt tolerance factor (t) is approximately 0.75, the corundum and corundum derivative structure types are predicted to be stable.[56] The eponymous corundum, Al_2O_3, crystallizes in the $R\bar{3}c$ space group, and as can be seen in **Figure 1.11**, consistis of face sharing AO_6 dimers oriented along the *c* axis. These AO_6 octahedra edge share within the layers and corner share between layers. If cations of different sizes and charges are substituted for some of the A cations, derivative compounds of increasing complexity result. At first, it can feel overwhelming to tell these structures apart, but one will soon see that they are easily distinguished by following the c axis and noticing the pattern of octahedral hole occupancies. The main

difference between ilmenite type (**Figure 1.11.b**) and lithium niobate-type (**Figure 1.11.c**) ordering is the orientation of the AO_6:BO_6 dimers. In ilmenite, the pattern is AO_6-BO_6-Vacancy-BO_6-AO_6, whereas in the lithium niobate type this pattern is AO_6-BO_6-Vacancy-AO_6-BO_6. The strategy is even more useful when distinguishing between *R*3 ordered-ilmenite-type (**Figure 1.11.d**) and *R*3 Ni_3TeO_6-type (**Figure 1.11.e**) compounds. These materials have distinct B and B' cations as well as two A cations that occupy distinct crystallographic positions (and which will be called A and A' for convenience, despite the fact that "A1" and "A2" may be more illustrative of the typical $A_2BB'O_6$ formula). The repeating ordering pattern for ordered (double) ilmenite is AO_6-$B'O_6$-vacancy-BO_6-$A'O_6$ whereas for Ni_3TeO_6-type compounds it is AO_6-$B'O_6$-vacancy-$A'O_6$-BO_6.

The nature of ions in the octahedral holes between face sharing dimers are not merely useful for distinguishing members of the corundum derivative family from one another. Polarization in noncentrosymmetric corundum derivatives is caused by differences in sizes and charges between the A and B (and A' and B') forcing the cations to displace from the octahedral centroid to different degrees, leading to polarization. In ferroelectric compounds, this polarization is switched via a proposed mechanism in which cations migrate through octahedral vacancies.[101] Thus, in a lithium niobate type ferroelectric, the pattern along the *c* axis would switch from AO_6-BO_6-Vacancy-AO_6-BO_6-Vacancy-AO_6 to AO_6-Vacancy-BO_6-AO_6-Vacancy-BO_6-AO_6. This physical migration, rather than off-centering displacement, makes corundum derivative compounds attractive as potential multiferroic materials when compared to classic perovskites. Firstly, ferroelectric switching in corundum derivatives does not require displacements facilitated through an empty d-shell,[102] so magnetic cations can be inserted into all A/A'-B/B' sites. Secondly, the large

displacement through a vacancy can lead to polarization constants that are orders of magnitude greater than in their perovskite counterparts.[103]

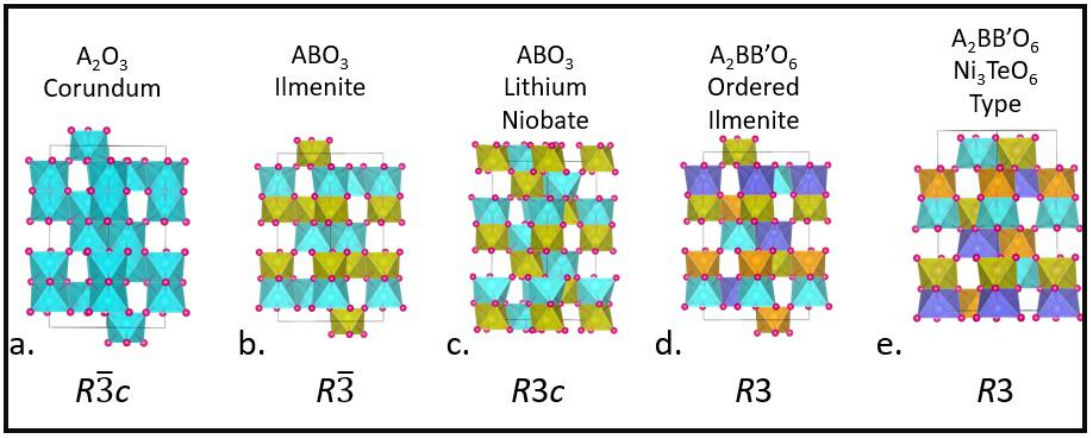

Figure 1.11 Examples of the corundum and double corundum parent compounds, adapted from published crystallographic information files, including a. $R\bar{3}c$ corundum[104], b. $R\bar{3}$ ilmenite-type[105], $R3c$ lithium niobate-type[106], d. $R3$ ordered ilmenite-type[107], and e. $R3$ Ni_3TeO_6-type[108]. In these figures, AO_6 octahedra are light blue, BO_6 are gold, $A'O_6$ are purple, and $B'O_6$ are orange.

It is still impossible to predict whether a $t < 0.8$ material will form at ambient pressure, as in the case of ilmenite-derived $(Mn_{1-x}Fe_x)TiO_3$ ($0 \leq x \leq 1$),[109] but most corundum derivative compounds require high pressure and temperature synthesis techniques to form.[110] In collaboration with the David Walker lab of Columbia University, the Greenblatt group has been at the forefront of synthesizing new corundum derivative compounds with potential multiferroic applications since 2013.[111] Out of the 21 noncentrosymmetric magnetic corundum derivatives listed in **Table 1.2**, 48% were first reported by the Greenblatt group.

Table 1.2 A List of noncentrosymmetric magnetic double corundum derivatives synthesized at high pressure (compounds made by the Greenblatt group are written in green ink).

Material	Space Group	Type of Magnetic Order	Transition Temperature (T_C/T_N)	Reference
Mn_2MnWO_6	*R*3	AFM	52 K	112
$FeTiO_3$-II	*R*3*c*	AFM	110 K	113
$In_{1-x}M_xMO_3$ (x = 0.112–0.176 and M = $Fe_{0.5}Mn_{0.5}$)	*R*3*c*	AFM	240-290 K	114
$MnTiO_3$	*R*3*c*	AFM	25 K	54
$MnSnO_3$	*R*3*c*	AFM	50 K	54
$ScFeO_3$	*R*3*c*	FM	356 K	115
Zn_2FeTaO_6	*R*3*c*	AFM	22 K	116
Mn_2FeMoO_6	*R*3	FiM	337 K	117
Mn_2FeMoO_6-high temperature phase	*R*3*c*	FiM	229 K	118
Mn_2FeWO_6	*R*3	AFM	75 K	119
$MnTaO_2N$	*R*3*c*	Helical spin order	25 K	120
Mn_2ScSbO_6	*R*3	FiM	42 K	110
$InFeO_3$	*R*3*c*	AFM	545 K	121
$GaFeO_3$	*R*3*c*	AFM	408 K	107
Mn_2InSbO_6	R3	FiM	38 K	107
Co_2ScSbO_6	R3	FiM	59 K	122
Mn_2ScNbO_6	*R*3	FiM	53 K	123
Mn_2ScTaO_6	*R*3	FiM	50 K	123
Zn_2FeNbO_6	*R*3*c*	AFM	21 K	124
Mn_2FeTaO_6	*R*3*c*	AFM	80 K	111
Mn_2FeNbO_6	*R*3*c*	AFM	90 K	111

The most recently published of these compounds, Zn_2FeNbO_6,[124] was reported earlier this year as a semiconducting antiferromagnet (T_N = 21 K) that crystallizes in the *R*3*c* space group. During the nuclear structure refinements, researchers found evidence of a superlattice caused by A-site atomic splitting (~1.0-1.2 Å between the split-atom pair), which was confirmed by high angle annular dark field scanning transmission electron microscopy. Previously published A = Zn, Mn *R*3*c* compounds Zn_2FeTaO_6, Mn_2FeNbO_6, and Mn_2FeTaO_6 were also re-evaluated for the possibility of A-site splitting and compared to $ZnSnO_3$. It was found that all investigated mixed B-site lithium niobate type compounds showed evidence of A-site splitting to some

degree, with A = Zn being much more noticeable than A = Mn (~0.2 Å atomic displacement). Splitting was not observed for $ZnSnO_3$, which does not have a mixed B-site. As structure and properties are so closely related in solid state compounds, a more precise understanding of crystal structure and atomic placements is a promising advancement that could lead to new, more subtle strategies for producing materials with specific desirable properties.

1.3 High Pressure Synthesis, A Note on Technique

Pressure is a fundamental thermodynamic variable that is often outside of synthetic reach, but engaging pressure during synthesis can lead to unexpected[82, 111, 113, 117] and often exciting [97, 118-119, 121] results. High pressure synthesis can unlock previously inaccessible portions of the phase diagram, leading to new compounds and unusual states of matter.[55] Furthermore, high pressure can be used to synthesize thermodynamically metastable phases, many of which can be quenched at high pressure and remain kinetically stable at ambient pressure practically indefinitely.[125]

The history of high pressure research has been thoroughly documented previously.[126-127] In fact, this section functions in a way as an abridgement of the excellent anecdotal history written by Liebermann in 2011,[126] rather than adding new details to the history itself, and interested readers should look to his review for a deeper and more personal historical account. Advancements and anecdotes could fill several reference books, though a definitive text remains unwritten.[128-132]

The earliest high pressure devices resided in geology laboratories, where they were (and still are) used to simulate the pressure and temperature conditions of the deep earth.[133] H. Tracy Hall, the “Father of [the] Multi-Anvil Apparatus” developed his tetrahedral anvil device in the late 1950’s after a secrecy order from the US

Department of Commerce and the General Electric corporation prohibited him from utilizing the belt-type high pressure apparatus at Brigham Young University in his research.[126] This original device consisted of a piston driven by four independent hydraulic rams which compressed the cell assembly. The design was refined over the next few years and then quickly spread internationally. Reportedly, Syun-iti Akimoto constructed a full-sized tetrahedral anvil device using only a photograph of Hall's original model as a reference.[126]

The next major advancement in high pressure apparatuses were cubic-anvil devices, which were developed separately by several different labs,[134-136] and which used six orthogonal pistons to compress a cubic cell assembly. That is, until Jiro Osugi and Kazuo Yasunami developed an apparatus in which the external force is applied along only the vertical axis, rather than all three axes at once. In this design, the force is transferred from the vertical to the horizontal by four trapezoidal end blocks which slide along one another, compressing the cubic cell assembly "hydrostatically."[126, 137] Additional advancements to multi-anvil apparatus designs fell out of fashion until the late 1970's in favor of the smaller diamond anvil cell. These advancements were concentrated primarily in Japan until the 1980's, and included the split-sphere style USSA-2000 apparatus (modelled on the USSA-5000) that was brought back to Stoneybrook University.[126]

The next major leap forward in multi-anvil technology was, yet again, inspired by necessity. David Walker of Columbia University was an early guest of the USSA-2000 facility at Stoneybrook. When he and his student Carl Agee were banned[126] from pushing the pressure limits of this press, his response was to design and develop his own multi-anvil module while on sabbatical.[128] The Walker-type module, now

manufactured and sold worldwide by Rockland Research, simplified the design of multi-anvil presses and brought high pressure research “to the masses.”[126]

The Walker type multi-anvil press takes inspiration from previous split-sphere devices. A two stage assembly consisting of six wedge shaped first-stage anvils and eight second-stage anvils applies pressure down the vertical axis of the apparatus which is transmitted to the sample hydrostatically due to compression of the assembly across the wedges (**Figure 1.12**). A heater, typically thermally conductive lanthanum chromite, graphite, or steel, is inserted into a cylindrical hole drilled through the octahedrally shaped, highly thermally stable ceramic pressure medium. A thermocouple is passed through the heater and the octahedron, and a capsule, usually consisting of platinum wrapped sample in an MgO or Al_2O_3 crucible, is inserted and packed with MgO or Al_2O_3 powder such that there are no remaining void spaces. Eight truncated tungsten carbide cubes are attached to the outside of the octahedron and stabilized by pyrophyllite gaskets on each phase, which serve to protect the tungsten carbide from direct contact with the wedge anvils. This simplified description (**Figure 1.13**) of the “mass market appropriate” Walker method illustrates the difficulty of high-pressure syntheses, and perhaps explains why high pressure solid state chemistry labs are still relatively rare, despite the enticing possibilities that high pressure unlocks.

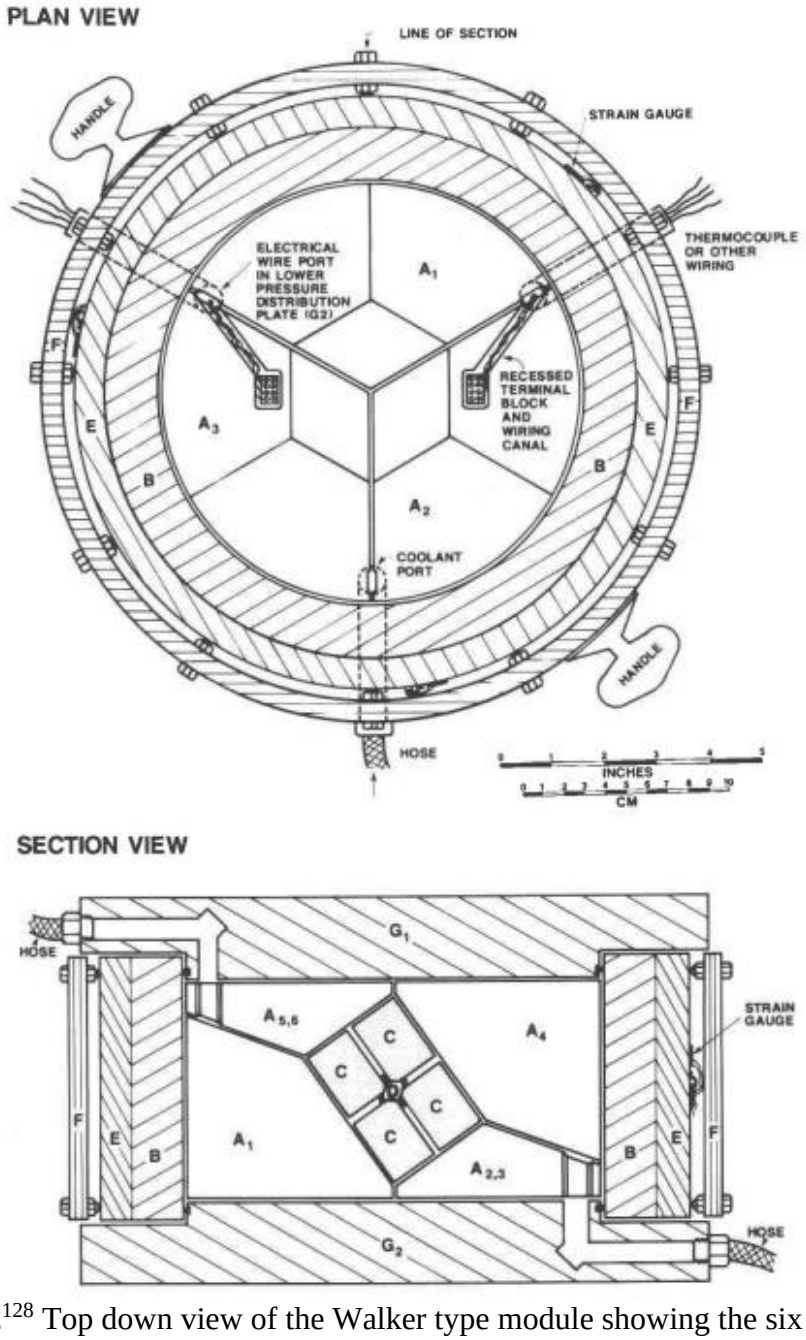

Figure 1.12[128] Top down view of the Walker type module showing the six wedges and (below) a side view of the same, which shows how the tungsten carbide cubes (labelled c) surround the octahedral pressure cell.

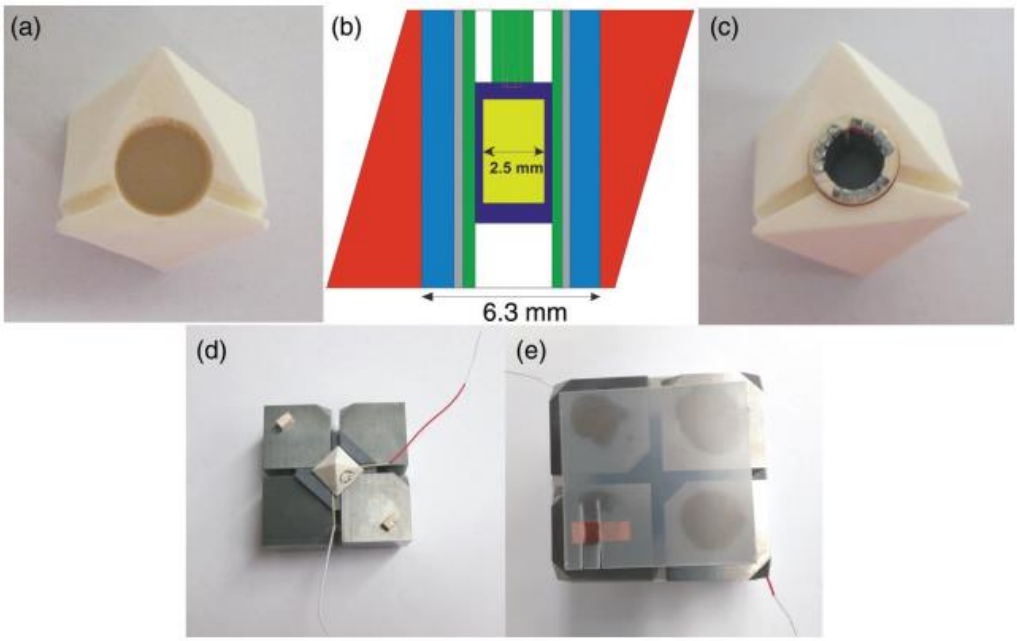

Figure 1.13[127].Views of: **a**. the typical octahedral pressure medium, **b**. cross section of the cylindrical hole in the octahedron (red) containing the heater (blue) and sample (yellow) in a crucible (purple), **c**. the octahedron with the filled heater inserted, **d**. the octahedron with thermocouple installed on the truncated tungsten carbide cubes, and **e**. completed assembly with pyrophyllite gaskets attached.

1.4 References

1. Saini, S.; Frankel, R.; Stark, D.; Ferrucci Jr, J., Magnetism: a primer and review. *American Journal of Roentgenology* **1988,** *150* (4), 735-743.
2. Wiberg, E.; Holleman, A. F.; Wiberg, N.; Eagleson, M.; Brewer, W., *Inorganic Chemistry*. Academic Press: 2001.
3. Klemm, W., *Magnetochemie*. Akademische Verlagsgesellschaft mbH: 1936; Vol. 1.
4. Lancashire, R. J. Magnetism. https://chem.libretexts.org/Bookshelves/Inorganic_Chemistry/Modules_and_Websites_(Inorganic_Chemistry)/Crystal_Field_Theory/Magnetism.
5. Spaldin, N. A., *Magnetic materials: Fundamentals and device applications*. Cambridge University Press Cambridge: 2003.
6. Suckling, E.; Kashy, E.; Bleaney, B.; Robinson, F. N., Magnetism. In *Encyclopædia Britannica*, Encyclopædia Britannica Inc.: 2019.
7. Kotnala, R. K.; Shah, J., Chapter 4 - Ferrite Materials: Nano to Spintronics Regime. In *Handbook of Magnetic Materials*, Buschow, K. H. J., Ed. Elsevier: 2015; Vol. 23, pp 291-379.
8. West, A. R., *Solid state chemistry and its applications*. John Wiley & Sons: 2014.
9. Heilbron, J. L., Rutherford–Bohr atom. *American Journal of Physics* **1981,** *49* (3), 223-231.
10. Si, N.; Yao, Q.; Jiang, Y.; Li, H.; Zhou, D.; Ji, Q.; Huang, H.; Li, H.; Niu, T., Recent Advances in Tin: From Two-Dimensional Quantum Spin Hall Insulator to Bulk Dirac Semimetal. *The Journal of Physical Chemistry Letters* **2020,** *11* (4), 1317-1329.
11. Morin, F. J.; Maita, J. P., Conductivity and Hall Effect in the Intrinsic Range of Germanium. *Physical Review* **1954,** *94* (6), 1525-1529.

12. Grochala, W., The generalized maximum hardness principle revisited and applied to solids (Part 2). *Physical Chemistry Chemical Physics* **2017,** *19* (46), 30984-31006.
13. Nolan, M.; Elliott, S. D., The p-type conduction mechanism in Cu_2O: a first principles study. *Physical Chemistry Chemical Physics* **2006,** *8* (45), 5350-5358.
14. Bendjedidi, H.; Attaf, A.; Saidi, H.; Aida, M. s.; Semmari, S.; Bouhdjer, A.; Benkhetta, Y., Properties of n-Type SnO_2 semiconductor prepared by spray ultrasonic technique for photovoltaic applications. *Journal of Semiconductors* **2015,** *36*.
15. Bierwagen, O., Indium oxide—a transparent, wide-band gap semiconductor for (opto)electronic applications. *Semiconductor Science and Technology* **2015,** *30* (2), 024001.
16. Chu, T. L.; Chu, S. S., Degenerate cadmium oxide films for electronic devices. *Journal of Electronic Materials* **1990,** *19* (9), 1003-1005.
17. Özgür, Ü.; Alivov, Y. I.; Liu, C.; Teke, A.; Reshchikov, M. A.; Doğan, S.; Avrutin, V.; Cho, S.-J.; Morkoç, H., A comprehensive review of ZnO materials and devices. *Journal of Applied Physics* **2005,** *98* (4), 041301.
18. Lin, X.; Xing, J.; Wang, W.; Shan, Z.; Xu, F.; Huang, F., Photocatalytic Activities of Heterojunction Semiconductors Bi_2O_3/$BaTiO_3$: A Strategy for the Design of Efficient Combined Photocatalysts. *The Journal of Physical Chemistry C* **2007,** *111* (49), 18288-18293.
19. Shuk, P.; Wiemhöfer, H. D.; Guth, U.; Göpel, W.; Greenblatt, M., Oxide ion conducting solid electrolytes based on Bi_2O_3. *Solid State Ionics* **1996,** *89* (3), 179-196.
20. Takahashi, K.; Yoshikawa, A.; Sandhu, A., *Wide Bandgap Semiconductors*. Springer, Berlin, Heidelberg: New York, 2007.
21. West, A. R., *Basic Solid State Chemistry*. John Wiley & Sons, Ltd: Chichester, England, 1999.
22. A century of ferroelectricity. *Nat. Mater.* **2020,** *19* (2), 129-129.
23. Valasek, J., Piezo-Electric and Allied Phenomena in Rochelle Salt. *Physical Review* **1921,** *17* (4).
24. Cohen, R. E., Origin of ferroelectricity in perovskite oxides. *Nature* **1992,** *358* (6382), 136-138.
25. Megaw, H., Origin of ferroelectricity in barium titanate and other perovskite-type crystals. *Acta Crystallographica* **1952,** *5* (6), 739-749.
26. Schmid, H., Multi-ferroic magnetoelectrics. *Ferroelectrics* **1994,** *162* (1), 317-338.
27. Fiebig, M., Revival of the magnetoelectric effect. *Journal of Physics D: Applied Physics* **2005,** *38* (8), R123-R152.
28. O'Dell, T. H., *The electrodynamics of magneto-electric media*. North-Holland Publishing Company: 1970; Vol. 11.
29. Fiebig, M.; Lottermoser, T.; Meier, D.; Trassin, M., The evolution of multiferroics. *Nature Reviews Materials* **2016,** *1*, 16046.
30. Lobo, R. "Types of Multiferroics". www.lpem.espci.fr/ocg/res_mf_types.html.
31. Hill, N. A., Why Are There so Few Magnetic Ferroelectrics? *The Journal of Physical Chemistry B* **2000,** *104* (29), 6694-6709.
32. J. Paul Attfield; Philip Lightfoot; Morris, R. E., "Perovskites". *Dalton Transactions* **2015,** *44*, 10541-10542.
33. Rose, G., “Ueber Einige Neue Mineralien Des Urals.”. *Journal Für Praktische Chemie* **1840,** *19* (1), 459-68.
34. Park, C. H.; Chadi, D. J., Microscopic study of oxygen-vacancy defects in ferroelectric perovskites. *Physical Review B* **1998,** *57* (22), R13961-R13964.
35. Cao, X.; Tian, H.; Hu, C.; Huang, F.; Wang, Y.; Sun, X.; Zhou, Z., Defect dipole evolution and its impact on the ferroelectric properties of Fe-doped KTN single crystals. *Journal of the American Ceramic Society* **2019,** *102* (6), 3117-3122.
36. Wu, L.; Podpirka, A.; Spanier, J. E.; Davies, P. K., Ferroelectric, Optical, and Photovoltaic Properties of Morphotropic Phase Boundary Compositions in the

$PbTiO_3$–$BiFeO_3$–$Bi(Ni_{1/2}Ti_{1/2})O_3$ System. *Chemistry of Materials* **2019,** *31* (11), 4184-4194.

37. Jin, L.; Pang, J.; Pu, Y.; Xu, N.; Tian, Y.; Jing, R.; Du, H.; Wei, X.; Xu, Z.; Guo, D.; Xu, J.; Gao, F., Thermally stable electrostrains and composition-dependent electrostrictive coefficient Q33 in lead-free ferroelectric ceramics. *Ceramics International* **2019,** *45* (17, Part B), 22854-22861.
38. Kornev, I. A.; Bellaiche, L.; Bouvier, P.; Janolin, P. E.; Dkhil, B.; Kreisel, J., Ferroelectricity of Perovskites under Pressure. *Physical Review Letters* **2005,** *95* (19), 196804.
39. Halder, A.; Rakita, Y.; Cahen, D.; Sarkar, S. K., Effect of Low Pressure on Tetragonal to Cubic Phase Transition of Methylammonium Lead Iodide Perovskite. *The Journal of Physical Chemistry Letters* **2020,** *11* (4), 1473-1476.
40. Buscaglia, V.; Randall, C. A., Size and scaling effects in barium titanate. An overview. *Journal of the European Ceramic Society* **2020**.
41. Papet, P.; Dougherty, J. P.; Shrout, T. R., Particle and grain size effects on the dielectric behavior of the relaxor ferroelectric $Pb(Mg_{1/3}Nb_{2/3})O_3$. *Journal of Materials Research* **1990,** *5* (12), 2902-2909.
42. Anderson, M. T.; Greenwood, K. B.; Taylor, G. A.; Poeppelmeier, K. R., B-cation arrangements in double perovskites. *Progress in Solid State Chemistry* **1993,** *22* (3), 197-233.
43. Benedek, N. A.; Fennie, C. J., Why Are There So Few Perovskite Ferroelectrics? *The Journal of Physical Chemistry C* **2013,** *117* (26), 13339-13349.
44. Blasse, G., Some Magnetic Properties of Mixed Metal Oxides with Ordered Perovskite Structure. *Phillips Research Reports* **1965,** *20*, 327-336.
45. Hossain, A.; Bandyopadhyay, P.; Roy, S., An overview of double perovskites $A_2B'B''O_6$ with small ions at A site: Synthesis, structure and magnetic properties. *J. Alloy Compd.* **2018,** *740*, 414-427.
46. Howard, C. J.; Kennedy, B. J.; Woodward, P. M., Ordered double perovskites – a group-theoretical analysis. *Acta Crystallographica Section B* **2003,** *B59*, 463-471.
47. Filippetti, A.; Hill., N. A., "Coexistence of magnetism and ferroelectricity in perovskites.". *Physical Review B* **2002,** *65* (19), 195120.
48. Zu, N.; Li, R.; Ai, R., Structural, electronic and magnetic properties and pressure-induced half metallicity in double perovskite Ca_2AOsO_6 (A = Cr, Mo). *Journal of Magnetism and Magnetic Materials* **2018,** *467* (1), 145-149.
49. Silva, R. B. d.; J.M.Soares; Costa, J. A. P. d.; Araújo, J. H. d.; A.R.Rodrigues; Machado, F. L. A., Local iron ion distribution and magnetic properties of the perovskites $La_{1-x}Sr_xFeO_{3-\gamma}$. *Journal of Magnetism and Magnetic Materials* **2018,** *466*, 306-310.
50. Goldschmidt, V. M., Die Gesetze der Krystallochemie. *Naturwissenschaften* **1926,** *14* (21), 477-485.
51. Nelmes, R. J.; Meyer, G. M.; Hutton, J., Thermal motion in $SrTiO_3$ at room temperature: Anharmonic or disordered? *Ferroelectrics* **1978,** *21* (1), 461-462.
52. Belik, A. A.; Yi, W., High-pressure synthesis, crystal chemistry and physics of perovskites with small cations at the A site. *J. Phys. Condens. Matter* **2014,** *26*, 163201.
53. Živković, I.; Prša, K.; Zaharko, O.; Berger, H., Ni_3TeO_6—a collinear antiferromagnet with ferromagnetic honeycomb planes. *Journal of Physics: Condensed Matter* **2010,** *22* (5), 056002.
54. Aimi, A.; Katsumata, T.; Mori, D.; Fu, D.; Itoh, M.; Kyômen, T.; Hiraki, K.-i.; Takahashi, T.; Inaguma, Y., High-Pressure Synthesis and Correlation between Structure, Magnetic, and Dielectric Properties in $LiNbO_3$-Type $MnMO_3$ (M = Ti, Sn). *Inorganic Chemistry* **2011,** *50* (13), 6392-6398.
55. Badding, J. V., High-Pressure synthesis, characterization, and tuning of solid state materials. *Annual Review of Materials Science* **1998,** *28* (1), 631-658.

56. Dos santos-García, A. J.; Solana-Madruga, E.; Ritter, C.; Ávila-Brande, D.; Fabelo, O.; Sáez-Puche, R., Synthesis, structures and magnetic properties of the dimorphic Mn_2CrSbO_6 oxide. *Dalton Transactions* **2015,** *44* (23), 10665-10672.
57. Vasala, S.; Karppinen, M., $A_2B'B''O_6$ perovskites: A review. *Prog. Solid State Chem.* **2015,** *43* (1), 1-36.
58. Yang, J.; Zhang, P.; Wei, S.-H., Band Structure Engineering of $Cs_2AgBiBr_6$ Perovskite through Order–Disordered Transition: A First-Principle Study. *The Journal of Physical Chemistry Letters* **2018,** *9* (1), 31-35.
59. Chen, Q.; Svoboda, C.; Zheng, Q.; Sales, B. C.; Mandrus, D. G.; Zhou, H. D.; Zhou, J. S.; McComb, D.; Randeria, M.; Trivedi, N.; Yan, J. Q., Magnetism out of antisite disorder in the J=0 compound Ba_2YIrO_6. *Physical Review B* **2017,** *96* (14), 144423.
60. Sakhnenko, V. P.; Ter-Oganessian, N. V., Theory of order-disorder phase transitions of B-cations in $AB'_{1/2}B''_{1/2}O_3$ perovskites. *Acta Crystallographica Section B* **2018,** *74* (3), 264-273.
61. King, G.; Woodward, P. M., Cation ordering in perovskites. *Journal of Materials Chemistry* **2010,** *20* (28), 5785-5796.
62. Burton, B. P.; Cockayne, E., Why $Pb(B,B')O_3$ perovskites disorder at lower temperatures than $Ba(B,B')O_3$ perovskites. *Physical Review B* **1999,** *60* (18), R12542-R12545.
63. Kobayashi, K. I.; Kimura, T.; Sawada, H.; Terakura, K.; Tokura, Y., Room-temperature magnetoresistance in an oxide material with an ordered double-perovskite structure. *Nature* **1998,** *395*, 677.
64. Goodenough, J. B., Theory of the Role of Covalence in the Perovskite-Type Manganites [La, M(II)]MnO_3. *Physical Review* **1955,** *100* (2), 564-573.
65. Kanamori, J., Superexchange interaction and symmetry properties of electron orbitals. *Journal of Physics and Chemistry of Solids* **1959,** *10* (2), 87-98.
66. Ivanov, S. A.; Eriksson, S. G.; Tellgren, R.; Rundlöf, H.; Tseggai, M., The magnetoelectric perovskite Sr_2CoMoO_6: An insight from neutron powder diffraction. *Materials Research Bulletin* **2005,** *40* (5), 840-849.
67. Muñoz, A.; Alonso, J. A.; Casais, M. T.; Mart nez-Lope, M. J.; Fern ndez-D az, M. T., Crystal and magnetic structure of the complex oxides Sr_2MnMoO_6, $Sr_2MnWO_6$and Ca_2MnWO_6: a neutron diffraction study. *Journal of Physics: Condensed Matter* **2002,** *14* (38), 8817-8830.
68. Sarma, D. D., A new class of magnetic materials: Sr_2FeMoO_6 and related compounds. *Current Opinion in Solid State and Materials Science* **2001,** *5* (4), 261-268.
69. Sarma, D. D.; Sampathkumaran, E. V.; Ray, S.; Nagarajan, R.; Majumdar, S.; Kumar, A.; Nalini, G.; Guru Row, T. N., Magnetoresistance in ordered and disordered double perovskite oxide, Sr_2FeMoO_6. *Solid State Communications* **2000,** *114* (9), 465-468.
70. Kalanda, M.; Suchaneck, G.; Saad, A. M.; Demyanov, S.; Gerlach, G., Influence of Oxygen Stoichiometry and Cation Ordering on Magnetoresistive Properties of $Sr_2FeMoO_{6\pm\delta}$. *Materials Science Forum* **2010,** *636-637*, 338-343.
71. Taz, H.; Prasad, B.; Huang, Y.-L.; Chen, Z.; Hsu, S.-L.; Xu, R.; Thakare, V.; Sakthivel, T. S.; Liu, C.; Hettick, M.; Mukherjee, R.; Seal, S.; Martin, L. W.; Javey, A.; Duscher, G.; Ramesh, R.; Kalyanaraman, R., Integration of amorphous ferromagnetic oxides with multiferroic materials for room temperature magnetoelectric spintronics. *Scientific reports* **2020,** *10* (1), 3583.
72. Saloaro, M.; Hoffmann, M.; Adeagbo, W. A.; Granroth, S.; Deniz, H.; Palonen, H.; Huhtinen, H.; Majumdar, S.; Laukkanen, P.; Hergert, W.; Ernst, A.; Paturi, P., Toward Versatile Sr_2FeMoO_6-Based Spintronics by Exploiting Nanoscale Defects. *ACS Applied Materials & Interfaces* **2016,** *8* (31), 20440-20447.
73. Haghiri-Gosnet, A. M.; Arnal, T.; Soulimane, R.; Koubaa, M.; Renard, J. P., Spintronics: perspectives for the half-metallic oxides. *physica status solidi (a)* **2004,** *201* (7), 1392-1397.

74. Reyes, A. M.; Montoya, J. A.; Navarro, O., Demise of half-metallicity upon increasing of disorder in the double perovskite $Sr_{2-y}La_yFeMoO_6$. *Journal of Magnetism and Magnetic Materials* **2020,** *495*, 165877.
75. Belik, A.; Yi, W., High-pressure synthesis, crystal chemistry and physics of perovskites with small cations at the A site. *Journal of physics. Condensed matter : an Institute of Physics journal* **2014,** *26*, 163201.
76. Yi, W.; Liang, Q.; Matsushita, Y.; Tanaka, M.; Belik, A. A., High-Pressure Synthesis, Crystal Structure, and Properties of In_2NiMnO_6 with Antiferromagnetic Order and Field-Induced Phase Transition. *Inorganic Chemistry* **2013,** *52* (24), 14108-14115.
77. Yi, W.; Princep, A. J.; Guo, Y.; Johnson, R. D.; Khalyavin, D.; Manuel, P.; Senyshyn, A.; Presniakov, I. A.; Sobolev, A. V.; Matsushita, Y.; Tanaka, M.; Belik, A. A.; Boothroyd, A. T., Sc_2NiMnO_6: A Double-Perovskite with a Magnetodielectric Response Driven by Multiple Magnetic Orders. *Inorganic Chemistry* **2015,** *54* (16), 8012-8021.
78. Li, M. R.; Retuerto, M.; Deng, Z.; Stephens, P. W.; Croft, M.; Huang, Q.; Wu, H.; Deng, X.; Kotliar, G.; Sánchez-Benítez, J.; Hadermann, J.; Walker, D.; Greenblatt, M., Giant Magnetoresistance in the Half-Metallic Double-Perovskite Ferrimagnet Mn_2FeReO_6. *Angew. Chem. Int. Ed. Engl.* **2015,** *54* (41), 12069-12073.
79. Li, M. R.; Hodges, J. P.; Retuerto, M.; Deng, Z.; Stephens, P. W.; Croft, M. C.; Deng, X. Y.; Kotliar, G.; Sanchez-Benitez, J.; Walker, D.; Greenblatt, M., Mn_2MnReO_6: Synthesis and Magnetic Structure Determination of a New Transition-Metal-Only Double Perovskite Canted Antiferromagnet. *Chemistry of Materials* **2016,** *28* (9), 3148-3158.
80. Arévalo-López, A. M.; McNally, G. M.; Attfield, J. P., Large Magnetization and Frustration Switching of Magnetoresistance in the Double-Perovskite Ferrimagnet Mn_2FeReO_6. *Angew. Chem. Int. Ed* **2015,** *54* (41), 12074-12077.
81. Arévalo-López, A. M.; Stegemann, F.; Attfield, J. P., Competing antiferromagnetic orders in the double perovskite Mn_2MnReO_6 (Mn_3ReO_6). *Chemical Communications* **2016,** *52* (32), 5558-5560.
82. M.-R. Li; P. W. Stephens; M. Croft; Z. Deng; W. Li; C. Jin; M. Retuerto; J. P. Hodges; C. E. Frank; M. Wu; D. Walker; Greenblatt, M., $Mn_2(Fe_{0.8}Mo_{0.2})MoO_6$: A Double Perovskite with Multiple Transition Metal Sublattice Magnetic Effects. *Chem. Mater.* **2018,** *30*, 4508-4514.
83. Frank, C. E.; McCabe, E. E.; Orlandi, F.; Manuel, P.; Tan, X.; Deng, Z.; Croft, M.; Cascos, V.; Emge, T.; Feng, H. L.; Lapidus, S.; Jin, C.; Wu, M.; Li, M. R.; Ehrlich, S.; Khalid, S.; Quackenbush, N.; Yu, S.; Walker, D.; Greenblatt, M., Mn_2CoReO_6: a robust multisublattice antiferromagnetic perovskite with small A-site cations. *Chemical Communications* **2019,** *55* (23), 3331-3334.
84. Belik, A. A.; Matsushita, Y.; Kumagai, Y.; Katsuya, Y.; Tanaka, M.; Stefanovich, S. Y.; Lazoryak, B. I.; Fumiyasu Oba, a. K. Y., Complex Structural Behavior of $BiMn_7O_{12}$ Quadruple Perovskite. *Inorganic Chemistry* **2017,** *56* (20), 12272-12281.
85. Shimakawa, Y., A-Site-Ordered Perovskites with Intriguing Physical Properties. *Inorganic Chemistry* **2008,** *47* (19), 8562-8570.
86. Long, Y., A -site ordered quadruple perovskite oxides. *Chinese Physics B* **2016,** *25* (7), 078108.
87. Vasil'ev, A. N.; Volkova, O. S., New functional materials $AC_3B_4O_{12}$ (Review). *Low Temperature Physics* **2007,** *33* (11), 895-914.
88. Chenavas, J.; Joubert, J. C.; Marezio, M.; Bochu, B., The synthesis and crystal structure of $CaCu_3Mn_4O_{12}$: A new ferromagnetic-perovskite-like compound. *Journal of Solid State Chemistry* **1975,** *14* (1), 25-32.
89. Subramanian, M. A.; Li, D.; Duan, N.; Reisner, B. A.; Sleight, A. W., High Dielectric Constant in $ACu_3Ti_4O_{12}$ and $ACu_3Ti_3FeO_{12}$ Phases. *Journal of Solid State Chemistry* **2000,** *151* (2), 323-325.

90. Bochu, B.; Chenavas, J.; Joubert, J. C.; Marezio, M., High-Pressure Synthesis and Crystal-Structure of a New Series of Perovskite-Like Compounds CMn_7O_{12} (C = Na, Ca, Cd, Sr, La, Nd). *Journal of Solid State Chemistry* **1974,** *11* (2), 88-93.
91. Prodi, A.; Gilioli, E.; Gauzzi, A.; Licci, F.; Marezio, M.; Bolzoni, F.; Huang, Q.; Santoro, A.; Lynn, J. W., Charge, orbital, and spin ordering phenomena in the mixed valence manganite $(NaMn^{3+3})(Mn^{3+2}Mn^{4+2})O_{12}$. *Nat. Mater.* **2004,** *3* (1), 48-52.
92. Streltsov, S.; Khomskii, D., Jahn-Teller distortion and charge, orbital, and magnetic order in $NaMn_7O_{12}$. *Physical Review B* **2014,** *89*.
93. Bergerhoff, G. B., I.D., Inorganic Crystal Structure Database. In FIZ Karlsruhe: 2020.
94. Yamada, I.; Tsuchida, K.; Ohgushi, K.; Hayashi, N.; Kim, J.; Tsuji, N.; Takahashi, R.; Matsushita, M.; Nishiyama, N.; Inoue, T.; Irifune, T.; Kato, K.; Takata, M.; Takano, M., Giant Negative Thermal Expansion in the Iron Perovskite $SrCu_3Fe_4O_{12}$. *Angewandte Chemie International Edition* **2011,** *50* (29), 6579-6582.
95. Shimakawa, Y., Crystal and magnetic structures of $CaCu_3Fe_4O_{12}$and $LaCu_3Fe4O_{12}$: distinct charge transitions of unusual high valence Fe. *Journal of Physics D: Applied Physics* **2015,** *48* (50), 504006.
96. Yamada, I.; Takata, K.; Hayashi, N.; Shinohara, S.; Azuma, M.; Mori, S.; Muranaka, S.; Shimakawa, Y.; Takano, M., A Perovskite Containing Quadrivalent Iron as a Charge-Disproportionated Ferrimagnet. *Angewandte Chemie International Edition* **2008,** *47* (37), 7032-7035.
97. Yamada, I.; Ochi, M.; Mizumaki, M.; Hariki, A.; Uozumi, T.; Takahashi, R.; Irifune, T., High-Pressure Synthesis, Crystal Structure, and Unusual Valence State of Novel Perovskite Oxide $CaCu_3Rh_4O_{12}$. *Inorganic Chemistry* **2014,** *53* (14), 7089-7091.
98. Belik, A. A., Rise of A-site columnar-ordered $A_2A'A''B_4O_{12}$ quadruple perovskites with intrinsic triple order. *Dalton Transactions* **2018,** *47* (10), 3209-3217.
99. Ramirez, A. P.; Subramanian, M. A.; Gardel, M.; Blumberg, G.; Li, D.; Vogt, T.; Shapiro, S. M., Giant dielectric constant response in a copper-titanate. *Solid State Communications* **2000,** *115* (5), 217-220.
100. Mezzadri, F.; Calestani, G.; Calicchio, M.; Gilioli, E.; Bolzoni, F.; Cabassi, R.; Marezio, M.; Migliori, A., Synthesis and characterization of multiferroic BiMn7 O12. *Physical Review B* **2009,** *79* (10), 100106.
101. Ye, M.; Vanderbilt, D., Ferroelectricity in corundum derivatives. *Physical Review B* **2016,** *93* (13), 134303.
102. Cai, G.-H.; Greenblatt, M.; Li, M.-R., Polar Magnets in Double Corundum Oxides. *Chemistry of Materials* **2017,** *29* (13), 5447-5457.
103. Bristow, J. K.; Tiana, D.; Parker, S. C.; Walsh, A., Defect chemistry of Ti and Fe impurities and aggregates in Al_2O_3. *J. Mater. Chem. A* **2014,** *2* (17), 6198-6208.
104. Finger, L. W.; Hazen, R. M., Crystal structure and compression of ruby to 46 kbar. *Journal of Applied Physics* **1978,** *49* (12), 5823-5826.
105. Morosin, B.; Baughman, R. J.; Ginley, D. S.; Butler, M. A., The influence of crystal structure on the photoresponse of iron-titanium oxide electrodes. *Journal of Applied Crystallography* **1978,** *11* (2), 121-124.
106. Megaw, H., A note on the structure of lithium niobate, $LiNbO_3$. *Acta Crystallographica Section A* **1968,** *24* (6), 583-588.
107. Arévalo-López, Á. M.; Solana-Madruga, E.; Arévalo-López, E. P.; Khalyavin, D.; Kepa, M.; Dos santos-García, A. J.; Sáez-Puche, R.; Attfield, J. P., Evolving spin periodicity and lock-in transition in the frustrated ordered ilmenite-type β-Mn_2InSbO_6. *Physical Review B* **2018,** *98* (21), 214403.
108. Newnham, R. E.; Meagher, E. P., Crystal structure of Ni_3TeO_6. *Materials Research Bulletin* **1967,** *2* (5), 549-554.
109. Wu, X.; Qin, S.; Dubrovinsky, L., Structural characterization of the $FeTiO_3$–$MnTiO_3$ solid solution. *Journal of Solid State Chemistry* **2010,** *183* (10), 2483-2489.
110. Solana-Madruga, E.; Dos santos-García, A. J.; Arévalo-López, A. M.; Ávila-Brande, D.; Ritter, C.; Attfield, J. P.; Sáez-Puche, R., High pressure synthesis of polar and

non-polar cation-ordered polymorphs of Mn_2ScSbO_6. *Dalton Transactions* **2015,** *44* (47), 20441-20448.

111. Li, M. R.; Walker, D.; Retuerto, M.; Sarkar, T.; Hadermann, J.; Stephens, P. W.; Croft, M.; Ignatov, A.; Grams, C. P.; Hemberger, J.; Nowik, I.; Halasyamani, P. S.; Tran, T. T.; Mukherjee, S.; Dasgupta, T. S.; Greenblatt, M., Polar and magnetic Mn_2FeMO_6 (M=Nb, Ta) with $LiNbO_3$-type structure: high-pressure synthesis. *Angew. Chem. Int. Ed. Engl.* **2013,** *52* (32), 8406-10.
112. Li, M.-R.; McCabe, E. E.; Stephens, P. W.; Croft, M.; Collins, L.; Kalinin, S. V.; Deng, Z.; Retuerto, M.; Sen Gupta, A.; Padmanabhan, H.; Gopalan, V.; Grams, C. P.; Hemberger, J.; Orlandi, F.; Manuel, P.; Li, W.-M.; Jin, C.-Q.; Walker, D.; Greenblatt, M., Magnetostriction-polarization coupling in multiferroic Mn_2MnWO_6. *Nature Communications* **2017,** *8* (1), 2037.
113. Varga, T.; Kumar, A.; Vlahos, E.; Denev, S.; Park, M.; Hong, S.; Sanehira, T.; Wang, Y.; Fennie, C. J.; Streiffer, S. K.; Ke, X.; Schiffer, P.; Gopalan, V.; Mitchell, J. F., Coexistence of Weak Ferromagnetism and Ferroelectricity in the High Pressure $LiNbO_3$-Type Phase of $FeTiO_3$. *Physical Review Letters* **2009,** *103* (4), 4.
114. Belik, A. A.; Furubayashi, T.; Matsushita, Y.; Tanaka, M.; Hishita, S.; Takayama-Muromachi, E., Indium-Based Perovskites: A New Class of Near-Room-Temperature Multiferroics. *Angewandte Chemie International Edition* **2009,** *48* (33), 6117-6120.
115. Kawamoto, T.; Fujita, K.; Yamada, I.; Matoba, T.; Kim, S. J.; Gao, P.; Pan, X.; Findlay, S. D.; Tassel, C.; Kageyama, H.; Studer, A. J.; Hester, J.; Irifune, T.; Akamatsu, H.; Tanaka, K., Room-Temperature Polar Ferromagnet $ScFeO_3$ Transformed from a High-Pressure Orthorhombic Perovskite Phase. *Journal of the American Chemical Society* **2014,** *136* (43), 15291-15299.
116. Li, M. R.; Stephens, P. W.; Retuerto, M.; Sarkar, T.; Grams, C. P.; Hemberger, J.; Croft, M. C.; Walker, D.; Greenblatt, M., Designing Polar and Magnetic Oxides: Zn_2FeTaO_6 - in Search of Multiferroics. *Journal of the American Chemical Society* **2014,** *136* (24), 8508-8511.
117. Li, M. R.; Retuerto, M.; Walker, D.; Sarkar, T.; Stephens, P. W.; Mukherjee, S.; Dasgupta, T. S.; Hodges, J. P.; Croft, M.; Grams, C. P.; Hemberger, J.; Sanchez-Benitez, J.; Huq, A.; Saouma, F. O.; Jang, J. I.; Greenblatt, M., Magnetic-Structure-Stabilized Polarization in an Above-Room-Temperature Ferrimagnet. *Angewandte Chemie-International Edition* **2014,** *53* (40), 10774-10778.
118. Li, M. R.; Retuerto, M.; Stephens, P. W.; Croft, M.; Sheptyakov, D.; Pomjakushin, V.; Deng, Z.; Akamatsu, H.; Gopalan, V.; Sanchez-Benitez, J.; Saouma, F. O.; Jang, J. I.; Walker, D.; Greenblatt, M., Low-Temperature Cationic Rearrangement in a Bulk Metal Oxide. *Angew. Chem. Int. Ed. Engl.* **2016,** *55* (34), 9862-7.
119. Li, M. R.; Croft, M.; Stephens, P. W.; Ye, M.; Vanderbilt, D.; Retuerto, M.; Deng, Z.; Grams, C. P.; Hemberger, J.; Hadermann, J.; Li, W. M.; Jin, C. Q.; Saouma, F. O.; Jang, J. I.; Akamatsu, H.; Gopalan, V.; Walker, D.; Greenblatt, M., Mn_2FeWO_6 : A new Ni_3TeO_6-type polar and magnetic oxide. *Advanced materials (Deerfield Beach, Fla.)* **2015,** *27* (13), 2177-81.
120. Tassel, C.; Kuno, Y.; Goto, Y.; Yamamoto, T.; Brown, C. M.; Hester, J.; Fujita, K.; Higashi, M.; Abe, R.; Tanaka, K.; Kobayashi, Y.; Kageyama, H., MnTaO2N: Polar $LiNbO_3$-type Oxynitride with a Helical Spin Order. *Angewandte Chemie International Edition* **2015,** *54* (2), 516-521.
121. Fujita, K.; Kawamoto, T.; Yamada, I.; Hernandez, O.; Hayashi, N.; Akamatsu, H.; Lafargue-Dit-Hauret, W.; Rocquefelte, X.; Fukuzumi, M.; Manuel, P.; Studer, A. J.; Knee, C. S.; Tanaka, K., $LiNbO_3$-Type $InFeO_3$: Room-Temperature Polar Magnet without Second-Order Jahn–Teller Active Ions. *Chemistry of Materials* **2016,** *28* (18), 6644-6655.
122. Ji, K.-l.; Solana-Madruga, E.; Arevalo-Lopez, A. M.; Manuel, P.; Ritter, C.; Senyshyn, A.; Attfield, J. P., Lock-in spin structures and ferrimagnetism in polar $Ni_{2-x}Co_xScSbO_6$ oxides. *Chemical Communications* **2018,** *54* (88), 12523-12526.

123. Feng, H.; Deng, Z.; Croft, M.; Lapidus, S.; Zu, R.; Gopalan, V.; Grams, C.; Hemberger, J.; Liu, S.; Tyson, T.; Frank, C.; Jin, C.; Walker, D.; Greenblatt, M., High-Pressure Synthesis and Ferrimagnetism of Ni_3TeO_6-Type Mn_2ScMO_6 (M = Nb, Ta). *Inorganic Chemistry* **2019**.
124. Han, Y.; Zeng, Y.; Hendrickx, M.; Hadermann, J.; Stephens, P. W.; Zhu, C.; Grams, C. P.; Hemberger, J.; Frank, C.; Li, S.; Wu, M.; Retuerto, M.; Croft, M.; Walker, D.; Yao, D.-X.; Greenblatt, M.; Li, M.-R., Universal A-Cation Splitting in $LiNbO_3$-Type Structure Driven by Intrapositional Multivalent Coupling. *Journal of the American Chemical Society* **2020,** *142* (15), 7168-7178.
125. Walsh, J. P. S.; Freedman, D. E., High-Pressure Synthesis: A New Frontier in the Search for Next-Generation Intermetallic Compounds. *Accounts of Chemical Research* **2018,** *51* (6), 1315-1323.
126. Liebermann, R. C., Multi-anvil, high pressure apparatus: a half-century of development and progress. *High Pressure Research* **2011,** *31* (4), 493-532.
127. Landskron, K., High Pressure Chemistry. In *Kirk-Othmer Encyclopedia of Chemical Technology*, 2016; pp 1-45.
128. Walker, D.; Carpenter, M. A.; Hitch, C. M., Some simplifications to multianvil devices for high pressure experiments. *American Mineralogist* **1990,** *75* (9-10), 1020-1028.
129. Walker, D., Lubrication, gasketing, and precision in multianvil experiments. *American Mineralogist* **1991,** *76* (7-8), 1092-1100.
130. Walker, D.; Li, J., Castable solid pressure media for multianvil devices. *Matter and Radiation at Extremes* **2020,** *5* (1), 018402.
131. Leinenweber, K.; Mosenfelder, J.; Diedrich, T.; Soignard, E.; Sharp, T. G.; Tyburczy, J. A.; Wang, Y., High-pressure cells for in situ multi-anvil experiments. *High Pressure Research* **2006,** *26* (3), 283-292.
132. Leinenweber, K. D.; Tyburczy, J. A.; Sharp, T. G.; Soignard, E.; Diedrich, T.; Petuskey, W. B.; Wang, Y.; Mosenfelder, J. L., Cell assemblies for reproducible multi-anvil experiments (the COMPRES assemblies). *American Mineralogist* **2012,** *97* (2-3), 353-368.
133. Ito, E.; Schubert, G.; Romanowicz, B.; Dziewonski, A., Theory and practice-multianvil cells and high-pressure experimental methods. *Treatise on geophysics* **2007,** *2*, 197-230.
134. Hall, H. T., High pressure apparatus: ram-in-tie-bar multianvil presses. **1967**.
135. Lloyd, E.; Hutton, U.; Johnson, D., Compact multi-anvil wedge-type high pressure apparatus. *J. Res. NBS* **1959,** *63* (1), 59.
136. Houck, J. C.; Hutton, U. O., Correlation of factors influencing the pressures generated in multi-anvil devices. *High-Pressure Measurement. AA Giardini, EC Lloyd (eds). Butterworths, London* **1963**.
137. Osugi, J.; Shimizu, K.; Inoue, K.; Yasunami, K., A compact cubic anvil high pressure apparatus. **1964**.

Chapter 2: Materials and Methods

2.1 Synthesis

The materials detailed herein were synthesized exclusively at high pressure in a Walker-type multi-anvil press at Columbia University Lamont-Doherty Earth Observatory with the assistance and instruction of David Walker. Numerous trials, both at high pressure and ambient pressure (at Rutgers University), were attempted to synthesize perovskite and corundum derivative materials with small A-site cations for potential multiferroic or spintronic applications. Herein, syntheses which produced the most phase pure candidate materials are described.

2.1.1 Synthesis of Mn_2CoReO_6

Small (< 0.1 mm) black, plate-like crystals of Mn_2CoReO_6 were synthesized at high pressure and temperature (HPHT) in a Walker-Type multi-anvil device. Stoichiometric amounts of MnO (99%, Sigma-Aldrich), Co_3O_4 (99.9985%, Alfa Aesar), Re (Strem Chemicals, 99.99%), and ReO_3 (Alfa Aesar, 99.9%) were thoroughly ground in an agate mortar and sealed in a platinum capsule. The ReO_3 was stored in a 200˚ C drying oven, and the Co_3O_4 was dried overnight at 700˚ C before being ground, since both are mildly hygroscopic. The capsule was pressurized to 8 GPa and heated at 1623 K for 30 min before being quenched to room temperature by turning off power to the resistance furnace. The pressure was maintained throughout the heating and quenching process, then slowly released over 8-12 hours.

2.1.2 Synthesis of $LaMn_3Rh_4O_{12}$

Polycrystalline $LaMn_3Rh_4O_{12}$ was synthesized by solid-state reaction at HPHT. Stoichiometric amounts of La_2O_3, Mn_2O_3, (preheated at 950˚ C and 850˚ C, respectively, for 12 hours in air) and Rh_2O_3 (preheated to 800˚ C for 12 hours in flowing oxygen) were thoroughly ground in an agate mortar and sealed in a platinum foil capsule, which was then pressurized overnight in a Walker-type multi-anvil press to 8 GPa and heated at 1,150˚ C for 3 days. Finally, the sample was quenched at pressure and depressurized overnight.

2.1.3 Synthesis of $Fe_{3-x}InSn_xO_6$ (x = 0, 0.25, 0.5)

Powders of SnO_2, (Sigma Aldrich, 99.9%) Fe_2O_3, In_2O_3, and Fe (Alfa Aesar 99.998%, 99.99%, and 99.9%, respectively) were weighed in appropriate stoichiometric quantities and thoroughly ground in an agate mortar. The mixed powder was then wrapped in platinum foil and loaded into a Walker-type multi anvil apparatus. Samples were pressurized to 6 GPa over 8-12 hours then heated between 1400-1450˚C for 0.5-2 hours, with longer times preferred to promote the growth of larger single crystals (up to 1 mm) and shorter times optimized to preserve aggregated dense pellets (appropriate for certain properties measurements). Samples were quenched by turning off power to the heater and depressurized over the course of several hours.

2.1.4 Synthesis of $In_2Mn_{1.1}Sn_{0.9}O_6$

Powders of MnO and SnO_2 (Sigma-Aldrich 99.9%) and In_2O_3 (Alfa Aesar 99.99%) were ground for 20-30 minutes in an agate mortar after being weighed in appropriate stoichiometric quantities under the mentorship of Dr. Xiaoyan Tan, who lead this project. Powders were wrapped in platinum foil and loaded into a Walker-type multi anvil apparatus. Samples were pressurized to 6 GPa overnight hours then

heated between 1400-1450˚C for 0.5 hours. Samples were quenched by turning off power to the heater and slowly depressurized overnight.

2.2 X-ray, Synchrotron, and Neutron Diffraction

2.2.1 Powder X-ray Diffraction

X-ray diffraction is possible because crystalline materials act as a 3-dimensional diffraction grating that causes an interference pattern when interacting with a beam of X-rays. The position and intensities of the peaks of this pattern are thus directly dependent on the arrangement of the atoms in the planes of a crystal, which can be determined by collecting the diffracted X-rays at different angles. **Figure 2.1** shows a representation of the beam path of a typical powder X-ray diffraction (PXD) diffractometer, upon which a finely ground sample at fixed position is bombarded by X-rays of a known wavelength. The detector, D, (which detects the intensity of the diffracted X-rays) and the X-ray generator, R, rotate at constant rate along the "measuring circle" by means of a goniometer (an instrument that can rotate to a precise angle). The diffraction angle, 2θ, is equal to twice the glancing angle, θ.

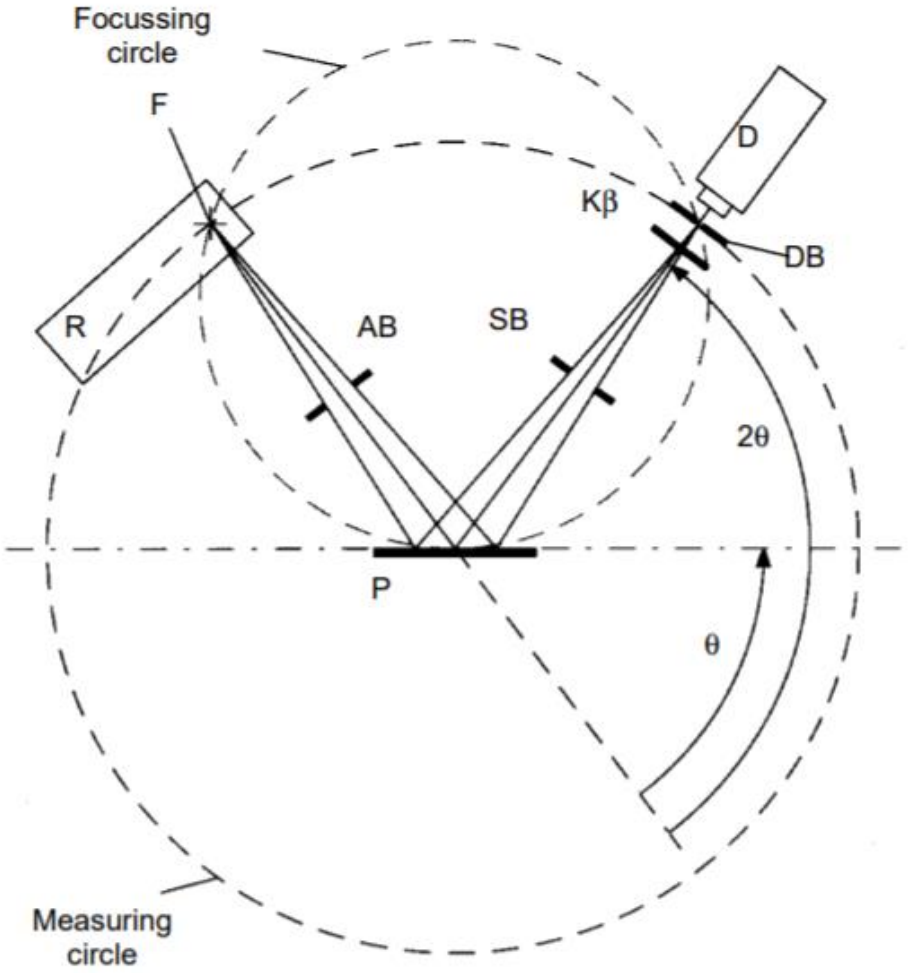

Figure 2.1[138] Beam path of a D-8 Advance powder diffractometer, from the manual. θ and 2θ are the glancing angle and the diffraction angle; AB, SB, and DB are the aperture, scattered-radiation, and detector slits, respectively (which reduce divergence and focus the X-ray beam); D is the detector; F is the Focus; R is the X-ray tube; and P is the sample.

The intensities and peak positions measured this way are of significance because from them one can determine the arrangement of atoms in the crystalline unit cell. According to Bragg's Law,

$$n\lambda = 2d\sin(\theta) \tag{2.1}$$

(θ is the glancing angle of the incident X-rays, d is the distance between the lattice planes, λ is the wavelength of the incident beam, and n is a positive integer); therefore if one knows the wavelength of the incident beam and measures the angle at which

peaks (positive interference) occur, *d* can be deduced. This allows the determination of lattice parameters and symmetry, that is, space group (though powder diffraction often cannot determine the difference between centrosymmetric and noncentrosymmetric space groups).[2, 139-140] Additionally, as the relative intensities of these peaks are determined by the distribution of atoms in the unit cell (in our case, but it should be noted that X-ray scattering matter can also be molecules or ions) consideration of the entire powder pattern can lead to a detailed understanding and description of the crystal structure via a refinement technique such as Rietveld[141] refinement (See **Figure 2.2**).[140]

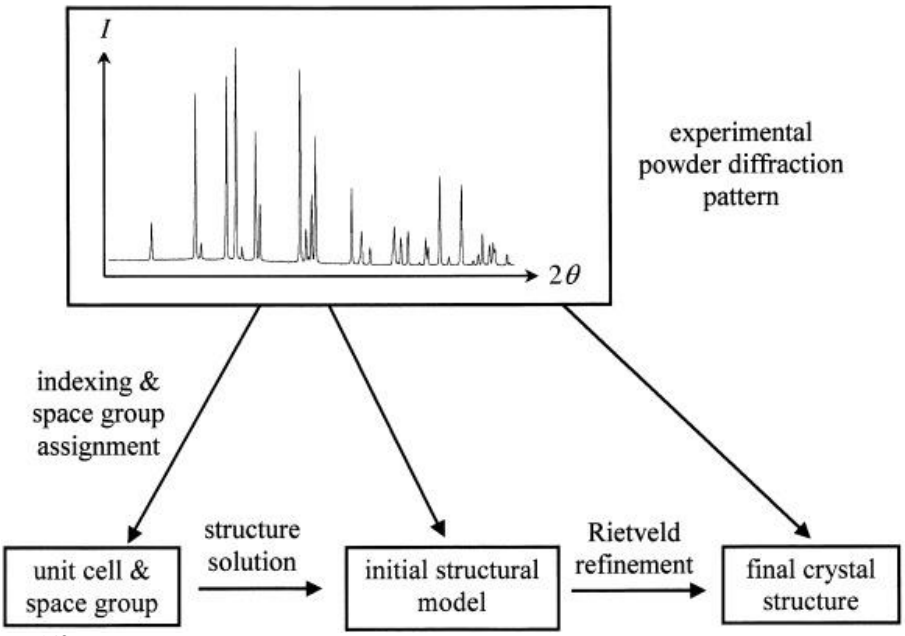

Figure 2.2[140] A general outline of the stages of structure solution from PXD experimental data. The unit cell and space group are determined from peak positions, and the structure is refined from the relative intensities of the peaks.

All samples discussed in this work were initially characterized by room temperature PXD after being finely ground to avoid preferred orientation effects, obtain accurate reflection intensities from as many reflections as possible, and to a lesser degree, minimize anomalous scattering that can be caused by grain size

irregularities. Sometimes even with careful powdering these effects cannot be avoided, but all efforts were made to minimize them. These measurements were performed to ascertain sample phase and purity; PXD is ideal for this purpose as it is both rapid and (other than the powdering process) non-destructive.

PXD data were collected on powders or ground crystals of samples with a Bruker D8 Advance Diffractometer with a SOL-X solid state detector (Cu K_α, λ = 1.5418 Å). Data was collected in the 2θ range of 10° to 80° with a step of 0.02°, typically, with some collection ranges increasing to 120°. PXD patterns were analized using HighScore Plus suite[142] and structural refinements performed with either Topas Academic[143] or GSAS-II[144] software packages. For $LaMn_3Rh_4O_{12}$, PXD analysis between 10 and 120° (step size 0.02°, 10 seconds per step) was carried out at room temperature (RT) with a PANalytical Empyrean diffractometer (Cu Kα, λ = 1.5148 Å) by collaborators Man Rong Li and Meixia Wu at Sun Yat-Sen University in China.

2.2.2 Single Crystal X-ray Diffraction

Samples of Mn_2CoReO_6 and $Fe_{3-x}InSn_xO6$ (x = 0, 0.25, 0.5) were synthesized serendipitously as small (approximately 0.040 x 0.020 x 0.010 mm^3), plate-like crystals which were suitable for single crystal X-ray diffraction (SCXRD). SCXRD has been described as the "most important and powerful technique for elucidation of crystal... structures" available in the laboratory.[140] Although the basic diffraction principles that govern PXD also apply to SCXRD (please see Crystal Structure Analysis: A Primer[145] by Pickworth Glusker and Trueblood for a much more thorough plain-language introduction than space here allows) lattice parameters and atomic positions derived from PXD are generally less accurate when compared to those derived from single crystals.[140] A single crystal can be (and must be in order to obtain a complete set of reflections) rotated in any direction to capture individual lattice

planes, whereas powder data is collected all at once over all the average orientation of planes, with no possibility of differentiating between them post-collection. This precise sensitivity to plane orientation also makes SCXRD sensitive to site-ordering, in contrast to PXD.

Once a stable, single phase crystal without cracks or imperfections is obtained (arguably the most difficult step in any SCXD experiment) the crystal is mounted and moved into an intense X-ray beam. **Figure 2.3** shows a graphical representation of an SCXRD pattern generated at one crystal orientation. The X-ray beam enters from the left of the sample in this case, and a portion of the beam is scattered in so-called Debye cones with an opening angle of 2θ.[146] As the crystal is slowly rotated, the spots seen in **Figure 2.3** will change in intensity, reducing or disappearing as others grow in intensity or new ones appear. For each crystal orientation, a new 2-D diffraction pattern will be generated, and an entire set of orientations can consist of thousands of individual patterns.[146] Multiple collection steps, or sweeps, may be used to obtain these data, which are then combined and reduced using various software packages. Finally, as in PXD, the structure of the sample is refined.

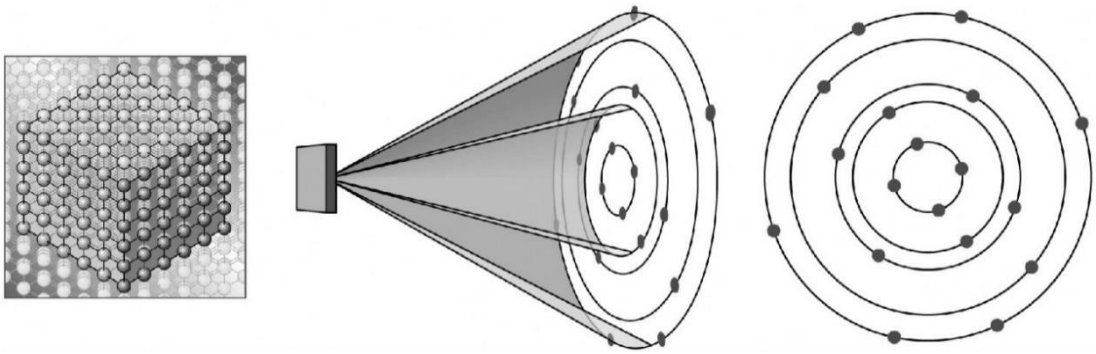

Figure 2.3[146] A visualization of a 2-D diffraction pattern caused by passing an intense X-ray beam (where $\lambda \approx$ the inter-atomic distances of the sample) through a single crystal. Spots of various intensities appear where Bragg's law is satisfied.

SCXRD data presented in this work were collected with Mo K_α, $\lambda = 0.7107$ Å, at room temperature on a Bruker Smart APEX system with charge-coupled device (CCD) area detector and mono-capillary collimation. The structure was solved with the SHELXT-2014/15 and refined with SHELXL-2014/7 software packages with data reduction performed in BRUKER APEX 3 and SAINT.[147,148,149,150] Data collection and analysis were all performed with the supervision, assistance, and instruction of Dr. Thomas Emge.

2.2.3 Synchrotron Powder X-ray Diffraction

To more accurately determine the purity and average nuclear structure of powder samples, all samples- including those analyzed by SCXRD- were also analyzed via synchrotron powder X-ray diffraction (SPXD) collected at Argonne National Laboratory Advanced Photon Source.

Synchrotrons are cyclic particle accelerators descended from cyclotrons.[2] At Argonne National Laboratory, electrons are accelerated to near light-speed in a linear accelerator, then injected into the synchrotron accelerator where a series of electromagnets further accelerate the electrons before injecting them into the storage ring made of more than 1000 electromagnetics with a total circumference of 1,104 meters.[151]

Synchrotron beamlines have several advantages over laboratory diffractometers, including the flexibility to choose the wavelength of X-rays used from a continuous spectrum. Additionally, SPXD beamlines have much higher flux density (the number of photons per second passing through a defined area) and brilliance (intensity and directionality of an X-ray beam) than can possibly be achieved via a laboratory X-ray diffractometer. Finally, SPXD beams have higher spatial precision (higher resolution) than laboratory diffractometers because a synchrotron concentrates beam intensity

into a fine, near-parallel beam instead of spreading its intensity over a wider, comparatively divergent beam. Higher resolution leads to less peak broadening and overlap, making structure refinement and modelling much more accurate, especially in cases where sample type itself causes peak broadening (as in the case of samples consisting of multiple polymorphs) which can be difficult to distinguish from peak broadening caused by limitations of laboratory PXD instrumentation.[140]

Samples are prepared with thorough grinding, (similar to preparations for PXD analysis) to minimize preferred orientation and to ensure that the experimental sample is truly representative of the average composition of the bulk. Due to this careful and representative preparation, SPXD experiments are useful even in the cases where SCXRD is possible. Any one crystal chosen for SCXRD may not be representative of the main phase; instead it may be an impurity or a polymorph.[140] Additionally, even if the main phase is selected for analysis, impurities (such as SnO_2 in the case of the $Fe_{3-x}InSn_xO_6$ samples, discussed in Chapter 5 of this work) will not be seen in an analysis of a single crystal, but will be present when the bulk product is ground. From there, percent composition of main phase vs impurities can be determined, and impurity effects on apparent properties of the bulk sample can be understood and, ideally, accounted for.

Room temperature synchrotron powder X-ray diffraction data discussed in this work were collected at Argonne National Laboratory on beamline 11-BM ($\lambda \approx 0.413$ Å), or in the case of Mn_2CoReO_6 (which was sealed in an evacuated quartz ampule), on the high energy beamline 11-ID-C ($\lambda = 0.1173$ Å) by collaborator Saul Lapidus via the mail in service. As in PXD experiments, structural refinements were performed with either Topas Academic[143] or GSAS-II[144] software packages.

2.2.4 Neutron Powder Diffraction

Time-of-flight neutron powder diffraction (NPD) data were collected by collaborators for Mn_2CoReO_6 and $Fe_{2.5}InSn_{0.5}O_6$. NPD is a powerful technique used to determine the nuclear and magnetic structures of materials. The structural information provided by NPD is still dictated by Bragg's law, and should be complementary to that which is generated via SPXD and PXD, however the principles which dictate neutron scattering are slightly different than those of X-rays. This is because X-rays are scattered primarily by the electron cloud of an atom and scattering potential increases with increasing electron density via:

$$I_0 = z^2 * I_e \tag{2.2}$$

where I_0 is the total scattered intensity for all in-phase beams (that is, a coherent beam at $2\theta = 0^\circ$; at other angles there will be some destructive interference but the proportional relationship between Z and I remains regardless of beam angle or coherence) Z is the atomic number, and I_e is the scattering of a single electron. Neutrons, on the other hand, are scattered by atoms' nuclei, with a scattering potential that varies from isotope to isotope, rather than proportionally to Z.

This means that cations such as In^{3+} and Sn^{4+}, which have the same number of electrons and thus are identical to X-rays, are distinguishable by NPD.[152] Additionally, and critically for understanding complex magnetic and spintronic phenomena, neutrons possess spin. This makes neutrons sensitive to magnetic spin, which means that a beam of neutrons (of $\lambda \approx$ lattice parameters) passing through a magnetic crystalline material will be affected by the magnetic structure of the sample. It should be noted that as long as the nuclear magnetic moments are not all aligned with the incident beam, the additional reflections which arise from magnetic ordering

should not interfere with the neutrons diffracted by the nuclear structure- the two patterns are, rather, “additive” and superimposed on one another.[153]

For experiments discussed in this work, NPD data were collected by collaborators (Professor Emma McCabe, Dr. Fabio Orlandi, and Dr. Pascal Manuel) on the WISH diffractometer at the ISIS Neutron and Muon Source in the UK.[154] The precise details of each NPD experiment will be discussed in the relevant chapters, as the preparations differed significantly. Data were analyzed by collaborators Fabio Orlandi, Pascal Manuel, and Emma McCabe with the TopasAcademic software[143] and ISODISTORT[155] which was used to explore possible magnetic structures and to give a description of the magnetic structures in terms of the nuclear structure and symmetry-adapted magnetic modes.

2.3 Physical Measurements

2.3.1 Initial Optical Analysis

For all high-pressure samples, a fragment of the as-made densely packed pellet of powder (or crystals and crystallites) was embedded in epoxy resin by Dr. David Walker before being ground and polished for analysis. Optical analysis resulted in a doubly-polarized incident illumination image in which sample contrast is caused by the rotation of polarized light through a sample. This technique is commonly used in the field of geology, specifically optical minerology, for the identification of thin sections of rocks and minerals, stones, and even meteorite and lunar samples.[156] For a synthetic chemist, this is a useful tool for early phase estimation (as many substances have known optical characteristics dictated by structure and symmetry), evaluation of the approximate number of phases present, and assessment of synthetic conditions, however it should be noted that the initial estimates are simply that, and the sample

must be evaluated by a precise chemical analytical techniques such as EDAX or microprobe to accurately assess sample purity and identity.

Optical analysis was of particular use in the synthesis of $LaMn_3Rh_4O_{12}$ and will be discussed in detail in Chapter 4. This quadruple perovskite crystallizes in the highly symmetric space group $I\bar{3}m$, which means that the PXD pattern is dominated by a few very strong reflections. This can make it challenging to identify small impurities, and to confidently evaluate whether changing synthetic conditions was resulting in improvements to the synthetic outcome. Optical analysis, however, showed not only the different phases present in addition to the main phase, but the relative completeness of the reaction when it was quenched at pressure. Upon close optical inspection, it became apparent not that the reaction conditions were not necessarily inappropriate to form a pure single phase, but that the reaction itself had not yet reached completion. The timescale of the $LaMn_3Rh_4O_{12}$ high pressure reaction was therefore increased until finally complete at ~72 hours. Considering that typical high pressure reaction times for solid state syntheses are between 0.5-2 hours, this increase would likely not have been pursued without optical analysis to track the relative reaction progress, and $LaMn_3Rh_4O_{12}$ would not have been synthesized at purities which allowed for accurate properties analysis (as some eliminated impurities were both magnetic and magnetoresistive).

2.3.2 Scanning Electron Microscopy-Energy Dispersive X-ray Spectroscopy (SEM-EDX) and Electron Microprobe

The composition of some samples was analyzed by scanning electron microscopy-energy dispersive X-ray spectroscopy (SEM-EDX) and Microprobe microscopy. SEM-EDX images are considered a semi-quantitative but useful check particularly in conjunction with SCXD (which allows for the precise refinement of

electron densities. Microprobe analysis is generally accepted to be a quantitative chemical analysis.

Both microprobe and SEM-EDX devices work because elements produce what is known as characteristic X-rays when bombarded with a beam of electrons. When an inner shell electron is excited by this beam, and the energy absorbed is equal to or greater than its binding energy, the electron may be ejected. This ejection leaves behind an electron hole. An outer shell electron (that is, one with a higher energy) may then move to the lower energy inner shell to fill the hole, releasing the energy difference in the form of an X-ray. Characteristic X-rays are identified by both the shell in which the electron hole occurs (K, L, or M) and the shell from which the higher energy electron falls (e.g. Kα, Kβ; see **Figure 2.4**). Critically, the energies of characteristic X-rays are unique for each element and thus careful measurement can allow for both the qualitative determination of which elements are present in a sample and the quantitative determination of their relative concentrations.

The key difference between electron microprobe and SEM-EDX, both in required experiment time and in explaining why microprobe is considered much more quantitatively accurate than EDX, lies in their detectors. An EDX detector relies on a solid-state detector composed of a semiconductor. As each X-ray hits the semiconductor, a small amount of current is produced, and the original energy of the characteristic X-ray is calculated from the current produced by each X-ray photon. The peaks in an EDX spectrum can therefore be thought of as histograms of the number of X-rays which strike the detector at each energy.[157] This leads to relatively wide energy peaks which can be collected very quickly.

An electron microprobe utilizes a wavelength dispersive spectrometer (WDS) with a crystal which diffracts characteristic X-rays and directs them to the X-ray

detector. A WDS detector produces narrow peaks of strong resolution but can only measure X-rays of one wavelength at a time. Typically, microprobe instruments will consist of approximately five WDS spectrometers so that five elements can be simultaneously analyzed, and each spectrometer will have anywhere from one to four crystals, with the crystals all being of different lattice spacings to maximize the range of wavelengths that can potentially be diffracted.[157] The strong resolution of peaks generated by WDS systems means that data collected on a WDS system is typically both more accurate and precise than that generated by an EDX system, but this sacrifices both speed of collection and flexibility of detection. While the accuracy of EDX detectors is consistently improving, the two techniques are considered complementary and many microprobe WDS experiments, especially on complex or unknown samples, begin with an EDX analysis.[157-159]

As a flat surface is necessary to collect accurate scattering data, the prepared optical analysis samples were typically repurposed for SEM-EDX or microprobe data. For both polycrystalline samples and large single crystals (in the cases of $Fe_{2.75}InSn_{0.25}O_6$ and $Fe_{2.5}InSn_{0.5}O_6$ only) a fragment of as-made sample was embedded in epoxy resin and ground so that there was a flat surface. The sample was then coated in a thin (3-10 nm) coating of carbon simultaneously with known standards before being loaded into the system for analysis.

SEM-EDX images for Mn_2CoReO_6 were generated with a Ziess-Sigma Field Emission SEM with Oxford INCA Energy 250 Microanalysis system, and measurements were performed at a working distance of 8.5 mm and an accelerating potential of 15 KeV. SEM-EDX experiments for $In_2Mn_{1.1}Sn_{0.9}O_6$ were conducted on a JEOL 5510 scanning electron microscope equipped with an INCAx-sight 6587 system (Oxford Instruments) by collaborators Dr. Maria Batuk and Professor Joke

Hadermann. In-L, Mn-K, and Sn-L lines were used for the compositional determination.

Microprobe images were generated in both point-select and multi-line scan modes for $LaMn_3Rh_4O_{12}$ and $Fe_{3-x}InSn_xO_6$ (x = 0, 0.25, 0.5) on a JEOL JXA Superprobe at the Rutgers University Department of Geology with the assistance and instruction of Paul Burger and Juliane Gross, and on a 5-spectrometer Cameca SX5-Tactis located at the America Museum of Natural History Earth and Planetary Sciences Laboratory in New York with the assistance and instruction of Adrien Fiege and David Walker with column conditions of 15 Kev, 10 nA.

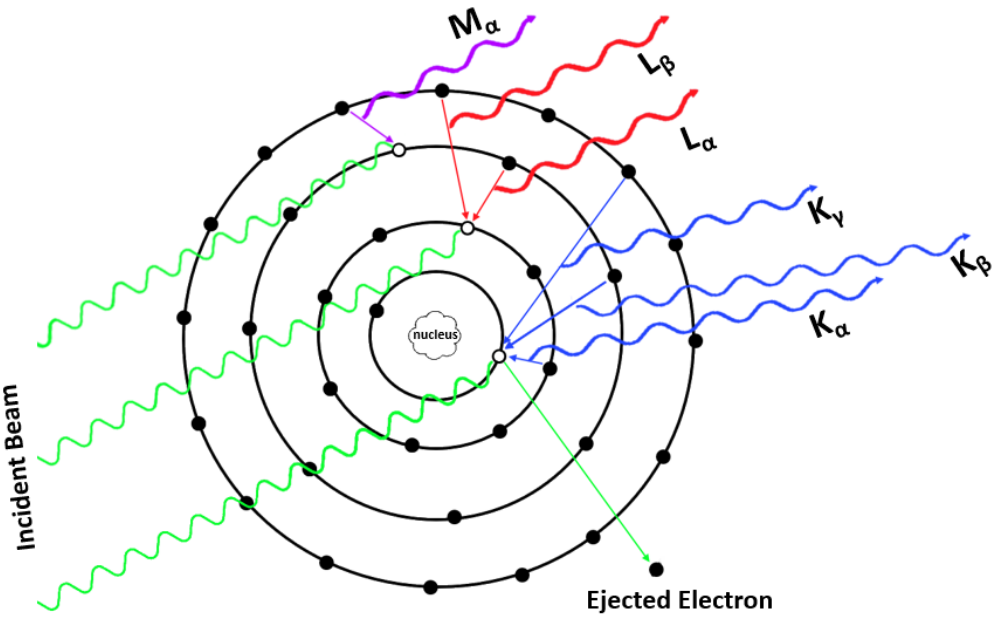

Figure 2.4 A graphical representation of an incident beam (green) interacting with an inner shell electron such that it gains enough energy to be ejected. An electron from a higher energy will then transition to the inner shell, releasing the excess energy as characteristic X-rays (sometimes instead of being ejected as X-rays, the energy from the transition will excite an additional electron in an outer shell, which will then be released as an auger electron- not shown). K_α, K_β, and K_γ (blue) are generated when a hole in the K shell is filled by an L, M, or N shell electron, respectively (K_γ radiation is possible, but not typical). L_α and L_β radiation (red) is produced when a hole in the L shell is filled by an electron from the M or N shells, M_α radiation (purple) is generated when an electron from an N shell fills a hole in the M shell.

2.3.3 Transition Electron Microscopy

High angle annular dark field (HAADF) scanning transmission electron microscopy (STEM) is another powerful technique for visualizing the structure of materials. HAADF-STEM collects scattered electrons from an annulus around the electron beam, allowing for the collection of atomic resolution images. As can be seen in **Figure 2.5**, a high intensity electron beam is passed through a thin sample which has been evenly distributed on a holey grid. This beam is accelerated using a cold field emission source, rather than a thermal source, to maximize the signal-to-noise ratio of the beam. Atomic level resolution images require an incident electron beam that is nearly monochromatic.[160]

The intense beam is focused on a small spot of the sample and then scanned across the surface of the sample (hence "scanning" transition electron microscopy). The annular detector collects electrons which are deflected at large angles (wide-angle scattering, which is the consequence of the electrons interacting with the atomic nuclei).[160-161] The intensity (I) of wide angle scattering at a deflection angle (χ) is predicted by the following equation:

$$I(\chi) = \left(\frac{Q_1 Q_2}{4E}\right)^2 cosec^4\left(\frac{\chi}{2}\right) \quad (2.3)$$

where E is the collision energy and Q_1 and Q_2 are charge of the electrons ($Q_1 = -1$) and atomic nuclei ($Q_2 = Z$) respectively.[160] The scattering is, therefore, more intense from atoms with a higher atomic number. This makes HAADF-STEM an ideal complementary technique to determine the precise positions of atoms in a unit cell relative to one another, allowing determination whether synthesized samples are centrosymmetric or noncentrosymmetric. As discussed earlier, such distinction is not possible by X-ray diffraction alone. HAAF-STEM can also be useful as a complement

to other techniques, such as second harmonic generation, which will be discussed shortly (see page 63).

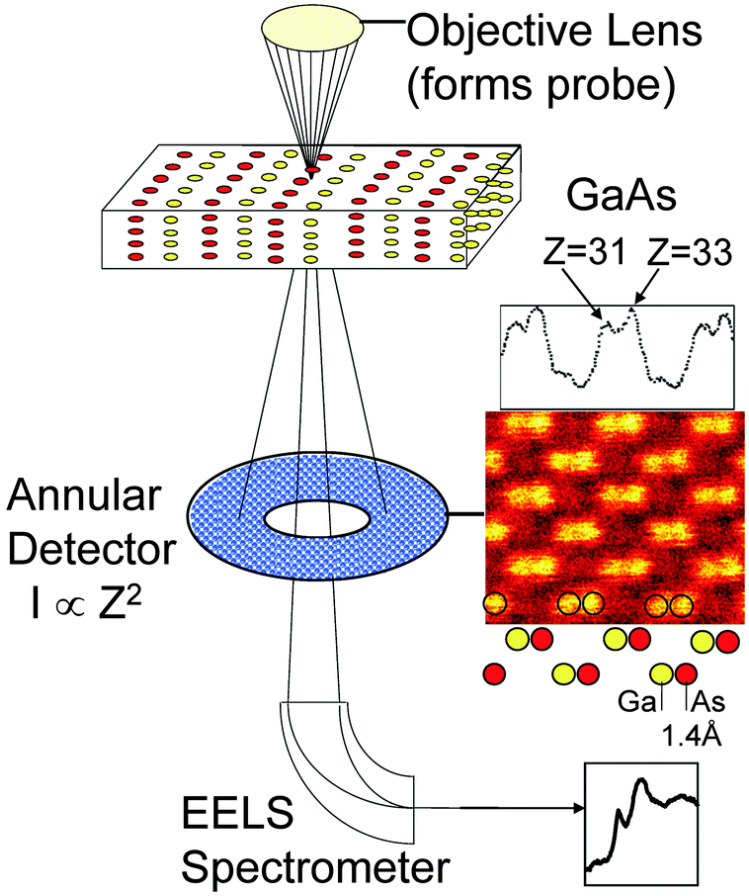

Figure 2.5[160] Schematic of an HAADF-STEM (with a simultaneous electron energy loss spectroscopy detector). After passing a high intensity electron beam through a thin sample, the transmitted electrons are collected and analyzed by intensity and position, allowing for a high resolution image that can be used to visualize atoms in real space (as seen in the visualization of GaAs dimers, above).

Samples for the TEM analysis were prepared by collaborators at the University of Antwerp by mixing finely ground powders with ethanol using ultrasonic bath and depositing of few drops of the obtained suspension onto the holey TEM grid covered with carbon. Electron diffraction patterns were acquired using Phillips CM20 microscope operated at 200 kV. HAADF-STEM images were acquired by Joke Hadermann and Maria Batuk at the University of Antwerp using a FEI Titan 80-300

"cubed" microscope operated at 300 kV. The simulated HAADF-STEM images were calculated using QSTEM software by the collaborators.

2.3.4 Specific Heat Capacity

Specific heat capacity (at constant pressure, C_p) is the energy required to warm 1 g of a material by 1 K, and is fundamentally a measure of the total entropy of a system.[2] Any property of a material which is temperature dependent contributes to the entropy, and thus contributes to the total specific heat capacity.[162] Additionally, changes in entropy caused by the magnetic contribution to heat capacity (C_M) can be precisely extracted from the total heat capacity by subtracting out any non-magnetic contributions using the following equation:

$$C_M = C_p - (C_{el} + C_{ph} + C_{Sch}{}^{+} \ldots) \tag{2.4}$$

where C_M is the contribution to specific heat associated with magnetic order, C_p is the total specific heat measured at constant pressure, and C_{el}, C_{ph}, and C_{Sch} are representative potential non-magnetic contributions to specific heat capacity. Representative contributions in this equation include: C_{ph}, the phonon specific heat (caused by thermal lattice vibrations); C_{el}, the electron specific heat (necessary in compounds with conduction electrons); and C_{Sch}, the Schottky paramagnetic contribution to specific heat (accounting for crystal field splitting effects on the ground state energies of compounds).[162]

Because the total value of C_p is additive, it is not strictly necessary to precisely separate out the individual contribution of C_M to C_p to use specific heat capacity measurements to identify a magnetic transition temperature. As a magnetic transition is a phase transition, often second order (from a phase with disordered spins to a

phase with aligned spins), this manifests thermodynamically as an "entropy discontinuity," or anomaly, at the point of change. This makes specific heat capacity measurements an invaluable tool to corroborate magnetic transitions as identified in magnetic susceptibility experiments, as the transition temperature found by susceptibility measurements can broaden depending on measurement field strength and thus prove difficult to identify precisely.[83, 163] Additionally, the shape of a transition can reveal a great deal about the nature of a solid state phase transition. For example, first order phase transitions in magnetic materials are typically marked by sharp peaks in Cp, "reminiscent to the letter λ."[164] These first order phase transitions include magnetostructural ferromagnetic phase transitions.[164]

Specific heat can also be used to describe more than merely the temperature of a magnetic or structural transition. At low temperatures, below about a twelfth[165] of the Debye temperature (θ_D a fundamental property of mater that describes the highest temperature of a crystal's normal mode of vibration), the electronic contribution to the specific heat can be determined by fitting to the following function:

$$C = \gamma T + \beta T^3 \tag{2.5}$$

where C is the specific heat capacity at constant pressure or volume, β is the specific heat coefficient, which is a function of θ_D, and the Sommerfeld coefficient, γ, is proportional to the Fermi density-of-states. The low temperature heat capacity of a material thus provides useful information about electronic structure as well as magnetic properties, and can be especially useful in the case of superconductors.[166]

For Mn_2CoReO_6 and $LaMn_3Rh_4O_{12}$, C_p was measured upon cooling at 0 magnetic field on a PPMS from 150 – 2 K by collaborators at the Institute of Physics, Chinese Academy of Sciences and from 80-20 K by collaborators at Sun Yat-Sen

University, respectively. The PPMS at the Chinese Academy of Sciences was made by Quantum Design with Heat Capacity Option 2.7.2 Build 2.

2.3.5 Magnetism and Magnetotransport

The fundamental principles behind magnetic and transport measurements were discussed in detail in **Chapter 1** (see pages 1, 5). These measurements were performed on $LaMn_3Rh_4O_{12}$ by collaborators at Sun Yat-Sen University; all other samples were measured at the Institute of Physics, Chinese Academy of Sciences. The measurements were performed on as-made pressed pellets of samples which, due to being made at high pressure, were very dense. Since many of the exact measurement conditions were quite different from sample to sample, specifics will be discussed in the relevant chapters. In general Field Cooled (FC) and Zero Field Cooled (ZFC) magnetic measurements were carried out with either a superconducting quantum interference device (SQUID) magnetometer or a physical property measurement system (PPMS, EvenCool II, Quantum Design) equipped with a vibrating sample magnetometer (VSM). The room temperature resistivity of $In_2Mn_{1.1}Sn_{0.9}O_6$ was measured at Rutgers University with a two-probe method, and was found to be highly insulating, therefore transport measurements on a SQUID or PPMS device were not attempted.

2.3.6 X-ray Absorption Near Edge Spectroscopy

X-ray absorption near edge structure (XANES) is a non-destructive technique used to verify the oxidation states and coordination environments of cations in synthesized compounds. XANES is an inner-shell spectroscopy technique, meaning that the incident X-ray beam interacts with core electrons rather than valence electrons, primarily. When an X-ray beam of sufficient energy to excite a core

electron to either an excitonic state (an empty bound below the ionization threshold) or to the continuum that is above the ionization energy, bombards a condensed matter sample, a core electron may be excited leaving a hole behind. This hole will decay in approximately 1 femtosecond by either X-ray fluorescence (where an electron of higher energy falls into the hole, releasing the energy difference as a characteristic X-ray) or the ejection of an auger electron (when the characteristic X-ray, instead of being ejected, excites an additional electron in an outer shell).[167]

The probability that a sample will absorb X-rays is called the absorption coefficient, μ, and is predicted according to the following equation:

$$I = I_0 e^{-\mu t} \tag{2.6}$$

where I is the intensity transmitted through the sample, I_0 is the intensity of the incident beam, and t is the sample thickness. At most energies, μ is a smooth function that is roughly equal to

$$\mu \approx (\rho Z^4)/(AE^3) \tag{2.7}$$

where ρ is the density of the sample, Z is its atomic number, A is its atomic mass, and E is the energy of the X-ray.[167] However, when the incident X-ray beam has an energy equal to that of a core electron, an absorption edge occurs (see **Figure 2.6**). The energy at which an edge occurs is element specific, and so can be used to identify the elements present in a condensed matter sample.

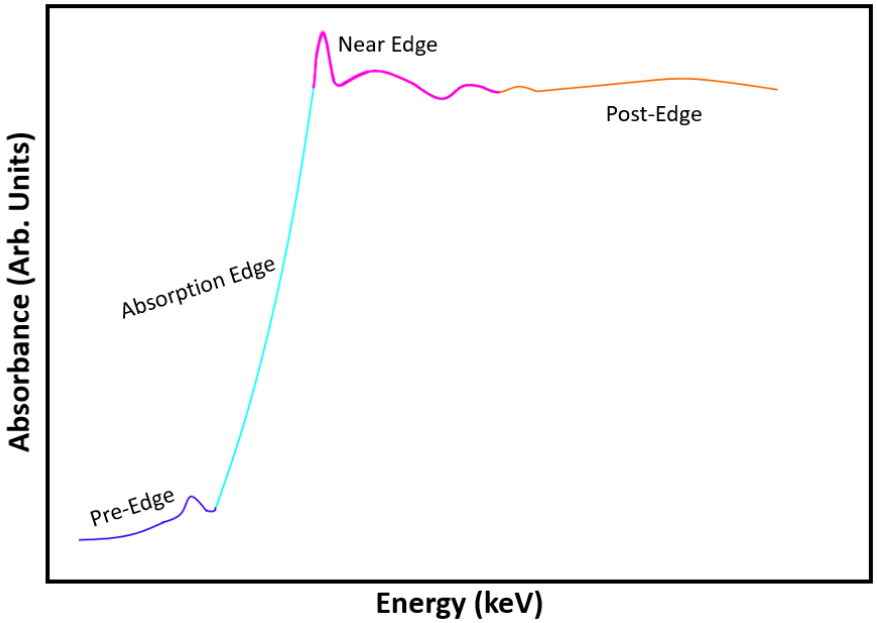

Figure 2.6 An idealized representation of a XANES K-edge spectrum including the pre-edge (purple) resonances, the absorption edge (light blue), the XANES near edge region (pink), and the post-edge region (orange) which is the region used for Extended X-ray Absorption Fine Structure (EXAFS) analyses.

XANES has been successfully used for decades to accurately measure the local coordination environment and oxidation state of transition metals.[168-171] As the oxidation state of a material increases, electrons are attracted more strongly overall to the nucleus, thus the energy needed to excite a core electron increases. This is reflected in XANES spectra by a shift right to higher energies. Comparisons between the chemical shifts of a sample with that of known standards should therefore reveal the oxidation state of the sample. Additionally, comparing the overall shape of an edge and pre-edge spectrum can reveal further information about an element's local coordination environment, including subtle geometrical distortions.[172] For example, tetrahedrally coordinated Cr-containing materials such as $CaCrO_4$ exhibit one intense pre-edge peak which is attributed to the transition between the 1s electron and the antibonding t_2* orbital. However in octahedrally coordinated Cr_2O_3 the pre-edge

structure shows two small resonances, and in Cr metal, the pre-edge resonance does not appear at all (**Figure 2.7**)

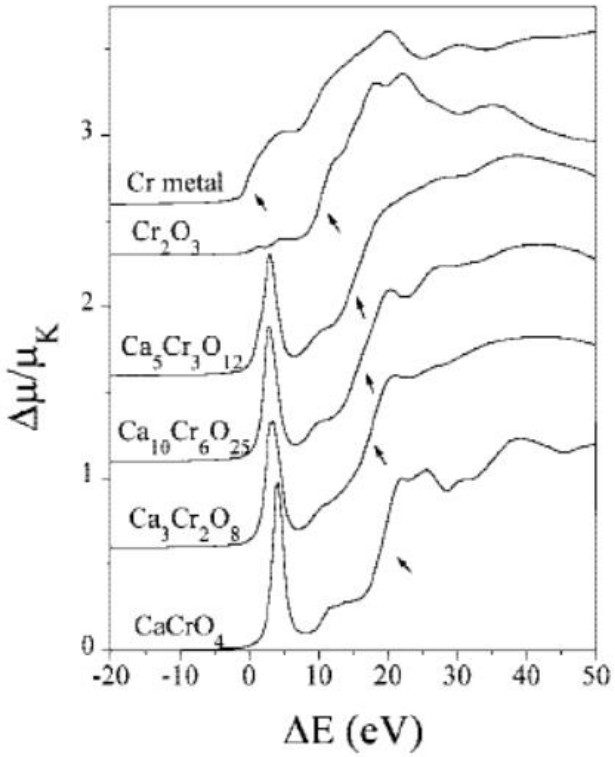

Figure 2.7[173] Cr *K*-edge spectra for Cr containing samples in different coordination environments, displaced vertically. Arrows denote the precise position of the Cr *K*-edge.

Specific preparations and detailed analyses will be discussed in the relevant chapters, but generally for this work, XANES data were collected by collaborators at Argonne Nation Laboratory (specifically Dr. Carlo Segre) via the mail-in system, or by Prof Mark Croft at Brookhaven National Laboratory in both the transmission and fluorescence mode with simultaneous standards. Data analysis was performed with the assistance and instruction of Prof Croft, who also prepared and selected figures and standards for publication.

2.3.7 Second Harmonic Generation

Second harmonic generation (SHG), also known as "frequency doubling," is a nondestructive coherent optical process that can be used to distinguish centrosymmetric from noncentrosymmetric materials. The environment of the harmonophores (the medium that permits SHG) must be noncentrosymmetric at the scale of λ_{SHG} for the SHG signal to persist. In dielectric materials polarization is not simply linearly proportional to the applied electric field; it can be expanded into component terms as follows:

$$P = \chi^{(1)}E^1 + \chi^{(2)}E^2 + \chi^{(3)}E^3 + \ldots \quad (2.8)$$

where *P* is the polarization, E is the electric field vector, and $\chi^{(n)}$ is the *n*th order nonlinear susceptibility.[174] In the above equation, the tensor $\chi^{(2)}$ governs second harmonic generation. The second order nonlinear susceptibility is directly dependent on the first hyperpolarizability of the permanent dipole moment of molecules in an electric field:

$$d^2 = \beta E^2 \quad (2.9)$$

where d is the permanent dipole moment, and β is the first hyperpolarizability. This molecular property relates to the bulk property that is the second nonlinear susceptibility through the following relationship:

$$\chi^{(2)} = N_s\langle\beta\rangle \quad (2.10)$$

where N_s is the average number of molecules involved in SHG generation and $\langle\beta\rangle$ is the average orientation of β.[175] Randomly oriented β tensors lead to an average orientation, $\langle\beta\rangle$, that is equal to 0, and so $\chi^{(2)}$ is also 0 in these materials and SHG will not occur. These mathematical relationships show that SHG is theoretically impossible in materials with an inversion center because SHG is impossible without

polarization. Reality, however, is far more complicated, and researchers should be mindful of SHG effects that are caused by strain or surface effects in centrosymmetric samples.[176-177]

As stated above, another name for SHG is “frequency doubling” because during the SHG process two photons with the same frequency interact and, in essence, combine within the harmonophore to generate a new photon with twice the frequency of the original wave (**Figure 2.8**). For the materials mentioned in this work, $Fe_{3-x}InSn_xO_6$ (x = 0.5, 0.25, 0), SHG measurements were performed on a modified Witec microscopic system using an 80 fs, 800 nm femtosecond laser. The reflected incident beam was filtered out by a band pass filter and 400 nm SHG light from the samples was detected by a photomultipler Tube (PMT). The polarization angle of incident laser beam was continuously rotated from 0° to 360°, by $\lambda/2$ wave plate. For single crystal measurements, the analyzer was fixed either parallel or perpendicular to c axis of crystal. Measurements were performed by collaborators Dr. Shukai Yu and Hugo Wang at Pennsylvania State University under the direction of Professor Venkatraman Gopalan.

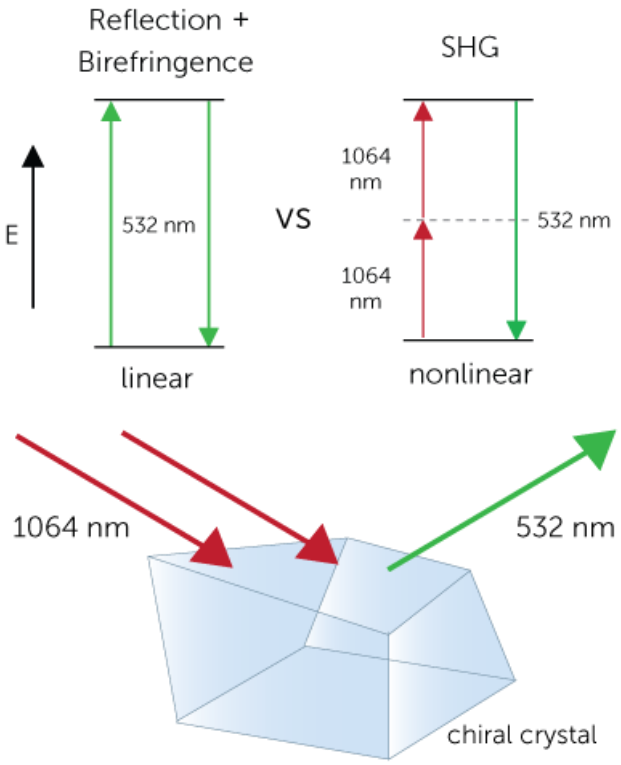

Figure 2.8[178] An illustration of the SHG effect in a chiral (noncentrosymmetric) crystal where two photons of the same frequency "combine" in the crystal to form a photon with twice the frequency. SHG involves a virtual transition (top right) and the frequency is doubled exactly. This is contrasted with reflection and birefringence (top left) which do not involve a virtual transition.

2.4 References

2. Wiberg, E.; Holleman, A. F.; Wiberg, N.; Eagleson, M.; Brewer, W., *Inorganic Chemistry*. Academic Press: 2001.
83. Frank, C. E.; McCabe, E. E.; Orlandi, F.; Manuel, P.; Tan, X.; Deng, Z.; Croft, M.; Cascos, V.; Emge, T.; Feng, H. L.; Lapidus, S.; Jin, C.; Wu, M.; Li, M. R.; Ehrlich, S.; Khalid, S.; Quackenbush, N.; Yu, S.; Walker, D.; Greenblatt, M., Mn_2CoReO_6: a robust multisublattice antiferromagnetic perovskite with small A-site cations. *Chemical Communications* **2019,** *55* (23), 3331-3334.
138. D8 X-ray Diffractometer Vol. I. Buker: Vol. 1.
139. Humphreys, C., The significance of Bragg's law in electron diffraction and microscopy, and Bragg's second law. *Acta Crystallographica Section A* **2013,** *69* (1), 45-50.
140. Harris, K. D. M.; Tremayne, M.; Kariuki, B. M., Contemporary Advances in the Use of Powder X-Ray Diffraction for Structure Determination. *Angewandte Chemie International Edition* **2001,** *40* (9), 1626-1651.
141. Rietveld, H., A profile refinement method for nuclear and magnetic structures. *Journal of applied Crystallography* **1969,** *2* (2), 65-71.
142. *HighScore Plus 3.0.5*. PANalytical B. V.: Almelo, Netherlands.

143. Coelho, A., TOPAS Academic: General Profile and Structure Analysis Software for Powder Diffraction Data,(2012) Bruker AXS. *Karlsruhe, Germany*.
144. Toby, B. H.; Von Dreele, R. B., GSAS-II: the genesis of a modern open-source all purpose crystallography software package. *Journal of Applied Crystallography* **2013,** *46* (2), 544-549.
145. Glusker, J. P.; Trueblood, K. N., *Crystal Structure Analysis A Primer*. Third Edition ed.; Oxford University Press: Oxford, UK, 2010.
146. Brügemann, L.; Gerndt, E. K. E., Detectors for X-ray diffraction and scattering: a user's overview. *Nuclear Instruments and Methods in Physics Research Section A: Accelerators, Spectrometers, Detectors and Associated Equipment* **2004,** *531* (1), 292-301.
147. *APEX3 version 2015.9-0; Bruker AXS: Madison, WI, 2015.*
148. *SAINT*, version 8.34A; Bruker AXS: Madison, WI, 2013.
149. Sheldrick, G. M., *SHELXT-2014/5*, University of Göttingen: Göttingen, Germany, 2014.
150. Sheldrick, G. M., SHELXL-2014/7. *Acta Crystallographica* **2015,** (C71), 3-8.
151. The Advanced Photon Source U.S. Department of Energy Office of Science User Facility. https://www.aps.anl.gov/About/Overview/APS-Systems-Map.
152. Piccoli, P. M. B.; Koetzle, T. F.; Schultz, A. J., Single Crystal Neutron Diffraction for the Inorganic Chemist - A Practical Guide. *Comments on Inorganic Chemistry* **2007,** *28* (1-2), 3-38.
153. Shull, C. G.; Strauser, W. A.; Wollan, E. O., Neutron Diffraction by Paramagnetic and Antiferromagnetic Substances. *Physical Review* **1951,** *83* (2), 333-345.
154. Chapon, L. C.; Manuel, P.; Radaelli, P. G.; Benson, C.; Perrott, L.; Ansell, S.; Rhodes, N. J.; Raspino, D.; Duxbury, D.; Spill, E., Wish: The new powder and single crystal magnetic diffractometer on the second target station. *Neutron News* **2011,** *22* (2), 22-25.
155. Campbell, B. J.; Stokes, H. T.; Tanner, D. E.; Hatch, D. M., ISODISTORT. *J. Appl. Cryst.* **2006,** *39*, 607-614.
156. Davidson, M. W.; Lofgren, G. E., Photomicrography in the Geological Sciences. *Journal of Geological Education* **1991,** *39* (5), 403-418.
157. McSwiggen, P. Tech Notes: WDS vs EDS. http://www.mcswiggen.com/TechNotes/WDSvsEDS.htm.
158. Newbury, D. E.; Ritchie, N. W., Is scanning electron microscopy/energy dispersive X-ray spectrometry (SEM/EDS) quantitative? *Scanning* **2013,** *35* (3), 141-168.
159. Kuisma-Kursula, P., Accuracy, precision and detection limits of SEM–WDS, SEM–EDS and PIXE in the multi-elemental analysis of medieval glass. *X-Ray Spectrometry: An International Journal* **2000,** *29* (1), 111-118.
160. Sohlberg, K.; Pennycook, T. J.; Zhou, W.; Pennycook, S. J., Insights into the physical chemistry of materials from advances in HAADF-STEM. *Physical Chemistry Chemical Physics* **2015,** *17* (6), 3982-4006.
161. Pennycook, S. J.; Jesson, D. E., High-resolution Z-contrast imaging of crystals. *Ultramicroscopy* **1991,** *37* (1), 14-38.
162. Čermák, P., Magnetic properties of Ce compounds studied by specific heat. **2012**.
163. Wu, M.; Frank, C. E.; Han, Y.; Croft, M.; Walker, D.; Greenblatt, M.; Li, M.-R., $LaMn_3Rh_4O_{12}$: An Antiferromagnetic Quadruple Perovskite Synthesized at High Pressure. *Inorganic Chemistry* **2019,** *58* (15), 10280-10286.
164. Mnyukh, Y., On the Phase Transitions That Cannot Materialize. *arXiv preprint arXiv:1310.5009* **2013**.
165. Collings, E. W., Low-Temperature Specific Heat. In *Applied Superconductivity, Metallurgy, and Physics of Titanium Alloys: Fundamentals Alloy Superconductors: Their Metallurgical, Physical, and Magnetic-Mixed-State Properties*, Collings, E. W., Ed. Springer US: Boston, MA, 1986; pp 307-333.
166. Wang, Y.; Plackowski, T.; Junod, A., Specific heat in the superconducting and normal state (2–300 K, 0–16 T), and magnetic susceptibility of the 38 K

superconductor MgB2: evidence for a multicomponent gap. *Physica C: Superconductivity* **2001,** *355* (3-4), 179-193.
167. Newville, M., Fundamentals of XAFS. *Reviews in Mineralogy and Geochemistry* **2014,** *78* (1), 33-74.
168. Monesi, C.; Meneghini, C.; Bardelli, F.; Benfatto, M.; Mobilio, S.; Manju, U.; Sarma, D. D., Quantitative structural refinement of MnK edge XANES in $LaMnO_3$ and $CaMnO_3$ perovskites. *Nuclear Instruments and Methods in Physics Research Section B: Beam Interactions with Materials and Atoms* **2006,** *246* (1), 158-164.
169. Naoki, S.; Yoshio, T.; Yoshitaka, Y.; Kiyoshi, S.; Tomoya, U., Direct Speciation of Tin Compounds in Environmental Samples Using Sn K-edge XANES. *Chemistry Letters* **2004,** *33* (3), 264-265.
170. Retuerto, M.; Jiménez-Villacorta, F.; Martínez-Lope, M. J.; Huttel, Y.; Roman, E.; Fernández-Díaz, M. T.; Alonso, J. A., Study of the valence state and electronic structure in Sr_2FeMO_6 (M = W, Mo, Re and Sb) double perovskites. *Phys. Chem. Chem. Phys.* **2010,** *12* (41), 13616-13625.
171. Stueben, B. L.; Cantrelle, B.; Sneddon, J.; Beck, J. N., Manganese K-edge XANES studies of Mn speciation in Lac des Allemands as a function of depth. *Microchemical Journal* **2004,** *76* (1), 113-120.
172. Ohnuma, T.; Kobayashi, T., X-ray absorption near edge structure simulation of $LiNi_{0.5}Co_{0.2}Mn_{0.3}O_2$ via first-principles calculation. *RSC Advances* **2019,** *9* (61), 35655-35661.
173. Arcon, I.; Mirtic, B.; Kodre, A., Determination of Valence States of Chromium in Calcium Chromates by Using X-ray Absorption Near-Edge Structure (XANES) Spectroscopy. *Journal of the American Ceramic Society* **2005,** *81*, 222-224.
174. Chen, X.; Nadiarynkh, O.; Plotnikov, S.; Campagnola, P. J., Second harmonic generation microscopy for quantitative analysis of collagen fibrillar structure. *Nature Protocols* **2012,** *7* (4), 654-669.
175. Pavone, F. S.; Campagnola, P. J., *Second harmonic generation imaging*. CRC Press: 2016.
176. Defregger, S.; Engel, G. F.; Krempl, P. W., Linear and nonlinear optical properties of quartz-type $GaPO_4$. *Physical Review B* **1990,** *43* (8), 6733-6738.
177. Winta, C. J.; Gewinner, S.; Schöllkopf, W.; Wolf, M.; Paarmann, A., Second-harmonic phonon spectroscopy of α–quartz. *Physical Review B* **2018,** *97* (9), 094108.
178. Second Harmonic Generation (SHG). https://formulatrix.com/protein-crystallization-systems/sonicc-protein-crystal-detection/how-it-works/.

Chapter 3: Mn_2CoReO_6 - A Robust Multisublattice Antiferromagnetic Perovskite with Small A-Site Cations

3.1 Introduction

The search for new materials with potential spintronics applications is increasingly important to the future of microelectronics as industry comes to terms with the limit of Moore's Law.[179-180] Double perovskite (DP) oxides ($A_2BB'O_6$) (A = alkali or rare earth metal, B = 3d transition metal, B' = 4d/5d transition metal) have been particularly important to this search since the discovery of Sr_2FeMoO_6 by Kobayashi *et al*.[63, 170, 181-184] The seminal double perovskite has large magnetoresistance, high magnetic transition temperature (418 K), and completely polarized conduction band.[63, 181 170, 182] This exciting discovery inspired many more researchers to investigate DPs in the decades since, and progress is still made in designing and synthesizing new materials in this versatile structure type. Interesting examples of double perovskite oxides (DPs) with potential spintronic applications, a large *A*-site cation, a 3d metal on the B site, and a 4d/5d B' transition metal, include Ba_2FeMoO_6 (Tc = 340 K)[183] and Sr_2FeReO_6 (Tc = 415 K),[184] two above room temperature magnetoresistant materials. Despite a difference in 4d/5d conduction band electrons when compared to Sr_2FeMoO_6, Sr_2FeReO_6 (Tc = 415 K) shows a magnetoresistance of up to 7% at 7 T and 300 K.[184]

Interesting magnetic properties in these materials are attributed to double-exchange or super - exchange interactions between the B and B'-cations, and so strategies to tune properties are generally directed to changing the occupancies of these two sites while maintaining a late transition metal on the B'-site to promote spin

orbit coupling and spin polarization.[185-186] Potential candidates for new room-temperature spintronic materials need to be carefully chosen.

In a DP, three types of order are typically seen between the B and B'-site cation octahedra that surround the large (12-coordinated) A cation polyhedra: rock salt ordered, layered, or disordered. The ordering is generally governed by the degree of difference in size and charge between the B and B' cations.[42] For example, in recently investigated antiferromagnetic A_2CoReO_6 perovskites (A = Ba^{2+}, Pb^{2+}, Sr^{2+}), the size and charge differences between Co^{2+} (0.745 Å) and Re^{6+}(VI) (0.55 Å) are sufficiently large that the B and B' cations fully order in a rock salt configuration.[187-189] Pb_2CoReO_6 is particularly interesting because it exhibits bulk antiferromagnetic order (T_N= 16 K) combined with local ferro-or-ferrimagnetic interactions and a negative magnetoresistance of -23% at 10 K (H = 9 T).[188]

The rule of thumb that predicts stability of perovskite structure-type compounds is the Goldschmidt tolerance factor, which corresponds to the ratios of the radii of the A and B cations and the oxygen anions.[57, 190] An ideal perovskite will have a cubic structure with t = 1, however, the BO_6 and $B'O_6$ octahedra can tilt and distort to accommodate A cations with a less-than-perfect tolerance factor (t < 1). [52] Exceptions exist, as in the case of double corundum Ni_2MnTeO_6 (t ≈ 0.71), but generally double perovskites with t < 0.85 are unlikely to form under ambient pressure conditions. Instead, DPs with small A-site cations tend be metastable and require high pressure and temperature to form.[191]

The two first transition metal-only $A_2BB'O_6$ perovskites reported were synthesized at high pressure and temperature, Mn_2FeReO_6 and Mn_2MnReO_6, both crystallize in the distorted monoclinic $P2_1/n$ space group. Mn_2FeReO_6 was reported by our group in 2015 to be a half-metallic ferrimagnet with giant magnetoresistance

(220%) at 5K.[78] Its isostructural analogue, Mn_2MnReO_6demonstrated no magnetoresistance.[22] The lack of magnetoresistance in this compound was attributed to the antiferromagnetic coupling of the A and B site magnetic sublattices.[79, 81] These compounds were independently discovered at approximately the same time by Arévalo-Lopez et al. with similar properties, who assigned the Mn A-site cations a full 12 O-coordination, despite four of the Mn-O bonds being unusually long. In contrast, our group assigned only eight coordination of Mn-O bonds at the Mn A-site.[80]

Further complicating matters of synthesis: often it is corundum $A_2BB'O_6$, not perovskite, which is the thermodynamically stable structure even at high pressure. Stabilizing the double perovskite of a particular composition typically requires even higher applied pressure.[192-193] Unfortunately for the synthetic chemist, it is not yet possible to predict a priori which conditions will stabilize the double perovskite phase; the exact conditions and relative stabilities of the structures are both highly dependent on composition.

Recently, our group also published the structural and magnetic properties of $Mn_2(Fe_{0.8}Mo_{0.2})MoO_6$, the third known transition-metal-only double perovskite oxide.[82] $Mn_2(Fe_{0.8}Mo_{0.2})MoO_6$, a line phase of the polar ferrimagnetic double corundum Mn_2FeMoO_6[117] (space group *R3*, T_c = 337K), illustrates well the aforementioned difficulty of predicting the stable structure of a given compound. Both the parent compound and the line phase are synthesized at 8 GPa and 1623 K, so it clearly cannot be simply synthetic conditions which are key to the formation of double perovskite vs corundum in this case. In Mn_2MnReO_6 and Mn_2FeReO_6, the stabilization of a double perovskite phase over double corundum was attributed to the specific spin-structures of each compound, combined, perhaps, with spin-orbit

coupling from Re on the B'-site.[78, 194] As $Mn_2(Fe_{0.8}Mo_{0.2})MoO_6$, is the only known line phase of $Mn_2(Fe_{1-x}Mo_x)MoO_6$, its formation suggests a "synergy" of spin and crystal structure and thermodynamics. Presently, finding more of these types of compounds are of interest to reveal the underlying principles that govern the formation and properties of these complex structures.

This work presents the fourth known transition-metal only DP with small *A*-site cations, Mn_2CoReO_6. Like its predecessors, Mn_2CoReO_6 crystalizes in the $P2_1/n$ space group, and like Mn_2MnReO_6 and A_2CoReO_6 (A = Ba, Pb, Sr) compounds it exhibits long range antiferromagnetic (AFM) order.[81, 187-189, 194] The AFM character of the initial transition is exceptionally robust, persisting at fields of up to 7 T (Figure 2 (main text)). Herein, we describe the nuclear and magnetic structures and the magnetic and magnetotransport properties of Mn_2CoReO_6.

3.2 Results and Discussion

3.2.1 Preliminary Characterization

Optical Analysis

Optical analysis (Figure 3.1), prepared by Professor David Walker, resulted in a doubly-polarized incident illumination image which indicates that the sample is approximately pure (> 90%) single phase. Dark grey crystallites are posited to be a Mn-rich contaminate phase, whereas the lighter, more irregular-edged crystallites are likely Re-rich oxides. The sharp grain boundaries between Mn_2CoReO_6 crystals are also apparent. Optical analysis is a useful tool for early phase identification and evaluation of synthetic conditions, however it should be noted that the initial estimates are simply that, and the sample must be evaluated by a precise analytical technique such as PXD (Figure 3.2) to accurately assess sample composition.

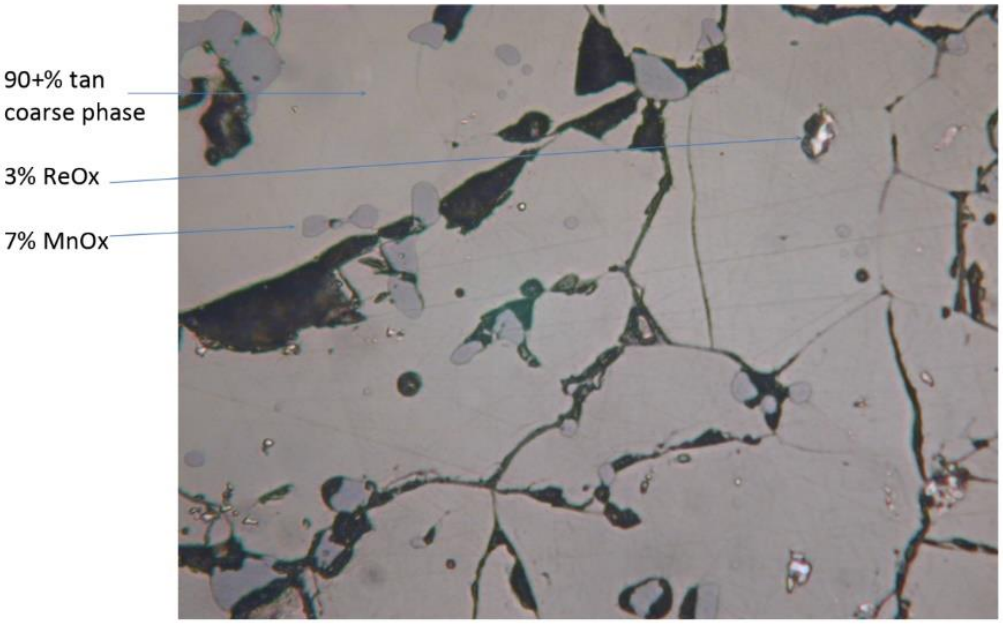

Figure 3.1 Doubly-polarized incident illumination image of Mn_2CoReO_6 embedded in epoxy resin.

Powder X-ray Diffraction (PXD)

PXD data were collected at room temperature on ground crystals of Mn_2CoReO_6 and were initially compared to known transition-metal-only double perovskites Mn_2MnReO_6 and Mn_2FeReO_6 (**Figure 3.2**).[78, 81, 194] Mn_2CoReO_6 peaks are well indexed in space group 14 ($P2_1/n$) when compared to these known samples, with trace impurities not perceptible by laboratory X-ray. As is typical of double perovskites, in Mn_2CoReO_6 the B and B' cations are each surrounded by six oxygen atoms. Atypically, the Mn *A*-cations are 8 coordinated, rather than twelve, due to significant B and B' octahedral tilting necessitated by the small atomic radii of the *A*-cations. This feature is consistent with the *A*-cation environments and also observed in the previously reported transition-metal-only double perovskites.

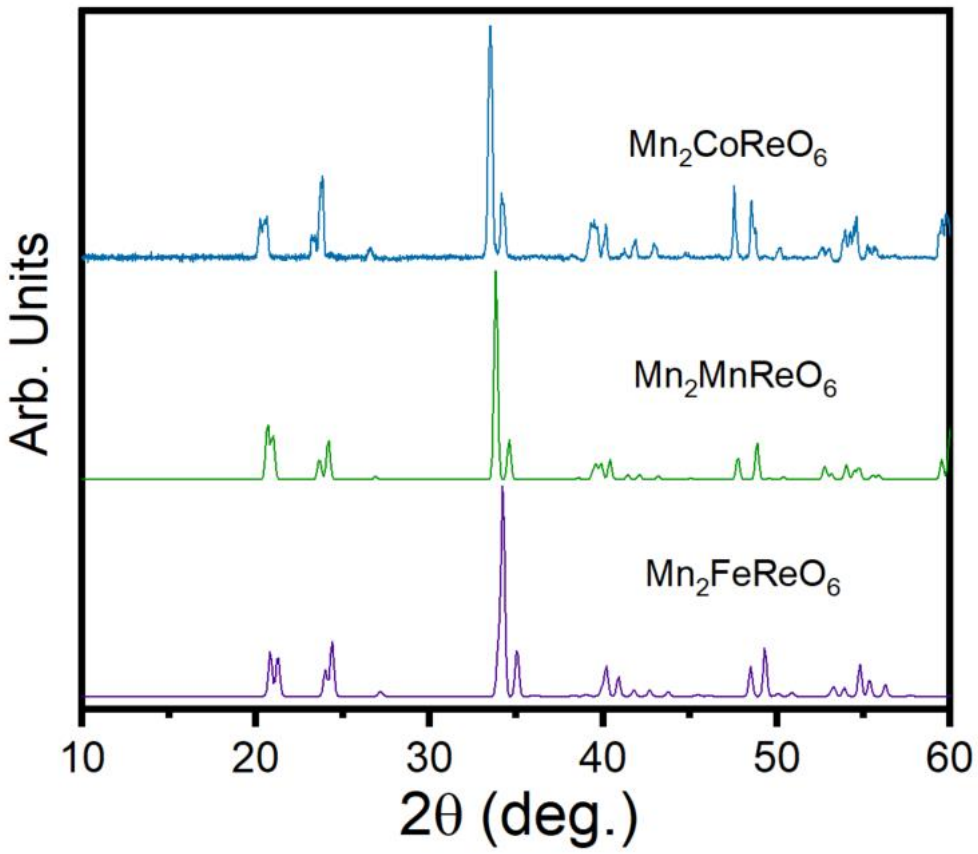

Figure 3.2 Laboratory PXD data for Mn_2CoReO_6 compared with scans of $P2_1/n$ Mn_2MnReO_6 and Mn_2FeReO_6 calculated from literature.

3.2.2 Single Crystal X-ray Diffraction (SCXRD)

Room temperature SCXRD refinements (details in **Table 3.1** and **Table 3.2**) were collected with Mo K_α, $\lambda = 0.7107$ Å, at room temperature on a Bruker Smart APEX system with charge-coupled device (CCD) area detector and mono-capillary collimation. The structure was solved with the SHELXT-2014/15 and refined with SHELXL-2014/7 software packages with data reduction performed in BRUKER APEX 3 and SAINT.[147,148,149,150] Data collection an analysis were all performed with the assistance and instruction of Dr. Thomas Emge. These analyses indicate that Mn_2CoReO_6 crystalizes in the highly distorted monoclinic space group $P2_1/n$ with a = 5.2356(2) Å b =5.3536(2) Å, c = 7.6330(3) Å, β = 89.9627(19). Based on electron

densities from SCXRD, the *B* site refines to 97.6(2)% Co and 2.4(2)% Re, with a coordinating result for the majority-Re *B'* site.

According to SCXRD, the average bond lengths of <Re-O> (1.928(3) Å) are somewhat smaller than those found in Mn_2FeReO_6 (1.961(9) Å), where Re is in oxidation state 5+ (d^2),[78] but closer to those in Mn_2MnReO_6 where the Re valence is a mixture of V and VI (1.930(2) Å).[194] The slightly shortened <Re-O> bond distance in Mn_2CoReO_6 compared to analogous Mn_2MReO_6 perovskites can reasonably be attributed to the fact that the B' site of Mn_2CoReO_6 is wholly populated by d^1 Re(VI), while the other two structures show either ~d^2 Re(V) or a mixture of ~$d^{1/2}$ Re(VI/V), respectively. Bond valence sum (BVS) calculations for Mn_2CoReO_6 support this interpretation, and indicate formal oxidation states of $Mn^{2+}{}_2Co^{2+}Re^{6+}O_6$ (Table ESI3.1), which have been confirmed by X-ray absorption near edge spectroscopy (vide infra).

As can be clearly seen in **Figure 3.3**, the *B/B*' octahedra are extremely tilted (tilt scheme of a-a- c+ in Glazer notation)[46]with a concomitant decrease in symmetry when compared to perovskites with no (or less severe) octahedral tilting. The Re-O-Co superexchange bond angles around the oxygen are 141.03(17)°, 137.18(16)°, and 139.07(14)°, respectively. These are much smaller than what was previously observed in Sr_2CoReO_6 (180.0°, 165.97(9)°, 173°), which had a tilt magnitude of 7.0° for the CoO_6 octahedra. The octahedra in Mn_2CoReO_6 must tilt much more severely in order to accommodate a smaller *A*-site Mn^{2+} cation. The magnitude of octahedral tilting, φ, can be calculated with the formula $\varphi\ ° = (180 - \theta)/2$ where θ = Co-O(2)-Re angle.[189] In Mn_2CoReO_6, φ of the CoO_6 octahedral tilting is 21.4 °, three times greater than that of the sister compound Sr_2CoReO_6.

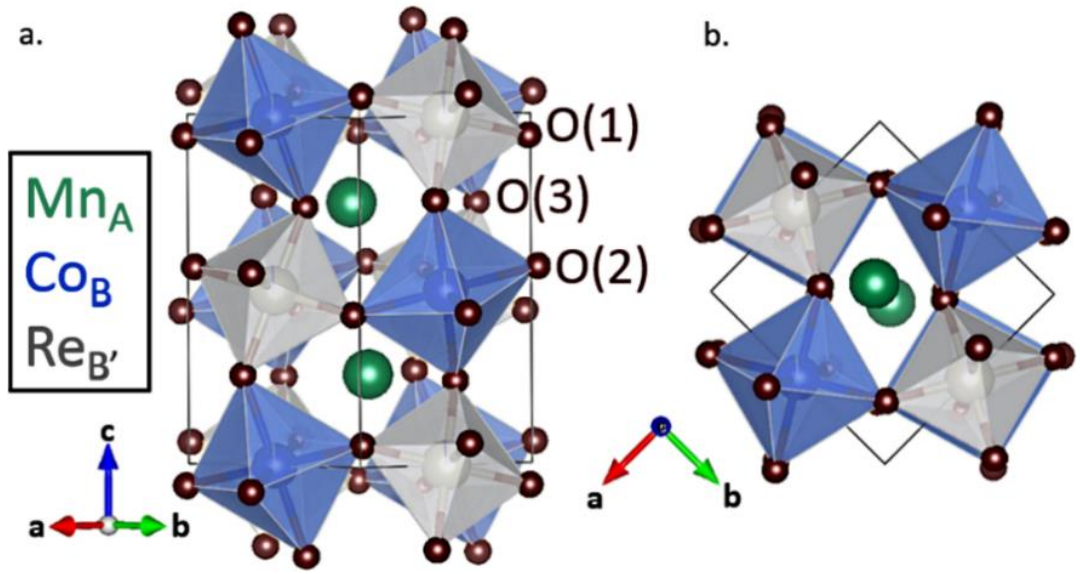

Figure 3.3 Illustration of the *P*2$_1$/*n* double perovskite structure of Mn_2CoReO_6, viewed along the A-B plane, as found by SCXRD. The Mn eight-coordinated A-site cations are represented in green and the CoO_6 and ReO_6 B/B' octahedra, in an a-a-c+ tilt scheme, are blue and grey, respectively. Oxygen atoms are represented in red.

Table 3.1 Select details of the single crystal structural refinements.

Empirical Formula	Mn_2CoReO_6
Formula Weight	451.01 g/mol
Temperature	571(2) K
Wavelength	0.71073 Å
Crystal System	Monoclinic
Space group	$P2_1/n$ (14)
Unit cell dimensions	a = 5.2356(2) Å b = 5.3536(2) Å c = 7.6330(3) Å α = ϒ = 90 ° β = 89.9627(19)°.
Volume	213.948(14) $Å^3$
Z	2
Density (calculated)	7.001 Mg/m^3
Absorption coefficient	37.715 mm^{-1}
Crystal size	0.040 x 0.020 x 0.010 mm^3
Theta range for data collection	4.651 to 45.267°.
Reflections collected	5485
Independent reflections	1774 [R_{int} = 0.0722]
Completeness to theta = 25.242°	99.0 %
Goodness-of-fit on F^2	0.705
Final R indices [I>2sigma(I)]	R1 = 0.0248, wR^2 = 0.0474
R indices (all data)	R1 = 0.0364, wR^2 = 0.0512
Extinction coefficient	0.0061(3)
Largest diff. peak and hole	$\Delta\rho_{max}$ = 1.928 $eÅ^{-3}$ $\Delta\rho_{min}$ = -2.899 $eÅ^{-3}$

Table 3.2 Selected bond distances (Å) and bond valence sums (BVS) for Mn_2CoReO_6 at room temperature.

MnO_8		CoO_6	
Mn - O1	2.120(4) Å	Co -O1 x2	2.043(4) Å
	2.619(4) Å	-O2 x2	2.128(3) Å
	2.635(4) Å	-O3 x2	2.111(3) Å
-O2	2.590(3) Å	<Co-O>	2.094(3) Å
	2.729(4) Å	BVS	2.035
	2.123(3) Å		
-O3	2.103(3) Å	ReO_6	
	2.169(3) Å	Re -O1 x2	1.929(3) Å
<Mn-O>	2.386(4) Å	-O2 x2	1.892(3) Å
BVS	2.007	-O3 x2	1.963(3) Å
		<Re-O>	1.928(3) Å
		BVS	6.746

3.2.3 Synchrotron Powder X-ray Diffraction

SPXD data were used to confirm the average nuclear structure. In order to measure the sample in an air-and-moisture free environment, a ground sample of Mn_2CoReO_6 crystals was sealed in a quartz ampule, the thickness of which necessitated measurement at the high-energy beamline, 11-ID-C at ANL ($\lambda = 0.1173$ Å). The sample refined as 98.79% pure with space group $P2_1/n$ using GSAS-II software[144] (**Figure 3.4**), and so the trace impurities were not refined in this case. Rietveld Refinement indicates ordering between Co and Re, the B and B' cations to be nearly complete, with a *B/B'* antisite disorder of approximately 1.55%, which is in agreement with the SCXRD results (1.65%). The refined unit cell parameters are close to those from SCXRD and NPD refinements, though the average bond lengths and lattice parameters are slightly longer. This could be an overestimation of exact

positions due to the difficulty in fitting the large amorphous region at low angles. This amorphous region, unusual for SPXD data, is because the sample was measured in the sealed quartz ampule in which it was transported, rather than being transferred to a smaller capillary to minimize potential air/moisture exposure of the sample. Alternatively, the difference between atomic positions found by SPXD and SCXRD could be due to the age of the SPXD sample (the sealed sample was in the analysis queue at Argonne National Lab for approximately 10 months). However, neutron powder diffraction was also performed on this sample, serving as a final arbiter of the best model, and agrees more closely with single crystal refinements. SPXD data therefore in this case act as a complement to NPD and SCXRD, confirming the relative purity of the sample and the degree of antisite disorder. Refinement details and bond lengths are reported in **Table 3.3** and **Table 3.4**.

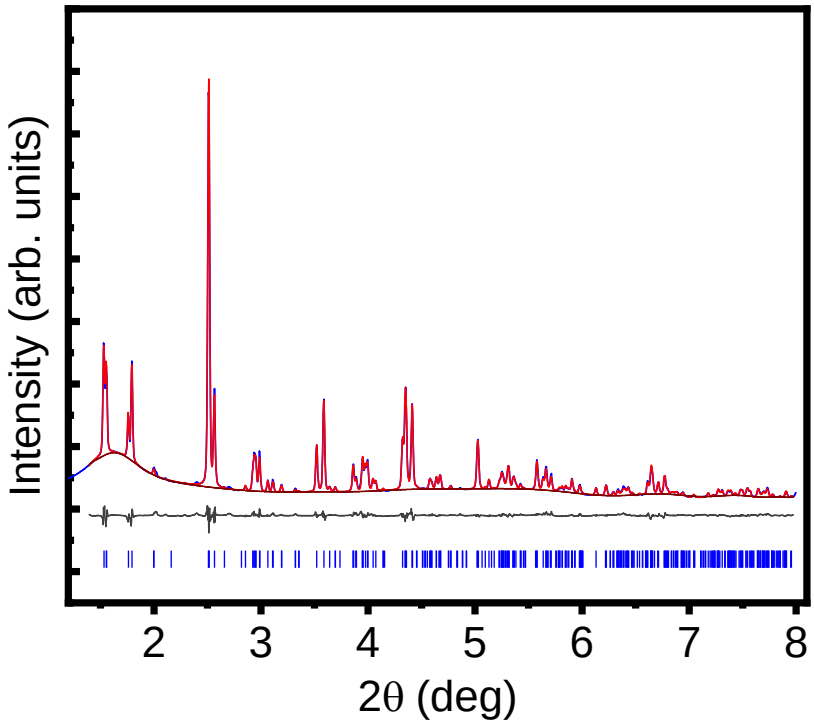

Figure 3.4 Refinement profile for Mn_2CoReO_6 using room temperature SPXD data in space group $P2_1/n$ (14). Data were collected on the high energy beamline 11-ID-C (λ = 0.71073 Å). The observed pattern, calculated pattern, difference, and background are shown in light blue, bright red, grey, and red-black lines, respectively. The Bragg positions of Mn_2CoReO_6 are shown as blue ticks.

Table 3.3 Select details of the SPXD refinement.

Empirical Formula	Mn_2CoReO_6
Formula Weight	451.01 g/mol
Wavelength	0.1173 Å
Crystal System	Monoclinic
Space group	$P2_1/n$ (14)
Unit cell dimensions	a = 5.24037 Å
	b = 5.35787 Å
	c = 7.63610 Å
	α = ϒ = 90 °
	β = 89.9143°.
Volume	214.40017 $Å^3$
Z	2
Reflections collected	2115
Independent reflections	370
Weight R (all data)	wR = 3.185%
R indices (phase)	RF^2: 4.520% , RF: 3.715%
Phase Fraction	98.7851%

Table 3.4 Selected bond distances (Å) for Mn_2CoReO_6 at room temperature collected on high energy beamline 11-ID-C.

MnO_8		CoO_6	
Mn - O1	2.0708 Å	Co -O1 x2	2.0839 Å
	2.5970 Å	-O2 x2	2.1998 Å
	2.6734 Å	-O3 x2	2. 0690Å
-O2	2.1098 Å	<Co-O>	2.1176 Å
	2.5528 Å		
	2.8108 Å		
-O3	2.1940 Å	ReO_6	
	2.2080 Å	Re -O1 x2	1.9096 Å
<Mn-O>	2.4021 Å	-O2 x2	1.8504 Å
		-O3 x2	1.9274 Å
		<Re-O>	1.8958 Å

3.2.4 Scanning Electron Microscopy – Energy Dispersive X-ray Spectroscopy (SEM-EDX)

To elucidate the molar ratio of composition, SEM-EDX was used. SEM-EDX is considered a semi-quantitative technique,[195-196] and thus can be used in concert with high sensitivity diffraction techniques (such as single crystal and neutron diffraction) to confirm a refined ratio. First, an element map was generated which showed one large main phase and some inclusions of two other phases, which look “dark” or

"bright" on the black and white SEM image. In the SEM-EDX map, the "dark" spots appear to be Re deficient and Co/Mn rich. Analysis of the targeted main phase implies an Mn:Co:Re ratio of 2:1:1, which, combined with high quality diffraction refinements confirms that the compound of interest in is indeed Mn_2CoReO_6.

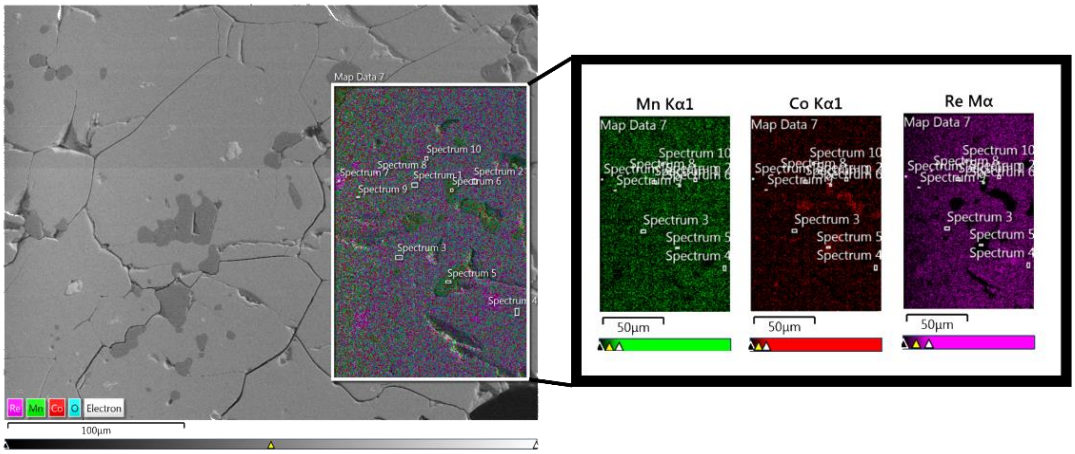

Figure 3.5 SEM image of Mn_2CoReO_6 with EDX map overlayed. Mn, Co, and Re are represented in green, red, and pink, respectively. The Mn/Co rich and Re defficient impurity can be clearly seen in the individual element maps. The ratio of Mn: Co: Re indicated by this technique is 2:1:1.

3.2.5 X-ray Absorption Near Edge Spectroscopy

XANES, used to investigate the transition metal oxidation states and analysis of the Mn and Co K edges (and pre-edge features), suggested that both are in 2+ oxidation states, while the Re $L_{2,3}$ edges were consistent with Re^{6+} ($5d^1$). Mn-K, Co-K and Re-L_3 X-ray absorption near edge spectroscopy (XANES) data were collected in both the transmission and fluorescence mode with simultaneous standards by Prof. Mark Croft, who directed the initial analysis and the plotting of figures. All spectra were fit to linear pre- and post-edge backgrounds and normalized to unity absorption edge step across the edge. The title compound XANES spectra were collected at the QAS, 7BM Beamline at NSLS-II using a Si(111) channel-cut monochromator in the "qick", continuous scanning mode. Some of the standard spectra were previously collected on beam line X-19A at NSLS-I with a Si-111 double crystal

monochromator. Selected standard spectra were also collected at NSLS-II 6BM taken with a Si (311) monochromator. It should be noted that the Mn_2CoReO_6 samples were prepared and packaged for transport to NSLS-II in a sealed nitrogen gas container. Moreover, the actual XANES measurements were performed with the sample in a sealed nitrogen gas bag mounted in the beam.

The shape and energies of spectra generated by the photoabsorption cross section of atoms are highly dependent on both coordination environment and valence state.[111, 168, 197-199] For a 3-d transition metal, the main K-edge features are dominated by peak-like 1s to 4p transitions and, like the step-feature continuum onset beneath them, typically exhibit a chemical shift to higher energies with increasing transition metal valance. In **Figure 3.6**(a), the Mn K-edge of Mn_2CoReO_6 is compared to the standards Mn^0, $Mn^{2+}O$, $LaMn^{3+}O_3$, and $CaMn^{4+}O_3$ and to Mn_2FeReO_6 and $Mn_2Fe_{0.8}Mo_{1.2}O_6$, where Mn(II) is eight-fold coordinated (i.e., reduced from the ideal un-distorted perovskite 12-fold A coordination) on the A site like in Mn_2CoReO_6. The chemical shift of the main edge rise for Mn_2CoReO_6 is clearly much lower than that for the Mn(III) or Mn(IV) standards, indicating that the formal oxidation state at the Mn sites is Mn^{2+}. In addition to oxidation states resulting in shifts in energy, local atomic coordination and bonding can split the 4p features in multiple ways. The degree of similarity between the shapes of the Mn_2FeReO_6, and $Mn_2Fe_{0.8}Mo_{1.2}O_6$ Mn K-edge spectra, with Mn_2CoReO_6 basically overlapping Mn_2FeReO_6, indicate that the Mn cations of both compounds not only share the same oxidation state but lie in very similar local coordination environments.

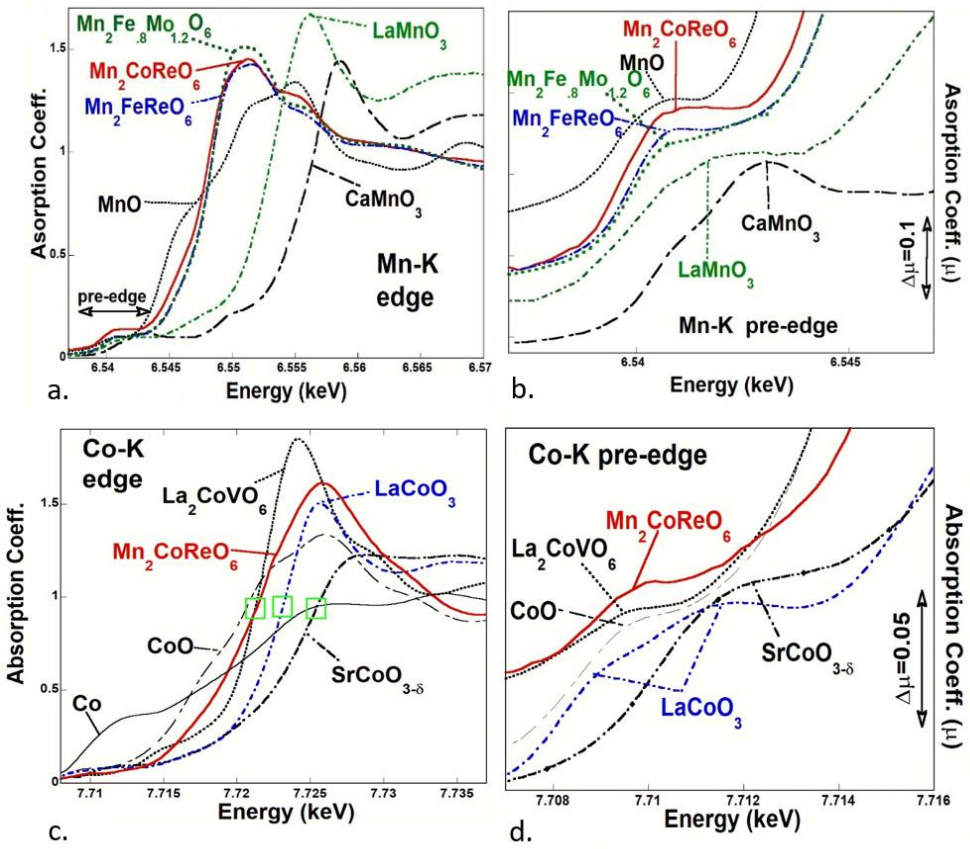

Figure 3.6 XANES spectra for the Mn K-edge (a) and Mn K pre-edge (b) compared to Mn^{0}, $Mn^{2+}O$, $LaMn^{3+}O_3$, and $CaMn^{4+}O_3$ standards and Mn_2FeReO_6 and $Mn_2Fe_{0.8}Mo_{1.2}O_6$ (in which Mn is eight-fold coordinated to oxygen). The Co K-edge (c), and Co K pre-edge (d) are compared to octahedrally coordinated standards with differing formal valences: Co^{0}, $Co^{2+}O$, $La_2Co^{2+}VO_6$, $LaCo^{3+}O_3$, and $SrCo^{4+}O_{3-\delta}$. Spectra were collected in continuous scanning mode; some standards were added after-the-fact from a database of past experiments.

In the Mn pre-edge (**Figure 3.6**(b)), the pre-edge feature is enhanced by d/p hybridization caused by highly distorted, noncentrosymmetric coordination, as seen in previous studies.[78, 194] Despite this intensification, the characteristic single low energy onset feature of Mn(II) is clearly visible in Mn_2CoReO_6, in contrast to the higher-oxidation standards. Comparison of the Mn_2CoReO_6 pre-edge feature to those of the standard compounds further supports the Mn^{2+} assignment for this compound. Thus, both the pre-edge and main-edge Mn K results support a Mn^{2+} state for Mn_2CoReO_6 with the main-edge results also strongly supporting a local coordination environment like that of Mn_2FeReO_6.

Figure 3.6(c) shows the Co-K main edge spectra for Mn_2CoReO_6 compared with several standards in which Co is octahedrally coordinated to oxygen: Co^0, $Co^{2+}O$, $La_2Co^{2+}VO_6$, $LaCo^{3+}O_3$, and $SrCo^{4+}O_{3-\delta}$. The chemical shift of the main edge spectra is consistent with the assignment of an oxidation state of Co(II). Likewise, the energy shift and overall shape of the Co pre-edge of Mn_2CoReO_6 (**Figure 3.6**(d)) correspond to those of the Co^{2+} standards.

Originally, XANES measurements were recorded on photographic film, so unabsorbed bands would lead to a white line appearing on the film. White line (WL) spectra, named for this phenomenon, manifest at the intense, atomic-like p to d transitions occurring at the $L_{2,3}$ near-edges of transition metals at the onsets of the edges.[112, 194, 199] In octahedrally coordinated rhenium, the 5d orbitals spilt into 6-fold-degernate t_{2g} and 4-fold-degerate e_g orbital states. In **Figure 3.7**, these states are represented in the 5d-L_3-spectra by a bimodal, A/B structure where A is related to t_{2g} and B to e_g final states (hole count), weighted by transition matrix element effects. In the standards here, the B-feature intensity is essentially constant because the e_g hole count is essentially constant. On the other hand, the relative prominence of the A-feature decreases dramatically as the t_{2g} hole count decreases from six in d^0 $SrFe_{3/4}Re_{1/4}O_3$ to three in d^3 ReO_2. To facilitate comparison despite chemical shift, a line has been drawn by Prof Croft from A-feature to A-feature and B-feature to B-feature down the series of standards. Mn_2CoReO_6 aligns very closely in both chemical shift and the relative strengths of the A/B bimodal features to the spectrum of the octahedrally-coordinated d^1 rhenium in Ba_2MnReO_6.

Comparing the L_3-edge, **Figure 3.7**, and L_2-edge, **Figure 3.8**, spectra, it is interesting to note that matrix element effects substantially enhance the A-feature intensity (and its change with hole count) especially in the high hole count regime.

Thus, the relative A/B feature intensities provides direct insight into the Re valence/d electron-configuration. For the purpose of illustrating the A/B intensity variation, with varying d-count, the L_2-edges in **Figure 3.8** have been shifted in energy so as to roughly align the B- features. In contrast, the L_3-edges in **Figure 3.7** are plotted on an absolute energy scale (determined via simultaneously run standards) thereby illustrating the chemical shift of the centrum of the WL-feature to higher energy with increasing Re-valence. In both figures, the comparison of the Mn_2CoReO_6 spectra to the systematic series of standards, can be seen to manifest a relative A/B feature intensity consistent with a ~Re^{6+}, d^1 configuration. Thus, both the spectral energy distribution and chemical shift concur in the ~Re^{6+}, d^1 configuration assignment for Mn_2CoReO_6.

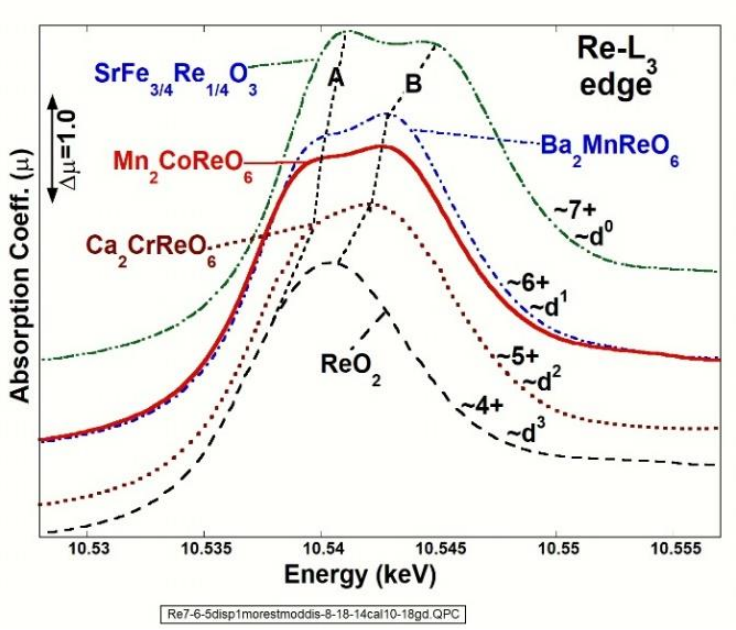

Figure 3.7 XANES Re L_3 edge for Mn_2CoReO_6 collected simultaneously with other XANES spectra for this sample. Results have been compared to several known octahedral Re standards ranging in oxidation state from Re(IV) to Re(VII): $Re^{4+}O_2$, $Ca_2CrRe^{5+}O_6$, $Ba_2MnRe^{6+}O_6$, and $SrFe_{3/4}Re^{7+}{}_{1/4}O_3$. Lines have been added to highlight the bimodal A/B structures typical of 5d transition metals.

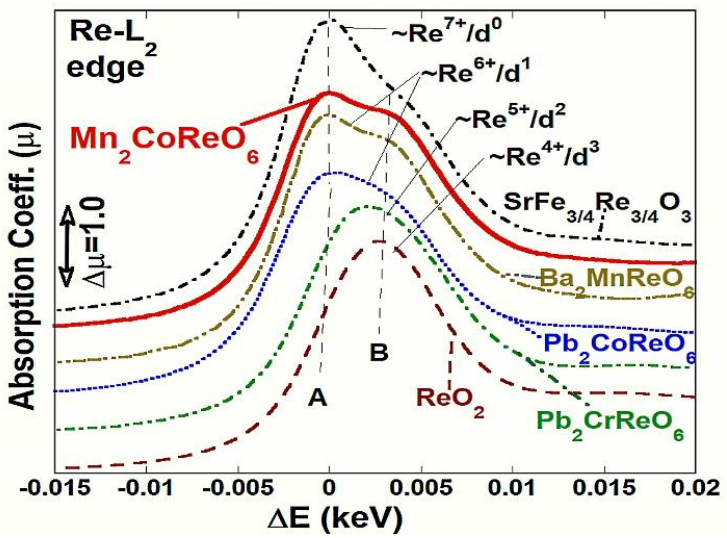

Figure 3.8 The Re L_2 edge for Mn_2CoReO_6 compared to those of other standard octahedral Re-O compounds (spanning Re^{7+}/d^0 - to – $Re^{5+/}d^3$). Spectra have been shifted in energy to approximately align the B (e_g-hole-related) features. The zero of the relative energy scale (ΔE) was chosen as the nominal position of the A(t_{2g}-hole-related) features. Spectra have been displaced vertically for clarity.

3.2.6 Heat Capacity

The specific heat at constant pressure (C_p) was measured on a PPMS by Quantum design with Heat Capacity Option 2.7.2 Build 2 by collaborators at the Chinese Academy of Sciences. A small pressed pellet sample weighing 27.3 mg and roughly cylindrical in shape was measured between 2 and 150 K in zero magnetic field. **Figure 3.9** very clearly manifests an asymmetric, rounded λ-anomaly peaking very near 96 K that closely corresponds to the sharp transition seen in the magnetic susceptibility at H = 0.5 T, confirming that the antiferromagnetic order in Mn_2CoReO_6 occurs at 94 K. Specific heat confirms T_N at ~94 K, as that is the midpoint between the onset of the large irregular anomaly at 108 K and the end of the most dramatic slope change at 81 K. Within material and experimental limits these results confirm the presence of a second order AFM transition in Mn_2CoReO_6 in this temperature range. There may be another transition near 50 K, where the slope changes slightly yet again, and while this corresponds with a change in measurement

mode and thus transition shape and exact position could be artificially affected, this latter transition is also observed in the NPD.

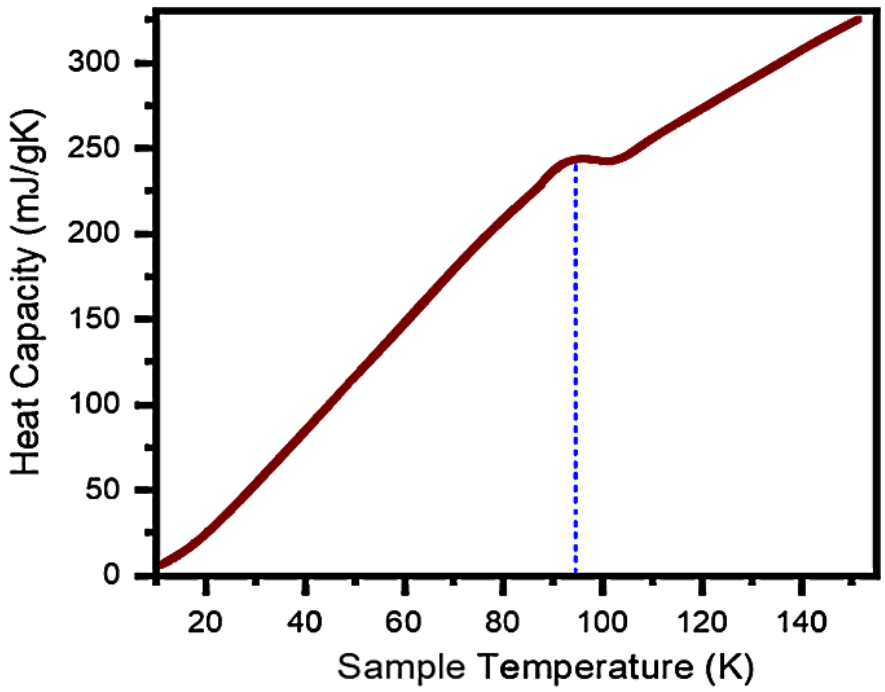

Figure 3.9 Specific heat capacity versus temperature for Mn_2CoReO_6.

3.2.7 Magnetic Properties

Field Cooled (FC) and Zero Field Cooled (ZFC) magnetic measurements were carried out by collaborators at the Institute of Physics, Chinese Academy of Sciences under the direction of Dr. Zheng Deng with a SQUID magnetometer in a temperature range of 5 - 400 K with an applied magnetic field of 0.5 T. At H = 0.1 T, FC and ZFC data were collected at a temperature range of 5 – 300 K. At H = 1, 2, 3, 5, and 7 T, FC and ZFC data were collected at a temperature range of 5 – 135 K. Isothermal magnetization curves were obtained at 5, 100, 150, and 300 K under an applied magnetic field which ranged from 6 T to -6 T. Magnetotransport measurements were performed on a pressed pellet sample of Mn_2CoReO_6 crystals with the standard four-probe technique in a Quantum Design physical property measurement system (PPMS)

at fields of 0 and 7 T. Analysis of the magnetic data in this section was performed with the close mentorship of Prof. Mark Croft.

The thermal variation of the inverse magnetic susceptibility, χ^{-1}, is also shown in **Figure 3.10**. Fitting χ^{-1} in the temperature range T > 210 K to the Curie-Weiss (CW) form,

$$\chi^{-1} = (T+\theta)/C \tag{3.1}$$

yields C= 9.76 emu·K mol^{-1} and a "ferromagnetic-like" θ = 25.6 K. This high temperature CW fit is shown as a dotted line in Figure 2 (main text). From the high temperature CW fit the μ_{eff} for Mn_2CoReO_6 is 8.84 μ_B/f.u. as per the following equation:[200]

$$\mu_{eff} = (\frac{3kC}{N})^{1/2} = (8C)^{1/2}\mu_B \tag{3.2}$$

Within a simple spin-only model, with Mn^{2+} (S =5/2 , μ_{eff} = 5.92 μ_B) and Co^{2+}(S = 3/2, μ_{eff} = 3.87 μ_B), and Re^{6+}(S = 1/2, μ_{eff} = 1.73 μ_B), and the relation[201]:

$$\mu_{eff} = \sqrt{2\mu_B(Mn^{2+})^2 + 1\mu_B(Co^{2+})^2 + 1\mu_B(Re^{6+})^2} \tag{3.3}$$

one calculates a theoretical μ_{eff} of 9.38 μ_B/fu. This agrees adequately with the fitted experimental 8.84 μ_B/f.u. value, with a slight lowering by spin-orbit coupling of Re^{6+}.

The presence of some ferromagnetic component in the system, despite the robust AFM anomaly near 94 K, is underscored by both the θ = 25.6 K and the downward curvature of the inverse susceptibility data away from the CW fit in the 200 K> T > 94 K temperature range. Indeed, the dramatic sharpness of the peak anomaly in χ(T) is enhanced by the FM response above the AFM ordering temperature T_N~ 94K. Discussion of this FM component will be returned to subsequently.

Below the first transition, the FC and ZFC curves diverge sharply, which may suggest competing magnetic interactions. It is possible that some form of spin reorientation transition (or evolution) is active in this temperature range. A change in the Re contribution in the magnetic order is also possible. Such changes are not inconsistent with the temperature dependent neutron scattering results but they are also not clear given the refinement limitations. The graph of χ^{-1} vs. T (**Figure 3.10**) data above 200 K exhibits Curie-Weiss behavior, albeit with some curvature which is slight in that region, but increases noticeably as the first magnetic transition approaches. This shape could be due to crystal field effects, as suggested by Retuerto et. al. to explain a similar curve observed in Sr_2CoReO_6[189] or could be influenced by the presence of a trace of ferrimagnetic Mn_3O_4-like phase. The calculated Curie constant, C, is 9.76 emu·K mol^{-1} and the Weiss temperature is approximately 25.6 K, despite the AFM character of the transition at 94 K. A positive Weiss constant is not unheard of in cobalt-containing antiferromagnets, and it could be that spin orbit effects decrease the reliability of θ to characterize magnetic order.[44, 202]

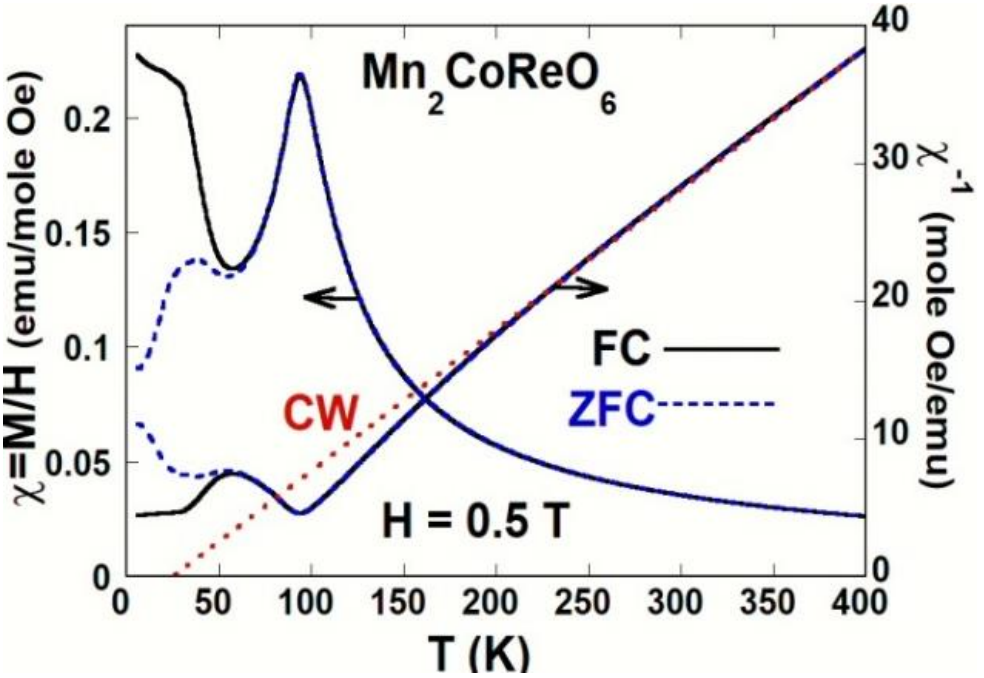

Figure 3.10 The H=0.5 T, temperature dependent magnetic susceptibility, χ, and the inverse susceptibilities, χ^{-1}, for Mn_2CoReO_6 collected under field cooled (FC) and zero field cooled (ZFC) conditions. The Curie Weiss (CW) fit to the high temperature χ^{-1} data is indicated by a dotted line.

Magnetization vs temperature measurements were performed in a series of increasing field strengths up to H= 7 T and are shown in **Figure 3.11**(a). The prominent AFM order induced M(T) peak near 94 K is clearly robust to the highest field studied and shifts down only slightly in temperature in the higher fields. The robustness of the M(T) signature in field would imply that the field induced reorientation of the AFM order parameter transverse to the external H-field does not occur in this field range. Moreover, magneto-crystalline anisotropy appears strong enough that the applied H-field is unable to induce any significant continuous canting of the AFM order away from its preferred crystalline ordering direction.

The results of selected temperature isothermal magnetization measurements, M(H), are shown in **Figure 3.11**(b). The linear behavior of M(H) data at 300 and 150 K are consistent with paramagnetism. However, the S-shaped curve for the M(H) at 100 K, indicates a weak FM component. This is the same temperature range above T_N

in which the magnetic susceptibility manifested a FM like curvature away from the CW fit, and the CW fit also showed a FM-like Weiss temperature.

The T = 5 K, M(H) curve (**Figure 3.11**(b)) varies smoothly with field with no sign of a field-induced transition even the first leg in which the field is increased from H = 0 to 6T. Additionally, the total magnetization at 5 K is only about 1 μ_B, consistent with the modest field response within an AFM state. Thirdly, the remnant magnetization, upon decreasing the field has a small ~0.1 μ_B value (and a coercive field of ~0.5 T) consistent with an induced field polarization/modification of the AFM domain structure. Moreover, the entire M(H) loop at 5 K is consistent with such gradual/modest field induced AFM domain structure modifications.

It is also possible that AFM domain effects are responsible for the T< 50 K magnetic behavior. The NPD structural refinement found an ~16% antisite disorder between *A*-site Mn and *B*-site Co. Such interchanging of S= 5/2 and 3/2 at sites allows for a local uncompensated moment that, when coupled to other disorder effects, can enhance the coupling of external magnetic field. Above T_N, AFM fluctuations with modest net magnetic moments would respond to an external field and could motivate the FM components observed in χ^{-1} for $T > T_N$ and in the M(H) at 100K. Similarly, FC conditions would lead to a nucleation and growth of AFM domains with larger net moments aligned with the field, whereas ZFC conditions would lead to a low-magnetization/random-domain growth.

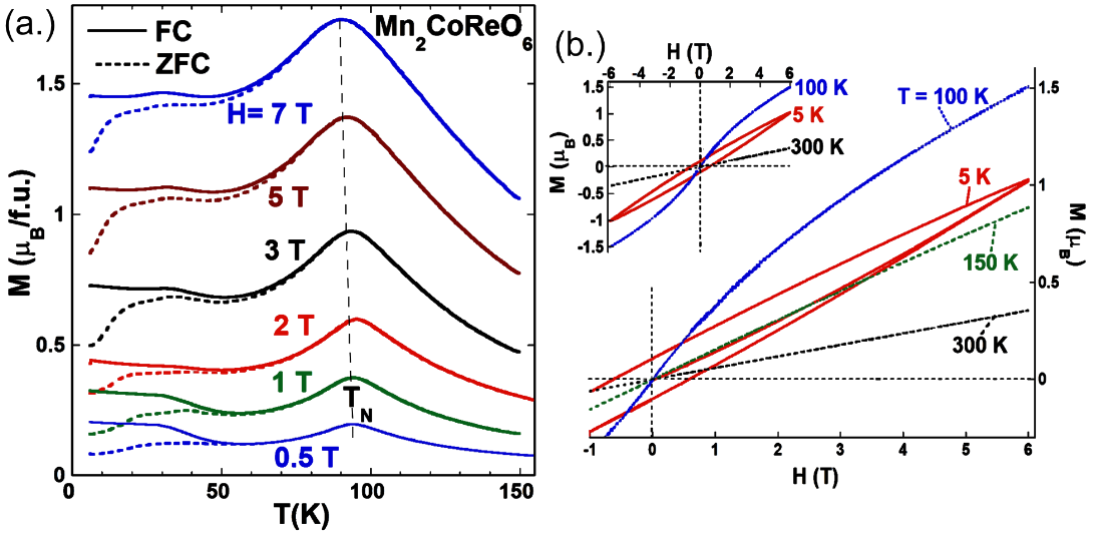

Figure 3.11 (a) Magnetization (M) vs temperature for Mn_2CoReO_6 measured at a series of fields (H). The field cooled (FC) and zero field cooled (ZFC) data collection curves are solid and dashed lines respectively. (b) A portion of the magnetization vs field curves, M(H), for Mn_2CoReO_6, measured at temperatures of 5, 100, 150, and 300 K (lower right). Inset (upper left) the full loop M(H) curves at 5, 100 and 300 K to emphasize the field-symmetry of the loops.

3.2.8 Magnetotransport Measurements

Additional magnetic properties were evaluated in the form of temperature dependent resistivity measurements under applied magnetic fields of 0 T and 7 T by collaborators at the Institute of Physics, Chinese Academy of Sciences under the direction of Dr. Zheng Deng, as shown in **Figure 3.12**. The resistance values are almost identical under 300 – 50 K, where resistivity becomes too high to accurately measure, which indicates a lack of magnetoresistance. At 300 K, roughly room temperature, the resistivity is approximately 6.98Ω cm and 7.05 Ω cm at 0 T and 7 T, respectively, similar to what was reported for the non-magnetoresistive half-metal Mn_2MnReO_6 at the same temperature (6.80 Ω cm and 8.10 Ω cm at 0 T and 9 T).[194] The temperature dependence of ρ, (**Figure 3.12**, inset) was found by trial-and-error fitting of the relation: $(1/T)^p$, with $p = 1/2$ giving the best linearity from 50 – 300 K. This fitting is consistent with that of an Efros-Shklovskii variable range-hopping semiconductor:

$$\rho = \rho_0 * e^{-(T_0/T)^{1/2}} \quad (3.4)$$

(where T_0 is the characteristic temperature and ρ_0 is a resistivity coefficient), in which a 'soft', or parabolic, gap in the density of states near the Fermi level is caused by Coulomb interactions between localized electrons.[203] The extracted values for $T_0^{1/2}$ and ρ_0 are 157.04 $K^{1/2}$ and 6.208×10^{-4} Ω cm, respectively for $T > 60$ K (below which Mn_2CoReO_6 becomes too resistive). The temperature-dependent resistivity measured under a magnetic field of 7 T results were practically identical to those measured at 0 T, confirming a lack of magnetoresistance.

Previously-explored $Mn_2BB'O_6$ compounds (B = Fe, Mn), have presented both giant magnetoresistance and no magnetoresistance.[78, 194] Mn_2FeReO_6, a half-metallic ferrimagnet, demonstrated giant positive magnetoresistance of 220% at 5K due to the magnetically ordered Mn sublattice interfering with Fe-O-Re exchange. Conversely, the *A* and *B-B'* magnetic sublattices in Mn_2MnReO_6 couple antiferromagnetically and hinder the possibility of ferrimagnetic interactions or a half metallic state between Re and Mn, greatly decreasing the probability of magnetoresistance. In Mn_2CoReO_6, the previously shown robust AFM character of the magnetic ordering also indicates a lack of ferrimagnetic interactions after T_N, and so magnetoresistance should not be expected in this case.

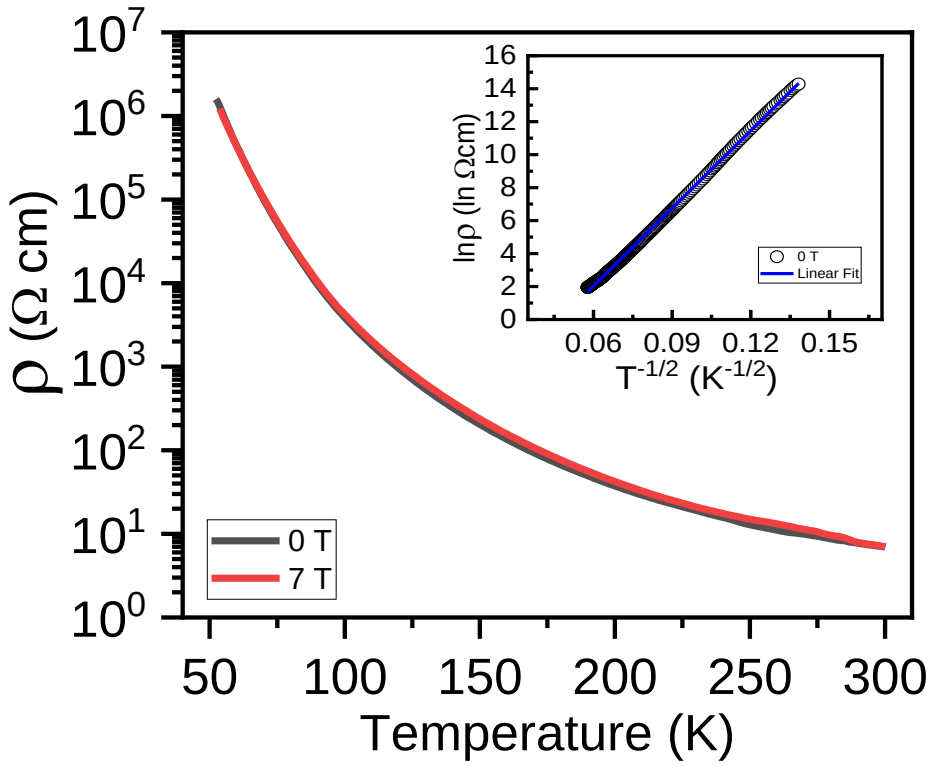

Figure 3.12 Mn_2CoReO_6 temperature dependent resistivity, ρ, measured at 0 T and the linear fit plot of ρ versus $T^{-1/2}$ (inset) which indicate an Efros–Shklovskii variable range hopping mechanism.

3.2.9 Neutron Powder Diffraction

NPD data were collected, refined, and analyzed by collaborators Prof. Emma McCabe, Dr. Fabio Orlandi, and Dr. Pascal Manuel, and will be discussed here briefly to complete the story of Mn_2CoReO_6. Approximately 100 mg of sample were transferred to a cylindrical, thin-walled vanadium can inside a glovebox and quickly loaded into a CCR and evacuated. A high quality NPD scan (80 μAmp hr) was collected at 2 K and shorter scans (16.7 μAmp hr) collected every 5 K on warming to 135 K. Data analyzed by collaborators with TopasAcademic software[143] and ISODISTORT[155] was used to explore possible magnetic structures and to give a description of the magnetic structures in terms of the nuclear structure and symmetry-adapted magnetic modes. (ISIS data available at DOI: 10.5286/ISIS.E.101137712)

NPD data collected at 200 K were used by the collaborators to investigate the nuclear structure of Mn_2CoReO_6 and the main peaks were consistent with the $P2_1/n$ ($a^-a^-c^+$) X-ray based structure reported for Mn_2FeReO_6,[78, 204] with a trace of a spinel-like impurity phase (such as Mn_3O_4 or $Mn_{3-x}Co_xO_4$).[204] The good contrast in neutron scattering lengths of the cations (Mn = -3.73(2) fm, Co = 2.50(3) fm, Re = 9.2(2) fm)[205] means that NPD data are sensitive to antisite disorder. Refinements using a single global temperature factor and constraints to maintain sample composition revealed almost complete ordering of Co and Re on the perovskite B sites (referred to as Co_B and Re_B), and ~16% disorder between Mn on the A site (Mn_A) and Co on the B site and this cation distribution was fixed in subsequent refinements.

Low temperature NPD data were used to investigate the magnetic ordering further. On cooling below ~100 K, additional magnetic Bragg reflections were observed and increased in intensity on cooling. ISODISTORT[155] was used to explore possible magnetic structures. Mode inclusion analysis[206-207] was used by the collaborators to consider possible magnetic structures and indicated ordered moments on all three sites. At temperatures down to ~50 K, the best fit was obtained with Co_B and Re_B moments along [010] (with constraints to give equal moments for all crystallographically equivalent sites). The Co_B and Re_B moments were strongly correlated in refinements (as noted for the B site ions in Mn_2MnReO_6[208]) and so the Re_B moment was constrained to be collinear and a third of the magnitude of the Co_B moment. The absolute orientation of the Mn_A site moments is hard to determine from powder diffraction data due to peak overlap and the slight monoclinic distortion. Good fits were obtained with Mn_A moments close to the [101].

While most magnetic reflections increase smoothly on cooling, some very weak reflections are only observed at lower temperatures (e.g. 110 reflection observed

below 40 K). We note that this is close in temperature to the FM-like feature suggested by magnetic susceptibility measurements and may indicate a second magnetic transition on cooling, although the feature in susceptibility measurements may also be attributed to the trace of ferrimagnetic impurity or by domain effects. The additional magnetic reflections observed for T < 40 K require some extra component described by a gamma point irrep of the parent structure, and all such possible magnetic modes on either the A or B sites were considered. It is likely that this component arises from the Co_B site because the ordered moment on this site shows an anomaly around 40 K, but none of our models gave significant improvement in fit. No clear peak in the heat capacity data is observed around 40 K, however, we note that a slight change in slope and this may indicate a change in magnetic behavior e.g. magnetic phase segregation, perhaps resulting from the cation Mn – Co antisite disorder, and further analysis to understand this low temperature magnetism is needed.

The 60 K magnetic structure described above is similar to that reported for Mn2MnReO6[81] in that spins on the A and B sites are close to perpendicular. This implies that, despite being described by the same irreducible representation, the coupling between the A and B sublattices in Mn2CoReO6 is very weak. This might explain the difference in transport properties between semiconducting Mn_2CoReO_6 (with no magnetoresistance) and the half-metallic Mn_2FeReO_6.[78] These two sublattices may order at slightly different temperatures, with the Co_B site ordering a few Kelvin above the Mn_A sublattice (analogous to the magnetic ordering reported for Mn2MnReO6[81]), but NPD data collected at smaller temperature intervals would be necessary to confirm this. The low moment observed for the Co^{2+} site from NPD is surprising and may indicate deficiencies of our model; the low temperature magnetic

behavior is not yet understood and the change in magnetic behavior suggested by magnetic susceptibility measurements below ~40 K may arise from the B sites ions and further investigations are needed.

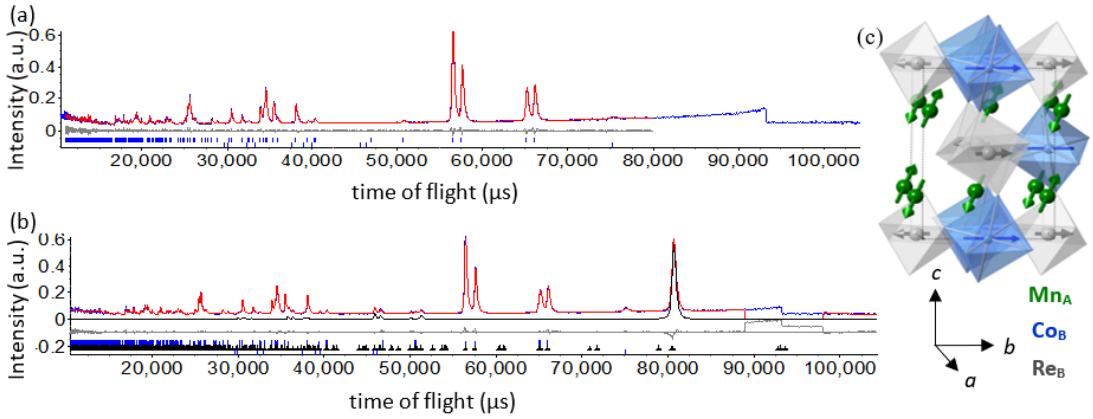

Figure 3.13 Refinement profiles for Mn_2CoReO_6 made by the collaboratorswith (a) 200 K NPD data (upper and lower blue ticks show peak positions for the main phase Mn_2FeRuO_6 and for $Mn_{3-x}Co_xO_4$ (fitted with Pawley phase), respectively) and (b) 60 K NPD data showing 90° bank data (upper, middle and lower ticks show peak positions for nuclear and magnetic phases and $Mn_{3-x}Co_xO_4$ Pawley phase, respectively). Observed, calculated and difference profiles are shown in blue, red and grey, respectively and in (b), magnetic scattering is highlighted in black. (c) shows 60 K magnetic structure with Mn_A, Co_B and Re_B moments in green, blue and grey, respectively (oxides omitted for clarity).

3.3 Conclusion

In conclusion, we have studied the nuclear and magnetic structures of Mn_2CoReO_6, the fourth known transition-metal-only double perovskite, prepared at high temperature and high pressure. Like its sister compounds Mn_2MnReO_6, Mn_2FeReO_6, and $Mn_2(Fe_{0.8}Mo_{0.2})MoO_6$ it crystallizes in the monoclinic space group $P2_1/n$. The BO_6/B'O_6 octahedra are heavily tilted, and Mn is only 8-fold coordinated to oxygen, rather than 12 as in an ideal perovskite, due to its small atomic radius. Transport measurements suggest that Mn_2CoReO_6 is an Efros–Shklovskii variable range hopping semiconductor with negligible magnetoresistance. Magnetization versus temperature measurements over fields from 0.1 T – 7 T indicate that the first

transition at 94 K is very robustly antiferromagnetic. According to PND, all the magnetic cations order with a k = (½ ½ 0) propagation vector below ~100K. The Mn A site cations orders with moment close to the [101] direction, whereas the B/B' cations order along the [010] direction. The different moment directions, joined with the observation of two close magnetic transition temperatures, indicates a weak inter-sublattice coupling suggesting an independent ordering of the A and B/B' site. A second transition, with propagation vector k=0, is observed around 40 K and it is likely related to a spin reorientation involving the B/B' ions, but further investigation are required to fully characterize this transition.

The crystal structures of known transitional metal only double perovskites have been consistently very similar, and yet the magnetic structures and transitions have not been so easily predicted. This suggests that the magnetic and transport properties of these perovskites are highly dependent on electronic structure, and in the case of Mn_2CoReO_6, potentially driven by the high degree of Russell-Sounders coupling present in both Co^{2+} and Re^{6+} B/B' cations. Future investigations, such as DFT, first principles calculations and further neutron experiments, will help to understand the electronic structure, fully elucidate the magnetic structure, and help guide new theory-driven investigations of transition metal double perovskites with small A-site cations.

3.4 References

42. Anderson, M. T.; Greenwood, K. B.; Taylor, G. A.; Poeppelmeier, K. R., B-cation arrangements in double perovskites. *Progress in Solid State Chemistry* **1993,** *22* (3), 197-233.
44. Blasse, G., Some Magnetic Properties of Mixed Metal Oxides with Ordered Perovskite Structure. *Phillips Research Reports* **1965,** *20*, 327-336.
46. Howard, C. J.; Kennedy, B. J.; Woodward, P. M., Ordered double perovskites – a group-theoretical analysis. *Acta Crystallographica Section B* **2003,** *B59*, 463-471.
52. Belik, A. A.; Yi, W., High-pressure synthesis, crystal chemistry and physics of perovskites with small cations at the A site. *J. Phys. Condens. Matter* **2014,** *26*, 163201.
57. Vasala, S.; Karppinen, M., $A_2B'B''O_6$ perovskites: A review. *Prog. Solid State Chem.* **2015,** *43* (1), 1-36.
63. Kobayashi, K. I.; Kimura, T.; Sawada, H.; Terakura, K.; Tokura, Y., Room-temperature magnetoresistance in an oxide material with an ordered double-perovskite structure. *Nature* **1998,** *395*, 677.
78. Li, M. R.; Retuerto, M.; Deng, Z.; Stephens, P. W.; Croft, M.; Huang, Q.; Wu, H.; Deng, X.; Kotliar, G.; Sánchez-Benítez, J.; Hadermann, J.; Walker, D.; Greenblatt, M., Giant Magnetoresistance in the Half-Metallic Double-Perovskite Ferrimagnet Mn_2FeReO_6. *Angew. Chem. Int. Ed. Engl.* **2015,** *54* (41), 12069-12073.
79. Li, M. R.; Hodges, J. P.; Retuerto, M.; Deng, Z.; Stephens, P. W.; Croft, M. C.; Deng, X. Y.; Kotliar, G.; Sanchez-Benitez, J.; Walker, D.; Greenblatt, M., Mn_2MnReO_6: Synthesis and Magnetic Structure Determination of a New Transition-Metal-Only Double Perovskite Canted Antiferromagnet. *Chemistry of Materials* **2016,** *28* (9), 3148-3158.
80. Arévalo-López, A. M.; McNally, G. M.; Attfield, J. P., Large Magnetization and Frustration Switching of Magnetoresistance in the Double-Perovskite Ferrimagnet Mn_2FeReO_6. *Angew. Chem. Int. Ed* **2015,** *54* (41), 12074-12077.
81. Arévalo-López, A. M.; Stegemann, F.; Attfield, J. P., Competing antiferromagnetic orders in the double perovskite Mn_2MnReO_6 (Mn_3ReO_6). *Chemical Communications* **2016,** *52* (32), 5558-5560.
82. M.-R. Li; P. W. Stephens; M. Croft; Z. Deng; W. Li; C. Jin; M. Retuerto; J. P. Hodges; C. E. Frank; M. Wu; D. Walker; Greenblatt, M., $Mn_2(Fe_{0.8}Mo_{0.2})MoO_6$: A Double Perovskite with Multiple Transition Metal Sublattice Magnetic Effects. *Chem. Mater.* **2018,** *30*, 4508-4514.
111. Li, M. R.; Walker, D.; Retuerto, M.; Sarkar, T.; Hadermann, J.; Stephens, P. W.; Croft, M.; Ignatov, A.; Grams, C. P.; Hemberger, J.; Nowik, I.; Halasyamani, P. S.; Tran, T. T.; Mukherjee, S.; Dasgupta, T. S.; Greenblatt, M., Polar and magnetic Mn_2FeMO_6 (M=Nb, Ta) with $LiNbO_3$-type structure: high-pressure synthesis. *Angew. Chem. Int. Ed. Engl.* **2013,** *52* (32), 8406-10.
112. Li, M.-R.; McCabe, E. E.; Stephens, P. W.; Croft, M.; Collins, L.; Kalinin, S. V.; Deng, Z.; Retuerto, M.; Sen Gupta, A.; Padmanabhan, H.; Gopalan, V.; Grams, C. P.; Hemberger, J.; Orlandi, F.; Manuel, P.; Li, W.-M.; Jin, C.-Q.; Walker, D.; Greenblatt, M., Magnetostriction-polarization coupling in multiferroic Mn_2MnWO_6. *Nature Communications* **2017,** *8* (1), 2037.
117. Li, M. R.; Retuerto, M.; Walker, D.; Sarkar, T.; Stephens, P. W.; Mukherjee, S.; Dasgupta, T. S.; Hodges, J. P.; Croft, M.; Grams, C. P.; Hemberger, J.; Sanchez-Benitez, J.; Huq, A.; Saouma, F. O.; Jang, J. I.; Greenblatt, M., Magnetic-Structure-Stabilized Polarization in an Above-Room-Temperature Ferrimagnet. *Angewandte Chemie-International Edition* **2014,** *53* (40), 10774-10778.
143. Coelho, A., TOPAS Academic: General Profile and Structure Analysis Software for Powder Diffraction Data,(2012) Bruker AXS. *Karlsruhe, Germany*.

144. Toby, B. H.; Von Dreele, R. B., GSAS-II: the genesis of a modern open-source all purpose crystallography software package. *Journal of Applied Crystallography* **2013,** *46* (2), 544-549.
147. *APEX3 version 2015.9-0; Bruker AXS: Madison, WI, 2015.*
148. *SAINT*, version 8.34A; Bruker AXS: Madison, WI, 2013.
149. Sheldrick, G. M., *SHELXT-2014/5*, University of Göttingen: Göttingen, Germany, 2014.
150. Sheldrick, G. M., SHELXL-2014/7. *Acta Crystallographica* **2015,** (C71), 3-8.
155. Campbell, B. J.; Stokes, H. T.; Tanner, D. E.; Hatch, D. M., ISODISTORT. *J. Appl. Cryst.* **2006,** *39*, 607-614.
168. Monesi, C.; Meneghini, C.; Bardelli, F.; Benfatto, M.; Mobilio, S.; Manju, U.; Sarma, D. D., Quantitative structural refinement of MnK edge XANES in $LaMnO_3$ and $CaMnO_3$ perovskites. *Nuclear Instruments and Methods in Physics Research Section B: Beam Interactions with Materials and Atoms* **2006,** *246* (1), 158-164.
170. Retuerto, M.; Jiménez-Villacorta, F.; Martínez-Lope, M. J.; Huttel, Y.; Roman, E.; Fernández-Díaz, M. T.; Alonso, J. A., Study of the valence state and electronic structure in Sr_2FeMO_6 (M = W, Mo, Re and Sb) double perovskites. *Phys. Chem. Chem. Phys.* **2010,** *12* (41), 13616-13625.
179. Khan, H. N.; Hounshell, D. A.; Fuchs, E. R. H., Science and research policy at the end of Moore's law. *Nat. Electron.* **2018,** *1* (1), 14-21.
180. Theis, T. N.; Wong, H.-S. P., The End of Moore's Law: A New Beginning for Information Technology. *Comput. Sci. Eng.* **2017,** *19* (2), 41-50.
181. Baur, W. H.; Joswig, W.; Pieper, G.; Kassner, D., $CoReO_4$, a new rutile-type derivative with ordering of two cations. *J. Solid State Chem.* **1992,** *99* (1), 207-211.
182. Paul, A. K.; Jansen, M.; Yan, B.; Felser, C.; Reehuis, M.; Abdala, P. M., Synthesis, Crystal Structure, and Physical Properties of Sr_2FeOsO_6. *Inorg. Chem.* **2013,** *52* (11), 6713-6719.
183. Park, J. S.; Han, B. J.; Kim, C. S.; Lee, B. W., Room temperature magnetoresistance in Ba_2FeMoO_6. *J. Magn. Magn. Mater.* **2001,** *226-230*, 741-742.
184. Kobayashi, K. I.; Kimura, T.; Tomioka, Y.; Sawada, H.; Terakura, K.; Tokura, Y., Intergrain Tunneling Magnetoresistance in Polycrystals of the Ordered Double Perovskite Sr_2FeReO_6. *Phys. Rev. B* **1999,** *59* (17), 11159-11162.
185. Sarma, D. D.; Mahadevan, P.; Saha-Dasgupta, T.; Ray, S.; Kumar, A., Electronic Structure of Sr_2FeMoO_6. *Phys. Rev. Lett.* **2000,** *85* (12), 2549-2552.
186. Lofland, S. E.; Scabarozi, T.; Moritomo, Y.; Xu, S., Magnetism of the double perovskite Sr_2FeMoO_6. *J. Magn. Magn. Mater.* **2003,** *260* (1), 181-183.
187. Musa Saad H.-E, M.; Rammeh, N., Crystal, magnetic and electronic structures of 3d–5d ordered double perovskite Ba_2CoReO_6. *Solid State Communications* **2016,** *248*, 129-133.
188. Retuerto, M.; Li, M.-R.; Stephens, P. W.; Sánchez-Benítez, J.; Deng, X.; Kotliar, G.; Croft, M. C.; Ignatov, A.; Walker, D.; Greenblatt, M., Half-Metallicity in Pb_2CoReO_6 Double Perovskite and High Magnetic Ordering Temperature in Pb_2CrReO_6 Perovskite. *Chem. Mater.* **2015,** *27* (12), 4450-4458.
189. Retuerto, M.; Martínez-Lope, M. J.; García-Hernández, M.; Fernández-Díaz, M. T.; Alonso, J. A., Crystal and Magnetic Structure of Sr_2MReO_6 (M = Ni, Co, Zn) Double Perovskites: A Neutron Diffraction Study. *Eur. J. Inorg. Chem.* **2008,** *2008* (4), 588-595.
190. Lufaso, M. W.; Woodward, P. M., Prediction of the crystal structures of perovskites using the software program SPuDS. *Acta Crystallogr. B* **2001,** *57* (6), 725-738.
191. Retuerto, M.; Skiadopoulou, S.; Borodavka, F.; Kadlec, C.; Kadlec, F.; Prokleška, J.; Deng, Z.; Alonso, J. A.; Fernandez-Diaz, M. T.; Saouma, F. O.; Jang, J. I.; Legut, D.; Kamba, S.; Greenblatt, M., Structural and spectroscopic properties of the polar antiferromagnet Ni_2MnTeO_6. *Phys. Rev. B* **2018,** *97* (14), 144418.

192. Bazuev, G. V.; Golovkin, B. G.; Lukin, N. V.; Kadyrova, N. I.; Zainulin, Y. G., High Pressure Synthesis and Polymorphism of Complex Oxides Mn_2BSbO_6(B= Fe, V, Cr, Ga, Al). *Journal of Solid State Chemistry* **1996,** *124* (2), 333-337.
193. Fukunaga, O.; Fujita, T., The relation between ionic radii and cell volumes in the perovskite compounds. *Journal of Solid State Chemistry* **1973,** *8* (4), 331-338.
194. Man-Rong Li; Jason P. Hodges; Maria Retuerto; Zheng Deng; Peter W. Stephens; Mark C. Croft; Xiaoyu Deng; Gabriel Kotliar; Javier Sánchez-Benítez; David Walker; Greenblatt, M., Mn_2MnReO_6: Synthesis and Magnetic Structure Determination of a New Transition-Metal-Only Double Perovskite Canted Antiferromagnet. *Chemistry of Materials* **2016,** *28* (9), 3148-3158.
195. Scimeca, M.; Bischetti, S.; Lamsira, H. K.; Bonfiglio, R.; Bonanno, E., Energy Dispersive X-ray (EDX) microanalysis: A powerful tool in biomedical research and diagnosis. *European journal of histochemistry : EJH* **2018,** *62* (1), 2841-2841.
196. Alsmadi, B. M.; Fox, P., Semi-quantitative analysis of changes in soil coatings by scanning electron microscope and energy dispersive X-ray mapping. *Colloids and Surfaces A: Physicochemical and Engineering Aspects* **2001,** *194* (1), 249-261.
197. Croft, M.; Sills, D.; Greenblatt, M.; Lee, C.; Cheong, S. W.; Ramanujachary, K. V.; Tran, D., Systematic Mn d-configuration change in the $La_{1-x}Ca_xMnO_3$ system: A Mn K-edge XAS study. *Physical Review B* **1997,** *55* (14), 8726-8732.
198. Huang, Y.-H.; Liang, G.; Croft, M.; Lehtimäki, M.; Karppinen, M.; Goodenough, J. B., Double-Perovskite Anode Materials Sr_2MMoO_6 (M = Co, Ni) for Solid Oxide Fuel Cells. *Chemistry of Materials* **2009,** *21* (11), 2319-2326.
199. Deng, Z.; Retuerto, M.; Liu, S.; Croft, M.; Stephens, P. W.; Calder, S.; Li, W.; Chen, B.; Jin, C.; Hu, Z.; Li, M.-R.; Lin, H.-J.; Chan, T.-S.; Chen, C.-T.; Kim, S. W.; Greenblatt, M., Dynamic Ferrimagnetic Order in a Highly Distorted Double Perovskite Y_2CoRuO_6. *Chemistry of Materials* **2018,** *30* (20), 7047-7054.
200. Xiangfan Xu; Lizhen Jiang; Jingqin Shen; Zhangjian Chen; Xu, Z., Relationship between spin state of Co ions and thermopower in $La_{1-x}Sr_xCoO_3$ ($0 << x << 0.5$). *Physics Letters A* **2006,** *351*, 431-434.
201. Filippetti, A., and Nicola A. Hill.,, "Coexistence of magnetism and ferroelectricity in perovskites.". *Physical Review B* **2002,** *65* (19), 195120.
202. Sleight, A. W.; Weiher, J. F., Magnetic and Electrical Properties of Ba_2MReO_6 Perovskites. *J. Phys. Chem. Solids.* **1972,** *33*, 679-687.
203. Efros, A. L.; Shklovskii, B. I., Coulomb gap and low temperature conductivity of disordered systems. *Journal of Physics C: Solid State Physics* **1975,** *8* (4), L49.
204. Zhang, Z.; Howard, C. J.; Kennedy, B. J.; Knight, K. S.; Zhou, Q., Crystal structure of $Ln_{1/3}NbO_3$ (Ln= Nd, Pr) and phase transition in $Nd_{1/3}NbO_3$. *Journal of Solid State Chemistry* **2007,** *180* (6), 1846-1851.
205. Sears, V. F., Neutron scattering lengths and cross sectioirn. *Neutron news* **1992,** *3* (3), 29-37.
206. Tuxworth, A. J.; McCabe, E. E.; Free, D. G.; Clark, S. J.; Evans, J. S., Structural characterization and physical properties of the new transition metal oxyselenide $La_2O_2ZnSe_2$. *Inorganic chemistry* **2013,** *52* (4), 2078-2085.
207. McCabe, E.; Stock, C.; Rodriguez, E.; Wills, A.; Taylor, J.; Evans, J., Weak spin interactions in Mott insulating $La_2O_2Fe_2OSe_2$. *Physical Review B* **2014,** *89* (10), 100402.
208. Arevalo-Lopez, A. M.; Attfield, J. P., Competing antiferromagnetic orders in the double perovskite Mn2MnReO6 (Mn3ReO6). *Chem. Commun.* **2016,** *52*, 5558.

Chapter 4: $LaMn_3Rh_4O_{12}$ - An Antiferromagnetic Quadruple Perovskite Synthesized at High Pressure

4.1 Introduction

Transition-metal (TM) perovskite oxides are a flexible class of materials in terms of structure, physical properties, and potential technological applications.[79, 112, 114] Most of this flexibility can be attributed to the structure's high tolerance for distortions caused by substitutions and vacancy formations.[32] The simplest perovskite form is ABO_3, in which a large A-cation is surrounded by a corner sharing array of smaller, octahedrally coordinated B-cations. However, when a Jahn-Teller active cation, such as Co^{2+} (low spin (LS) d^7), Cu^{2+}, and Mn^{3+} (high spin (HS) d^4) ions, or a square-planar d^8-ion like Pd^{2+} is substituted for 75% of the *A*-site cations, an *A*-site ordered quadruple perovskite ($AA'_3B_4O_{12}$) may form.[84, 87, 209-210] Here, the *A*-sites are generally occupied by moderately sized (usually between $Cu^{2+}$and Sr^{2+} as in $CuCu_3V_4O_{12}$ and $SrCu_3Fe_4O_{12}$)[211] mono- to tri-valent cations such as alkali, alkali earth, or rare earth metals, or Pb^{2+} and Bi^{3+}. As in many simple perovskites, the *B*-site favors TMs. [85-87]

Chemical and physical properties of quadruple perovskites are dominated by interactions within and/or between the *A*/*A*′- and *B*-sublattices, which arise in addition to the usual *B*-*B* interactions, and are also subtly affected by cationic electron configuration.[212] For given *A*- and *B*-site cations, small differences in electron configuration of the square-planar *A*′ and/or octahedral *B*-cations can cause dramatic modification of the physical properties. For example, the series $AMn_3V_4O_{12}$ (A = La^{3+}, 1.36 Å; Nd^{3+},1.27 Å; Gd^{3+}, >1.107 Å; Y^{3+}, >1.075 Å; Lu^{3+} > 1.032 Å) were

synthesized at high pressure and temperature, and the primary difference between them is the size or electron density of the A cation (information on the ionic radii of 12-coordinated Gd, Y, Lu were not available and the 9-coordinated radius is reported here for each) .[213-214] The size difference in A-cations shows a striking crystallographic result: where $AMn_3V_4O_{12}$ (A = the larger La, Nd, Gd) all form A-site ordered quadruple perovskites in the $Im\bar{3}$ space group, whereas the inclusion of smaller A cations cause $AMn_3V_4O_{12}$ (A = Y, Lu) to form an A-cation disordered *Pnma* perovskite, which can be more accurately described as $(A^{3+}_{1/4}Mn^{2+}_{3/4})V^{3.75+}O_3$. Even amongst the true quadruple perovskites, A = La, Nd, Gd, differences in A-cation matter. While A = Nd, Gd are both paramagnetic with no clear transition to a long range ordered state, A = La is antiferromagnetic with a transition at 45 K. The lack of clear transitions to an antiferromagnetic state for A = Nd, Gd were attributed to the large magnetic contributions A-site Nd^{3+} and Gd^{3+} moments (La^{3+} does not contribute to magnetism).

Due to the subtle interplay of A/A' and B-site lattices, substitutions on the B-site can also greatly affect properties, even when the overall structure remains largely the same. $LaMn_3Ti_4O_{12}$ and $LaMn_3Cr_4O_{12}$ both crytallize as $Im\bar{3}$ cubic quadruple perovskites.[212] $LaMn^{1.67+}_3Ti^{4+}_4O_{12}$ demonstrates a transition at 5 K to a spin glass-like state which is attributed to mixed valence $Mn^{+/2+}$ on the A'-site, as the inclusion of unusually low-valence Mn^{+} leads to effective hold doping and thus localization of spins. In contrast, $LaMn^{2+}_3Cr^{3+}_4O_{12}$ has two antiferromagnetic transitions. The first occurs at 150 K, when the Cr^{3+} spins align, and the second at 50 K when the Mn^{2+} spins align.

Recently, intense study has focused on quadruple perovskites with 4*d* or 5*d* TMs at the *B*-site with exotic physical properties.[97, 210, 215-233] As orbitals become more

delocalized, Coulomb interactions become weaker and crystal field effects become stronger, meaning that *4d* and *5d* TMs are more sensitive to small lattice distortions than *3d* TMs.[215] Additionally, spin orbit interactions come into play with heavier TMs, and as the energies of these effects approach on-site Coulomb interaction energies, unusual electronic structures begin to emerge. For example, Yamada *et al.* reported $CaCu_3Rh_4O_{12}$ in 2014.[97] While other quadruple perovskites with B-site 4d transition metals have been reported,[226, 234] $CaCu_3Rh_4O_{12}$ is the first quadruple perovskite to integrate rhodium on the B-site to our knowledge. The large crystal field splitting energy of rhodium, typical of octahedrally coordinated 4d TMs, forces rhodium to adopt a low spin configuration, and DFT calculations suggest that the unoccupied Rh e_g orbitals reside at energy levels above the Fermi level, while the t_{2g} orbitals lie at levels approximate to the Fermi energy, comparable in to the partially occupied Cu $d_{x^2-y^2}$ orbital. This means that Cu and Rh stabilize one another's partially filled orbitals, resulting in the unusual intermediate valence states of $Cu^{2.8+}$ ($d^{8.2}$ or $d^9\underline{L}^{0.8}$) and $Rh^{3.4+}$ ($t_{2g}^{5.6}e_g^0$).[97] While an unusually high valence of Cu, Cu^{3+}, has been seen in other quadruple perovskites, such as $A^{3+}Cu_3Fe_4O_{12}$,[95] in those cases Cu^{3+} is stabilized by ligand-hole transfer. Although *B*-site 4*d*TM quadruple perovskites have been investigated, most work has focused on $ACu_3B_4O_{12}$. To the best of our knowledge, no $AMn_3B_4O_{12}$ (*B* = 4*d*, 5*d* TMs) have been reported to date, meriting exploration due to the potentially intriguing unique properties that originate from the electron configuration variation between Mn and Cu.

In this work, we have synthesized the first *A*′-Mn quadruple perovskite with 4*d*-Rh at the *B* site, $LaMn_3Rh_4O_{12}$ (LMRO), at high-pressure and high-temperature (HPHT). The crystal structure and formal oxidation states of cations were investigated, the latter by both bond valence sums (BVS) and X-ray near-edge

absorption spectroscopy (XANES). The magnetic, magnetotransport, and dielectric properties are also reported herein.

4.2 Results and Discussion

4.2.1 Details of Synthetic Conditions

Synthesis at high pressure can often be prohibitively difficult and expensive, as repeated stress of pressurization and depressurization strains the anvil and can lead to breakage of the tungsten carbide cubes. As such, it can be difficult for an experimentalist to balance the need to find the best synthetic conditions for any given compound with the need to avoid falling into a sunk-cost fallacy. For this reason, detailed reports on the evolution of high pressure syntheses are thin on the ground, and could be instructive to discuss herein. Additionally, synthesis of $LaMn_3Rh_4O_{12}$ is unique in that the heating step lasts for three days; as many high pressure phases are metastable, most high pressure synthesis of solid state compounds feature heating steps of 15-60 minutes.[52, 78, 83, 86, 111-112, 116, 118, 192, 215, 235] The extreme divergence of this method from the norm is worth a brief discussion of the history of $LaMn_3Rh_4O_{12}$.

Initial investigations into $LaMn_3Rh_4O_{12}$ were focused on a more conventional high pressure snythetic approach. Stoichimetric amounts of La_2O_3 (dried at 900° C overnight before use), Mn_2O_3 (dried overnight at 700° C), and Rh_2O_3 (dried overnight at 800° C in flowing O_2) were thoroughly mixed in an agate mortar before being wraped in a Pt foil capsule and loaded into a Walker-type multianvil press. The sample was slowly pressurized overnight to 6 GPa, heated at 1400° C 1 hour before being quenched by turning off power to the heater and depressurized overnight. As can be seen in **Figure 4.1**(inset), the initial trials were not immediately promising.

Intial optical analysis showed a three phase, non-magnetic assemblage that included what is likely a rhodium oxide (black), a metallic phase, and two separate grey phases. Additionally, there appears to have been some evolution of gas at 6 GPa, which persists despite thoroughly drying the precursors and changing reaction conditions to increase pressure (7GPa) and decrease reaction temperature. At high pressures, gas evolution can lead to so-called blow outs and system failures and merited further investigations, if nothing else to prevent them from occuring again. PXD analysis of this trial performed at Rutgers indicated a majority cubic phase was present despite the large number of impurities visible in optical analysis (**Figure 4.1**). Microprobe analysis was employed to identify the phases.

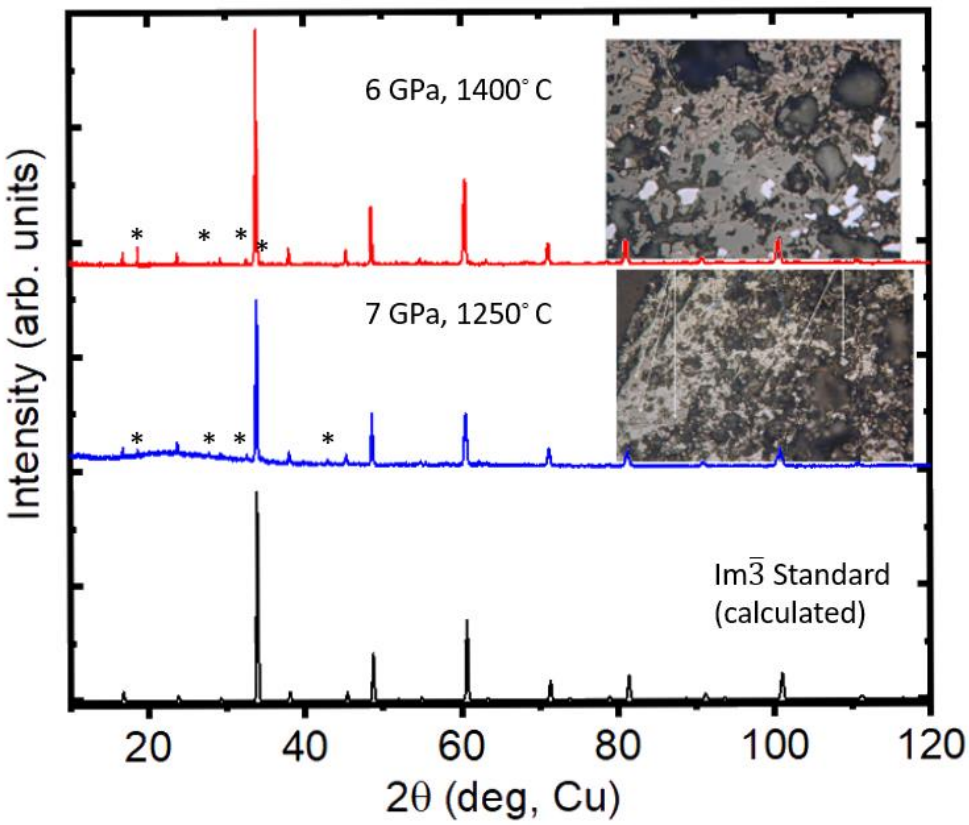

Figure 4.1 Initial PXD data for $LaMn_3Rh_4O_{12}$ synthesized at 6 GPa, 1400˚ C (top, red) and 7 GPa, 1250˚ C (middle, blue) compared to a calculated *Im*$\bar{3}$ standard (bottom). Some potential impurities are difficult to see, and so the smallest ones have been marked with an asterisk. Doubly polarized insident illumination microscopy of a highly magnified piece of of each sample is inset with the respective PXD data. Increasing synthesis pressure appears to improve the purity of the optical sample, but apparent improvement of the PXD experiments is more subtle.

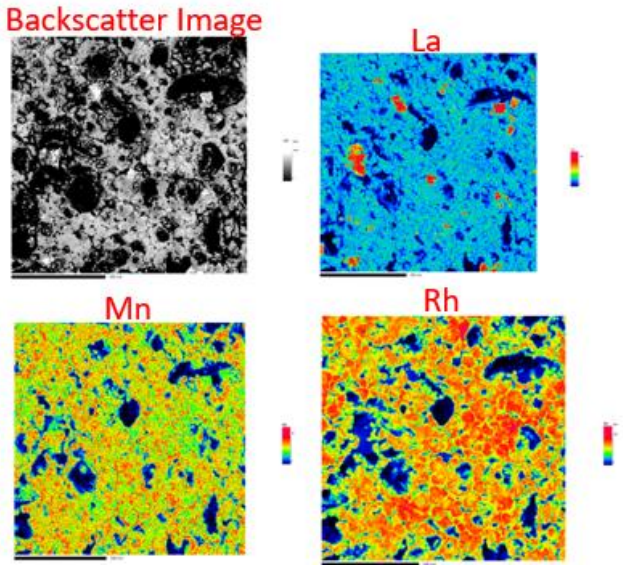

Figure 4.2 Scanning electron microscopy (top left) of the $LaMn_3Rh_4O_{12}$ sample made at 6 GPa, 1400° C, collected at Rutgers University. Electron dispersive X-ray heat maps of La (top right) Mn(bottom left) and Rh (bottom right) show the relative concentration of each element in the SEM image. Heat maps are relative to each element individually, and not relative as a whole.

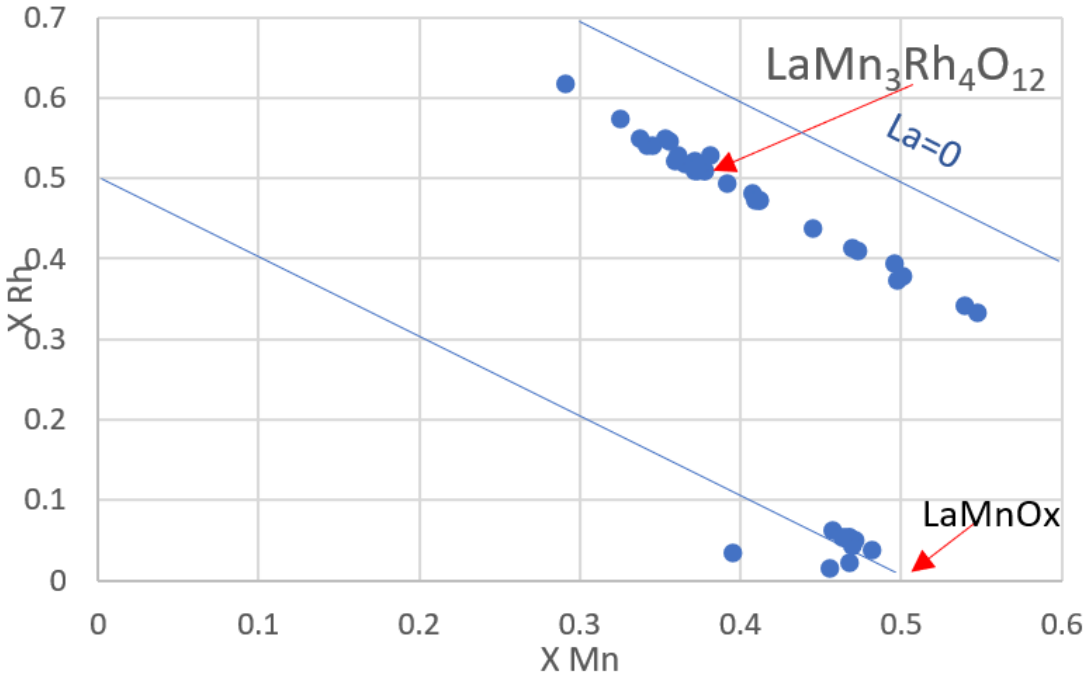

Figure 4.3 A two-dimensional representation microprobe experiments on the 6 GPa, 1400° C preparation of $LaMn_3Rh_4O_{12}$. The relative atomic ratios of each cation were summed to 100% and then plotted as a function of % Rh (y axis) vs % Mn (x axis). The region where an ideal $LaMn_3Rh_4O_{12}$ would be expected (Rh = 50 % of all cations, Mn = 37.5%) is highlighted via a red arrow. A region where magnetic impurity LaMnO3 is seen (Labelled as LaMnOx here as this calculation does not account for oxygen) on the bottom right, indicating the probably presence of an impurity with long range magnetic properties.

Figure 4.2 shows the SEM-EDX results for $LaMn_3Rh_4O_{12}$ as collected at Rutgers University. A fragment of as-made $LaMn_3Rh_4O_{12}$ was embedded in epoxy resin and ground. The sample was then coated in a thin (3-10 nm) coating of carbon. Initial measurements were performed at Rutgers University in both EDX-SEM and electron microprobe point select modes. The JEOL JXA Superprobe collects data on each element individually and projects concentration information as heat maps that are relative to the element itself, and not affected by the concentrations of the other elements. In these images one can see that rhodium is generally evenly distributed throughout the sample, whereas there are clear hot spots of lanthanum. These regions likely correspond to some LaMnOx impurity as the La hot spot would indicate a higher relative percent there versus the whole (50% La:Mn in LaMnOx vs 12.5% La:Mn+Rh).

After initial EDX heat maps were obtained, the microprobe was switched to point-select mode to collect more precise[236] relative concentration data, and these results are plotted in **Figure 4.3**. The relative atomic percentage of each cation were compared to one another and plotted in a two dimensional figure that is very similar to a conventional phase diagram where the y-axis corresponds to %Rh, and the x-axis corresponds to %Mn (oxygen is not accounted for in this figure because the concentrations of lighter elements can be difficult to accurately measure).[236] One can see here at these early stages that there is a wider distribution of relative atomic ratios than desirable, but a concentration of points near the target phase. This, combined with the promising PXD results, was deemed enough motive to continue.

Additional synthetic attempts focused on reducing temperature and increasing pressure, as lower temperatures seemed empirically to reduce the amount of “gas” bubbles observed in the optical analyses. Increasing pressure to 8 GPa while

decreasing the temperature to 1100 C for 1 hour resulted in a multiphase product with no evidence of gas evolution despite the same preparation of precursors.

In **Figure 4.4**, one can see that the higher pressure, lower temperature trial resulted in a grey main phase with blue-grey corona structures. In minerology, if an inclusion in a main phase is reacting with the main phase, a corona, or "reaction rim" may be visualized between them.[237] This distinct texture indicates that, in simple terms, a reaction may have been quenched before completion. Therefore, the timescale of the reaction was increased from 1 hour to allow adequate time for reaction completion. Corona structures were no longer visible after 3 days of reaction at 8 GPa and 1150 C (**Figure 4.6**(b) inset), and so microprobe experiments were repeated at the American Museum of Natural History on a Cameca SX5-Tactis in line scan and point select mode with column conditions of 15 Kev, 10 nA with an identical sample preparation as above. While EDX mapping is not available at the American Museum of Natural History, overnight collection of data points on a "Linescan" mode (where a line is chosen on the sample and a number of points are collected on that line automatically) is possible, leading to a larger statistical number of microprobe data points to analyze.

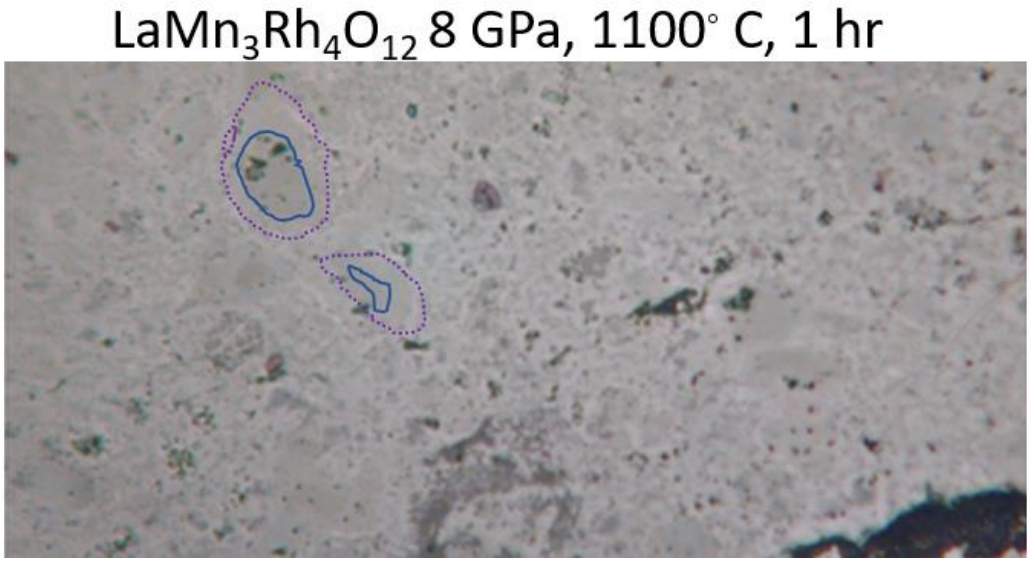

Figure 4.4 Doubly polarized insident illumination microscopy of a highly magnified piece of $LaMn_3Rh_4O_{12}$ synthesized at 8 GPa, 1100° C for 1 hour. The main phase is grey, but darker blue-grey inclusions are easily visualized, surounded by lighter corona structures. Two of these inclusions have been indicated by blue solid lines, while their coronae are indicated by purple dashed lines.

As can be seen in **Figure 4.5**, the three day synthesis resulted in a majority distribution of points near the desired ratio for a nominal average formula for $LaMn_3Rh_4O_{12}$. Outliers, which have been included here for completeness, likely lie on grain boundaries or places of physical irregularity and can be excluded if PXD refinements indicate purity. There is no trace of the LaMnOx impurity from earlier trials (the possible existence of which in small quantities was the motivation for choosing “line scan” over the more precise, but time consuming, “point select” mode. It was deemed important to sacrifice a small amount of statistical reliability in this trial to maximize chances of uncovering known impurities).

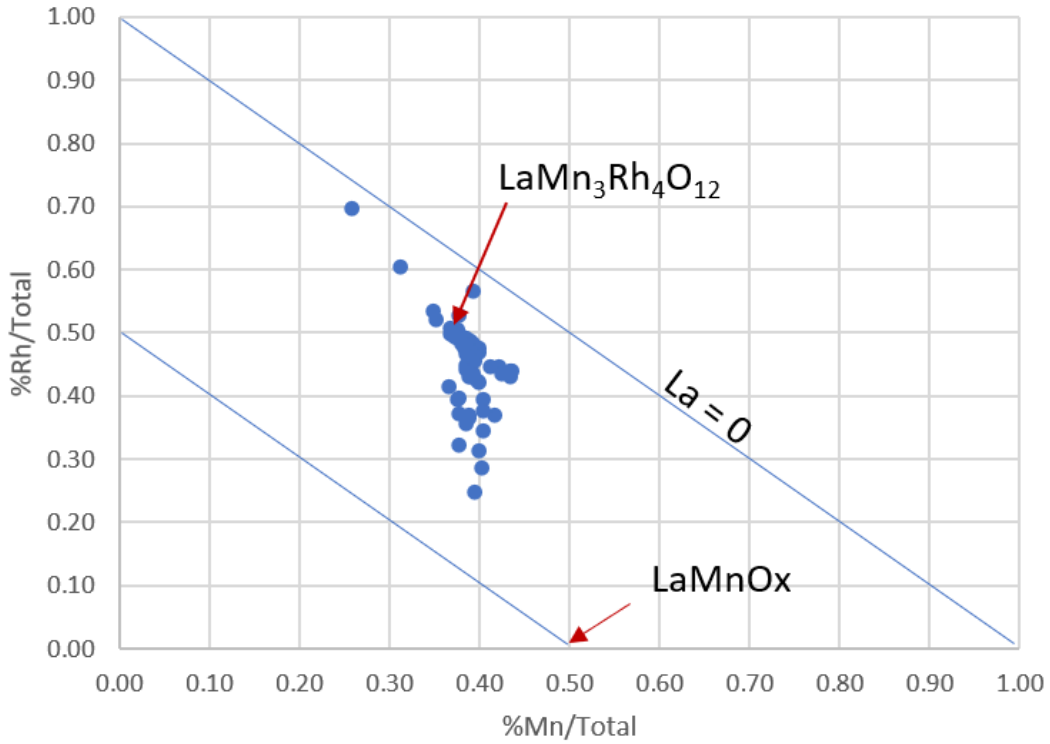

Figure 4.5 A two-dimensional representation of the microprobe experiments of the 8 GPa, 1150° C, 69.5 hour preparation of $LaMn_3Rh_4O_{12}$. The relative atomic ratios of each cation were summed to 100% and then plotted as a function of % Rh (y axis) vs % Mn (x axis). The region where an ideal $LaMn_3Rh_4O_{12}$ would be expected (Rh = 50 % of all cations, Mn = 37.5%) is highlighted via a red arrow. A region where magnetic impurity $LaMnO_3$ would be expected (Labelled as LaMnOx here as this calculation does not account for oxygen) is on the bottom right, indicating that this impurity was not found in this analysis.

4.2.2 Crystal Structure

Figure 4.6(b) (inset) shows the final preparation of $La_2Mn_3Rh_4O_{12}$ with no secondary phase readily identifiable, and approximately 1% of some dark impurity, which was found by PXD refinements to be about 0.75% RhO_2. Like many other A-site ordered quadruple perovskites,[213, 226, 234, 238] $LaMn_3Rh_4O_{12}$ adopts a cubic structure in the space group $Im\bar{3}$ (a = 7.4997(1) Å). Final PXD results (R_p/R_{wp} = 4.55/4.31%, **Figure 4.6**(b) were collected and refined by collaborators at Sun Yat-Sen university, but findings were in line with earlier refinements that were performed at

Rutgers University ($Im\bar{3}$, a = 7.5031(0) Å**, Figure 4.6**(a)), albeit on SPXD experiments collected on samples from the earlier synthesis procedures with contamination such that acceptable total fit could not be achieved. In both refinements, La, Mn, Rh, and O atoms are placed at the 2*a*, 6*b*, 8*c*, and 24*g* positions (**Figure 4.6**(c) and (d)), respectively. The valence states of cations from bond valence state calculations give indicate that the *A*′-site Mn is 2.67+ and *B*-site Rh is 3.44+, consistent with Mn^{3+} and Rh^{3+} determined by XANES (vide infra).

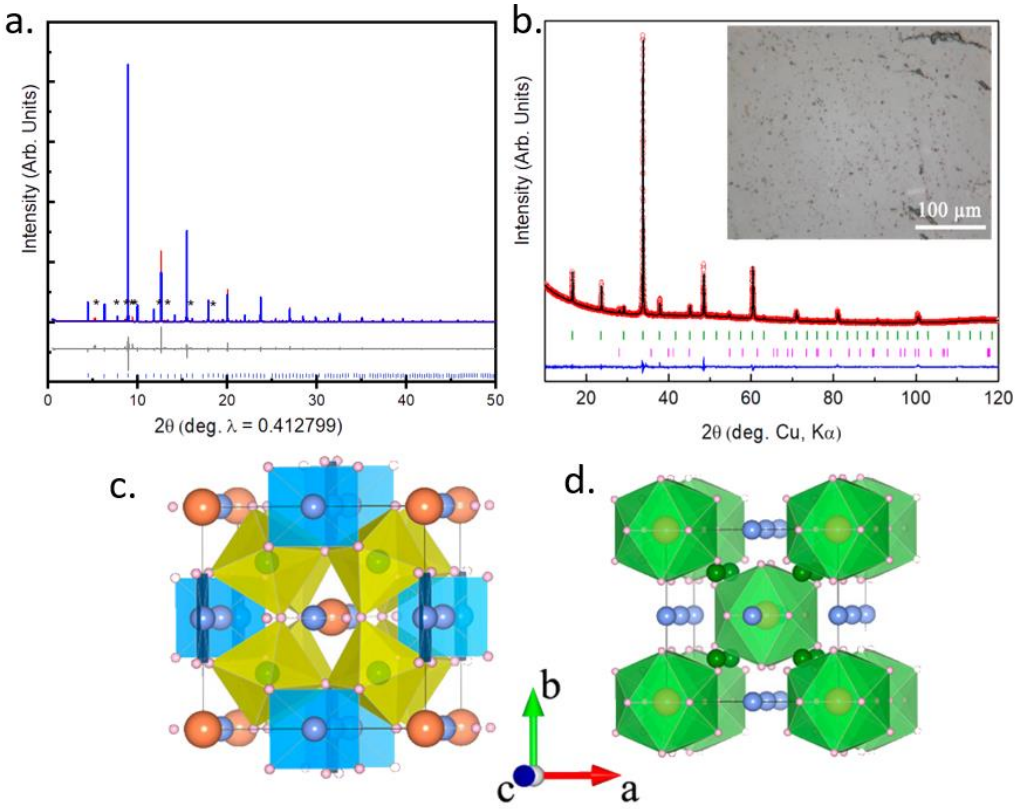

Figure 4.6 Rietveld refinements of the synchrotron powder diffraction pattern for $LaMn_3Rh_4O_{12}$ at room temperature. Blue ticks represent brag positions of the main phase. The observed (red), calculated (blue) and difference (grey) patterns show a large number of impurities which appear small due to the relatively strong intensities of the peaks in the highly symmetric $Im\bar{3}$ space group and have been marked with asterisks. (**b)** Shows results of PXD refinements on pure LMRO carried out at RT, showing the observed (red), calculated (black), and difference (blue) profiles. Green and pink ticks represent the Bragg reflection positions of LMRO and RhO_2, respectively. Inset shows an optical image from the polished surface of as-made LMRO. Refined crystal structure of LMRO with superimposed (**c**) MnO_4 planes and RhO_6 octahedral units, and (**d**) with LaO_{12}icosahedral units. La atoms: deep orange spheres; O atoms: small light pink spheres; MnO_4 planar: blue; RhO_6 octahedra: yellow; LaO_{12}cuboctahedra: green.

4.2.3 XANES

To accurately determine the valence states of Mn and Rh in $LaMn_3Rh_4O_{12}$, XANES measurements were collected at room temperature on the beam line X-19A at Brookhaven NSLS in both transmission and fluorescence modes with simultaneous standards by Mark Croft. Data was collected at the Rh-$L_{2,3}$ and Mn-K edges, and data analysis was performed primarily by Dr. Croft and used as instruction in the technique. As the shape and chemical shift of these edges are affected by both metal valence and coordination environment, it is important to choose standards which have in the same coordination environment as the target analyte. Spectra of 4d transition metals are dominated by intense white line (WL) features which are caused by the excitation of an inner 2p electron to an unfilled d orbital, and can thus be used to *d*-hole/valence states.[239-240] In **Figure 4.7**(a) the Rh L_3(L_2)-edges of the LMRO are compared to the standard spectra for Rh^0-metal, $Rh^{3+}{}_2O_3$, and $Rh^{4+}O_2$. The rise and chemical shift for LMRO is almost exactly that of the Rh_2O_3 standard for the L_3 and L_2 edges. Due to the sharpness and symmetry of the peak itself, it almost appears as though LMRO is a better Rh^{3+} standard than Rh_2O_3 itself. In order to evaluate this potential, in **Figure 4.7**(b) the chemical shift of the standard peak has been plotted versus the formal valence for the Rh standards and LMRO. It is clear the chemical shift of Rh^{3+} in LMRO is more consistent with the expected increase in peak shift vs valence than the Rh_2O_3 standard.

For first row transition metals, typically the K-edges, dominated by transitions from 1s to 4p orbitals, are the most distinct and typically used to determine formal valence. The Mn K-edge of LMRO was measured and compared to known standards Mn^{2+}-Sr_2ReMnO_6, Mn^{3+}-$LaMnO_3$, Mn^{4+}-$CaMnO_3$, where Mn is in octahedral coordination. To fully clarify the this spectrum, LMRO was also compared to

quadruple perovskites $CaCu_3Mn^{4+}{}_4O_{12}$[241] and $CaMn_7O_{12}$,[241] which were previously studied by the Greenblatt group. LMRO shows a complicated and unresolved splitting of features when broaden the main edge rise region. This splitting of features is consistent with such effects seen in the previously studied quadruple perovskite and is highlighted by the A' feature indicated in the **Figure 4.7**(c). Subtracting the B-site $CaCu_3Mn_4O_{12}$ spectrum from (with an appropriate downward energy shift to account for *B*-site Mn-valence reduction to about +3.25 and with a site ratio weight factor) from the $CaMn_7O_{12}$ spectrum reproduces a prominent *A′* feature produces this prominent A' feature, and the shape and rise of this spectrum is in very good agreement with LMRO. These features of LMRO are consistent with a formal valence of Mn^{3+}, as expected from the certain La^{3+} and the above determined Rh^{3+} state.

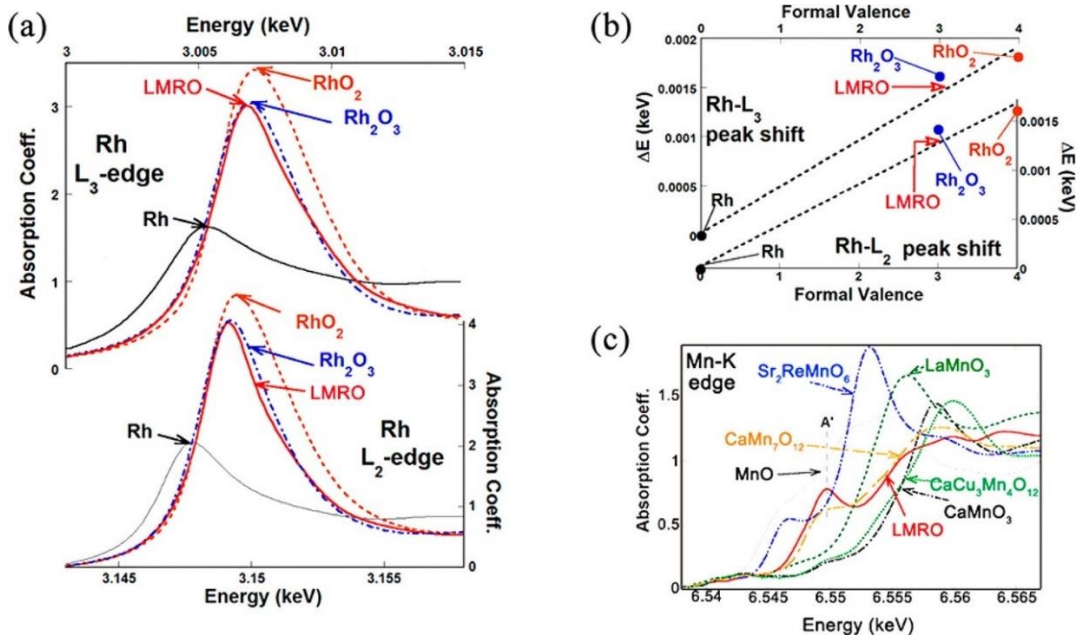

Figure 4.7 (**a**) Rh $L_3(L_2)$-edges for LMRO compared to the standard compound spectra for Ru^0: elemental Rh, Rh^{3+}: Rh_2O_3, and Rh^{4+}: RhO_2. (**b**) The energy shift of the $L_3(L_2)$ WL feature peaks (relative to the elemental-Rh peak), plotted as solid circles, versus the formal valence state of the material. The dashed lines are linear least-squares fit to the standard peak shift data. In both (**b**) top and bottom, a red arrow indicates the relative energy shift of the LMRO WL feature peak. (**c**) Mn K-edge spectrum along with Mn compounds with varying formal valences: $Mn^{2+}O$, $SrReMn^{2+}O_6$, $LaMn^{3+}O_3$, $CaMn^{4+}O_3$. Also included are the quadruple perovskite spectra for $CaCu_3Mn^{4+}{}_4O_{12}$ and $CaMn_7O_{12}$.

4.2.4 Magnetic Measurements

A physical property measurement system (PPMS, EvenCool II, Quantum Design) equipped with a vibrating sample magnetometer (VSM) was used to measure the magnetic hysteresis loops at different temperatures, and the magnetic susceptibility in zero-field-cooled (ZFC) and field-cooled (FC) modes between 5 and 380 K under an applied field of 0.1 T by collaborators at Sun Yat-Sen University. **Figure 4.8**(**a**) shows the magnetization vs temperature, which shows a single, sharp antiferromagnetic transition at T_N = 41 K. The FC and ZFC curves do not diverge from one another down to 5 K, unlike in spin glass materials like $LaMn_3Ti_4O_{12}$,[212] and there is no evidence of additional transitions or frustration effects. Plotting the inverse of the magnetic susceptibility, χ, reveals that linear Curie-Weiss behavior persists from 400 K to almost exactly T_N (**Figure 4.8**(**b**)). The extracted Weiss constant is -98.7 K, indicating that antiferromagnetic interactions dominate LMRO. The effective magnetic moment, μ_{eff} = 8.55 μ_B, is close to the spin only magnetic moment calculated for HS-Mn^{3+}, 8.49 μ_B. Only Mn^{3+} should be expected to contribute to the magnetic moment because the high crystal field splitting energy of rhodium should force it into a low spin arrangement ($t_{2g}^6 e_g^0$), as was seen in $CaCu_3Rh_4O_{12}$.[97] It can thus be reasonably assumed that the transition at 41 K can be attributed to a single antiferromagnetic lattice of A' Mn^{3+} cations as reported in other 4*d*/5*d* quadruple perovskite analogs.[91, 212, 242-243]

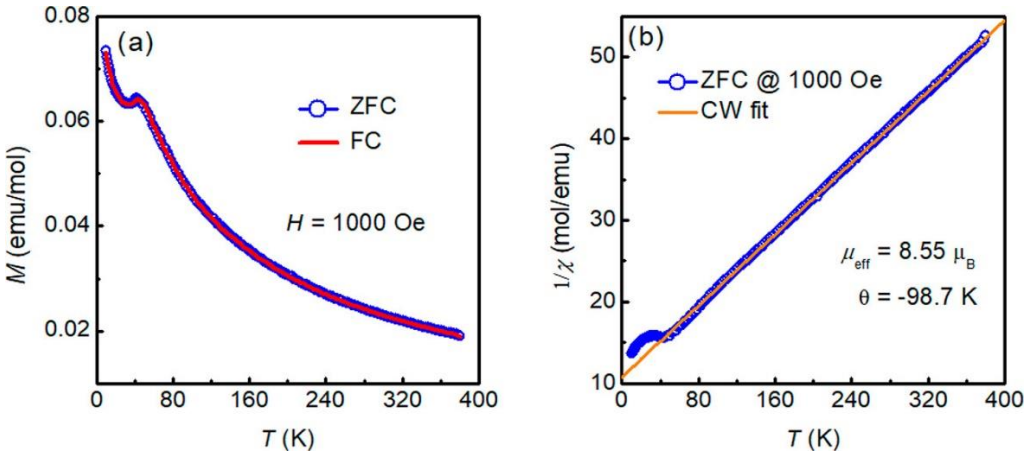

Figure 4.8 (**a**) Temperature dependence of magnetization of LMRO measured by applying external magnetic field of 0.1 T under zero-field-cooled (open circle) and field-cooled (solid line) conditions. (**b**) Curie–Weiss fitting of paramagnetic region of the 1/χ versus temperature plot.

4.2.5 Specific Heat

Specific heat measurements were performed on $LaMn_3Rh_4O_{12}$ between 2-60 K at magnetic fields of both 0 T and 1 T on a PPMS by collaborators at Sun Yat-Sen University. As can be seen in **Figure 4.9**, there is one sharp transition that corresponds to T_N and no divergence between the Cp plots as measured in different magnetic fields. The close correlation of the two measurements indicates that, indeed, LMRO is not a spin glass material, confirming the results of the magnetic measurements. The data below ~13 K were fit by collaborators using the following formula:

$$C_p = \gamma T + \beta T^3 \qquad (4.1)$$

where γ is the Sommerfeld coefficient, γT represents the electronic contribution, and βT^3 is the lattice contribution. The extracted γ values for both the 0 T and 1 T measurements are ~190 mJ/mol·K, which is quite large in comparison to previously reported semiconducting quadruple perovskites.[215,231]

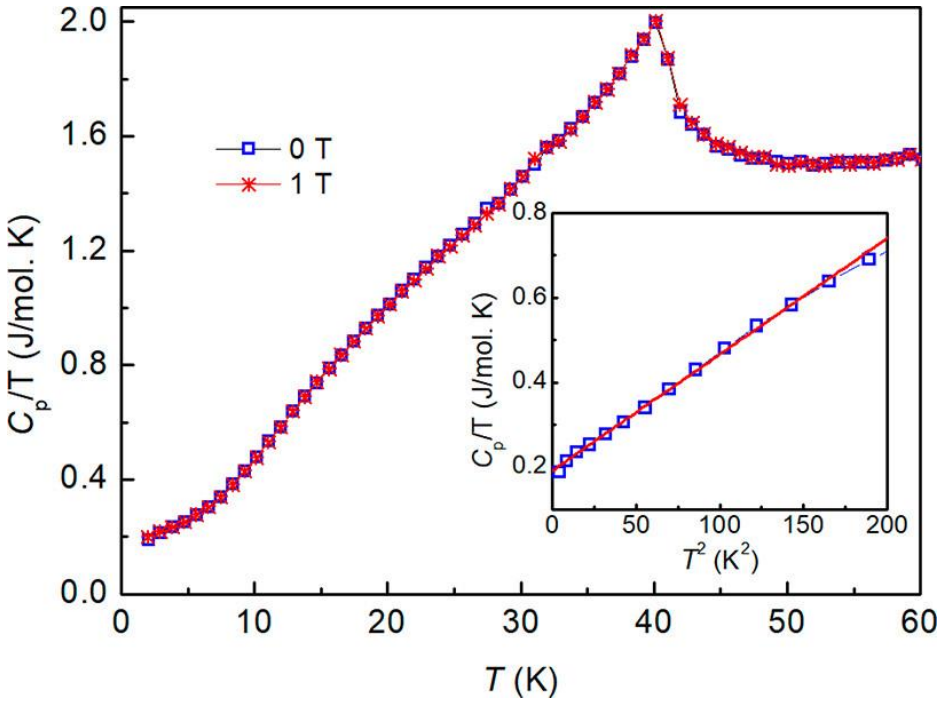

Figure 4.9 Specific heat of LMRO in temperature range of 2–60 K measured with H = 0 and 1 T, respectively. Inset shows the low-temperature C_p/T vs T^2 plot at zero magnetic field.

4.2.6 Magnetotransport

Figure 4.10 shows the temperature-dependent resistivity (ρ) measurements as collected under fields of 0, 1, 3, and 5 T, as measured using the four-probe method in the PPMS at Sun Yat-Sen University. It can be seen that the curves of the measurements taken at different fields do not diverge from one another, indicating that LMRO is not magnetoresitive. The RT resistivity of LMRO is ~1300 Ω·cm, comparable to that of the insulating $LaMn_3B_4O_{12}$ (B = Cr, Ti) with a 3d TM on the B site.[212]

As with other semiconductors, the temperature dependence of ρ, was found by trial-and-error fitting of the relation: $(1/T)^p$, with p = 1/4 giving the best fit, indicating that LMRO is a Mott variable-range hopping semiconductor with localized charge-carrier states.[244] This can be seen in **Figure 4.10** (inset) in comparison with p = 1,

which did not give a linear fit, and thus the relation between resistivity and temperature is:

$$\rho = \rho_0 * e^{-(T0/T)^{1/4}} \quad (4.2)$$

where T_0 is the characteristic temperature and ρ_0 is a coefficient related to the resistivity) . The extracted parameters T_0 and ρ_0 are 2.59×10^8 K and 7.56×10^{-11} Ω·cm, respectively, and are similar to other *A*-site-ordered perovskites.[245]

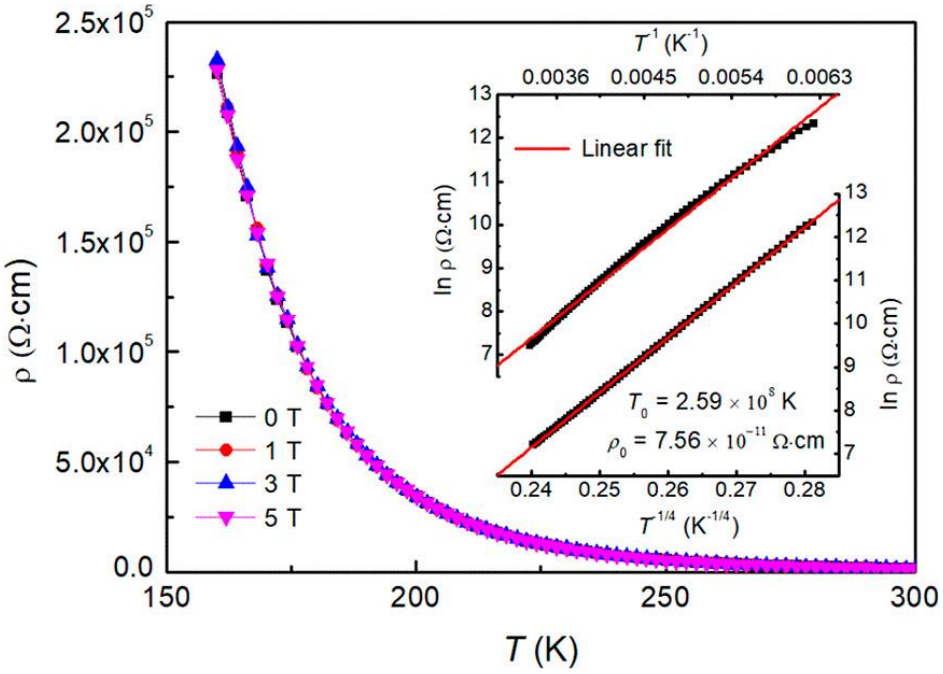

Figure 4.10 Temperature dependence of resistivity plots of LMRO at selected magnetic fields. The inset shows the linear fit to the plot of ln ρ versus T^{-1} and $T^{-1/4}$ in zero field.

4.3 Conclusion

In conclusion, we have prepared a new 4*d* transition-metal-containing *A*-site-ordered quadruple perovskite, $LaMn_3Rh_4O_{12}$, at high temperature and pressure after an extensive synthetic investigations that included forays into optical techniques generally reserved for geology. Electron microprobe measurements of initial and final preparations showed LMRO to be pure after an exceptionally long reaction time for a

HP/HT synthesis. Synchrotron powder X-ray diffraction data refinements show that $LaMn_3Rh_4O_{12}$ adopts a cubic structure (space group $Im\bar{3}$) with Mn^{3+} in the square planar A'-site. X-ray absorption near edge spectroscopy results show that the oxidation state of *A*′-site Mn and *B*-site Rh ions are primarily 3+, as supported by the observed effective magnetic moment and BVS calculations. The antiferromagnetic (T_N ~ 41 K) order is related solely to the *A*′-site Mn sublattice, as the crystal field splitting energy (and high ligand field stabilization energy) of octahedrally coordinated Rh^{3+} (d^6) drives that cation into a low spin (S = 0) arrangement. The temperature dependence of the resistivity exhibits three-dimensional Mott variable-range hopping mechanism between 300 and 150 K. The physical properties of $LaMn_3Rh_4O_{12}$ are very different from that of the only other B-site Rh containing quadruple perovskite to date, $CaCu_3Rh_4O_{12}$, which motivates further exploration of $AMn_3B_4O_{12}$ with *B* = 4*d* transition metals, and metals with large crystal field splitting energies.

4.4 References

32. J. Paul Attfield; Philip Lightfoot; Morris, R. E., "Perovskites". *Dalton Transactions* **2015,** *44*, 10541-10542.
52. Belik, A. A.; Yi, W., High-pressure synthesis, crystal chemistry and physics of perovskites with small cations at the A site. *J. Phys. Condens. Matter* **2014,** *26*, 163201.
78. Li, M. R.; Retuerto, M.; Deng, Z.; Stephens, P. W.; Croft, M.; Huang, Q.; Wu, H.; Deng, X.; Kotliar, G.; Sánchez-Benítez, J.; Hadermann, J.; Walker, D.; Greenblatt, M., Giant Magnetoresistance in the Half-Metallic Double-Perovskite Ferrimagnet Mn_2FeReO_6. *Angew. Chem. Int. Ed. Engl.* **2015,** *54* (41), 12069-12073.
79. Li, M. R.; Hodges, J. P.; Retuerto, M.; Deng, Z.; Stephens, P. W.; Croft, M. C.; Deng, X. Y.; Kotliar, G.; Sanchez-Benitez, J.; Walker, D.; Greenblatt, M., Mn_2MnReO_6: Synthesis and Magnetic Structure Determination of a New Transition-Metal-Only Double Perovskite Canted Antiferromagnet. *Chemistry of Materials* **2016,** *28* (9), 3148-3158.
83. Frank, C. E.; McCabe, E. E.; Orlandi, F.; Manuel, P.; Tan, X.; Deng, Z.; Croft, M.; Cascos, V.; Emge, T.; Feng, H. L.; Lapidus, S.; Jin, C.; Wu, M.; Li, M. R.; Ehrlich, S.; Khalid, S.; Quackenbush, N.; Yu, S.; Walker, D.; Greenblatt, M., Mn_2CoReO_6: a

robust multisublattice antiferromagnetic perovskite with small A-site cations. *Chemical Communications* **2019,** *55* (23), 3331-3334.

84. Belik, A. A.; Matsushita, Y.; Kumagai, Y.; Katsuya, Y.; Tanaka, M.; Stefanovich, S. Y.; Lazoryak, B. I.; Fumiyasu Oba, a. K. Y., Complex Structural Behavior of $BiMn_7O_{12}$ Quadruple Perovskite. *Inorganic Chemistry* **2017,** *56* (20), 12272-12281.
85. Shimakawa, Y., A-Site-Ordered Perovskites with Intriguing Physical Properties. *Inorganic Chemistry* **2008,** *47* (19), 8562-8570.
86. Long, Y., A -site ordered quadruple perovskite oxides. *Chinese Physics B* **2016,** *25* (7), 078108.
87. Vasil'ev, A. N.; Volkova, O. S., New functional materials $AC_3B_4O_{12}$ (Review). *Low Temperature Physics* **2007,** *33* (11), 895-914.
91. Prodi, A.; Gilioli, E.; Gauzzi, A.; Licci, F.; Marezio, M.; Bolzoni, F.; Huang, Q.; Santoro, A.; Lynn, J. W., Charge, orbital, and spin ordering phenomena in the mixed valence manganite $(NaMn^{3+3})(Mn^{3+2}Mn^{4+2})O_{12}$. *Nat. Mater.* **2004,** *3* (1), 48-52.
95. Shimakawa, Y., Crystal and magnetic structures of $CaCu_3Fe_4O_{12}$and $LaCu_3Fe4O_{12}$: distinct charge transitions of unusual high valence Fe. *Journal of Physics D: Applied Physics* **2015,** *48* (50), 504006.
97. Yamada, I.; Ochi, M.; Mizumaki, M.; Hariki, A.; Uozumi, T.; Takahashi, R.; Irifune, T., High-Pressure Synthesis, Crystal Structure, and Unusual Valence State of Novel Perovskite Oxide $CaCu_3Rh_4O_{12}$. *Inorganic Chemistry* **2014,** *53* (14), 7089-7091.
111. Li, M. R.; Walker, D.; Retuerto, M.; Sarkar, T.; Hadermann, J.; Stephens, P. W.; Croft, M.; Ignatov, A.; Grams, C. P.; Hemberger, J.; Nowik, I.; Halasyamani, P. S.; Tran, T. T.; Mukherjee, S.; Dasgupta, T. S.; Greenblatt, M., Polar and magnetic Mn_2FeMO_6 (M=Nb, Ta) with $LiNbO_3$-type structure: high-pressure synthesis. *Angew. Chem. Int. Ed. Engl.* **2013,** *52* (32), 8406-10.
112. Li, M.-R.; McCabe, E. E.; Stephens, P. W.; Croft, M.; Collins, L.; Kalinin, S. V.; Deng, Z.; Retuerto, M.; Sen Gupta, A.; Padmanabhan, H.; Gopalan, V.; Grams, C. P.; Hemberger, J.; Orlandi, F.; Manuel, P.; Li, W.-M.; Jin, C.-Q.; Walker, D.; Greenblatt, M., Magnetostriction-polarization coupling in multiferroic Mn_2MnWO_6. *Nature Communications* **2017,** *8* (1), 2037.
114. Belik, A. A.; Furubayashi, T.; Matsushita, Y.; Tanaka, M.; Hishita, S.; Takayama-Muromachi, E., Indium-Based Perovskites: A New Class of Near-Room-Temperature Multiferroics. *Angewandte Chemie International Edition* **2009,** *48* (33), 6117-6120.
116. Li, M. R.; Stephens, P. W.; Retuerto, M.; Sarkar, T.; Grams, C. P.; Hemberger, J.; Croft, M. C.; Walker, D.; Greenblatt, M., Designing Polar and Magnetic Oxides: Zn_2FeTaO_6 - in Search of Multiferroics. *Journal of the American Chemical Society* **2014,** *136* (24), 8508-8511.
118. Li, M. R.; Retuerto, M.; Stephens, P. W.; Croft, M.; Sheptyakov, D.; Pomjakushin, V.; Deng, Z.; Akamatsu, H.; Gopalan, V.; Sanchez-Benitez, J.; Saouma, F. O.; Jang, J. I.; Walker, D.; Greenblatt, M., Low-Temperature Cationic Rearrangement in a Bulk Metal Oxide. *Angew. Chem. Int. Ed. Engl.* **2016,** *55* (34), 9862-7.
192. Bazuev, G. V.; Golovkin, B. G.; Lukin, N. V.; Kadyrova, N. I.; Zainulin, Y. G., High Pressure Synthesis and Polymorphism of Complex Oxides Mn_2BSbO_6(B= Fe, V, Cr, Ga, Al). *Journal of Solid State Chemistry* **1996,** *124* (2), 333-337.
209. Ovsyannikov, S. V.; Zainulin, Y. G.; Kadyrova, N. I.; Tyutyunnik, A. P.; Semenova, A. S.; Kasinathan, D.; Tsirlin, A. A.; Miyajima, N.; Karkin, A. E., New antiferromagnetic perovskite $CaCo_3V_4O_{12}$ prepared at high-pressure and high-temperature conditions. *Inorganic Chemistry* **2013,** *52* (20), 11703-11710.
210. Shiro, K.; Yamada, I.; Ikeda, N.; Ohgushi, K.; Mizumaki, M.; Takahashi, R.; Nishiyama, N.; Inoue, T.; Irifune, T., Pd^{2+}-Incorporated Perovskite $CaPd_3B_4O_{12}$ (B= Ti, V). *Inorganic Chemistry* **2013,** *52* (3), 1604-1609.
211. Yamada, I.; Shiro, K.; Etani, H.; Marukawa, S.; Hayashi, N.; Mizumaki, M.; Kusano, Y.; Ueda, S.; Abe, H.; Irifune, T., Valence transitions in negative thermal expansion material $SrCu_3Fe_4O_{12}$. *Inorganic Chemistry* **2014,** *53* (19), 10563-10569.

212. Long, Y.; Saito, T.; Mizumaki, M.; Agui, A.; Shimakawa, Y., Various Valence States of Square-Coordinated Mn in A-Site-Ordered Perovskites. *Journal of the American Chemical Society* **2009,** *131* (44), 16244-16247.
213. Shimakawa, Y.; Zhang, S.; Saito, T.; Lufaso, M. W.; Woodward, P. M., Order–Disorder Transition Involving the A-Site Cations in $Ln^{3+}Mn_3V_4O_{12}$ Perovskites. *Inorganic Chemistry* **2014,** *53* (1), 594-599.
214. Shannon, R. D., Revised effective ionic radii and systematic studies of interatomic distances in halides and chalcogenides. *Acta Crystallographica Section A* **1976,** *32* (5), 751-767.
215. Li, M. R.; Retuerto, M.; Deng, Z.; Sarkar, T.; Sanchez-Benitez, J.; Croft, M. C.; Dasgupta, T. S.; Das, T.; Tyson, T. A.; Walker, D.; Greenblatt, M., Strong Electron Hybridization and Fermi-to-Non-Fermi Liquid Transition in $LaCu_3Ir_4O_{12}$. *Chemistry of Materials* **2015,** *27* (1), 211-217.
216. Cheng, J.-G.; Zhou, J.-S.; Yang, Y.-F.; Zhou, H.; Matsubayashi, K.; Uwatoko, Y.; MacDonald, A.; Goodenough, J., Possible Kondo physics near a metal-insulator crossover in the A-site ordered perovskite $CaCu_3Ir_4O_{12}$. *Physical Review Letters* **2013,** *111* (17), 176403.
217. Mizumaki, M.; Mizokawa, T.; Agui, A.; Tanaka, S.; Takatsu, H.; Yonezawa, S.; Maeno, Y., Oxygen hole state in A-site ordered perovskite $ACu_3Ru_4O_{12}$ (A= Na, Ca, and La) probed by resonant X-ray emission spectroscopy. *Journal of the Physical Society of Japan* **2013,** *82* (2), 024709.
218. Sudayama, T.; Wakisaka, Y.; Takubo, K.; Mizokawa, T.; Kobayashi, W.; Terasaki, I.; Tanaka, S.; Maeno, Y.; Arita, M.; Namatame, H., Bulk-sensitive photoemission study of $ACu_3Ru_4O_{12}$ (A= Ca, Na, and La) with heavy-fermion behavior. *Physical Review B* **2009,** *80* (7), 075113.
219. Yamada, I.; Takahashi, Y.; Ohgushi, K.; Nishiyama, N.; Takahashi, R.; Wada, K.; Kunimoto, T.; Ohfuji, H.; Kojima, Y.; Inoue, T., $CaCu_3Pt_4O_{12}$: the first perovskite with the B site fully occupied by Pt^{4+}. *Inorganic chemistry* **2010,** *49* (15), 6778-6780.
220. Ochi, M.; Yamada, I.; Ohgushi, K.; Kusano, Y.; Mizumaki, M.; Takahashi, R.; Yagi, S.; Nishiyama, N.; Inoue, T.; Irifune, T., *B*-site deficiencies in *A*-site-ordered perovskite $LaCu_3Pt_{3.75}O_{12}$. *Inorganic Chemistry* **2013,** *52* (7), 3985-3989.
221. Byeon, S.-H.; Lee, S.-S.; Parise, J. B.; Woodward, P. M.; Hur, N. H., High-pressure synthesis of metallic perovskite ruthenate $CaCu_3Ga_2Ru_2O_{12}$. *Chemistry of materials* **2004,** *16* (19), 3697-3701.
222. Chen, W.-t.; Mizumaki, M.; Seki, H.; Senn, M. S.; Saito, T.; Kan, D.; Attfield, J. P.; Shimakawa, Y., A half-metallic A-and B-site-ordered quadruple perovskite oxide $CaCu_3Fe_2Re_2O_{12}$ with large magnetization and a high transition temperature. *Nature Communications* **2014,** *5* (1), 1-7.
223. Wang, X.; Liu, M.; Shen, X.; Liu, Z.; Hu, Z.; Chen, K.; Ohresser, P.; Nataf, L.; Baudelet, F. o.; Lin, H.-J., High-temperature ferrimagnetic half metallicity with wide spin-up energy gap in $NaCu_3Fe_2Os_2O_{12}$. *Inorganic chemistry* **2018,** *58* (1), 320-326.
224. Ebbinghaus, S. G.; Weidenkaff, A.; Cava, R., Structural Investigations of $ACu_3Ru_4O_{12}$ (A= Na, Ca, Sr, La, Nd)—A Comparison between XRD-Rietveld and EXAFS Results. *Journal of Solid State Chemistry* **2002,** *167* (1), 126-136.
225. Schwingenschlögl, U.; Eyert, V.; Eckern, U., Octahedral Tilting in $ACu_3Ru_4O_{12}$ (A= Na, Ca, Sr, La, Nd). *Chemical physics letters* **2003,** *370* (5-6), 719-724.
226. Subramanian, M. A.; Sleight, A. W., $ACu_3Ti_4O_{12}$ and $ACu_3Ru_4O_{12}$ perovskites: high dielectric constants and valence degeneracy. *Solid State Sciences* **2002,** *4* (3), 347-351.
227. Hollmann, N.; Hu, Z.; Maignan, A.; Günther, A.; Jang, L.-Y.; Tanaka, A.; Lin, H.-J.; Chen, C.; Thalmeier, P.; Tjeng, L., Correlation effects in $CaCu_3Ru_4O_{12}$. *Physical Review B* **2013,** *87* (15), 155122.
228. Brizé, V.; Autret-Lambert, C.; Wolfman, J.; Gervais, M.; Gervais, F., Synthesis and microstructural TEM investigation of $CaCu_3Ru_4O_{12}$ ceramic and thin film. *Journal of Solid State Chemistry* **2011,** *184* (10), 2719-2723.

229. Tanaka, S.; Takatsu, H.; Yonezawa, S.; Maeno, Y., Suppression of the mass enhancement in $CaCu_3Ru_4O_{12}$. *Physical Review B* **2009,** *80* (3), 035113.
230. Krimmel, A.; Günther, A.; Kraetschmer, W.; Dekinger, H.; Büttgen, N.; Eyert, V.; Loidl, A.; Sheptyakov, D.; Scheidt, E.-W.; Scherer, W., Intermediate-valence behavior of the transition-metal oxide $CaCu_3Ru_4O_{12}$. *Physical Review B* **2009,** *80* (12), 121101.
231. Krimmel, A.; Günther, A.; Kraetschmer, W.; Dekinger, H.; Büttgen, N.; Loidl, A.; Ebbinghaus, S. G.; Scheidt, E. W.; Scherer, W., Non-Fermi-liquid behavior in $CaCu_3Ru_4O_{12}$. *Physical Review B* **2008,** *78* (16), 165126.
232. Mukherjee, S.; Sarkar, S.; Saha-Dasgupta, T., First-principles study of $CaCu_3B_4O_{12}$ (B= Co, Rh, Ir). *Journal of Materials Science* **2012,** *47* (21), 7660-7664.
233. Xin, Y.; Zhou, H.; Cheng, J.; Zhou, J.; Goodenough, J., Study of atomic structure and electronic structure of an $AA'_3B_4O_{12}$ double-perovskite $CaCu_3Ir_4O_{12}$ using STEM imaging and EELS techniques. *Ultramicroscopy* **2013,** *127*, 94-99.
234. Labeau, M.; Bochu, B.; Joubert, J. C.; Chenavas, J., Synthèse et caractérisation cristallographique et physique d'une série de composés $ACu_3Ru_4O_{12}$ de type perovskite. *Journal of Solid State Chemistry* **1980,** *33* (2), 257-261.
235. Li, M. R.; Walker, D.; Greenblatt, M., Design of Polar and Magnetic Compounds in Double Corundum Family. Poster Presented at: Strategies for Materials Discovery: Progress Toward Tomorrow's Materials, 2016 Gordon Research Conference, 2016.
236. Reed, S. J. B., *Electron microprobe analysis and scanning electron microscopy in geology*. Cambridge university press: 2005.
237. Weedon, D. S., Corona Structures in the Basic Igneous Masses of East Aberdeenshire. *Nature* **1965,** *208* (5013), 885-885.
238. Zhang, S.; Saito, T.; Mizumaki, M.; Chen, W.-t.; Tohyama, T.; Shimakawa, Y., Site-Selective Doping Effect in $AMn_3V_4O_{12}$ (A = Na^+, Ca^{2+}, and La^{3+}). *Journal of the American Chemical Society* **2013,** *135* (16), 6056-6060.
239. Bune, R. O.; Lobanov, M. V.; Popov, G.; Greenblatt, M.; Botez, C. E.; Stephens, P. W.; Croft, M.; Hadermann, J.; Van Tendeloo, G., Crystal structure and properties of Ru-stoichiometric $LaSrMnRuO_6$. *Chemistry of materials* **2006,** *18* (10), 2611-2617.
240. Popov, G.; Greenblatt, M.; Croft, M., Large effects of *A*-site average cation size on the properties of the double perovskites $Ba_{2-x}Sr_xMnReO_6$: *A* d^5–d^1 system. *Physical Review B* **2003,** *67* (2), 024406.
241. Zeng, Z.; Greenblatt, M.; Sunstrom, J. E.; Croft, M.; Khalid, S., Giant Magnetoresistance in $CaCu_3Mn_4O_{12}$-Based Oxides with Perovskite-Type Structure. *Journal of Solid State Chemistry* **1999,** *147* (1), 185-198.
242. Prodi, A.; Gilioli, E.; Cabassi, R.; Bolzoni, F.; Licci, F.; Huang, Q.; Lynn, J. W.; Affronte, M.; Gauzzi, A.; Marezio, M., Magnetic structure of the high-density single-valent e_g Jahn-Teller system $LaMn_7O_{12}$. *Physical Review B* **2009,** *79* (8), 085105.
243. Prodi, A.; Allodi, G.; Gilioli, E.; Licci, F.; Marezio, M.; Bolzoni, F.; Gauzzi, A.; De Renzi, R., μSR study of $AA_3'Mn_4O_{12}$ double perovskites. *Physica B: Condensed Matter* **2006,** *374*, 55-58.
244. Liu, H.; Pourret, A.; Guyot-Sionnest, P., Mott and Efros-Shklovskii Variable Range Hopping in CdSe Quantum Dots Films. *ACS Nano* **2010,** *4* (9), 5211-5216.
245. Zhang, L.; Tang, Z.-J., Polaron relaxation and variable-range-hopping conductivity in the giant-dielectric-constant material Ca Cu 3 Ti 4 O 12. *Phys. Rev. B* **2004,** *70* (17), 174306.

Chapter 5: $Fe_{3-x}InSn_xO_6$ (x = 0, 0.25, 0.5) - A Family of Magnetic Double Corundum Derivatives with Sn-induced Polarization

5.1 Introduction

Multiferroic materials- materials which exhibit two or more types of spontaneous, switchable ferroic orders- have been of great interest due to a multitude of potential electronics applications, such as in magnetic field sensors and spintronic devices, as well as understanding the fundamental phenomena involved.[26, 102] This is especially true in the even-rarer cases of magnetoelectrics, where application of an electrical field can induce magnetization and an external magnetic field can affect polarization.[246-248]

The perovskite structure type currently dominates both experimental and theoretical multiferroic research. Since the discovery of ferroelectricity in $BaTiO_3$,[249] the simplicity of the ABO_3 perovskite has made it the ideal model for detailed theoretical studies on the nature of ferroic order, and most practical ferroelectric devices are ABO_3 or $A_2BB'O_6$ perovskite-type oxides.[31] In these oxides, a three-dimensional (3D) array of corner-sharing $B/B'O_6$ octahedra create large AO_{12} cuboctohedral cavities occupied by the A cations. As described in previous chapters, the tolerance factor, *t*, of stable perovskites is expected to be approximately 1.

Ferroelectric polarization in perovskites is typically driven by displacement of the B cations within their octahedra with variation of temperature, leading to small polarization constants. For reasons not entirely clear, *d* shell electrons inhibit these structural distortions, possibly due to electronic structure effects[31]. In contrast,

unpaired *d*-electrons are essential for magnetism, causing ferroelectricity and ferromagnetism to be at best poorly compatible in perovskites.[101, 250]

A promising potentially multiferroic structure archetype, an alternative to the traditional perovskite-related oxides, is the corundum and double corundum structure family (space groups *R*3, $R\bar{3}$, *R*3c, and $R\bar{3}$c).[110, 116-117, 251-253] ABO_3 corundum and $A_2BB'O_6$ double corundum derivatives require relatively small A-site cations and crystallize in highly distorted perovskite-related structures ($t < 0.85$) with both the A/A' and B/B' ions located in octahedral sites. Due to the small tolerance factor, corundum derivative compounds must typically be synthesized at high temperature and pressure (HTHP).[111-112, 118-119] (While there are exceptions to this rule, it is not currently possible to predict when these exceptions will occur.)[53] In all corundums, A/A' and B/B' octahedra form face-sharing pairs (along the *c* axis), which edge share within each (*ab*) layer and corner-share between layers. Face sharing octahedra can lead to large polarization constants (Ps), as face sharing A/A' and B/B' cations displace from the shared face along the c-axis, due to large Coulomb repulsions. When the polarization is switchable, the reversal is driven by A/A' or B/B' cations migrating through an O_3 face to a vacant octahedral site, not through minor structural distortions,[101] thus d^0 electron configuration is not required, and transition metal cations with large magnetic moments can be placed in the A/A' and B/B' sites.[101, 106, 254] For example, Mn_2FeMoO_6, a polar double corundum ferrimagnet with a T_c above room temperature (337 K) has a Ps calculated to be 68 μC/cm^2 and magnetic cations on both the A- (d^3 Mn^{2+}) and B- (d^5 Fe^{3+}, d^1 Mo^{5+}) sites.[117] Other known polar corundum type materials with T_C/T_N above room temperature reported thus far include $LiNbO_3$-type $BiFeO_3$ (*R*3*c*, T_N = 643 K),[255] $ScFeO_3$ (*R*3*c*, T_N = 356 K),[256] $GaFeO_3$ (*R*3*c*, T_N = 408 K),[257] and $InFeO_3$ (*R*3*c*, T_N = 545 K).[121] To our knowledge,

other corundum and double corundum oxides reported thus far are either centrosymmetric, or have a T_c/T_N below room temperature.[102]

Hematite (α-Fe_2O_3), the centrosymmetric corundum (space group $R\bar{3}c$) that has inspired most of the above polar magnets, is a common red pigment and has interesting magnetic properties. Debate over the magnetic structure of hematite was once fierce due to its high apparent "Curie" temperature coupled with a minuscule macroscopic magnetic moment (0.0144 μ_B/f.u. just above the Morin transition, T_M).[258-261] In fact, hematite is a canted antiferromagnet ($T_N \approx 948$ K) with weak ferromagnetic interactions which persist up to T_M (250-260 K), below which pure samples of hematite become perfectly antiferromagnetic.[261] Substitutions of other metals into the $R\bar{3}c$ hematite lattice can lead to a suppression of the Morin temperature as Fe-O-Fe interactions are disrupted, as in the cases of Sn^{4+} doped and Sn^{4+}/Mg^{2+} co-doped hematite studied by Gaudon et al.[262] A maximum substitution of approximately 5%-10% Sn^{4+} was observed in that study, with the inclusion of Mg^{2+} leading to higher overall substitution as the increased positive charge Sn^{4+} in hematite must otherwise be compensated for by Fe^{3+} vacancies, which destabilize the lattice more strongly than substitution of Mg^{2+}. As previously mentioned, Fujita et. al recently synthesized polar $InFeO_3$ at 1450˚C, 15 GPa.[121] The transition temperature of this material is well above room temperature, but interestingly weak ferromagnetism is reported, due to canting of the otherwise antiferromagnetically-ordered structure.

In this work, we present $Fe_{3-x}InSn_xO_6$ (x = 0, 0.25, 0.5), a family of double corundum related compounds made at HP/HT (6 GPa, 1400-1450˚C). The parent compound, $InFe_3O_6$ and the x =0.25 phase crystallize in centrosymmetric $R\bar{3}c$, but a small increase in Sn^{4+} content causes the x = 0.5 compound to order in a $LiNbO_3$-type *R*3*c* polar structure at a much lower pressure than that required for $InFeO_3$. The

inclusion of Fe^{2+} ions allows for a high degree of Sn^{4+} substitution (up to 12.5%) which would otherwise need to be compensated for by Fe^{3+} or In^{3+} vacancies. These compounds are interesting examples of corundum compounds with magnetic transition temperatures well above room temperature. Our investigations and comparisons of these compounds aim to improve the overall design process and theoretical understanding of induced polarization in potential multiferroic materials with transition temperatures near or above room temperature.

5.2 Results and Discussion

5.2.1 Preliminary Characterization

Powder X-ray Diffraction (PXD)

Samples were initially characterized via PXD on a Bruker D8 Advance diffractometer. These initial characterizations indicated that samples of x = 0, 0.25, and 0.5 crystallize as either centrosymmetric $R\bar{3}c$ or noncentrosymmetric *R*3*c* (**Figure 5.1**). It is impossible to tell from X-ray powder patterns whether a sample is centrosymmetric or noncentrosymmetric due to limitations of the twin operation in Friedel's law.[263] The composition of crystals were also confirmed via microprobe analysis, to ensure that the large crystals were of consistent stoichiometry.

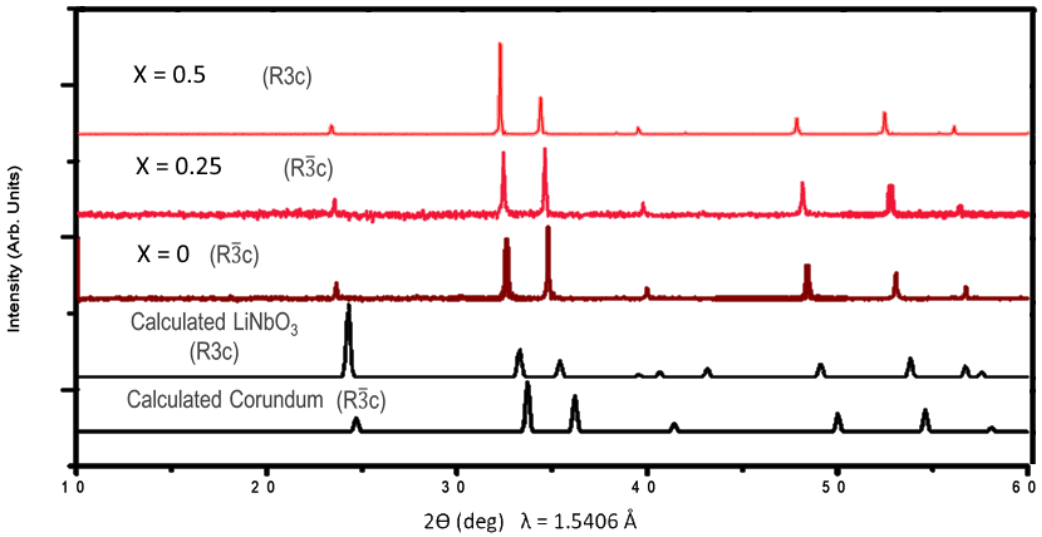

Figure 5.1 Initial PXD data for x = 0.5, 0.25, 0 compared to calculated standards in both *R*3*c* and *R*$\bar{3}$*c*. Note that it is impossible to tell *R*3*c* from *R*$\bar{3}$*c* from PXD alone, and so the nominal space group designations here were subsequently confirmed by SCXRD and SHG.

Second Harmonic Generation (SHG)

In order to determine to which space group each belonged, second-harmonic generation (SHG) analysis was employed by collaborators at Pennsylvania State University, Hugo Wang and Professor Venkatraman Gopalan. SHG is an optical technique in which two photons of the same frequency from the same incident electric field combine to create a photon with double the frequency of the incident photon. It is, like other even-order non-linear optical phenomena, possible only in materials without an inversion center. This seems to make SHG ideal for our purposes, as samples that crystallize in *R*3*c* should produce a detectable SHG signal, while crystals of *R*$\bar{3}$*c* will not.[264] Initial SHG trials were performed on polycrystalline pressed-pellets of samples which were embedded in epoxy resin and ground flat. As seen in **Figure 5.2**, the x = 0 sample generates no SHG signal when exposed to the linearly polarized incident beam, indicating that this sample is centrosymmetric. In contrast, both the x = 0.25 and x = 0.5 samples show illumination, which appears yellow in Figures **Figure 5.2**(b) and (c), and stand in contrast with the SHG-inactive epoxy

mount. As both the x = 0.25 and x = 0.5 samples demonstrate the SHG effect, both were initially indicated to be noncentrosymmetric, though the very slight response of the x = 0.25 sample was cause for further investigation. The x = 0.25 polycrystalline sample was thus measured under temperature-dependent conditions, and a maximum polarization was observed at around T_N. However, these initial results could not be verified without an oriented sample, and so single crystal SHG was planned for both x = 0.5 and 0.25.

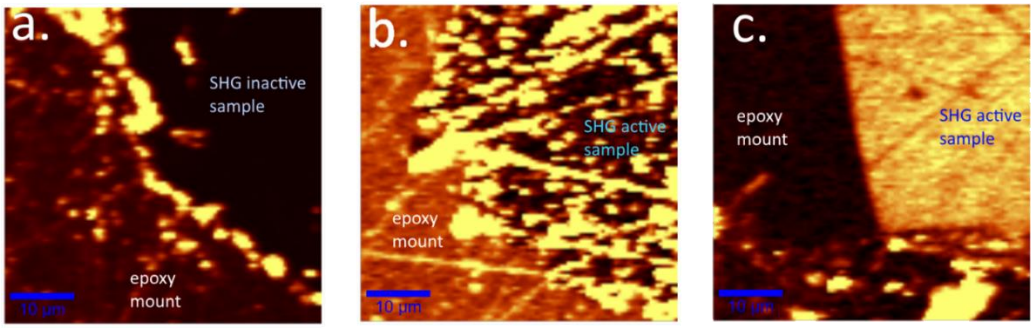

Figure 5.2 Images from second harmonic generation analysis of x = 0 (**a**) x = 0.25 (**b**) and x = 0.5 (**c**). Crystals of each sample type were embedded in an epoxy mount (labelled in white) and ground to expose a flat surface for analysis. The samples have been labelled in blue. For X = 0, no SHG signal was detected, indicating centrosymmetry and space group $R\bar{3}c$. For X = 0.25 and 0.5, an SHG signal is apparent, indicating that these compounds may crystallize in the noncentrosymmetric $R3c$ space group, though further investigations to determine if the signals are caused by another force such as strain.

Temperature dependent single crystal SHG experiments were attempted by collaborator Dr. Shukai Yu under the direction of Prof. Gopalan for single crystals of x = 0.25 and 0.5, which had been oriented along the three-fold axis via single crystal XRD (orientation performed by Dr. Thomas Emge). The x = 0.5 species is again shown to be strongly polar, without a clear temperature dependence. There is only a slight difference in SHG intensity from 298.15– 573.15 K. The x = 0.25 case was measured at 3 temperatures; 298.15 K, 523.15 K, and 623.15 K and shows a slightly different behavior: the SHG signal decreases as temperature is increased above room

temperature, implying that the polar nature of x = 0.25 is far less robust than that of the x = 0.5, if it exists at all (**Figure 5.3**). These crystals were highly twinned, however, and occasionally strain can induce an SHG signal to appear in a sample, which is centrosymmetric. The sudden disappearance of signal upon heating the x = 0.25 sample implies that this signal is likely due to strain at ambient temperature, which is then relaxed as the temperature is increased to 523.15 K as has been seen in quartz and quartz-type compounds such as $GaPO_4$.[176-177] The x = 0.5 sample shows no such temperature dependence, however, and therefore should be assigned to the noncentrosymmetric space group *R*3*c*. Further experiments and analyses are currently ongoing to fully elucidate the nature of the SHG response, and especially to thoroughly explain why the initial temperature-dependent SHG measurement of polycrystalline x = 0.25 showed potential polarization that was temperature dependent but initial oriented single crystal measurements did not.

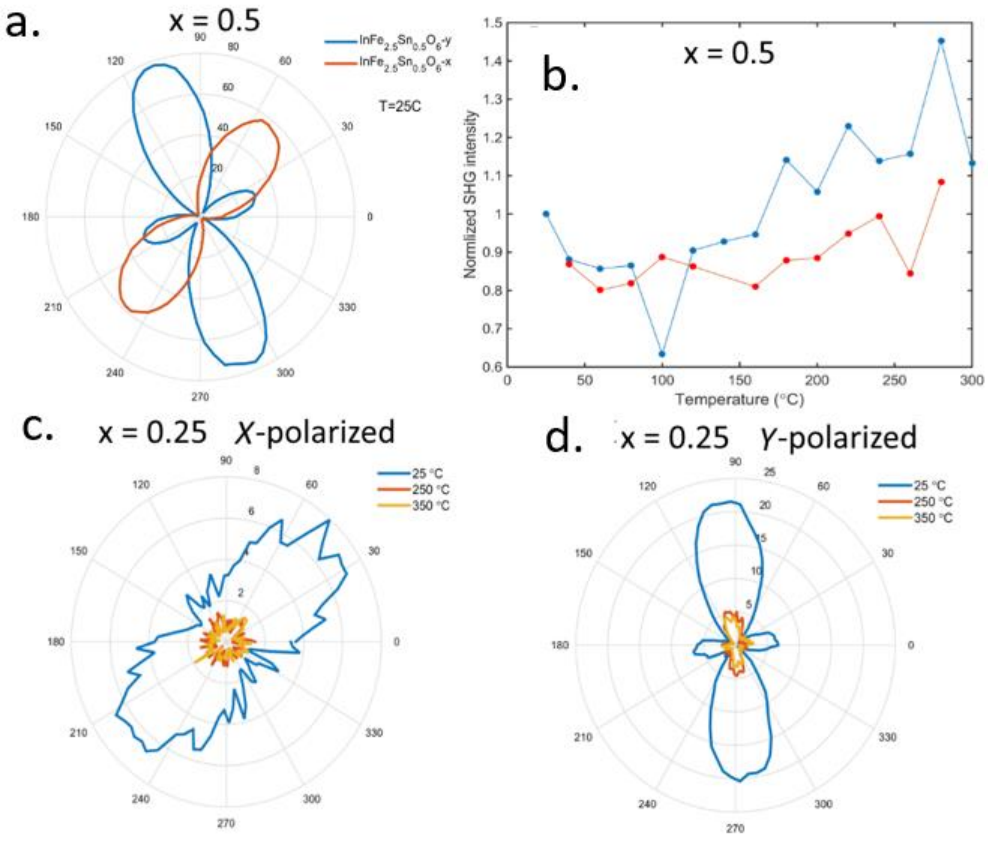

Figure 5.3 Temperature dependent single crystal SHG results for the x = 0.5, 0.25 samples. (**a**). Detectors in both the X and Y polarization show strong response from x = 0.5 at 25 ° C. (**b**). The SHG response for x = 0.5, which is not diminished appreciably on heating indicates that this sample should be assigned noncentrosymmetric *R*3*c*. This is in contrast with x = 0.25, which shows some response in both X (**c**.) and Y (**d**.) detector orientations at 25° C; this response disappears upon heating, which implies that the response is due to strain and that the sample is more likely to be highly twinned $R\bar{3}c$. 0.5, an SHG signal is apparent, indicating that this compound crystallizes in the noncentrosymmetric *R*3*c* space group.

Decomposition Analysis

Initial magnetic measurements (which will be discussed shortly) indicated that all three compounds have magnetic transitions above room temperature, and so it was important to study the stability of the structure upon heating to ensure that there was no decomposition. Many high pressure samples are metastable and thus can be easily affected or decomposed by changes in temperature, especially heating.[55, 118] Samples of as-made x = 0, 0.25, and 0.5 were ground thoroughly in agate mortars in air, and

small amounts (10-30 mg) were removed and placed in a Q-600 thermogravimetric analysis device made by TA-Instruments. Samples were then heated to 800 K (x = 0.25, 0.5) and 1000 K (x = 0) under flowing argon at 10 C/min then held at temperature for 30 minutes before being cooled at ~10 C/min. In all cases, there was no observed sharp drop in mass throughout the TGA experiment as would be expected in decomposition. Instead, a gradual loss of mass of approximately 2% was observed, which is consistent with instrument error or perhaps the evaporation of surface moisture from the sample. Additionally, the PXD scans from both before and after the heating experiments remained consistent in peak shape and number (see **Figure 5.4**). The post-heating PXD scans were subject to somewhat more noise than the initial scans due to sample size, yet there is no evidence of phase change or impurity peaks.

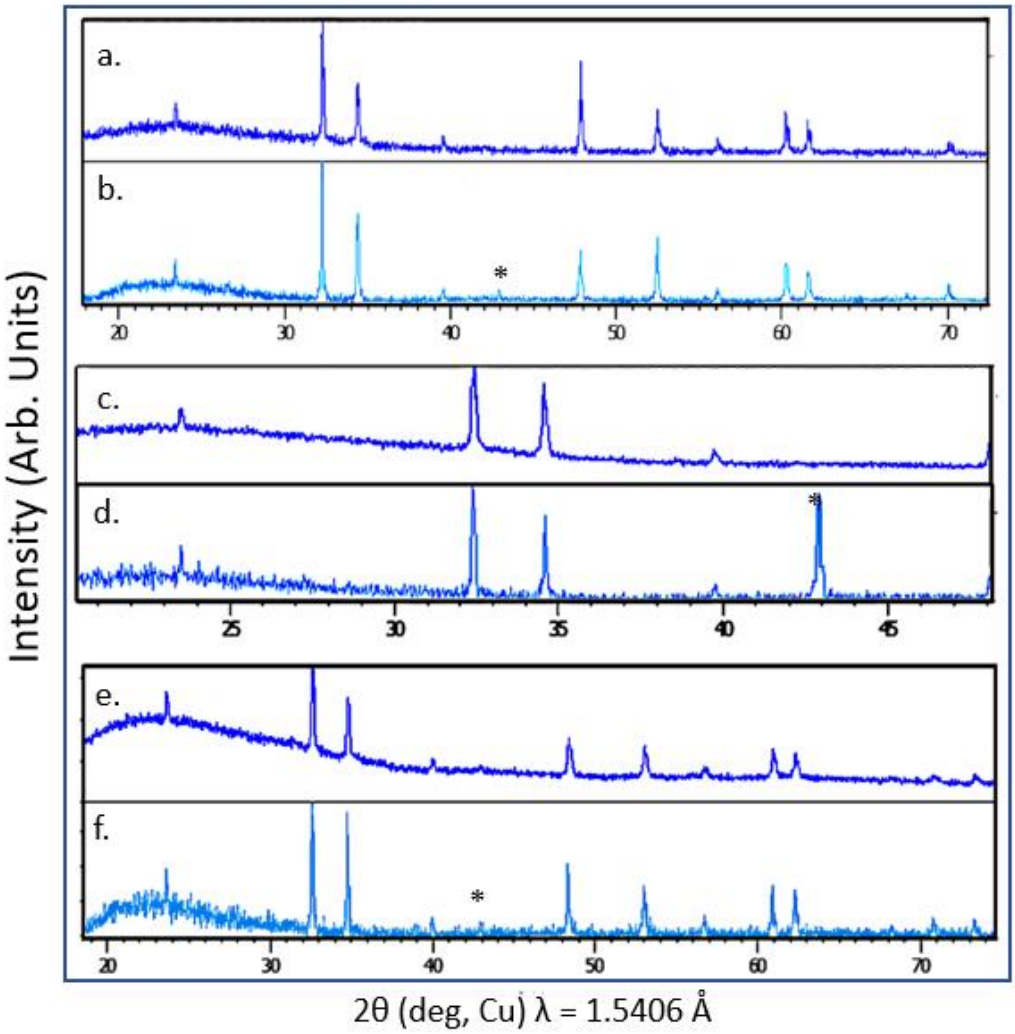

Figure 5.4 PXD scans for as made (**a, c, e**, dark blue) and post-thermal treatment (**b, d, f,** light blue) $Fe_{3-x}InSn_xO6$ compounds (x = 0.5, **a, b**; 0.25, **c, d**; 0, **e, f**). A small amount of MgO standard was added during heating experiments, and has been marked with an asterisk. PXD experiments are shown at different levels of magnification to highlight the similarities between the as-made and post-treatment samples in different regions of 2θ.

5.2.2 Detailed Structural Refinements

Sample structures were further refined via SPXD and single crystal refinement with the assistance and instruction of Dr. Thomas Emge. Comparison of SPXD patterns and single crystal structure factors show that all phases index well to either *R*3*c* (x = 0.5) or $R\bar{3}c$ (x = 0, 0.25) as seen in **Figure 5.5** and **Table 5.1**. The SHG results are corroborated by the single crystal refinements (**Table 5.2** and **Table 5.3**) in

that x = 0.25 was found to be highly twinned, and refined better as centrosymmetric than noncentrosymmetric (wR^2 improvement of ~0.5%). In contrast, although the x = 0.5 sample was also somewhat twinned, it did not refine better as centrosymmetric. Instead, comparison of the statistics of the expectation values of the structure factors suggest that x = 0.5 indicates the likelihood of a *hypercentric* distribution.[265]

In both *R*3*c* and $R\bar{3}c$, octahedral holes in a distorted hexagonal close-packed crystal structure are filled with $\frac{1}{3}$ A/A' cations, $\frac{1}{3}$ B/B' cations, and $\frac{1}{3}$ vacancies. Face sharing dimers of AO_6 and BO_6 octahedra (or in the case of x = 0 and 0.25, AO_6 octahedra only) cause the A and B cations to displace from the octahedral centroid, leading to three short and three long bonds along the *c*-axis. These dimers edge share along the layers and corner share between them, and in polar *R*3*c*, the AO_6 and BO_6 octahedra are arranged such that only AO_6 and BO_6 octahedra face share; BO_6-BO_6 and AO_6-AO_6 dimers do not occur.

As more of the larger Sn^{4+} (0.69 Å) is substituted for Fe^{3+} (0.645 Å) into the structure, lattice parameters and unit cell volume increase to accommodate the larger cations into the distorted lattice. $Fe_{3-x}InSn_xO_6$ is very sensitive to the addition of a small amount of Sn - just 12.5%, as in the case of x = 0.5, changes the space group from centrosymmetric $R\bar{3}c$ to noncentrosymmetric *R*3*c*. In all cases, the electron densities of the *A* and *B* sites refined to be equal, which indicates that there should be the same percentage of Fe on both sites. As XRD cannot distinguish between In^{3+} and Sn^{4+} due to matching electron densities, the Sn occupancy was fixed to one site for noncentrosymmetric x = 0.5. This was done initially because there were two distinct octahedral environments in the single crystal refinement - one a smaller, more regular octahedral environment, and one a more distorted environment which could be more accurately described as a triangular diprism. A precise refinement of the exact amount

of Sn on each site is still not possible without single crystal neutron diffraction, however. Neutron powder diffraction refinements on x = 0.5 (which will be discussed shortly) indicate that Sn^{4+} is isolated almost entirely to the smaller site. Due to the aforementioned limitations of the techniques, the possibility of Sn admixture on the other site was not explored with single crystal or synchrotron XRD refinements.

The average metal-oxygen distance for the Sn-containing site is comparable for the x = 0.25 and x = 0.5 (2.0841 Å and 2.0746 Å, respectively) samples; both are longer than the average <Fe/Sn-O> bond length for $Fe_{1.698}Sn^{4+}_{0.228}O_3$ (2.0298 Å), where Sn(IV) is compensated by Fe vacancies, and which has a lower concentration of Sn(IV) cations sharing a site with Fe(III).[266] These <Fe-O> bond lengths are also longer than what was observed in *R*3*c* $InFeO_3$ (2.0454 Å), where the B-site is entirely occupied by $Fe^{3+}O_6$ octahedra with no In^{3+} admixture.[121] Bond Valance Sum (BVS) calculations were attempted, however such calculations are somewhat simplistic to accurately reflect the valence states of cations in mixed-occupancy sites, and so have been omitted from this report.[267] The overall octahedral volume increase from the inclusion of Sn would cause standard BVS calculations to greatly underestimate the valence of Fe, for example, in any site that includes it. In order to reliably determine the valence states of the different cations, a more accurate technique, such as X-ray absorption near-edge spectroscopy (XANES) is necessary.

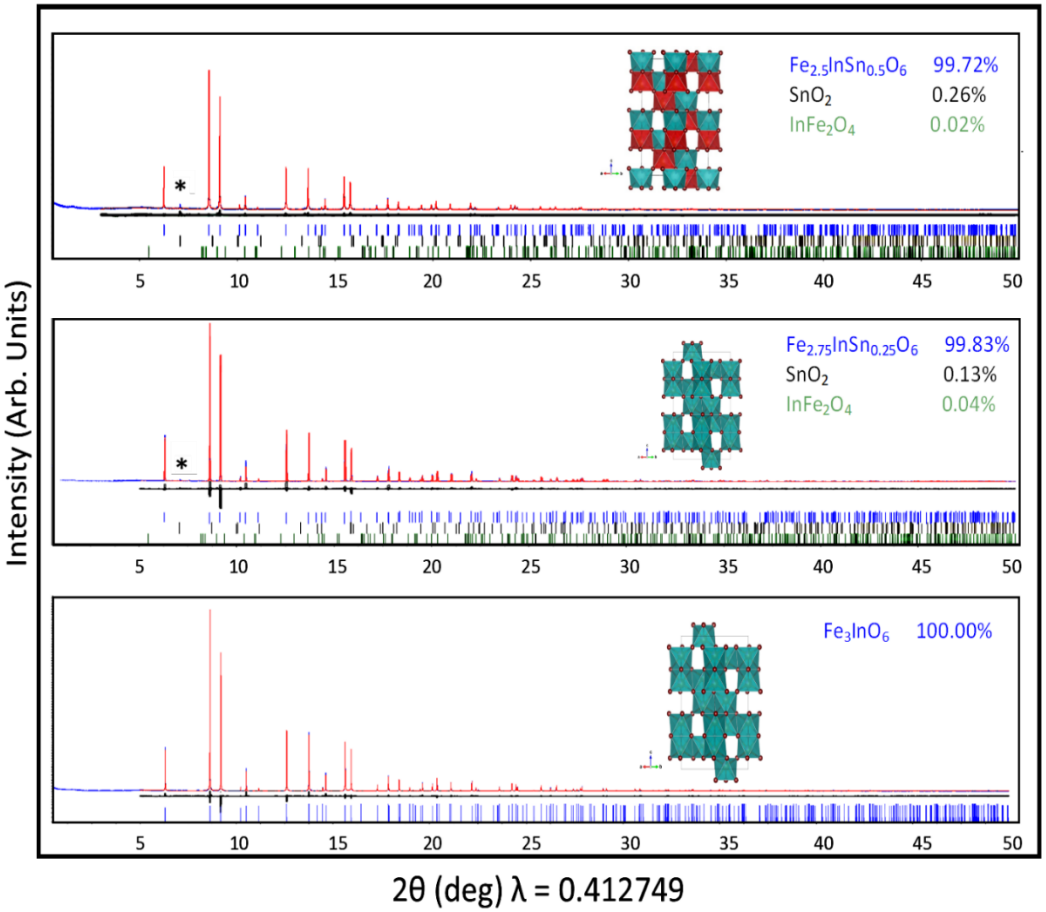

Figure 5.5 Refinement of $Fe_{3-x}InSn_xO_6$ Synchrotron powder diffraction in space group *R*3*c* (**a**), or *R*$\bar{3}$*c* (**b, c**) . In all cases, the collected pattern is shown in blue, calculated in red, and the difference in grey. Blue ticks indicate the main phase, while grey ticks indicate a small amount of SnO_2 impurity (main peak indicated with an asterisk) and green trace amounts of $InFe_2O_4$, which was also found in NPD refinements of x = 0.5. Inset in each is the *R*3*c* or *R*$\bar{3}$*c* structure viewed along the a-b plane.

Table 5.1 Lattice parameters and refinement statistics for $Fe_{3-x}InSn_xO_6$ generated through SPXD refinement. (Detailed explanation of lattice positions and occupancies have been reserved for discussion from single crystal, due to limitations of SPXD)

$Fe_{3-x}InSnxO6$	**x = 0**	**x = 0.25**	**x = 0.5**
Space Group	*R*$\bar{3}$*c* (167)	*R*$\bar{3}$*c* (167)	*R*3*c* (161)
a/Å	5.152(6)	5.1838(9)	5.21173(4)
c/ Å	13.9359(3)	14.0007(1)	14.06005(10)
V/ Å	320.645	325.831	330.736(5)
R_p, R_{wp}, R_{exp}	*7.3261, 9.7498, 7.2761*	*9.7256, 12.0114, 7.8502*	*8.6828, 10.7337, 9.7908*
GooF	1.33998	1.53006	1.096306

Table 5.2 Lattice parameters and positions for $Fe_{3-x}InSn_xO_6$ generated through SCXRD

$Fe_{3-x}InSn_xO_6$	**x = 0**	**x = 0.25**	**x = 0.5**
Space Group	*R*$\bar{3}$*c* (167)	*R*$\bar{3}$*c* (167)	*R*3*c* (161)
a/Å	5.1579(2)	5.1870(2)	5.2109(9)
c/ Å	13.9308(4)	14.0199(4)	14.050(3)
V/ Å	320.96(3)	326.67(3)	330.40(14)
A-site In/Fe			
Wyck.	12*c*	-	6*a*
U_{eq}/ Å^2	6.59(14)	-	9.4(12)
Occupancy	0.25/0.75	-	0.39(5)/0.61(5)
B-site In/Fe/Sn	-		
Wyck.	-	12*c*	6*a*
U_{eq}/ Å^2	-	9.58(7)	10.0(15)
Occupancy	-	0.250/0.688/0.063	0.12(2)/0.25(5)/0.62(7)
O			
Wyck.	18*e*	18*e*	18*b*
U_{eq}/ Å^2	10	12.06(14)	10.8(9)
Occupancy	1	1	1
wR^2	7.00%	8.86%	9.15%
GooF	1.059	1.333	1.058

Table 5.3 Lattice parameters and positions for $Fe_{3-x}InSn_xO_6$ generated through SCXRD

$Fe_{3-x}InSn_xO_6$	**x = 0**	**x = 0.25**	**x = 0.5**
	Selected bond lengths/Å		
In/FeO_6			
In/Fe-O x 3	1.9831(11)	-	2.000(11)
-O x 3	2.1625(6)	-	2.217(12)
<In/Fe-O>	2.0728	-	2.1084
		-	
In/Fe/SnO_6	-		
In/Fe/Sn-O x 3	-	1.9975(11)	2.025(12)
-O x 3	-	2.1706(6)	2.214(12)
<In/Fe/Sn-O>	-	2.0841	2.0746
	Selected Bond Angles/˚		
In/Fe-O-In/Fe	71.67(3)		
	94.65(3)		
	118.56(4)		
	131.20(6)		129.3(6)
In/Fe-O-In/Fe/Sn	-	-	86.7(3)
			92.8(6)
			96.4(6)
			118.4(4)
In/Fe/Sn-O-In/Fe/Sn	-	86.94(3)	133.5(6)
		94.56(3)	
		118.71(4)	
		131.33(6)	
O-In/Fe-O	77.68(3)	-	76.1(5)
	85.35(3)		84.4(3)
	90.17(6)		89.8(3)
	103.709(19)		105.6(5)
	160.84(3)		158.1(8)
O-In/Fe/Sn-O	-	77.88(3)	80.1(5)
		85.44(3)	86.2(3)
		90.25(6)	90.77(17)
		103.453(19)	101.0(6)
		161.18(3)	164.6(8)

5.2.3 XANES

X-ray absorption near-edge spectroscopy (XANES) data were collected by Prof Croft, who prepared and selected the figures for publication, at Brookhaven National Laboratory to determine the oxidation states of Fe and Sn in the x = 0.25 and x = 0.5 species. This would help to determine whether Fe(II) cations or Fe(III) vacancies charge balance the inclusion of Sn(IV). As there is only a small amount of Sn, and thus potential Fe(II), by mass, the results for x = 0.5 should be more significant than 0.25, an so will be discussed in detail here. In solid compounds, XANES is useful for determining the oxidation state and coordination environment of any element.[169, 268-269] An edge results when an element absorbs an X-ray of equivalent energy to the binding energy of an inner shell electron. In two samples with the same coordination environment but different oxidation states, the energies of the K-edge shifts increase with increasing effective oxidation state; more energy is required to ionize 1s electrons as the oxidation state increases.

Figure 5.6 (**a**) and (**b**) show the Fe K-edge and K pre-edge of x = 0.5, compared with standards of Fe in octahedral coordination. The spectrum for $Fe_{2.5}InSn_{0.5}O_6$ is most closely aligned with that of La_2FeVO_6, where Fe is 3+, but it is shifted slightly to the left with a gentler slope and much broader peak than the standard. This shift in energy and shape is consistent with some Fe^{2+} admixture, as the FeO standard shows a far gentler rise at a lower energy than the La_2FeVO_6 standard. This effect is seen even more dramatically in the Fe K pre-edge (Figure XANES.1b), where green boxes have been used to point out the Fe^{2+}, Fe^{3+}, and Fe^{4+} standards in comparison with $Fe_{2.5}InSn_{0.5}O_6$. In **Figure 5.6** (**c**) the Sn-K edge for x = 0.5 corresponds exactly to the slope onset, rise, and overall chemical shift of the $Sn^{4+}O_2$ standard. Likewise, the In K-edge correlates almost perfectly to the $In^{3+}{}_2O_3$ standard (**Figure 5.6** (**d**)),

confirming that both tin and indium are in the expected 4+ and 3+ oxidation states, respectively.

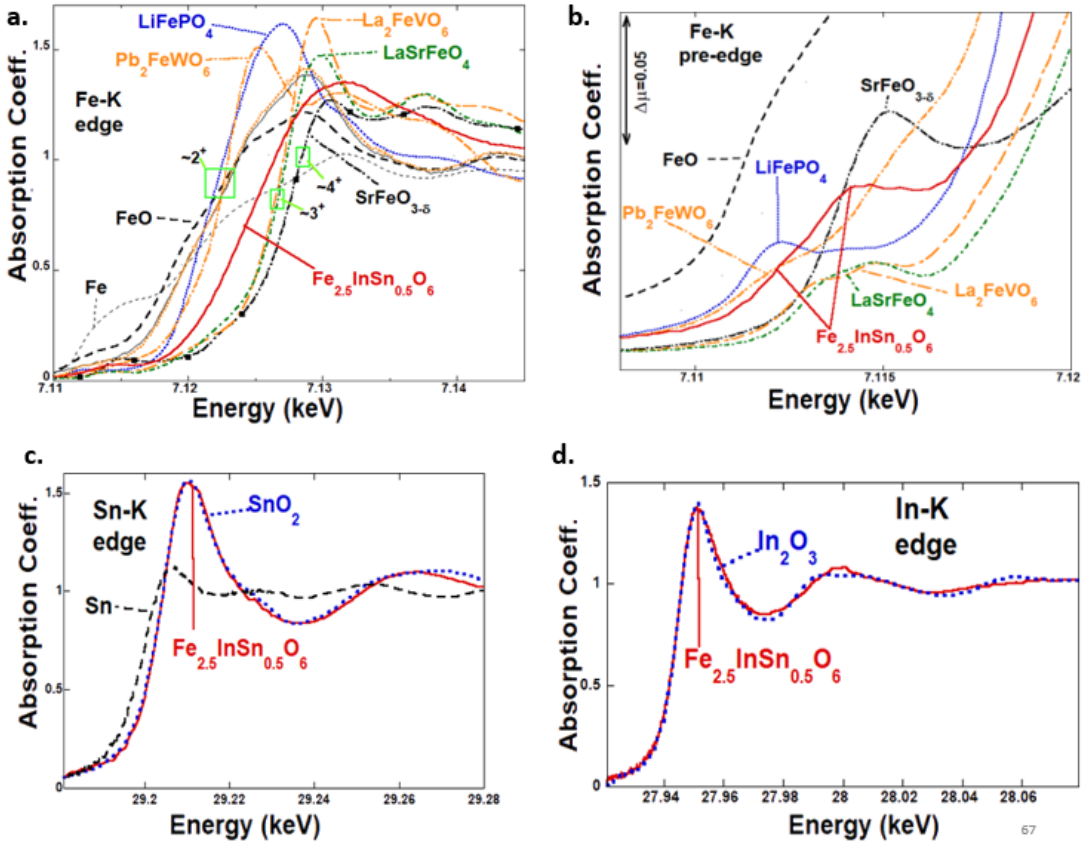

Figure 5.6 Fe K-edge (**a**) and Fe K pre-edge (**b**) spectra for $Fe_{2.5}InSn_{0.5}O_6$ (red) compared with Fe^0, $Fe^{2+}O$, $LiFe^{2+}PO_4$, $Pb_2Fe^{2+}WO_6$, $La_2Fe^{3+}VO_6$, and $SrFe^{4+}O_{3-\delta}$ standards. Below, the Sn K-edge is compared to Sn^0 and $Sn^{4+}O_2$ (**c**), and the In K-edge is compared to $In^{3+}{}_2O_3$ (**d**).

5.2.4 Magnetism in Finite Field

Magnetization vs temperature measurements were performed on x = 0, 0.25, and 0.5 in two sets - the first from 0-400 K with H = 0.1 T, the second from 400 – 800 K with H = 0.05 T. (Two sets of measurements were required as a heating attachment must be fitted to the magnetometer to measure above 400 K). Magnetization measurements were carried by Dr. Zheng Deng at the Institute of Physics, Chinese Academy of Sciences in a magnetometer with a superconducting quantum interference device (SQUID). FC and ZFC magnetic measurements were measured at

a temperature range of 5-400 K with an applied magnetic field of 1 T and from 400K-800K at 0.5 T. A sharp transition can be seen at T_N = ~615 K, ~550K, and ~445 K for x = 0 (**Figure 5.7**), 0.25 (**Figure 5.8**), and 0.5 (**Figure 5.9**), respectively, which appears ferro-or-ferrimagnetic in character. This implies that there are weak ferromagnetic, or canted antiferromagnetic, interactions present even at very high temperatures, similar to what is seen in hematite itself. In all three sets of M(T) measurements the field cooled (FC, red) and zero field cooled (ZFC, black) measurements are collinear near the highest temperatures, with x = 0 beginning to diverge before T_N at about 725 K, x = 0.25 diverging at about 650 K, and x = 0.5 FC/ZFC curves not diverging until after T_N. Linear Curie-Weiss behavior is not seen even at 800 K for these compounds; there remains a slight curvature, which increases as the transition approaches and is most easily visualized in χ^{-1} (plotted for x = 0.5 in **Figure 5.10**).

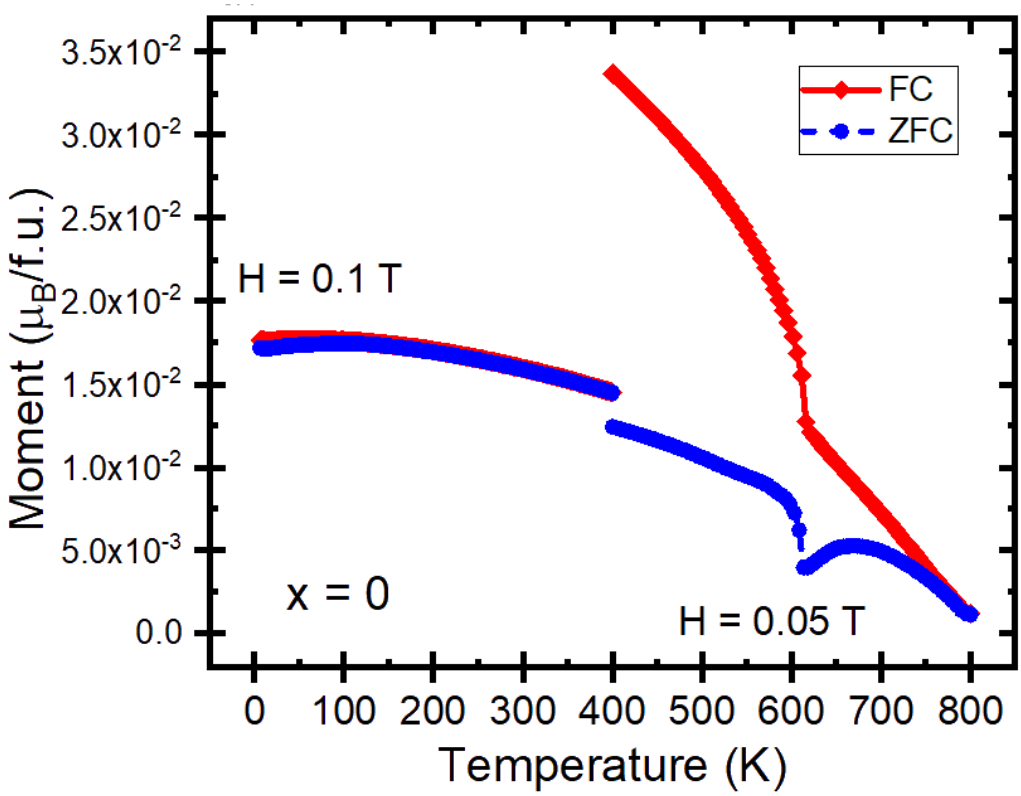

Figure 5.7 Magnetization vs Temperature curves for x = 0 showing a sharp transition at ~615 K. The FC and ZFC curves diverge to some degree after T_N, implying the possibility of frustration, and linear Curie-Weiss behavior is not observed above T_N up to 800 K, the limit of measurement. Measurements had to be performed in two sets- the first from 0 - 400 K (at H = 0.1 T) and the second from 400 – 800 K (at H = 0.05 T) due to limitations with the SQUID heating attachment. The differences in FC/ZFC divergence can be attributed to the fact that the 0 – 400 K trial did not heat the sample above the magnetic transition.

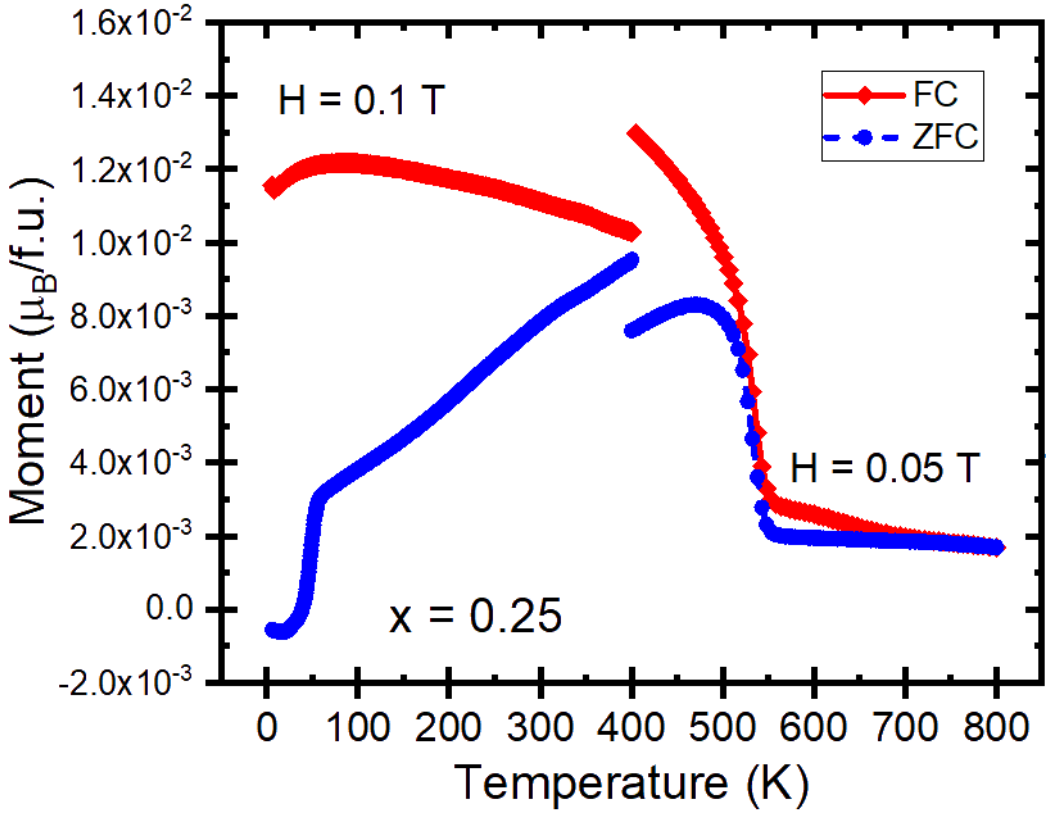

Figure 5.8 Magnetization vs Temperature curves for x = 0.25 showing a sharp transition at ~550K. (The apparent second transition at 50 K is an artifact of oxygen freezing). The FC and ZFC curves diverge to some degree after T_N, implying the possibility of frustration, and linear Curie-Weiss behavior is not observed above T_N up to 800 K, the limit of measurement. Measurements had to be performed in two sets- the first from 0 – 400 K (at H = 0.1 T) and the second from 400 – 800 K (at H = 0.05 T) due to limitations with the SQUID heating attachment. The differences in FC/ZFC divergence can be attributed to the fact that the 0 – 400 K trial did not heat the sample above the magnetic transition.

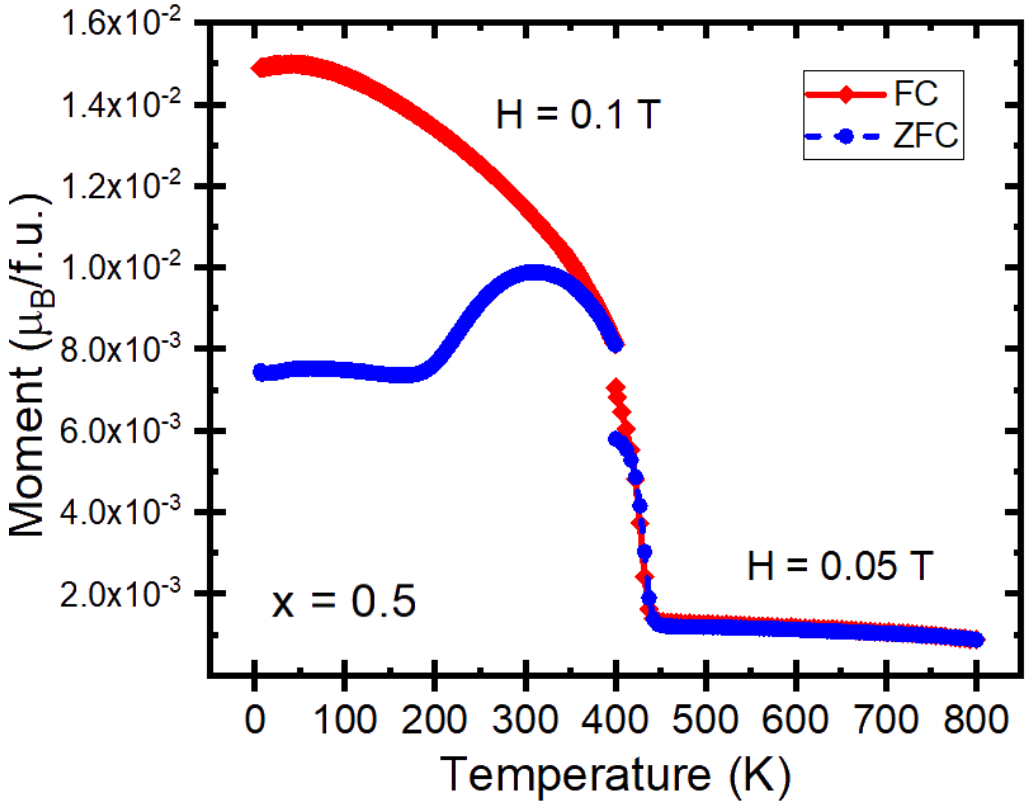

Figure 5.9 Magnetization vs Temperature curves for x = 0.5 showing a sharp transition at ~445 K. The FC and ZFC curves diverge to some degree after T_N, implying the possibility of frustration, and linear Curie-Weiss behavior is not observed above T_N up to 800 K, the limit of measurement. Measurements had to be performed in two sets- the first from 0 – 400 K (at H = 0.1 T) and the second from 400 – 800 K (at H = 0.05 T) due to limitations with the SQUID heating attachment. The differences in FC/ZFC divergence can be attributed to the fact that the 0 – 400 K trial did not heat the sample above the magnetic transition.

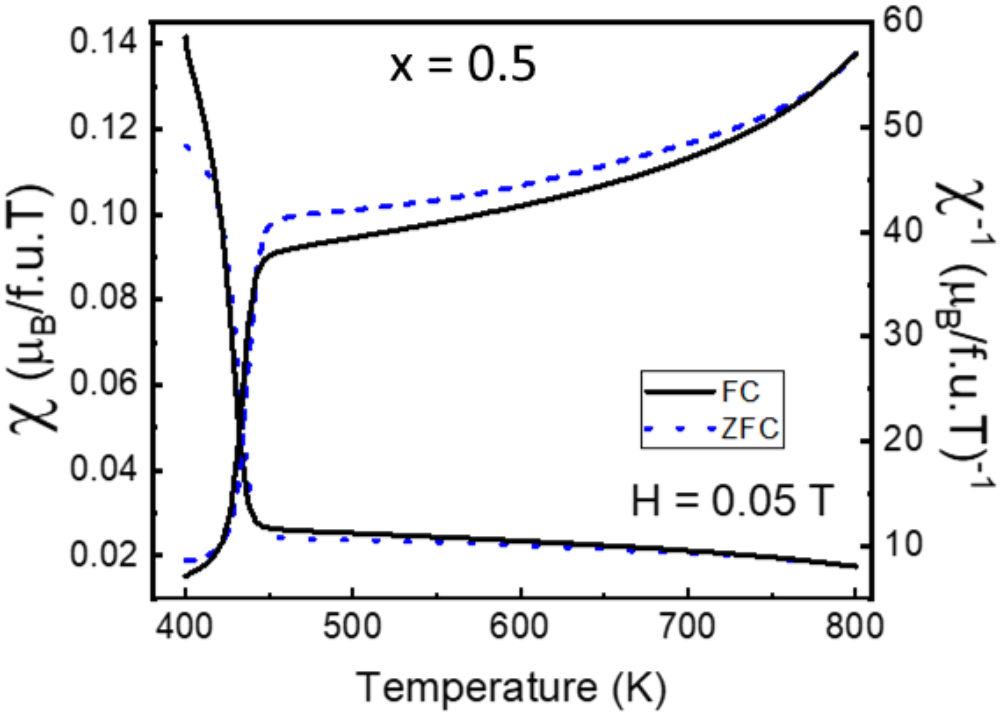

Figure 5.10 Magnetic susceptibility vs temperature (χ(T)) between 400 – 800 K for x = 0.5 measured in a field of H = 0.05 T. Curie-Weiss behavior is not observed up to 800 K, as can be seen in the χ^{-1} plot, which is only included to highlight this nonlinearity (inset).

Below T_N = 953 K, hematite's Fe(III) spins order in ferromagnetic layers with interlayer antiferromagnetic coupling.[270] (This is also seen in our compounds, and will be discussed in detail shortly.) Iron (III) containing members of the corundum family are perhaps most easily understood as dilutions of hematite, such as our x = 0, 0.25, 0.5 compounds, and $ScFeO_3$,[256] $GaFeO_3$,[257] and $InFeO_3$[121]. In these compounds, one could reasonably predict that a decrease in magnetic carrier concentration decreases T_N. However, dilution cannot be the only, or perhaps even the primary, factor that reduces magnetic exchange coupling in these materials, as $InFeO_3$ (T_N = 545 K), $GaFeO_3$ (T_N = 408 K), and $ScFeO_3$ (T_N = 356 K), all have different T_N values despite having a 50/50 M^{3+}/Fe^{3+} cation ratio (**Figure 5.11**). The reduction in T_N in these three polar double corundum compounds instead seems to correlate with increasing deviation of the corner-sharing M-O-M angle from the ideal 180˚ (138.5˚,

130.0˚,129.4˚, respectively), as has been previously observed in comparison with similar perovskite phases.[115]

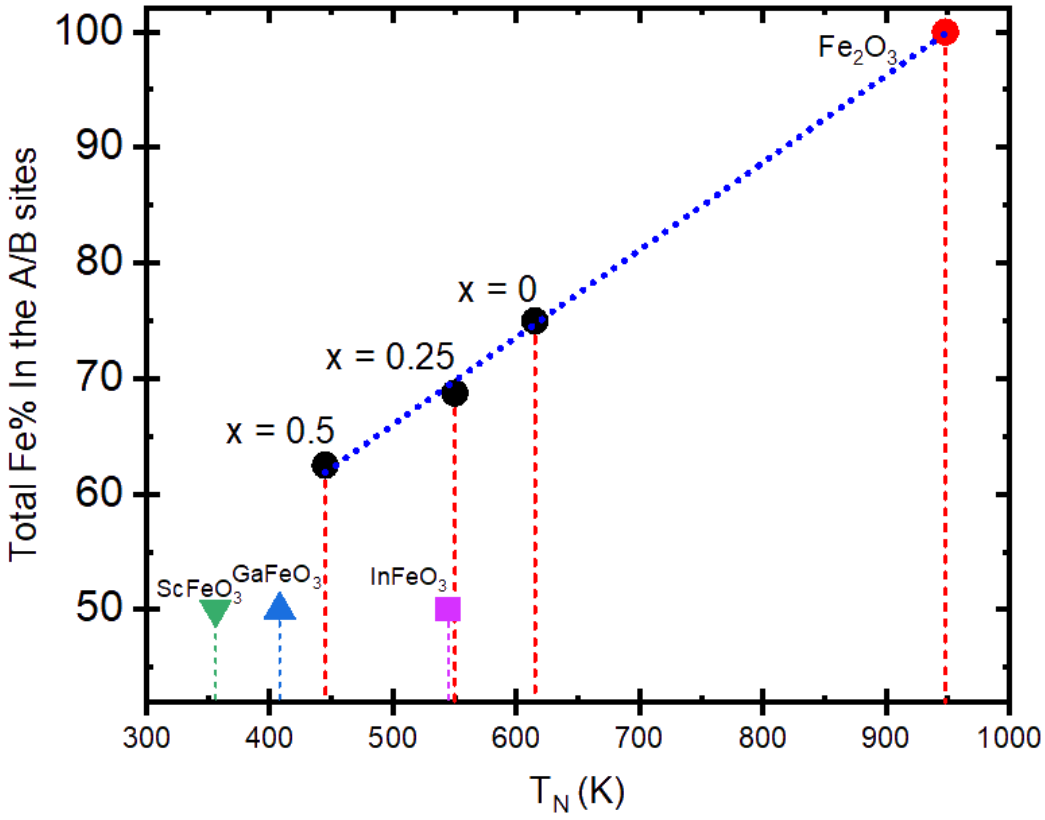

Figure 5.11 Plot of the percent Fe content vs transition temperature for x = 0, 0.25, 0.5 (black circles) compared to: Fe_2O_3[261] (T_N = 948 K, red circle), $InFeO_3$[121] (T_N = 545 K, purple square), $GaFeO_3$[257] (T_N = 408 K, blue triangle), and $ScFeO_3$[256] (T_N = 356 K, green triangle).

In $Fe_{3-x}InSn_xO_6$, the equivalent angle of M-O-M interlayer exchange is 131.33(6)˚ for x = 0.25 and 129.3(6)˚ for x = 0.5 (for the site with Sn) or 133.5(6) ˚ (for the one without), yet the T_N is 550 K and 445 K, respectively. For both, T_N is smaller than that for x = 0 (615 K, c-axis corner sharing angle 131.20(6)˚). Fe_3InO_6 has a tilt angle close to that of $InFeO_3$, but SCXRD refinements indicate a mixture of Fe on both the A and B sites, which seems to lead to greater magnetic exchange between layers than in $InFeO_3$, in which In and Fe do not site-share, and thus a higher

T_N. While the x = 0.25, 0.5 species both have Fe mixed in the A and B sites, and similarly small tilt angles, they also have closed shell d^{10} ions (In^{3+} and Sn^{4+}) admixed in the A and B sites. Closed shell d^{10} cations on the B/B' sites of antiferromagnetic perovskites have been demonstrated to reduce overall magnetic exchange interactions, [271] which should reduce T_N. As the inclusion of Sn^{4+} in x = 0.25, 0.5, and thus the increase in the percent of closed shell cations, is the only differing factor, and yet the T_N of x = 0, 0.25, 0.5 fall by approximately 100 K as d^{10} Sn content increases and the space group evolves from centrosymmetric to noncentrosymmetric, this phenomenon also seems to apply to the corundum structure type family.

To further characterize magnetic properties, isothermal magnetization vs field (M(H)) at various temperatures was collected for x = 0, 0.25, and 0.5 in zero field cooling between 6 T and -6 T in a magnetometer with a superconducting quantum interference device (SQUID). In **Figure 5.12**, below, one can see that at 5 K and 6 T the magnetization of x = 0.5 is about 0.14 μ_B/f.u., and is unsaturated, as is typical of antiferromagnetic coupling. The largest coercive field for x = 0.5 is observed at 5 K as Hc = approximately 0.77 T. M(H) could not be measured above the transition temperature due to limitations of the magnetometer heating attachment.

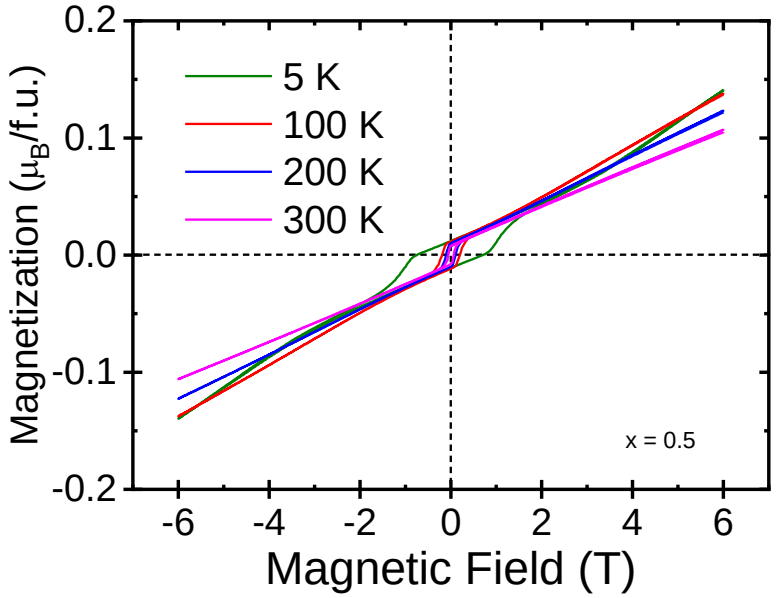

Figure 5.12 Magnetization vs field (M(H)) for x = 0.5 from H = -6 T to H = 6 T for T = 5 K, 100 K, 200 K, and 300 K.

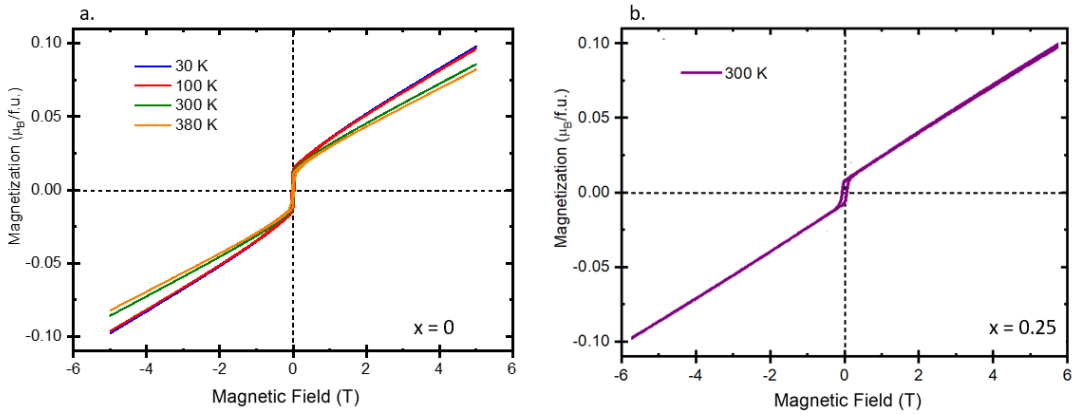

Figure 5.13 Magnetization vs field (M(H)) for x = 0 (**a**) and x = 0.25 (**b**) from H = -6 T to H = 6 T for T = 30 K, 100 K, 300 K, and 380 K and for T = 300 K, respectively.

5.2.5 Resistivity and Magnetotransport

To determine potential dielectric and magnetotransport properties, resistivity (ρ) versus temperature was measured for x = 0.25 and 0.5 from 300 to 150 K (below which the samples became too resistive to accurately measure) under applied magnetic fields of 0 T and 7 T. The x = 0 sample could not be measured despite multiple attempts due to pelletization and contact limitations. As can be seen in **Figure 5.14**, the shape of these curves are characteristic of semiconductors, and the

resistivities below 200 K do not deviate significantly between 0 T and 7 T, which indicate absence of magnetoresistance for both x =0.25 and x = 0.5. The temperature dependence of ρ was fitted by trial and error fitting of the relation $(1/T)^p$ with $p = ½$ giving the best fit for both x = 0.25 and 0.5, independently. This indicates that these compounds are Efros-Shklovskii variable range-hopping semiconductors, ($\rho = \rho_0 \exp(T_0/T)^{1/2}$ where T_0 is the characteristic temperature).[203] The extracted values for ρ_0 and T_0 are $\rho_0 = 5.523 \times 10^{-4}$ (Ohm*cm) $T_0 = 270.69(K^{1/2})$, and $\rho_0 = 1.157 \times 10^{-3}$ (Ohm*cm) and $T_0 = 251.7(0)$ $(K^{1/2})$ for x = 0.25 and x = 0.5, respectively.

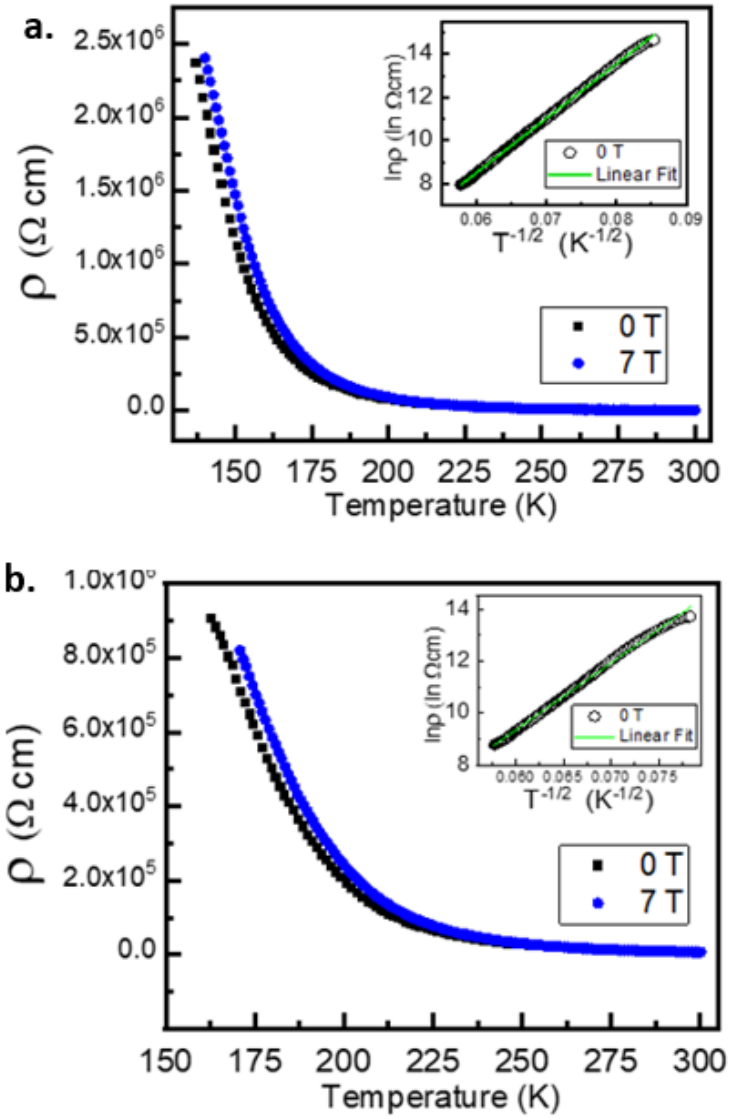

Figure 5.14 Temperature dependent resistivity, ρ, for x = 0.5 (**a**) and x = 0.25 (**b**) measured at 0 T and 7 T. The linear fit plots of ρ versus $T^{1/2}$(inset) indicate variable range hopping conduction

5.2.6 Neutron Powder Diffraction

To understand the nature of the magnetic ordering, neutron powder diffraction (NPD) data for the x = 0.5 sample (the sample most responsive to SHG) were collected and refined by collaborators Prof. Emma McCabe, Dr. Fabio Orlandi, and Dr. Pascal Manuel, and will be discussed here briefly to complete the story of these compounds. Time-of-flight NPD data were collected by collaborators on the WISH diffractometer at the ISIS Neutron and Muon Source.[154] The sample (0.1216 g) was

loaded into a 6 mm diameter cylindrical vanadium can sealed with a copper O-ring. Thirty minute scans were collected at 300 K and then at 50 K intervals up to 500 K. The sample was then cooled and data collected at 5 K and then at 15 K intervals on warming to 300 K. Rietveld refinements[141] were carried out with TopasAcademic software[143] by Emma McCabe, Pascal Manuel, and Fabio Orlandi using the higher resolution banks of data (average two theta of 152.8 and 121.6 degrees spanning a d-spacing range of ~0.7 – 5.2 Å) and no peaks of longer d-spacing were observed in lower angle banks of data in the temperature range studied. ISODISTORT[155] was used to explore possible magnetic structures.

NPD data collected at 500 K were used to determine the distribution of In and Sn over the *A* and *B* sites of x = 0.5 because of the strong contrast in their neutron scattering lengths (4.065 fm, 9.54 fm and 6.2257 fm for In, Fe and Sn, respectively).[205] Results from single crystal X-ray analysis were used to fix the distribution of Fe and In/Sn over the two 6*a* sites. Refinement using single crystal X-ray data for the *R*3*c* model suggested no ordering of Fe over the two sites (Fe occupancies of 0.62(8) for both cation sites (1) (at 0 0 *z*) and (2) (at 0 0 0; *z* coordinate fixed to define the origin of the unit cell along *z*) and so these occupancies were fixed at 0.625 for subsequent refinements. The In and Sn distribution was then refined, using constraints to maintain stoichiometry (a single global atomic displacement parameter factor was used for all sites). This suggested almost complete ordering of In and Sn, with Sn preferentially occupying the slightly smaller site. (An acceptable fit was also obtained with a fully-disordered (corundum) model of $R\bar{3}c$ symmetry, but this centrosymmetric model is not consistent with the SHG activity measured and would be surprising given the non-centrosymmetric structure reported for $InFeO_3$.

Given the very similar electron densities of In and Sn, other techniques such as X-ray diffraction and electron microscopy may not be sensitive to their ordering.)

Consideration of possible magnetic ordering modes using mode inclusion analysis[272] suggested that a good fit was obtained for models with moments in-plane described by $m\Gamma_3$ modes on both Fe sites, analogous to the magnetic structure reported for $InFeO_3$.[121]

This magnetic structure suggests that the magnetic ordering is dominated by AFM exchange between Fe^{3+} ions across the shared face of the AO_6-BO_6 dimers. This leads to FM (001) layers being stacked AFM, similar to that observed at collinear magnetic phase of β-Mn_2InSbO_6. [107] The magnetic moment refined at 5 K (3.88(1) μ_B per Fe) was slightly lower than that expected for high spin Fe^{3+}, possibly due to frustration or to the presence of Fe(II). The moments are predominantly in the (001) planes with equal moments on the A and B sites. Sequential Rietveld refinements suggest a smooth increase in unit cell volume on warming, and there is no evidence of a change in magnetic structure, or magnetostriction, from 5 K – 500 K. The magnetic ordering temperature in $Fe_{2.5}InSn_{0.5}O_6$ (~450 K) is close to that observed for $InFeO_3$,[121] but much higher than that of β-Mn_2InSbO_6[107], presumably reflecting strong Fe – O superexchange interactions. The origin of the small ferromagnetic component observed in magnetic susceptibility measurements may be the same as that suggested for a similarly small FM component in $InFeO_3$ (weak ferromagnetism due to Dzaloshinskii-Moriya interactions in this non-centrosymmetric structure giving a slight canting of Fe^{3+} moments away from this collinear structure).[121] However, our NPD data aren't sensitive to such subtle canting.

5.3 Conclusion and Future Measurements

In conclusion, we have studied the magnetic and structural properties of three new double corundum antiferromagnets with T_N well above room temperature. Structurally, $Fe_{3-x}InSn_xO_6$ is sensitive to small substitutions, with 12.5% closed shell d^{10} Sn^{4+} admixture on the B site enough to change the space group from centrosymmetric $R\bar{3}c$ to polar $R3c$. This transition from centrosymmetric to non centrosymmetric was confirmed via second harmonic generation, a nonlinear optical technique that is sensitive to inversion symmetry, and supported by structure factor single crystal refinement. Nevertheless, current SHG data are rather unsatisfactory, and the differences between polycrystalline temperature dependent and single crystal temperature dependent measurements are not adequately explained. Further SHG experiments are planned to collect more information on crystal domains, potential strain effects, and temperature dependent phenomena, and work in this aspect is ongoing. Adjustments to the SHG analysis when a more complete picture is available may likely effect the interpretation of data in other sections of the paper, especially structural refinements.

Despite having magnetic Fe^{3+} on both the A and B sites, and despite the corner sharing A- O – Fe angles along the c-axis as determined at this stage being between those of $InFeO_3$ (138.5˚ , T_N = 545 K), and $ScFeO_3$ (129.4˚ , T_N = 356 K), magnetic measurements in finite field indicate that x = 0, 0.25, and 0.5 have magnetic ordering transitions at 615 K, 550K, and 445 K, respectively. This indicates that, like in previously observed magnetic perovskites, the inclusion of closed shell d^{10} cations on the B-site has a dramatic effect on magnetic exchange interactions in the corundum structure type. CW behavior is not observed above these transitions transition,

potentially due to weak ferromagnetic or Dzaloshinskii-Moriya interactions canting the AFM Fe moments away from a collinear structure at a temperature above 800 K.

$Fe_{3-x}InSn_xO_6$, x = 0, 0.25, and 0.5 are interesting new corundum oxides with high temperature magnetic transitions and, for x = 0.5, a polar structure. Future investigations, such as DFT and First Principles calculations, will be essential to fully understanding how the inclusion of small amounts of closed shell d^{10} cations can reduce the symmetry of centrosymmetric parent structures, and future NPD measurements on oriented large single crystals synthesized at high pressure will distinguish between the potential *Cc* and *Cc'* magnetic models. These new compounds could potentially lead to many new multiferroic materials that do not sacrifice high temperature functionality in the pursuit of polarization.

5.4 References

26. Schmid, H., Multi-ferroic magnetoelectrics. *Ferroelectrics* **1994,** *162* (1), 317-338.
31. Hill, N. A., Why Are There so Few Magnetic Ferroelectrics? *The Journal of Physical Chemistry B* **2000,** *104* (29), 6694-6709.
53. Živković, I.; Prša, K.; Zaharko, O.; Berger, H., Ni_3TeO_6—a collinear antiferromagnet with ferromagnetic honeycomb planes. *Journal of Physics: Condensed Matter* **2010,** *22* (5), 056002.
55. Badding, J. V., High-Pressure synthesis, characterization, and tuning of solid state materials. *Annual Review of Materials Science* **1998,** *28* (1), 631-658.
101. Ye, M.; Vanderbilt, D., Ferroelectricity in corundum derivatives. *Physical Review B* **2016,** *93* (13), 134303.
102. Cai, G.-H.; Greenblatt, M.; Li, M.-R., Polar Magnets in Double Corundum Oxides. *Chemistry of Materials* **2017,** *29* (13), 5447-5457.
106. Megaw, H., A note on the structure of lithium niobate, $LiNbO_3$. *Acta Crystallographica Section A* **1968,** *24* (6), 583-588.
107. Arévalo-López, Á. M.; Solana-Madruga, E.; Arévalo-López, E. P.; Khalyavin, D.; Kepa, M.; Dos santos-García, A. J.; Sáez-Puche, R.; Attfield, J. P., Evolving spin periodicity and lock-in transition in the frustrated ordered ilmenite-type β-Mn_2InSbO_6. *Physical Review B* **2018,** *98* (21), 214403.
110. Solana-Madruga, E.; Dos santos-García, A. J.; Arévalo-López, A. M.; Ávila-Brande, D.; Ritter, C.; Attfield, J. P.; Sáez-Puche, R., High pressure synthesis of polar and non-polar cation-ordered polymorphs of Mn_2ScSbO_6. *Dalton Transactions* **2015,** *44* (47), 20441-20448.
111. Li, M. R.; Walker, D.; Retuerto, M.; Sarkar, T.; Hadermann, J.; Stephens, P. W.; Croft, M.; Ignatov, A.; Grams, C. P.; Hemberger, J.; Nowik, I.; Halasyamani, P. S.;

Tran, T. T.; Mukherjee, S.; Dasgupta, T. S.; Greenblatt, M., Polar and magnetic Mn_2FeMO_6 (M=Nb, Ta) with $LiNbO_3$-type structure: high-pressure synthesis. *Angew. Chem. Int. Ed. Engl.* **2013,** *52* (32), 8406-10.

112. Li, M.-R.; McCabe, E. E.; Stephens, P. W.; Croft, M.; Collins, L.; Kalinin, S. V.; Deng, Z.; Retuerto, M.; Sen Gupta, A.; Padmanabhan, H.; Gopalan, V.; Grams, C. P.; Hemberger, J.; Orlandi, F.; Manuel, P.; Li, W.-M.; Jin, C.-Q.; Walker, D.; Greenblatt, M., Magnetostriction-polarization coupling in multiferroic Mn_2MnWO_6. *Nature Communications* **2017,** *8* (1), 2037.

115. Kawamoto, T.; Fujita, K.; Yamada, I.; Matoba, T.; Kim, S. J.; Gao, P.; Pan, X.; Findlay, S. D.; Tassel, C.; Kageyama, H.; Studer, A. J.; Hester, J.; Irifune, T.; Akamatsu, H.; Tanaka, K., Room-Temperature Polar Ferromagnet $ScFeO_3$ Transformed from a High-Pressure Orthorhombic Perovskite Phase. *Journal of the American Chemical Society* **2014,** *136* (43), 15291-15299.

116. Li, M. R.; Stephens, P. W.; Retuerto, M.; Sarkar, T.; Grams, C. P.; Hemberger, J.; Croft, M. C.; Walker, D.; Greenblatt, M., Designing Polar and Magnetic Oxides: Zn_2FeTaO_6 - in Search of Multiferroics. *Journal of the American Chemical Society* **2014,** *136* (24), 8508-8511.

117. Li, M. R.; Retuerto, M.; Walker, D.; Sarkar, T.; Stephens, P. W.; Mukherjee, S.; Dasgupta, T. S.; Hodges, J. P.; Croft, M.; Grams, C. P.; Hemberger, J.; Sanchez-Benitez, J.; Huq, A.; Saouma, F. O.; Jang, J. I.; Greenblatt, M., Magnetic-Structure-Stabilized Polarization in an Above-Room-Temperature Ferrimagnet. *Angewandte Chemie-International Edition* **2014,** *53* (40), 10774-10778.

118. Li, M. R.; Retuerto, M.; Stephens, P. W.; Croft, M.; Sheptyakov, D.; Pomjakushin, V.; Deng, Z.; Akamatsu, H.; Gopalan, V.; Sanchez-Benitez, J.; Saouma, F. O.; Jang, J. I.; Walker, D.; Greenblatt, M., Low-Temperature Cationic Rearrangement in a Bulk Metal Oxide. *Angew. Chem. Int. Ed. Engl.* **2016,** *55* (34), 9862-7.

119. Li, M. R.; Croft, M.; Stephens, P. W.; Ye, M.; Vanderbilt, D.; Retuerto, M.; Deng, Z.; Grams, C. P.; Hemberger, J.; Hadermann, J.; Li, W. M.; Jin, C. Q.; Saouma, F. O.; Jang, J. I.; Akamatsu, H.; Gopalan, V.; Walker, D.; Greenblatt, M., Mn_2FeWO_6 : A new Ni_3TeO_6-type polar and magnetic oxide. *Advanced materials (Deerfield Beach, Fla.)* **2015,** *27* (13), 2177-81.

121. Fujita, K.; Kawamoto, T.; Yamada, I.; Hernandez, O.; Hayashi, N.; Akamatsu, H.; Lafargue-Dit-Hauret, W.; Rocquefelte, X.; Fukuzumi, M.; Manuel, P.; Studer, A. J.; Knee, C. S.; Tanaka, K., $LiNbO_3$-Type $InFeO_3$: Room-Temperature Polar Magnet without Second-Order Jahn–Teller Active Ions. *Chemistry of Materials* **2016,** *28* (18), 6644-6655.

141. Rietveld, H., A profile refinement method for nuclear and magnetic structures. *Journal of applied Crystallography* **1969,** *2* (2), 65-71.

143. Coelho, A., TOPAS Academic: General Profile and Structure Analysis Software for Powder Diffraction Data,(2012) Bruker AXS. *Karlsruhe, Germany*.

154. Chapon, L. C.; Manuel, P.; Radaelli, P. G.; Benson, C.; Perrott, L.; Ansell, S.; Rhodes, N. J.; Raspino, D.; Duxbury, D.; Spill, E., Wish: The new powder and single crystal magnetic diffractometer on the second target station. *Neutron News* **2011,** *22* (2), 22-25.

155. Campbell, B. J.; Stokes, H. T.; Tanner, D. E.; Hatch, D. M., ISODISTORT. *J. Appl. Cryst.* **2006,** *39*, 607-614.

169. Naoki, S.; Yoshio, T.; Yoshitaka, Y.; Kiyoshi, S.; Tomoya, U., Direct Speciation of Tin Compounds in Environmental Samples Using Sn K-edge XANES. *Chemistry Letters* **2004,** *33* (3), 264-265.

176. Defregger, S.; Engel, G. F.; Krempl, P. W., Linear and nonlinear optical properties of quartz-type $GaPO_4$. *Physical Review B* **1990,** *43* (8), 6733-6738.

177. Winta, C. J.; Gewinner, S.; Schöllkopf, W.; Wolf, M.; Paarmann, A., Second-harmonic phonon spectroscopy of α–quartz. *Physical Review B* **2018,** *97* (9), 094108.

203. Efros, A. L.; Shklovskii, B. I., Coulomb gap and low temperature conductivity of disordered systems. *Journal of Physics C: Solid State Physics* **1975,** *8* (4), L49.

205. Sears, V. F., Neutron scattering lengths and cross sectioirn. *Neutron news* **1992,** *3* (3), 29-37.
246. Zarzuela, R.; Kim, S. K.; Tserkovnyak, Y., Magnetoelectric antiferromagnets as platforms for the manipulation of solitons. *Physical Review B* **2018,** *97* (1), 014418.
247. Halley, D.; Najjari, N.; Majjad, H.; Joly, L.; Ohresser, P.; Scheurer, F.; Ulhaq-Bouillet, C.; Berciaud, S.; Doudin, B.; Henry, Y., Size-induced enhanced magnetoelectric effect and multiferroicity in chromium oxide nanoclusters. *Nature Communications* **2014,** *5*, 3167.
248. Nan, C.-W.; Bichurin, M. I.; Dong, S.; Viehland, D.; Srinivasan, G., Multiferroic magnetoelectric composites: Historical perspective, status, and future directions. *Journal of Applied Physics* **2008,** *103* (3).
249. Hippel, A. v., Ferroelectricity, Domain Structure, and Phase Transition of Barium Titanate. *Reviews of Modern Physics* **1950,** *22* (3), 221-237.
250. Khomskii, D. I., Multiferroics: Different ways to combine magnetism and ferroelectricity. *Journal of Magnetism and Magnetic Materials* **2006,** *306* (1), 1-8.
251. Ivanov, S. A.; Mathieu, R.; Nordblad, P.; Tellgren, R.; Ritter, C.; Politova, E.; Kaleva, G.; Mosunov, A.; Stefanovich, S.; Weil, M., Spin and Dipole Ordering in Ni_2InSbO_6 and Ni_2ScSbO_6 with Corundum-Related Structure. *Chemistry of Materials* **2013,** *25* (6), 935-945.
252. Zupan, J.; Kolar, D.; Urbanc, V., Magnetic Properties of Ni_3TeO_6. *Materials Research Bulletin* **1971,** *6* (12), 1353-1359.
253. Song, G.; Zhang, W., Comparative studies on the room-temperature ferrielectric and ferrimagnetic Ni_3TeO_6-type A_2FeMoO_6 compounds (A = Sc, Lu). *Scientific reports* **2016,** *6*, 20133.
254. Nassau, K.; Levinstein, H. J.; Loiacono, G. M., Ferroelectric lithium niobate. 1. Growth, domain structure, dislocations and etching. *Journal of Physics and Chemistry of Solids* **1966,** *27* (6), 983-988.
255. Chen, W.-t.; Williams, A. J.; Ortega-San-Martin, L.; Li, M.; Sinclair, D. C.; Zhou, W.; Attfield, J. P., Robust Antiferromagnetism and Structural Disorder in BixCa1−xFeO3 Perovskites. *Chemistry of Materials* **2009,** *21* (10), 2085-2093.
256. Li, M.-R.; Adem, U.; McMitchell, S. R. C.; Xu, Z.; Thomas, C. I.; Warren, J. E.; Giap, D. V.; Niu, H.; Wan, X.; Palgrave, R. G.; Schiffmann, F.; Cora, F.; Slater, B.; Burnett, T. L.; Cain, M. G.; Abakumov, A. M.; van Tendeloo, G.; Thomas, M. F.; Rosseinsky, M. J.; Claridge, J. B., A Polar Corundum Oxide Displaying Weak Ferromagnetism at Room Temperature. *Journal of the American Chemical Society* **2012,** *134* (8), 3737-3747.
257. Niu, H.; Pitcher, M. J.; Corkett, A. J.; Ling, S.; Mandal, P.; Zanella, M.; Dawson, K.; Stamenov, P.; Batuk, D.; Abakumov, A. M.; Bull, C. L.; Smith, R. I.; Murray, C. A.; Day, S. J.; Slater, B.; Cora, F.; Claridge, J. B.; Rosseinsky, M. J., Room Temperature Magnetically Ordered Polar Corundum $GaFeO_3$ Displaying Magnetoelectric Coupling. *Journal of the American Chemical Society* **2017,** *139* (4), 1520-1531.
258. Bozorth, R. M.; Walsh, D. E.; Williams, A. J., Magnetization of Ilmenite-Hematite System at Low Temperatures. *Physical Review* **1957,** *108* (1), 157-158.
259. Lin, S. T., Magnetic Properties of Hematite Single Crystals. I. Magnetization Isotherms, Antiferromagnetic Susceptibility, and Weak Ferromagnetism of a Natural Crystal. *Physical Review* **1959,** *116* (6), 1447-1452.
260. Haigh, G., Observations on the magnetic transition in hematite at-15° C. *Philosophical Magazine* **1957,** *2* (19), 877-890.
261. Morrish, A. H., *Canted antiferromagnetism: hematite*. World Scientific: 1994.
262. Gaudon, M.; Pailhé, N.; Majimel, J.; Wattiaux, A.; Abel, J.; Demourgues, A., Influence of Sn^{4+} and Sn^{4+}/Mg^{2+} doping on structural features and visible absorption properties of α-Fe_2O_3 hematite. *Journal of Solid State Chemistry* **2010,** *183* (9), 2101-2109.

263. Nespolo, M.; Ferraris, G., Applied geminography - symmetry analysis of twinned crystals and definition of twinning by reticular polyholohedry. *Acta Crystallographica Section A* **2004,** *60* (1), 89-95.
264. Kim, S. W.; Emge, T. J.; Deng, Z.; Uppuluri, R.; Collins, L.; Lapidus, S. H.; Segre, C. U.; Croft, M.; Jin, C.; Gopalan, V.; Kalinin, S. V.; Greenblatt, M., $YCrWO_6$: Polar and Magnetic Oxide with $CaTa_2O_6$-Related Structure. *Chemistry of Materials* **2018,** *30* (3), 1045-1054.
265. Lipson, H.; Woolfson, M. M., An extension of the use of intensity statistics. *Acta Crystallographica* **1952,** *5* (5), 680-682.
266. Berry, F. J.; Greaves, C.; Helgason, Ö.; McManus, J.; Palmer, H. M.; Williams, R. T., Structural and Magnetic Properties of Sn-, Ti-, and Mg-Substituted α-Fe_2O_3: A Study by Neutron Diffraction and Mössbauer Spectroscopy. *Journal of Solid State Chemistry* **2000,** *151* (2), 157-162.
267. Bosi, F., Bond valence at mixed occupancy sites. I. Regular polyhedra. *Acta Crystallographica Section B* **2014,** *70* (5), 864-870.
268. Waychunas, G. A.; Apted, M. J.; Brown, G. E., X-ray K-edge absorption spectra of Fe minerals and model compounds: Near-edge structure. *Physics and Chemistry of Minerals* **1983,** *10* (1), 1-9.
269. Ogi, T.; Tamaoki, K.; Saitoh, N.; Higashi, A.; Konishi, Y., Recovery of indium from aqueous solutions by the Gram-negative bacterium Shewanella algae. *Biochemical Engineering Journal* **2012,** *63*, 129-133.
270. Catti, M.; Valerio, G.; Dovesi, R., Theoretical study of electronic, magnetic, and structural properties of α–Fe_2O_3 (hematite). *Physical Review B* **1995,** *51* (12), 7441-7450.
271. Feng, H. L.; Yamaura, K.; Tjeng, L. H.; Jansen, M., The role of nonmagnetic d^0 vs. d^{10} B-type cations on the magnetic exchange interactions in osmium double perovskites. *Journal of Solid State Chemistry France* **2016,** *243*, 119.
272. McCabe, E. E.; Stock, C.; Bettis, J.; Rodriguez, E. E.; Whangbo, M. H.; Evans, J. S. O., Magnetism of Fe and Ce sublattices in ZrCuSiAs-related Ce2O2FeSe2: a combined NPD, INS and DFT study. *Phys. Rev. B* **2014,** *90*, 235115.

Chapter 6: $In_2Mn_{1.1}Sn_{0.9}O_6$ - A new corundum insulator with highly frustrated short-range magnetic interactions

6.1 Introduction

Scientists often face frustration in the laboratory, but an occasional amount of frustration is necessary to produce interesting results. In the case of magnetic materials, this is even more true for the creation than it is for the creator. In multiferroic and spintronic materials, frustration can lead to "the most complex magnetic order," including non collinear spin arrangements and long-wavelength magnetic modulations.[273] Magnetic frustration may emerge when a there is competition between magnetic sublattices, or when the geometry of a lattice is such that energy cannot be uniquely minimized.[274] In some materials, such as the extensively studied spin-glass alloy CuMn,[275-277] frustration is tied very closely to crystallographic disorder, which thus randomizes the location of spins (superimposing a somewhat amorphous, or even fully glass-like magnetic structure on a crystalline nuclear structure). Crystallographic disorder thus adds a degree of random, yet competing interactions to spins, resulting in frustration.[274]

In contrast to purely disorder-based frustration, frustration can also be caused by the geometry of the lattice itself.[278-282] Consider a 2-D kagomé lattice of spins that can point either up or down (AKA Ising spins), as shown in **Figure 6.1.** There is a large amount of degeneracy in this ground state. This is very different from traditional ferromagnetic (FM) or antiferromagnetic (AFM) crystals, where all unpaired electron spins align in one direction (↑↑↑↑) or align antiparallel (↑↓↑↓), respectively, which leads to long range order and macroscale magnetic effects. Theoretically speaking, in

AFM crystals where the unit cells are made up of triangular lattices, such as in pyrochlore or kagomé systems, or in some hexagonal honeycomb systems, there is no reason for spins to transition, or "freeze," into an ordered ground state, and some degree of spin fluctuation can persist even to very low temperatures.

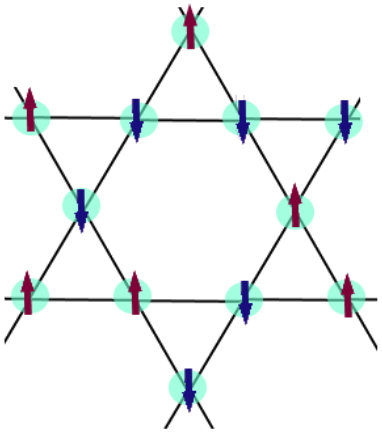

Figure 6.1 Simple Ising-model Frustration in a Kagome Lattice

In all cases, degree of frustration is discussed in terms of the frustration factor, *f*

$$f = \frac{|\theta|}{T_N} \tag{6.1}$$

where θ is the Weiss constant, and T_N is the antiferromagnetic transition temperature (which in the case of ferrimagnets can be substituted for T_C). A value of $f > 1$ indicates the presence of frustration, and $f > 5$ is associated with highly frustrated materials, especially those which involve multiple magnetic sublattices, however values of *f* as high as $f = \infty$ have been theoretically proposed.[274]

$InMnO_3$ (space group $P6_3cm$) is a particularly interesting example of an antiferromagnet with a high degree of frustration ($f \approx 6.65$), as the frustration in this case drives the magnetic order.[283] Typically, frustration in hexagonal manganites arises due to a combination of triangular AFM first-neighbor interactions within the planes (geometric frustration) and competing magnetic interactions between Mn

cations in neighbors between planes.[284] The large difference in magnitude between these two sets of interactions in $InMnO_3$ implies instead pseudodipolar interactions between the Mn of different planes, which are expected[285] (and seen) to be weaker than other exchange interactions by up to an order of magnitude. While $InMnO_3$ is not ferroelectric (no hysteresis is seen below 250 K), an anomaly in low frequency permittivity that occurs near T_N = 118 K implies magnetoelectric coupling.

In 2011, Aimi *et. al.* reported $MnSnO_3$, a polar *R*3*c* corundum derivative synthesized at high temperature and pressure.[54] This compound exhibits a sharp AFM magnetic transition at 53 K, and a Weiss temperature of -130 K, indicating that there is significant frustration present in the magnetic interactions of this material ($f \approx 2.45$). Interestingly, $MnSnO_3$ exhibits a second transition to weak ferromagnetism at 50 K, which corresponds to an anomaly in the dielectric permittivity, indicating that these properties could be correlated. $MnSnO_3$ is therefore considered a good candidate for theoretical investigations into multiferroicity, and detailed calculational studies indicate that ferroelectricity in this compound is primarily dependent on distortions of the B-site cations.[286]

Two years later, Yi *et. al.* reported In_2NiMnO_6, a distorted double perovskite (space group $P2_1/n$, $f \approx 2.24$) with small A-site cations synthesized at high pressure and temperature.[76] Antiferromagnetic order begins in this compound at 26 K, and a field induced transition to a FM state is observed from 18 KOe at 5 K. Further studies on In_2NiMnO_6 by Terada *et al.*[287] showed that strong ferroelectric polarization ($P \simeq 30 \mu C/m^2$ at 26 K) coincides with the magnetic transition, and is attributed to a complicated spin structure which combines B-site chemical order, octahedral tilting, and spin helicity which results in a so-called “ferriaxial” polarization mechanism.

In this work we present $In_2Mn_{1.1}Sn_{0.9}O_6$, synthesized at high temperature and pressure (6 GPa, 1400° C) with the mentorship and guidance of Professor Xiaoyan Tan, who lead this project. The tolerance factor, t = 0.72, is slightly smaller than that of the related In_2NiMnO_6 (t = 0.77) and as might be expected from t factor trends, $In_2Mn_{1.1}Sn_{0.9}O_6$ crystallizes in the $R\bar{3}c$ double corundum structure type rather than as a distorted double perovskite.[56] Magnetism in this compound is dominated by antiferromagnetic interactions as indicated by the negative Weiss coefficient (θ = -87 K). Moreover, these interactions are likely highly frustrated, as indicated by a potential frustration factor of f > 15 and low potential transition or spin freeze temperature (T_N < 5 K) possibly driven by the competing interactions of Mn^{2+} cations in the disordered R$\bar{3}$c lattice. Resistivity measurements were attempted, but the sample was found to be too resistive, and thus an insulator. Herein, the nuclear structure is reported in detail, and the initial magnetic measurements are described.

6.2 Results and Discussion

6.2.1 Initial Characterization

Preliminary powder X-ray diffraction experiments (λ =1.5418 Å) indicated that $In_2Mn_{1.1}Sn_{0.9}O_6$ crystallizes as either centrosymmetric $R\bar{3}c$ or noncentrosymmetric $R3c$. As Friedel's Law states that a twin operation is equivalent to an inversion center in terms of intensities when converting from real space to reciprocal space, it is impossible to distinguish between these two space groups with PXD alone.[263] A secondary characterization technique, such as high angle annular dark field (HAADF) scanning transmission electron microscopy (STEM) must be employed to determine if the structure is centrosymmetric or noncentrosymmetric. For $In_2Mn_{1.1}Sn_{0.9}O_6$, these data (as well as 27 separate SEM/EDX point analyses which showed an average composition of $In_{1.98(6)}Mn_{1.10(4)}Sn_{0.91(3)}O_x$) were collected and analyzed in detail by

collaborators at the University of Antwerp, Prof. Joke Hadermann and Dr. Maria Batuk.

HAADF-STEM images of $In_2Mn_{1.1}Sn_{0.9}O_6$ were taken along the [100] and [241] directions. As can be visualized in **Figure 6.2**, the *R*3*c* and $R\bar{3}c$ space groups consist of face-sharing dimers of AO_6 and B/B'O_6 octahedra which edge share within the layers and corner share between them. One third of the octahedral holes are vacancies. (In $R\bar{3}c$, as seen **Figure 6.4**, the octahedra would be a single color as there is no distinction between the A and B/B' sites. Otherwise, the two structures are identical). Along the chosen [100] and [241] directions, distinct columns of A and B/B' cations can be clearly seen, especially in **Figure 6.2**(**b**). In STEM images, the brightness of dots is proportional to the average atomic number in each column (intensity ~ Z^2 , Z_{In} = 49, Z_{Mn} = 25, Z_{Sn} = 50). Since the Z of In the nominal A site is higher than the average Z of Mn and Sn in the nominal B/B' site, it should be that the A columns appear brighter if $In_2Mn_{1.1}Sn_{0.9}O_6$ crystallizes as ordered *R*3*c* (**Figure 6.3**).

Experimental HAADF-STEM results did not correspond with the theoretical projections for *R*3*c*. Instead, as can be seen in **Figure 6.4**, the distribution of intensities between the nominal A and B/B' sites is random, indicating that there is no order between these sites. A statistical distribution of In and Mn/Sn over these sites indicates that $In_2Mn_{1.1}Sn_{0.9}O_6$ crystallizes in the centrosymmetric $R\bar{3}c$ space group.

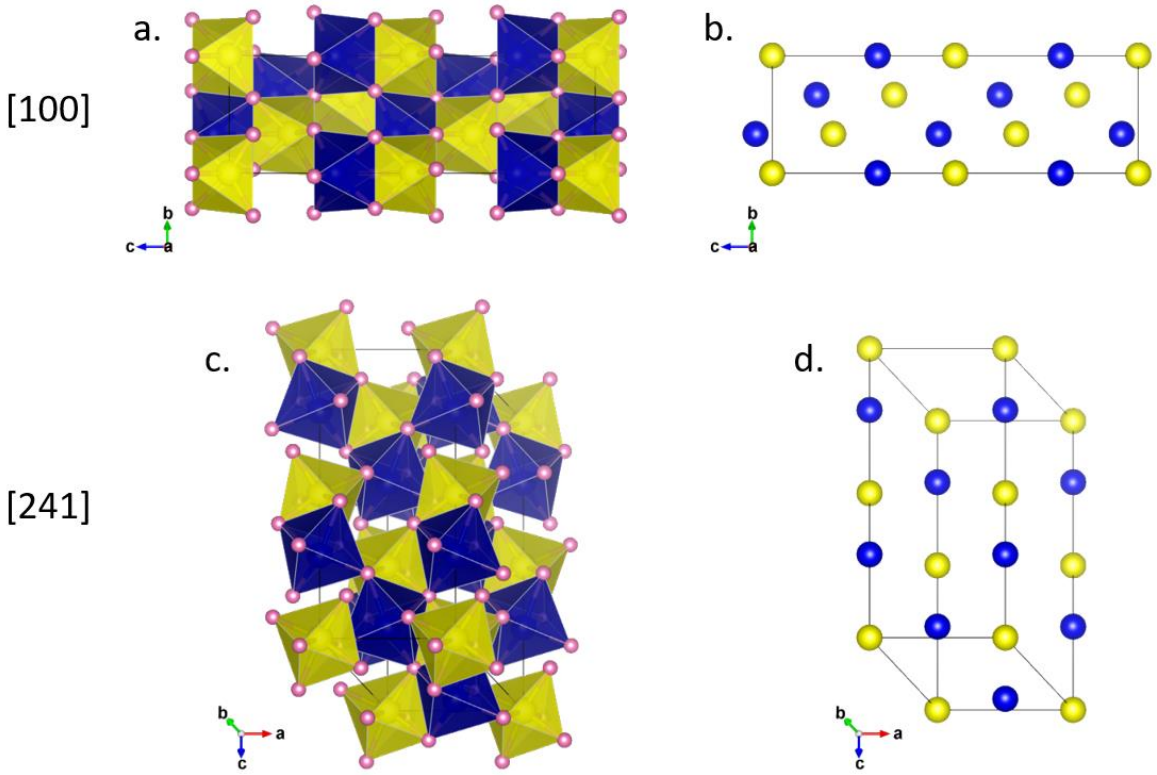

Figure 6.2 Projections of a theoretical *R*3*c* structure for $In_2Mn_{1.1}Sn_{0.9}O_6$. The yellow A (In) cation octahedra form face sharing dimers with the blue B/B' (Mn/Sn) cation octahedra (**a, c**). These octahedra align in the ordered space group so that there are columns of A and B cations. This structure is viewed along the [100] direction with octahedra (**a**) and with the octahedra and oxygen omitted (**b**) to more clearly show the expected A and B columns. A second projection along the [241] direction with octahedra (**c**) and with octahedra and oxygen atoms omitted (**d**) is also depicted.

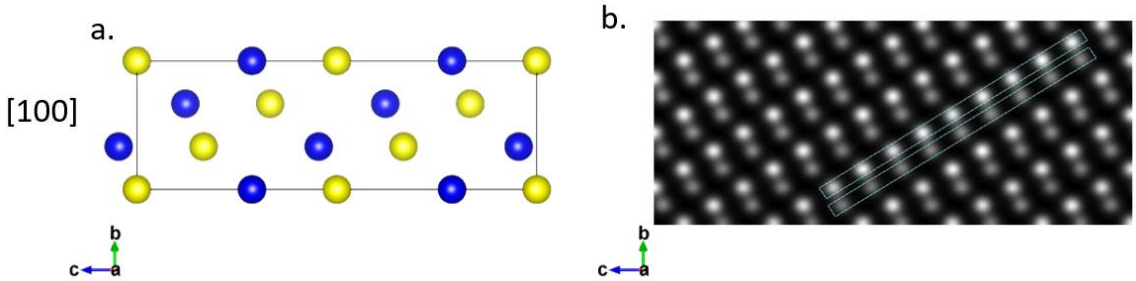

Figure 6.3 Graphical (**a**) and calculated (**b**) HAADF-STEM images of the theoretical *R*3*c* structure of $In_2Mn_{1.1}Sn_{0.9}O_6$ along the [100] direction (calculated by collaborators at the University of Antwerp) showing that the A and B atomic columns should have different intensity on the HAADF-STEM images in case of ordering.

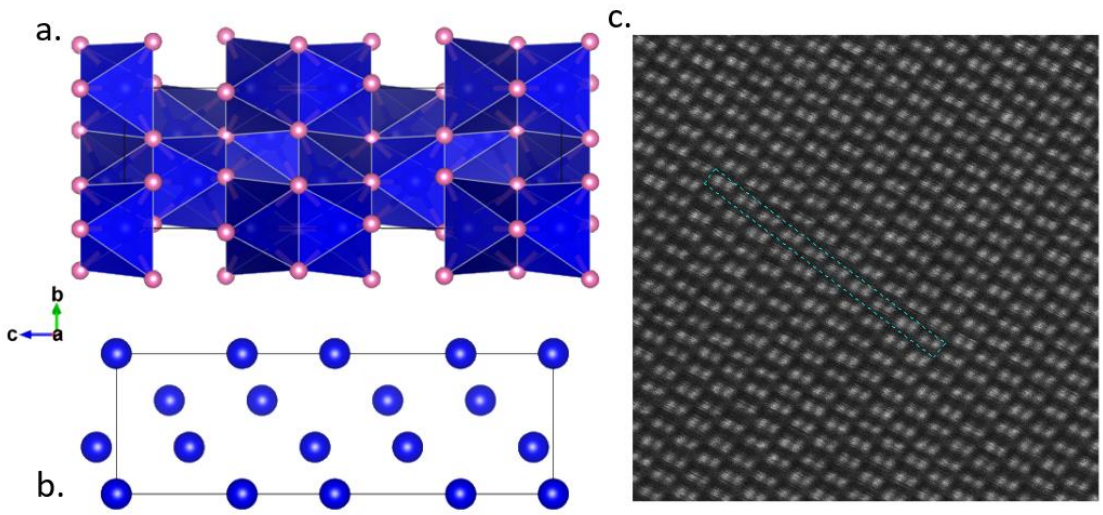

Figure 6.4 Graphical (**a, b**) and experimental HAADF-STEM (**c**) images of the actual $R\bar{3}c$ structure of $In_2Mn_{1.1}Sn_{0.9}O_6$. Octahedra and oxygen are shown in (**a**) and omitted from (**b**) for clarity. The intensities of the A and B/B' cation columns are equal, indicating that $In_2Mn_{1.1}Sn_{0.9}O_6$ crystallizes as disordered $R\bar{3}c$.

6.2.2 Crystal Structure of $In_2Mn_{1.1}Sn_{0.9}O_6$

Room temperature powder synchrotron diffraction data was collected at Argonne National Laboratory 11-BM beamline by Dr. Saul Lapidus via the mail-in service. Results of Reitveld refinements (**Figure 6.5**) indicate that $In_2Mn_{1.1}Sn_{0.9}O_6$ crystallizes in hexagonal $R\bar{3}c$ with a = 5.423(8) Å and b = 14.416(9) Å (**Figure 6.6**), and show 1.89% SnO_2 impurity and trace amounts of an $In_3Sn_4O_{12}$-like Sn-doped indium oxide impurity as well. Other possible impurities, such as magnetic $MnSnO_3$, $In_2Mn_2O_7$, and Mn_2SnO_4, were added to the refinement after the main phase was fit, but refined as 0.01% or less, so are not included in this analysis. The occupancies of the cations site were fixed and based on the empirical formula found via SEM/EDX analysis, then refined one at a time, with constraints added to ensure 100% occupancy.

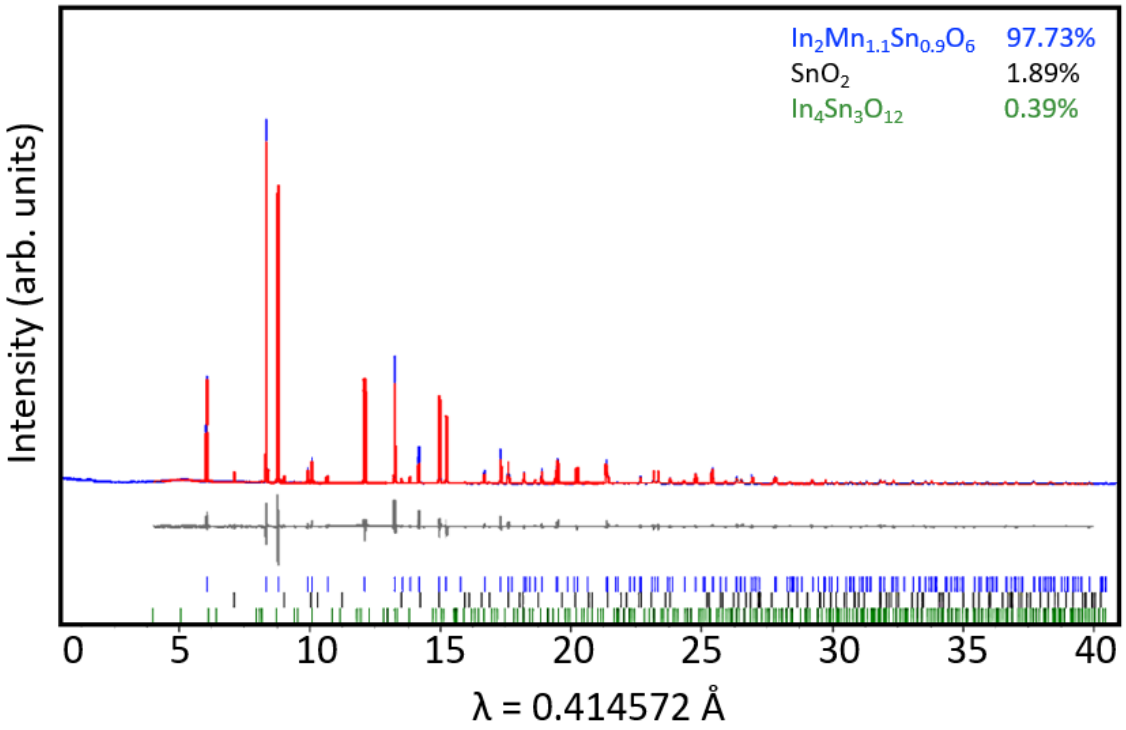

Figure 6.5 Refinement profile for $In_2Mn_{1.1}Sn_{0.9}O_6$ using room temperature SPXD data in space group $R\bar{3}c$ in the hexagonal setting. The observed pattern, calculated pattern, and difference pattern are shown in light blue, bright red, and grey lines, respectively. The Bragg positions of the main phase are shown as blue ticks, SnO_2 as grey ticks, and the trace Sn-doped indium oxide-like phase ($In_4Sn_3O_{12}$) as green.

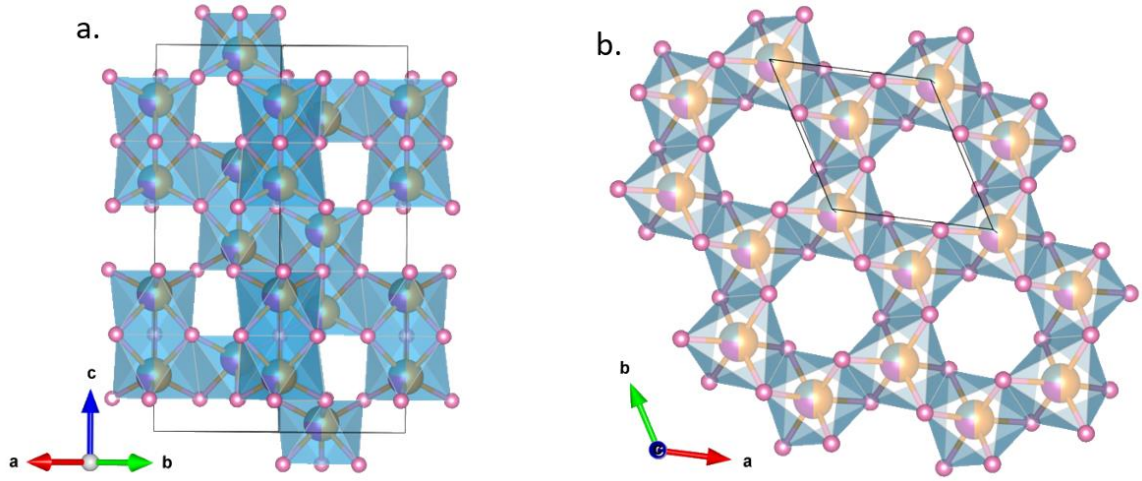

Figure 6.6 Illustration a single R$\bar{3}$c double corundum unit cell of $In_2Mn_{1.1}Sn_{0.9}O_6$, viewed along the A-B plane (**a**) and down the c axis in a single plane (with the x, and with the x, and y coordinates projected from -1.5 to 1.5 to show the honeycomb-like edge sharing of octahedra within each layer, **b**) , as found by SPXD. Indium is in gold, manganese pink, and tin grey.

Select details of synchrotron structural refinements are presented in **Table 6.1**, as are bond lengths and angles (**Table 6.2**). To our knowledge, there are only three other high pressure double corundum derivatives that contain at least one magnetic cation and crystallize in the centrosymmetric $R\bar{3}c$ space group: Mn_2FeRuO_6, which was published by our group in 2018,[288] and $Fe_{3-x}InSn_xO_6$ (Sn = 0, 0.25), which were discussed in **Chapter 5** of this work (hematite itself is not typically synthesized[289] at high pressure).

The two sets of metal-oxygen bond lengths, 2.09(3)and 2.23(6) Å in the $In_2Mn_{1.1}Sn_{0.9}O_6$ MO_6 face sharing octahedra are somewhat longer for $In_2Mn_{1.1}Sn_{0.9}O_6$ than isostructural Mn_2FeRuO_6 (1.997(1) and 2.090(1) Å, as refined from neutron powder diffraction) which is reasonable considering the increased size of In^{3+} (0.8 Å) and Sn^{4+} (0.69 Å) over $Mn^{2+/3+}$ (0.83/0.645 Å) and $Ru^{3+/4+}$ (0.68/0.62 Å).[288] The average bond length of 2.165 Å is much closer to that of $R\bar{3}c$ Fe_3InO_6 (2.073 Å) and $Fe_{2.75}InSn_{0.25}O_6$ (2.084 Å), which is reasonable as these compounds at least have in In^{3+} common with $In_2Mn_{1.1}Sn_{0.9}O_6$.

The $In_2Mn_{1.1}Sn_{0.9}O_6$ metal-oxygen-metal angle between edge sharing MO_6 octahedra within the layers is 86.04(5)° and 131.45(7)° between corner-sharing cations in separate layers, thus magnetic exchange could potentially be ferromagnetic within the layers and antiferromagnetic between the layers,[65] as is common in double corundum type compounds.[121, 266, 288] However, this is not guaranteed despite precedent as NPD experiments on Mn_2FeRuO_6, NPD showed a single collinear magnetic sublattice in which all spins were of apparently equal magnitude. This was attributed to, but cannot be fully explained by, disorder as Fe_2O_3 itself consists of FM layers with AFM coupling between them.

Bond Valance Sum (BVS) calculations indicate that In is ~+3, Mn ~+2, and that Sn has an average oxidation state of ~+3. It should be noted that BVS calculations are generally too simplistic to accurately estimate the valence states of cations in mixed-occupancy sites, and so the oxidation state of Sn is likely to be underestmated.[267] The true valence of the cations in $In_2Mn_{1.1}Sn_{0.9}O_6$ was therefore determined via X-ray absorption near-edge spectroscopy (XANES), which will be discussed shortly.

Table 6.1 Lattice parameters and positions for $In_2Mn_{1.1}Sn_{0.9}O_6$ generated through SPXD

$In_2Mn_{1.1}Sn_{0.9}O_6$	
Temperature	Room Temperature
Wavelength	0.414572 Å
Crystal System	Trigonal
Space Group	$R\bar{3}c$ (167)
a/Å	5.423(8)
c/ Å	14.416(9)
V/ Å	367.29(5)
In/Mn/Sn, A-site	
Wyck.	12c
Biso /Å^2	0.56(7)
Occupancy	0.49576/0.27598/0.22826
O	
Wyck.	18*e*
Occupancy	1
Biso /Å^2	0.56(8)
R_p, R_{wp}, R_{exp}	*9.91309, 13.03295, 8.82997*

Table 6.2 Select bond distances and angles for $In_2Mn_{1.1}Sn_{0.9}O_6$ generated through SPXD

$In_2Mn_{1.1}Sn_{0.9}O_6$			
Selected bond lengths/Å			
AO_6			
A-O x 3	2.09(3)		
-O x 3	2.23(6)		
<A-O>	2.165		
Selected Bond Angles/˚		Selected Bond Angles/˚	
A-O-A	86.0456(0)	O-A-O	78.5637(0)
	95.1810(0)		84.8190(0
	118.0646(0)		90.0179(0)
	131.4572(0)		103.6894(0)
			161.3746(0)
Bond Valence Sums			
In/Mn/Sn	3.006/2.059/3.030		

6.2.3 XANES

In order to accurately determine the oxidation states of the cations in $In_2Mn_{1.1}Sn_{0.9}O_6$, XANES data were collected concurrently with several standards of different oxidation states in similar coordination environments at Brookhaven National Laboratory by Professor Mark Croft, and by Professor Carlo Segre at Argonne National Laboratory via the mail-in service. Sample analysis and interpretation was performed with the close mentorship of Prof. Mark Croft, who prepared and selected the figures.

Simplistically speaking, a sample will absorb an X-ray of appropriate energy to cause a core-shell electron of a specific ion in the substance to transition to a higher energy level. Cations in higher oxidation states require more energy to eject a core electron, and thus the XANES spectra will move to the right (higher energy) as oxidation state increases. By comparing an unknown sample to standards of known oxidation state and coordination (as coordination which also affects the shape and rise

of the absorption edge) one can reliably deduce the oxidation state of the metal ions in almost any condensed matter material.[168-171]

Figure 6.7 shows the Mn-K pre-edge (**a**) and Mn K-edge (**b**) of $In_2Mn_{1.1}Sn_{0.9}O_6$ compared with several standards from 0 to 4+ oxidation states. The K-edge and pre-edge of most transition metals is dominated by transitions from 1s to 4p orbitals, and typically takes the form of a step-continuum-onset structure.[83] There is a strong double peak on the main edge of $In_2Mn_{1.1}Sn_{0.9}O_6$ that is not seen at all in the two highest oxidation state standards, but which is apparent (albeit much more subtly) in the $Mn^{2+}O$ standard. Additionally the energy shift and rise of both the pre-edge and main edges corresponds very closely to that of the $Mn^{2+}O$ standard. This, combined with previous BVS calculations, indicates that the Mn is indeed in the 2+ oxidation state.

Figure 6.8 shows the In K-edge (**a**) and Sn K-edge (**b**) structures compared to several standards. The In K-edge of $In_2Mn_{1.1}Sn_{0.9}O_6$ corresponds almost perfectly with the In^{3+} standard in terms of both chemical shift and the shape and intensity of the slope of the curve. Likewise, the Sn K-edge structure is almost perfectly overlaid with the Sn^{4+} standard, indicating that Sn in this compound is in the +4 oxidation state.

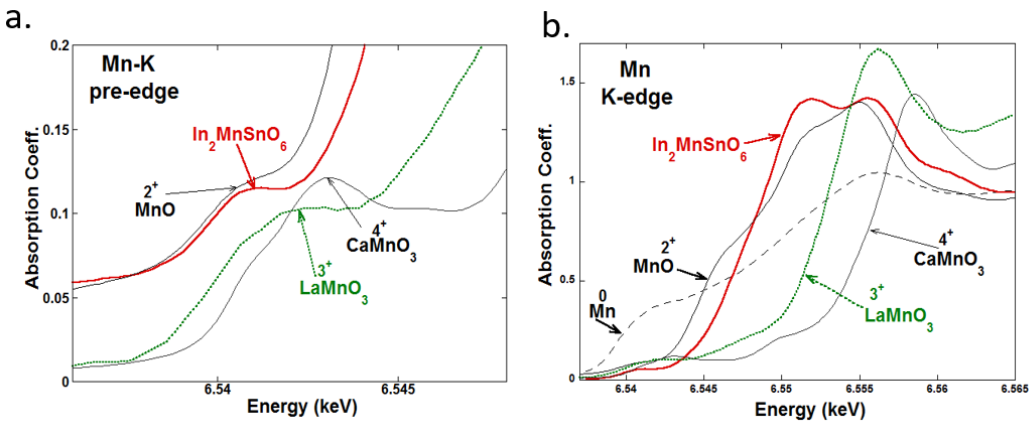

Figure 6.7 The Mn K-pre-edge (**a**) and K-edge (**b**) spectra for $In_2Mn_{1.1}Sn_{0.9}O_6$ compared with Mn^0 metal (**b** only) $Mn^{2+}O$, $LaMn^{3+}O_3$, and $CaMn^{4+}O_4$ standards.

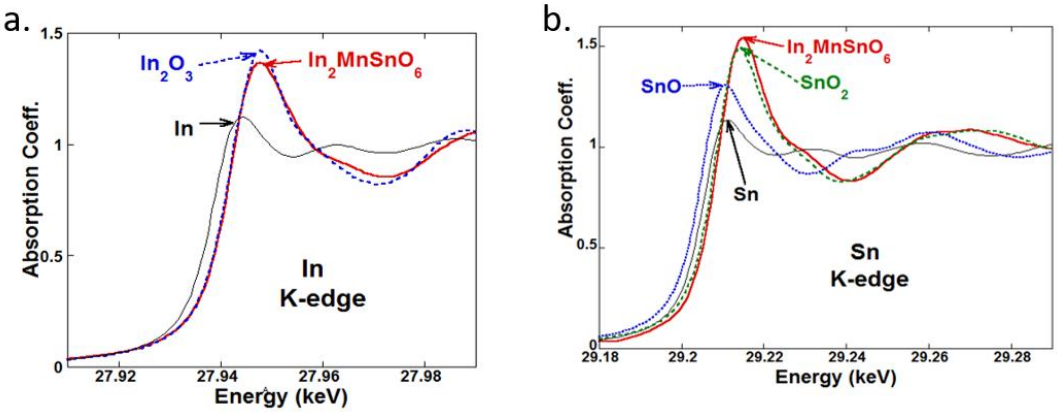

Figure 6.8 The In K-edge (**a**) compared to In^0 and $In^{3+}{}_2O_3$ standards as well as the Sn K-edge (**b**) compared to Sn^0, $Sn^{2+}O$, and $Sn^{4+}O_2$ standards.

6.2.4 Magnetic Measurements

Field cooled (FC) and zero field cooled (ZFC) magnetic measurements were performed for $In_2Mn_{1.1}Sn_{0.9}O_6$ from 5 – 300 K at a field of H = 0.1 T in a magnetometer with a superconducting quantum interference device (SQUID) at the Institute of Physics, Chinese Academy of Sciences by Dr. Zheng Deng. The susceptibility curve (**Figure 6.9**) shows that there is no distinct magnetic transition over this temperature range, and the shape of χ is visually consistent with

paramagnetism in this temperature range. By plotting the inverse susceptibility (χ^{-1}), we see more clearly that the susceptibility is not entirely consistent with a simple paramagnetic phase; there is a small anomaly at ~225 K, where the FC curve deviates from the ZFC. This anomaly is not consistent with a magnetic transition nor is it in line with the characteristic irreversibility expected from spin glass behavior, and so could be due to impurities. However, the potential magnetic impurities that we found through literature searches[54, 286, 290-295] all have transitions well below the anomaly present here; ferromagnetic pyrochlore $In_2Mn_2O_7$, the potential impurity with the highest transition temperature (T_C = ~ 150 K)[296] still transitions ~75 K below the measured anomaly. This could indicate that the "impurity" present consists of clusters or domains within the $In_2Mn_{1.1}Sn_{0.9}O_6$ sample itself. Measuring the magnetization vs temperature of $In_2Mn_{1.1}Sn_{0.9}O_6$ at a range different fields could elucidate the origin of this anomaly. At higher fields, impurity effects would be suppressed. At lower fields, subtle magnetic effects, if present, could become more apparent, as is the case for hexagonal $P6_3cm$ $InMnO_3$, which exhibits no magnetic transition to 5 K, but does show subtle anomalies in χ at 120, 40, and 15 K in fields of H < 0.05 T which correspond to frustration-driven local order.[283, 292]

Fitting χ^{-1} in the temperature range of 200-300 K (where the FC/ZFC curves correlate), gives a strongly negative Weiss constant (θ = -87 K) indicating that antiferromagnetic interactions are present and dominate the local magnetic interactions of $In_2Mn_{1.1}Sn_{0.9}O_6$. The extracted value of the Curie constant from the Curie-Weiss fit, C = 4.34 emu K mol^{-1}, indicates an effective magnetic moment of μ_{eff} = 5.89 μ_B, which is close to the expected spin only moment of high spin d^5 Mn^{2+}(S = 5/2, $\mu_{s.o.}$ = 5.92 μ_B).

At approximately 50 K, χ^{-1} begins to slope away from linearity, as might be expected in advance of a magnetic transition (particularly an AFM transition) which could occur at very low temperature. However, this deviation is also very common in frustrated paramagnetic materials and in spin glasses.[297-299] In this case, the Curie tail region can be linearly fit and compared to the high temperature values (CW_2, **Figure 6.9**) in order to estimate the percentage of paramagnetic defects/clusters or the rough percentage of paramagnetic impurities.[300] The extracted values for the low temperature linear region (below 30 K) are θ = -6.54 K, close to 0 K, and C = 1.71 emu K mol^{-1}. Comparing the Curie constants extracted from the high temperature and low temperature regions estimates that there are almost 39% paramagnetic spins per manganese. Considering the high percentage estimated, it seems unlikely that these paramagnetic spins are from an external impurity and are instead intrinsic to the sample of $In_2Mn_{1.1}Sn_{0.9}O_6$ measured. This could reflect crystallographic disorder preventing long range magnetic exchange between Mn^{2+} cations.

Magnetization vs field (M(H), **Figure 6.10**) measurements were performed from -7 to 7 T at 300 K and 5 K. At 300 K, magnetic interactions are clearly paramagnetic, however at 5 K, the minimum of our measurement range, a slight hysteresis begins to emerge. This hysteresis does not saturate, consistent with an AFM material just above transition (perhaps with some spin canting or FiM component).[83] However, the relatively small maximum of the magnetization (~0.8 μ_B/f.u.) is cause to question whether an AFM transition looms at extremely low temperatures. Instead, perhaps the shape of this curve is due to freezing of some paramagnetic spin clusters, analogous to the phenomenon present in superparamagnets.

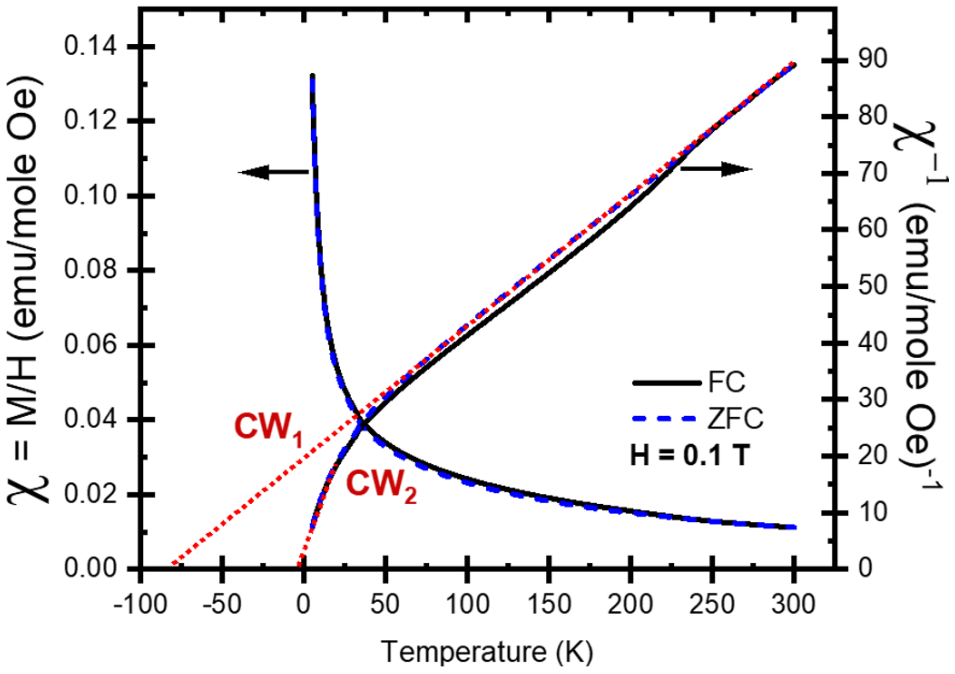

Figure 6.9 The temperature dependent magnetic susceptibility, χ, and inverse susceptibility, χ^{-1}, for $In_2Mn_{1.1}Sn_{0.9}O_6$ measured from 5-300 K at H = 0.1 T under field cooled (solid black) and zero field cooled (dashed blue) conditions. The Curie-Weiss fits of the high temperature (CW_1) and low temperature (CW_2) data are indicated by red dotted lines.

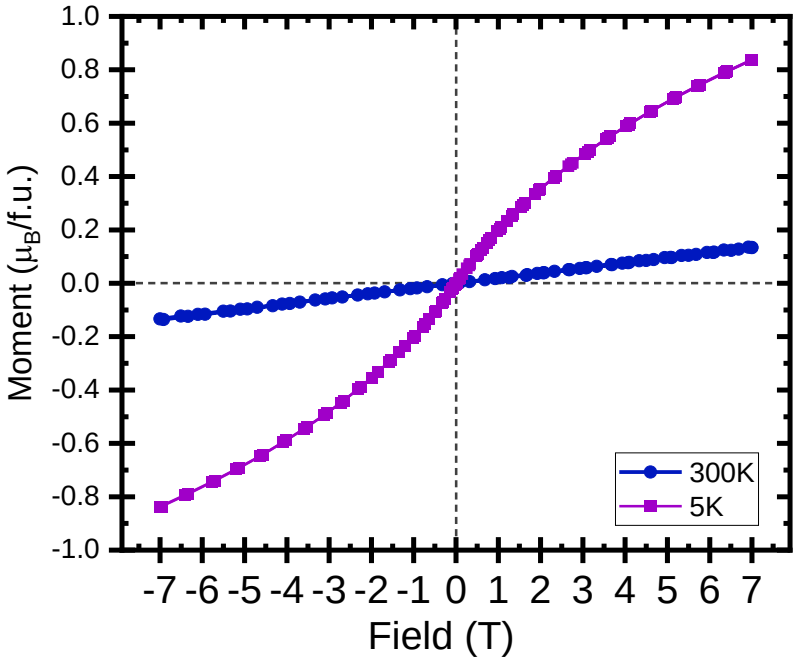

Figure 6.10 Magnetization vs field (M(H)) curves from -7 – 7 T for $In_2Mn_{1.1}Sn_{0.9}O_6$ measured at 5 K (pink squares) and 300 K (purple circles). At 300 K, magnetic interactions are clearly paramagnetic, whereas at 5 K a slight hysteresis, suggestive of AFM ordering or ordering of local paramagnetic clusters, develops, though with a very low maximum saturation.

That $In_2Mn_{1.1}Sn_{0.9}O_6$ exhibits no transition down to 5 K, coupled with the high degree of frustration, is most likely attributed to crystallographic disorder interfering with magnetic exchange. While both isostructural Mn_2FeRuO_6[288] and Fe_3InO_6 have transitions above room temperature (T_N = 400 K and 615 K, respectively), the percentages of MO_6 octahedra occupied by a magnetically active cation (100 % and 75%, respectively) allow for a much higher percentage of magnetic superexchange and even direct exchange interactions when compared with $In_2Mn_{1.1}Sn_{0.9}O_6$ (only ~25% of cations have unpaired *d* electrons). Additionally, the estimated frustration factor for $In_2Mn_{1.1}Sn_{0.9}O_6$ ($f \geq 17$) is very large-larger than any reported frustration factor for double corundum-related phases synthesized at high temperature and pressure of which we are aware (see **Table 6.3** for a representative list). While it has

been proposed that spin polarization can lead to a triangular spin arrangement (that is, geometrically frustrated exchange) oxygen planes in α-Fe_2O_3,[301] the corundum structure type is typically recognized as having no geometric frustration. Instead, frustration in $In_2Mn_{1.1}Sn_{0.9}O_6$ is likely due to disorder, and disorder-based spin glass materials (AKA, quenched paramagnets) often have very large frustration factors.[300, 302-303]

As frustration is often linked to complex magnetic order[274] and interesting or unusual magnetic effects,[282, 286, 304] further investigation into the detailed magnetic structure of $In_2Mn_{1.1}Sn_{0.9}O_6$ is certainly warranted if additional low temperature magnetization measurements confirm the presence of an antiferromagnetic transition or if measurements performed at weaker field or under low field AC magnetization conditions confirm the presence of subtle magnetic anomalies.

Table 6.3 A representative list of double corundum derivatives with known *f* values.

Compound	Space Group	d_A	d_B	$d_{B'}$	$T_{N/C}$	θ	*f*	Reference
$In_2Mn_{1.1}Sn_{0.9}O_6$	$R\bar{3}c$	d^0	d^5	d^0	None to 5 K	-87	17.40*	This work
$InMnO_3$***	$P6_3cm$	d^0	d^4	-	118	-785	6.65	283
Mn_3TeO_6	$R\bar{3}c$	d^5	d^5	d^0	23	-119.6	5.20	305
Mn_2MnWO_6	$R3$	d^5	d^5	d^1	58	-279.2	4.81	112
Zn_2FeTaO_6	$R3c$	d^0	d^5	d^0	22	-94	4.27	116
Mn_2ScTaO_6	$R\bar{3}$	d^5	d^0	d^0	50	-196	3.92	123
Mn_2ScNbO_6	$R\bar{3}$	d^5	d^0	d^0	53	-206	3.89	123
In_2RuFeO_6***	$Ia\bar{3}$	d^0	d^4	d^6	95	-282	2.97	306
$MnSnO_3$	$R3c$	d^5	d^0	-	53	-130	2.45	54
Ni_2InSbO_6	$R3$	d^8	d^0	d^0	76	-184	2.42	251
In_2NiMnO_6***	$P2_1/n$	d^0	d^8	d^3	26	58.3	2.24	76, 287
Ni_2ScSbO_6	$R3$	d^8	d^0	d^0	60	-120	2.00	251
$InCrO_3$***	$Pnma$	d^0	d^3	-	93	-167	1.80	75
Ni_3TeO_6	$R3$	d^8	d^8	d^0	52	-49	0.94	305
In_2RuMnO_6***	$Ia\bar{3}$	d^0	d^4	d^5	46	35.1	0.76	306
Mn_2FeMoO_6	$R3$	d^5	d^5	d^1	337	239.9	0.71	117

*Proposed

**Note that only oxides with reported $T_{N/C}$ and reported θ are listed here.

***These have been included due to similarities to $In_2Mn_{1.1}Sn_{0.9}O_6$ in composition, or due to being discussed earlier.

6.3 Conclusions and Future Work

In conclusion, we have studied in detail the nuclear structure and oxidation states of the new double corundum oxide, $In_2Mn_{1.1}Sn_{0.9}O_6$, which crystalizes in the disordered space group $R\bar{3}c$. Magnetic susceptibility measurements in finite field measured at H = 0.1 T imply that the magnetic structure of $In_2Mn_{1.1}Sn_{0.9}O_6$ is dominated by antiferromagnetic exchange, despite no clear magnetic transition above 5 K. The shape of magnetization vs field measurements between -7 and 7 T indicate

that there is potentially some degree of AFM order present at 5 K, though the maximum saturation is very small, which is more in line with paramagnetism. Likely magnetic contaminates $MnSnO_3$ (in both *R*3*c* and $R\bar{3}c$ polymorphs), $In_2Mn_2O_7$, and Mn_2SnO_4, and were not detected in Reitveld refinements or in SEM/EDX analyses, which combined with the large estimated percentage of paramagnetic spins (~39%) implies that Curie and Weiss constants extracted from susceptibility measurements are the product of magnetic interactions intrinsic to $In_2Mn_{1.1}Sn_{0.9}O_6$ itself. Resistivity measurements were attempted, but the sample was found to be insulating at room temperature.

Future investigations should include M(T) measurements below 5 K and at different fields. Higher field measurements will suppress any potential magnetic impurity contributions, while lower field measurements could reveal subtle magnetic anomalies that could be due to localized magnetic order or even spin freezing. In addition, AC magnetic measurements (measurements performed in a sinusoidally varying magnetic field) can distinguish between a spin glass state or a paramagnetic state if cusps appear in the low-frequency AC measurement. If a transition or subtle anomaly is identified, detailed magnetic structural refinements (neutron powder diffraction) should be performed. These could elucidate the potentially unique magnetic interactions that lead to a potential frustration factor of up to approximately $f = 17$ in this material, which would be the highest frustration factor in a known double corundum derivative to date.

6.4 References

54. Aimi, A.; Katsumata, T.; Mori, D.; Fu, D.; Itoh, M.; Kyômen, T.; Hiraki, K.-i.; Takahashi, T.; Inaguma, Y., High-Pressure Synthesis and Correlation between Structure, Magnetic, and Dielectric Properties in LiNbO3-Type MnMO3 (M = Ti, Sn). Inorganic Chemistry 2011, 50 (13), 6392-6398.
56. Dos santos-García, A. J.; Solana-Madruga, E.; Ritter, C.; Ávila-Brande, D.; Fabelo, O.; Sáez-Puche, R., Synthesis, structures and magnetic properties of the dimorphic Mn2CrSbO6 oxide. Dalton Transactions 2015, 44 (23), 10665-10672.
65. Kanamori, J., Superexchange interaction and symmetry properties of electron orbitals. Journal of Physics and Chemistry of Solids 1959, 10 (2), 87-98.
75. Belik, A.; Yi, W., High-pressure synthesis, crystal chemistry and physics of perovskites with small cations at the A site. Journal of physics. Condensed matter : an Institute of Physics journal 2014, 26, 163201.
76. Yi, W.; Liang, Q.; Matsushita, Y.; Tanaka, M.; Belik, A. A., High-Pressure Synthesis, Crystal Structure, and Properties of In2NiMnO6 with Antiferromagnetic Order and Field-Induced Phase Transition. Inorganic Chemistry 2013, 52 (24), 14108-14115.
83. Frank, C. E.; McCabe, E. E.; Orlandi, F.; Manuel, P.; Tan, X.; Deng, Z.; Croft, M.; Cascos, V.; Emge, T.; Feng, H. L.; Lapidus, S.; Jin, C.; Wu, M.; Li, M. R.; Ehrlich, S.; Khalid, S.; Quackenbush, N.; Yu, S.; Walker, D.; Greenblatt, M., Mn2CoReO6: a robust multisublattice antiferromagnetic perovskite with small A-site cations. Chemical Communications 2019, 55 (23), 3331-3334.
112. Li, M.-R.; McCabe, E. E.; Stephens, P. W.; Croft, M.; Collins, L.; Kalinin, S. V.; Deng, Z.; Retuerto, M.; Sen Gupta, A.; Padmanabhan, H.; Gopalan, V.; Grams, C. P.; Hemberger, J.; Orlandi, F.; Manuel, P.; Li, W.-M.; Jin, C.-Q.; Walker, D.; Greenblatt, M., Magnetostriction-polarization coupling in multiferroic Mn2MnWO6. Nature Communications 2017, 8 (1), 2037.
116. Li, M. R.; Stephens, P. W.; Retuerto, M.; Sarkar, T.; Grams, C. P.; Hemberger, J.; Croft, M. C.; Walker, D.; Greenblatt, M., Designing Polar and Magnetic Oxides: Zn2FeTaO6 - in Search of Multiferroics. Journal of the American Chemical Society 2014, 136 (24), 8508-8511.
117. Li, M. R.; Retuerto, M.; Walker, D.; Sarkar, T.; Stephens, P. W.; Mukherjee, S.; Dasgupta, T. S.; Hodges, J. P.; Croft, M.; Grams, C. P.; Hemberger, J.; Sanchez-Benitez, J.; Huq, A.; Saouma, F. O.; Jang, J. I.; Greenblatt, M., Magnetic-Structure-Stabilized Polarization in an Above-Room-Temperature Ferrimagnet. Angewandte Chemie-International Edition 2014, 53 (40), 10774-10778.
121. Fujita, K.; Kawamoto, T.; Yamada, I.; Hernandez, O.; Hayashi, N.; Akamatsu, H.; Lafargue-Dit-Hauret, W.; Rocquefelte, X.; Fukuzumi, M.; Manuel, P.; Studer, A. J.; Knee, C. S.; Tanaka, K., LiNbO3-Type InFeO3: Room-Temperature Polar Magnet without Second-Order Jahn–Teller Active Ions. Chemistry of Materials 2016, 28 (18), 6644-6655.
123. Feng, H.; Deng, Z.; Croft, M.; Lapidus, S.; Zu, R.; Gopalan, V.; Grams, C.; Hemberger, J.; Liu, S.; Tyson, T.; Frank, C.; Jin, C.; Walker, D.; Greenblatt, M., High-Pressure Synthesis and Ferrimagnetism of Ni3TeO6-Type Mn2ScMO6 (M = Nb, Ta). Inorganic Chemistry 2019.
168. Monesi, C.; Meneghini, C.; Bardelli, F.; Benfatto, M.; Mobilio, S.; Manju, U.; Sarma, D. D., Quantitative structural refinement of MnK edge XANES in LaMnO3 and CaMnO3 perovskites. Nuclear Instruments and Methods in Physics Research Section B: Beam Interactions with Materials and Atoms 2006, 246 (1), 158-164.
169. Naoki, S.; Yoshio, T.; Yoshitaka, Y.; Kiyoshi, S.; Tomoya, U., Direct Speciation of Tin Compounds in Environmental Samples Using Sn K-edge XANES. Chemistry Letters 2004, 33 (3), 264-265.
170. Retuerto, M.; Jiménez-Villacorta, F.; Martínez-Lope, M. J.; Huttel, Y.; Roman, E.; Fernández-Díaz, M. T.; Alonso, J. A., Study of the valence state and electronic

structure in Sr2FeMO6 (M = W, Mo, Re and Sb) double perovskites. Phys. Chem. Chem. Phys. 2010, 12 (41), 13616-13625.
171. Stueben, B. L.; Cantrelle, B.; Sneddon, J.; Beck, J. N., Manganese K-edge XANES studies of Mn speciation in Lac des Allemands as a function of depth. Microchemical Journal 2004, 76 (1), 113-120.
251. Ivanov, S. A.; Mathieu, R.; Nordblad, P.; Tellgren, R.; Ritter, C.; Politova, E.; Kaleva, G.; Mosunov, A.; Stefanovich, S.; Weil, M., Spin and Dipole Ordering in Ni2InSbO6 and Ni2ScSbO6 with Corundum-Related Structure. Chemistry of Materials 2013, 25 (6), 935-945.
263. Nespolo, M.; Ferraris, G., Applied geminography - symmetry analysis of twinned crystals and definition of twinning by reticular polyholohedry. Acta Crystallographica Section A 2004, 60 (1), 89-95.
266. Berry, F. J.; Greaves, C.; Helgason, Ö.; McManus, J.; Palmer, H. M.; Williams, R. T., Structural and Magnetic Properties of Sn-, Ti-, and Mg-Substituted α-Fe2O3: A Study by Neutron Diffraction and Mössbauer Spectroscopy. Journal of Solid State Chemistry 2000, 151 (2), 157-162.
267. Bosi, F., Bond valence at mixed occupancy sites. I. Regular polyhedra. Acta Crystallographica Section B 2014, 70 (5), 864-870.
273. Marrows, C. H.; Chapon, L. C.; Langridge, S., Spintronics and functional materials. Materials Today 2009, 12 (7), 70-77.
274. Ramirez, A., Strongly Geometrically Frustrated Magnets. Annual Review of Materials Science 1994, 24, 453-480.
275. Monod, P.; Préjean, J. J.; Tissier, B., Magnetic hysteresis of CuMn in the spin glass state. Journal of Applied Physics 1979, 50 (B11), 7324-7329.
276. Guchhait, S.; Orbach, R. L., Magnetic Field Dependence of Spin Glass Free Energy Barriers. Physical Review Letters 2017, 118 (15), 157203.
277. Levy, P. M.; Fert, A., Anisotropy induced by nonmagnetic impurities in Cu Mn spin-glass alloys. Physical Review B 1981, 23 (9), 4667-4690.
278. Bramwell, S. T.; Gingras, M. J., Spin ice state in frustrated magnetic pyrochlore materials. Science 2001, 294 (5546), 1495-1501.
279. Schäfer, R.; Hagymási, I.; Moessner, R.; Luitz, D. J., The pyrochlore S= 1/2 Heisenberg antiferromagnet at finite temperature. arXiv preprint arXiv:2003.04898 2020.
280. Khuntia, P.; Velazquez, M.; Barthélemy, Q.; Bert, F.; Kermarrec, E.; Legros, A.; Bernu, B.; Messio, L.; Zorko, A.; Mendels, P., Gapless ground state in the archetypal quantum kagome antiferromagnet ZnCu3(OH)6Cl2. Nature Physics 2020, 16 (4), 469-474.
281. Feng, E.; Xu, X.; Emmanouilidou, E.; Kim, J. W.; Wu, Y.; DING, L.; Kolesnikov, A.; Ni, N.; Cheong, S.-W.; Cao, H., Magnetic structure of the stuffed honeycomb antiferromagnet GdInO3. Bulletin of the American Physical Society 2020.
282. Paul, B.; Chatterjee, S.; Roy, A.; Midya, A.; Mandal, P.; Grover, V.; Tyagi, A., Geometrically frustrated GdInO 3: an exotic system to study negative thermal expansion and spin-lattice coupling. Physical Review B 2017, 95 (5), 054103.
283. Fabrèges, X.; Mirebeau, I.; Petit, S.; Bonville, P.; Belik, A. A., Frustration-driven magnetic order in hexagonal InMnO3. Physical Review B 2011, 84 (5), 054455.
284. Lottermoser, T.; Fiebig, M.; Fröhlich, D.; Leute, S.; Kohn, K., Magnetic structure of hexagonal manganites RMnO3 (R=Sc,Y,Ho,Er,Tm,Yb,Lu). Journal of Magnetism and Magnetic Materials 2001, 226-230, 1131-1133.
285. Ishizuka, H., Temperature-dependent magnetic anisotropy from pseudo-dipolar interactions. Physical Review B 2017, 95 (18), 184413.
286. Hao, X. F.; Xu, Y. H.; Franchini, C.; Gao, F. M., Covalent effects in magnetic ferroelectrics MnMO3 (M = Ti, Sn). Phys. Status Solidi B-Basic Solid State Phys. 2015, 252 (3), 626-634.

287. Terada, N.; Khalyavin, D. D.; Manuel, P.; Yi, W.; Suzuki, H. S.; Tsujii, N.; Imanaka, Y.; Belik, A. A., Ferroelectricity induced by ferriaxial crystal rotation and spin helicity in a B-site-ordered double-perovskite multiferroic In2NiMnO6. Physical Review B 2015, 91 (10).
288. Tan, X.; McCabe, E. E.; Orlandi, F.; Manuel, P.; Batuk, M.; Hadermann, J.; Deng, Z.; Jin, C.; Nowik, I.; Herber, R.; Segre, C. U.; Liu, S.; Croft, M.; Kang, C.-J.; Lapidus, S.; Frank, C. E.; Padmanabhan, H.; Gopalan, V.; Wu, M.; Li, M.-R.; Kotliar, G.; Walker, D.; Greenblatt, M., MnFe0.5Ru0.5O3: an above-room-temperature antiferromagnetic semiconductor. Journal of Materials Chemistry C 2019, 7 (3), 509-522.
289. Dang, M. Z.; Rancourt, D. G.; Dutrizac, J. E.; Lamarche, G.; Provencher, R., Interplay of surface conditions, particle size, stoichiometry, cell parameters, and magnetism in synthetic hematite-like materials. Hyperfine Interactions 1998, 117 (1), 271-319.
290. Martínez-Lope, M. J.; Retuerto, M.; de la Calle, C.; Porcher, F.; Alonso, J. A., Why MnIn2O4 spinel is not a transparent conducting oxide? Journal of Solid State Chemistry 2012, 187, 172-176.
291. Belik, A. A.; Matsushita, Y.; Tanaka, M.; Takayama-Muromachi, E., (In1−yMny)MnO3 (1/9≤y≤1/3): Unusual Perovskites with Unusual Properties. Angewandte Chemie International Edition 2010, 49 (42), 7723-7727.
292. Greedan, J. E.; Bieringer, M.; Britten, J. F.; Giaquinta, D. M.; zur Loye, H. C., Synthesis, Crystal Structure, and Unusual Magnetic Properties of InMnO3. Journal of Solid State Chemistry 1995, 116 (1), 118-130.
293. Regulski, M.; Przeniosło, R.; Sosnowska, I.; Hohlwein, D.; Schneider, R., Neutron diffraction study of the magnetic structure of α-Mn2O3. Journal of Alloys and Compounds 2004, 362 (1), 236-240.
294. Tackett, R.; Lawes, G.; Melot, B. C.; Grossman, M.; Toberer, E. S.; Seshadri, R., Magnetodielectric coupling in Mn3O4. Physical Review B 2007, 76 (2), 024409.
295. Roth, W., Magnetic structures of MnO, FeO, CoO, and NiO. Physical Review 1958, 110 (6), 1333.
296. Shimakawa, Y.; Kubo, Y.; Hamada, N.; Jorgensen, J. D.; Hu, Z.; Short, S.; Nohara, M.; Takagi, H., Crystal structure, magnetic and transport properties, and electronic band structure of A2Mn2O7 pyrochlores (A = Y, In, Lu, and Tl). Physical Review B 1999, 59 (2), 1249-1254.
297. Feng, H. L.; Jansen, M., Ba3CuOs2O9 and Ba3ZnOs2O9, a comparative study. Journal of Solid State Chemistry 2018, 258, 776-780.
298. Li, M.-R.; Deng, Z.; Lapidus, S. H.; Stephens, P. W.; Segre, C. U.; Croft, M.; Paria Sena, R.; Hadermann, J.; Walker, D.; Greenblatt, M., Ba3(Cr0.97(1)Te0.03(1))2TeO9: in Search of Jahn–Teller Distorted Cr(II) Oxide. Inorganic Chemistry 2016, 55 (20), 10135-10142.
299. Hiroi, Z.; Yoshida, H.; Okamoto, Y.; Takigawa, M. In Spin-1/2 kagome compounds: volborthite vs herbertsmithite, Journal of Physics: Conference Series, IOP Publishing: 2009; p 012002.
300. Wang, C.-H.; Avdeev, M.; Kennedy, B. J.; Küpers, M.; Ling, C. D., YCa3(CrO)3(BO3)4: A Cr3+ Kagomé Lattice Compound Showing No Magnetic Order down to 2 K. Inorganic Chemistry 2016, 55 (15), 7535-7541.
301. Theissmann, R.; Fuess, H.; Tsuda, K., Experimental charge density of hematite in its magnetic low temperature and high temperature phases. Ultramicroscopy 2012, 120, 1-9.
302. Fischer, K. H.; Hertz, J. A., Spin glasses. Cambridge university press: 1993; Vol. 1.
303. Binder, K.; Young, A. P., Spin glasses: Experimental facts, theoretical concepts, and open questions. Reviews of Modern Physics 1986, 58 (4), 801-976.

304. Zhong, R.; Guo, S.; Xu, G.; Xu, Z.; Cava, R. J., Strong quantum fluctuations in a quantum spin liquid candidate with a Co-based triangular lattice. Proceedings of the National Academy of Sciences 2019, 116 (29), 14505-14510.
305. Mathieu, R.; Ivanov, S. A.; Nordblad, P.; Weil, M., Enhancement of antiferromagnetic interaction and transition temperature in M3TeO6 systems (M = Mn, Co, Ni, Cu). Eur. Phys. J. B 2013, 86 (8), 361.
306. de la Calle, C.; Martínez-Lope, M. J.; Pomjakushin, V.; Porcher, F.; Alonso, J. A., Structure and magnetic properties of In2RuMnO6 and In2RuFeO6 : Heavily transition-metal doped In2O3 -type bixbyites. Solid State Communications 2012, 152 (2), 95-99.